

**Electrolytic Reduction of SiO<sub>2</sub>  
at Liquid Zn Cathode in Molten Salts  
and Precipitation of Si from Liquid Si–Zn Alloy**

Yuanjia Ma

2022



# Contents

|   |             |
|---|-------------|
| <b>Contents</b> .....   | <b>i</b>    |
| <b>List of Tables</b> .....   | <b>v</b>    |
| <b>List of Figures</b> .....  | <b>viii</b> |
| <b>Chapter 1 General Introduction</b> .....   | <b>1</b>    |
| 1.1 Energy Trend and Situation of Solar Photovoltaic Power .....  | 1           |
| 1.2 Solar Photovoltaic Power Generation .....   | 4           |
| 1.3 Current Commercial Production Processes of Solar-grade Silicon .....  | 6           |
| 1.4 Studies on Next-generation SOG-Si Production Processes .....  | 7           |
| 1.4.1 Purification of MG-Si.....  | 7           |
| 1.4.1.1 Electrorefining of MG-Si in Molten Salts .....  | 8           |
| 1.4.1.2 Solvent Refining of MG-Si .....   | 9           |
| 1.4.2 Metallothermic Reduction of Silicon Halides .....   | 11          |
| 1.4.2.1 Zincothermic reduction .....  | 12          |
| 1.4.2.2 Aluminothermic reduction .....  | 14          |
| 1.4.3 Electrochemical Reduction of SiO <sub>2</sub> in Molten Salts .....   | 15          |
| 1.4.3.1 Electrochemical Reduction of Solid SiO <sub>2</sub> .....   | 15          |
| 1.4.3.2 Electrodeposition of Si from Dissolved SiO <sub>2</sub> .....   | 19          |
| 1.5 Background and Purposes of This Study .....   | 22          |
| 1.5.1 Background.....   | 22          |
| 1.5.1.1 Issues of the Conventional Electrochemical Reduction of SiO <sub>2</sub> .....  | 22          |
| 1.5.1.2 A New SOG-Si Production Process Using Electrochemical Reduction of Solid SiO <sub>2</sub> at a Liquid Zn Cathode .....  | 22          |
| 1.5.2 Purposes of This Study.....   | 24          |
| 1.5.2.1 Electrochemical Reduction of Solid SiO <sub>2</sub> at a Liquid Zn Electrode in Molten CaCl <sub>2</sub> .....          | 24          |
| 1.5.2.2 Electrochemical Reduction of Dissolved SiO <sub>2</sub> at a Liquid Zn Electrode in Molten CaCl <sub>2</sub> .....      | 24          |
| 1.5.2.3 Electrochemical Reduction of Dissolved SiO <sub>2</sub> at a Liquid Zn Electrode in Molten NaCl–CaCl <sub>2</sub> ..... | 25          |
| 1.5.2.4 Silicon Refining by Solidification from Liquid Si–Zn Alloy and Floating Zone  |             |

|                                  |    |
|----------------------------------|----|
| Method.....                      | 26 |
| 1.6 Overview of This Study ..... | 26 |
| 1.7 Reference List .....         | 28 |

**Chapter 2 Mechanism of Electrochemical Reduction of SiO<sub>2</sub> at a Liquid Zn Electrode in Molten CaCl<sub>2</sub>.....38**

|   |    |
|---|----|
| 2.1 Introduction.....   | 38 |
| 2.2 Experimental .....  | 38 |
| 2.2.1 Cyclic Voltammetry .....                                      | 38 |
| 2.2.2 Electrochemical Reduction of SiO <sub>2</sub> Plates .....    | 40 |
| 2.2.3 Electrochemical Reduction of SiO <sub>2</sub> Particles ..... | 41 |
| 2.3 Results and Discussion.....                                     | 42 |
| 2.3.1 Cyclic Voltammetry .....                                      | 42 |
| 2.3.2 Electrochemical Reduction of SiO <sub>2</sub> Plates .....    | 43 |
| 2.3.3 Electrochemical Reduction of SiO <sub>2</sub> Particles ..... | 45 |
| 2.4 Conclusion .....  | 47 |
| 2.5 Reference List .....  | 48 |

**Chapter 3 Raman Analysis and Electrochemical Reduction of Silicate Ions in Molten CaCl<sub>2</sub>.....50**

|  |    |
|--|----|
| 3.1 Introduction.....  | 50 |
| 3.2 Experimental .....   | 51 |
| 3.2.1 Raman Spectroscopy of Silicate Ions .....                                      | 51 |
| 3.2.2 Electrochemical Reduction of Silicate Ions at a Solid Graphite Electrode ..... | 52 |
| 3.2.3 Electrochemical Reduction of Silicate Ions at a Liquid Zn Electrode .....      | 54 |
| 3.3 Results and Discussion.....  | 54 |
| 3.3.1 Ionic Species of Silicates .....   | 54 |
| 3.3.2 Electrochemical Reduction of Silicate Ions at a Solid Graphite Electrode ..... | 58 |
| 3.3.2.1 Cyclic Voltammetry .....   | 58 |
| 3.3.2.2 Potentiostatic Electrolysis .....  | 61 |
| 3.3.3 Electrochemical Reduction of Silicate Ions at a Liquid Zn Electrode .....      | 67 |
| 3.3.3.1 Cyclic Voltammetry .....   | 67 |
| 3.3.3.2 Potentiostatic Electrolysis .....  | 69 |
| 3.4 Conclusion .....   | 75 |
| 3.5 Reference List .....   | 76 |

## **Chapter 4 Raman Analysis and Electrochemical Reduction of Silicate Ions in Molten NaCl–CaCl<sub>2</sub> .....78**

|         |  |    |
|---------|--|----|
| 4.1     | Introduction .....   | 78 |
| 4.2     | Experimental .....   | 78 |
| 4.2.1   | Raman Spectroscopy of Silicate Ions .....                              | 79 |
| 4.2.2   | Electrochemical Window of Molten Eutectic NaCl–CaCl <sub>2</sub> ..... | 79 |
| 4.2.3   | Electrochemical Reduction of Silicate Ions .....                       | 79 |
| 4.3     | Results and Discussion.....  | 80 |
| 4.3.1   | Ionic Species of Silicates.....  | 80 |
| 4.3.2   | Electrochemical Window of Molten Eutectic NaCl–CaCl <sub>2</sub> ..... | 83 |
| 4.3.3   | Electrochemical Reduction of Silicate Ions .....                       | 85 |
| 4.3.3.1 | Cyclic Voltammetry at 1023 K.....                                      | 85 |
| 4.3.3.2 | Potentiostatic Electrolysis at 1023 K.....                             | 87 |
| 4.3.3.3 | Potentiostatic Electrolysis at 1123 K.....                             | 93 |
| 4.4     | Conclusion .....   | 98 |
| 4.5     | Reference List .....   | 99 |

## **Chapter 5 Electrochemical Reduction of Silicate Ions at a Liquid Zn Electrode in Molten NaCl–CaCl<sub>2</sub> .....100**

|         |                                   |     |
|---------|-----------------------------------|-----|
| 5.1     | Introduction .....                | 100 |
| 5.2     | Experimental .....                | 100 |
| 5.3     | Results and Discussion.....       | 102 |
| 5.3.1   | Cyclic Voltammetry .....          | 102 |
| 5.3.1.1 | Voltammetry at 1023 K .....       | 102 |
| 5.3.1.2 | Voltammetry at 1123 K.....        | 104 |
| 5.3.2   | Potentiostatic Electrolysis ..... | 106 |
| 5.3.2.1 | Electrolysis at 1023 K .....      | 106 |
| 5.3.2.2 | Electrolysis at 1123 K .....      | 112 |
| 5.4     | Conclusion .....                  | 118 |
| 5.5     | Reference List .....              | 119 |

## **Chapter 6 Silicon Refining by Solidification from Liquid Si–Zn Alloy and Floating Zone Method .....120**

|       |  |     |
|-------|--|-----|
| 6.1   | Introduction .....   | 120 |
| 6.2   | Experimental .....   | 120 |
| 6.2.1 | Si Refining by Solidification from Liquid Si–Zn Alloy..... | 120 |

|                             |  |            |
|-----------------------------|--|------------|
| 6.2.2                       | Si Refinement and Zn Evaporation by the FZ Method .....  | 122        |
| 6.2.3                       | Impurity Analysis of Si Samples .....  | 122        |
| 6.3                         | Thermodynamic Calculations .....   | 123        |
| 6.4                         | Results and Discussion.....  | 130        |
| 6.4.1                       | Si Refining by Solidification from Liquid Si–Zn Alloy and the FZ Method.....                                       | 130        |
| 6.4.2                       | Impurity Analysis of Si Samples .....  | 132        |
| 6.5                         | Conclusion .....   | 135        |
| 6.6                         | Reference List .....   | 135        |
| <b>Chapter 7</b>            | <b>General Conclusion .....</b>  | <b>139</b> |
| <b>List of Publications</b> | <b>.....</b>   | <b>144</b> |
| <b>Appendix</b>             | <b>.....</b>   | <b>145</b> |
| A.1                         | Previous Studies on the Electrochemical Reduction of SiO <sub>2</sub> for the Production of Other Si Products..... | 145        |
| A.1.1                       | Electrochemical Reduction of SiO <sub>2</sub> for the Production of Si Nanomaterials.....                          | 145        |
| A.1.2                       | Electrochemical Reduction of SiO <sub>2</sub> for the Production of Si Compounds.....                              | 147        |
| A.2                         | Effect of Cooling Rate on Precipitation Behavior of Si from Liquid Si–Zn Alloy .....                               | 149        |
| A.2.1                       | Experimental.....  | 149        |
| A.2.2                       | Results and Discussion .....   | 151        |
| A.3                         | Si Recovery from Liquid Si–Zn Alloy by Si Precipitation on Si Rod.....   | 156        |
| A.3.1                       | Experimental.....  | 156        |
| A.3.2                       | Results and Discussion .....   | 157        |
| A.4                         | Reference List .....   | 161        |
| <b>Acknowledgement.....</b> | <b>.....</b>   | <b>164</b> |

## List of Tables

|           |   |
|-----------|---|
| Table 1-1 | Lifecycle CO <sub>2</sub> emissions by electricity supply technologies (gCO <sub>2</sub> -eq kWh <sup>-1</sup> ) [2]. . 2   |
| Table 1-2 | Highest conversion efficiencies and features of solar photovoltaic cell technologies [6, 7]. ..... 5  |
| Table 1-3 | Previous studies on electrorefining of MG-Si in molten salts. .... 9  |
| Table 1-4 | Previous studies on solvent refining with various Si–metal solvent..... 11  |
| Table 1-5 | Si production process based on zincothermic reduction of SiCl <sub>4</sub> [132]. ..... 14  |
| Table 1-6 | Si production process based on aluminothermic reduction of SiCl <sub>4</sub> [132]. ..... 15  |
| Table 1-7 | Previous studies on the electrochemical reduction of solid SiO <sub>2</sub> in chloride-based molten salts. .... 17   |
| Table 1-8 | Previous studies on the electrodeposition of Si from SiO <sub>2</sub> in chloride-based molten salts..... 20  |
| Table 1-9 | Previous studies on the electrodeposition of Si from SiO <sub>2</sub> in fluoride-based and fluoride–chloride mixture molten salts. .... 21   |
| Table 2-1 | Impurity contents of Si granules obtained after acid leaching, and target levels for primary Si of SOG-Si. The electrochemical reduction of SiO <sub>2</sub> particles was conducted at 0.6 V for 50 h at a liquid Zn electrode in molten CaCl <sub>2</sub> at 1123 K..... 47   |
| Table 3-1 | Deconvolved wavenumbers of Raman spectra for samples obtained in molten CaCl <sub>2</sub> with the addition of (i) 4.0 mol% of CaSiO <sub>3</sub> ( $r_{O^{2-}/SiO_2} = 1.0$ ), (ii) 2.0 mol% of CaO and 4.0 mol% of CaSiO <sub>3</sub> ( $r_{O^{2-}/SiO_2} = 1.5$ ), and (iii) 4.0 mol% of CaO and 4.0 mol% of CaSiO <sub>3</sub> ( $r_{O^{2-}/SiO_2} = 2.0$ ) at 1123 K..... 57   |
| Table 3-2 | Standard Gibbs energies for the decomposition reactions of CaSiO <sub>3</sub> ( <i>s</i> ), Ca <sub>3</sub> Si <sub>2</sub> O <sub>7</sub> ( <i>s</i> ) and Ca <sub>2</sub> SiO <sub>4</sub> ( <i>s</i> ) to Si( <i>s</i> ), CaO( <i>l</i> ), and O <sub>2</sub> ( <i>g</i> ) at 1123 K. .... 61  |
| Table 3-3 | XRD results for the samples obtained in molten CaCl <sub>2</sub> with the addition of (i) 4.0 mol% of CaSiO <sub>3</sub> ( $r_{O^{2-}/SiO_2} = 1.0$ ), (ii) 2.0 mol% of CaO and 4.0 mol% of CaSiO <sub>3</sub> ( $r_{O^{2-}/SiO_2} = 1.5$ ), and (iii) 4.0 mol% of CaO and 4.0 mol% of CaSiO <sub>3</sub> ( $r_{O^{2-}/SiO_2} = 2.0$ ) at 1123 K. .... 65   |
| Table 3-4 | Weight of the recovered Si, current efficiency, and Ca concentration in the Zn electrodes after the electrolysis conducted in molten CaCl <sub>2</sub> with the addition of (i) 4.0 mol% of CaSiO <sub>3</sub> ( $r_{O^{2-}/SiO_2} = 1.0$ ), (ii) 2.0 mol% of CaO and 4.0 mol% of CaSiO <sub>3</sub> ( $r_{O^{2-}/SiO_2} = 1.5$ ), and (iii) 4.0 mol% of CaO and 4.0 mol% of CaSiO <sub>3</sub> ( $r_{O^{2-}/SiO_2} = 2.0$ ) at 1123 K. Charge: –590.3 C (theoretical formation of 1.0 mol% Si–Zn alloy). .... 73 |
| Table 4-1 | Deconvolved wavenumbers of Raman spectra for samples obtained in molten NaCl–CaCl <sub>2</sub> with the addition of (i) 1.0 mol% of CaSiO <sub>3</sub> ( $r_{O^{2-}/SiO_2} = 1.0$ ), (ii) 0.5 mol% of CaO and 1.0 mol% of CaSiO <sub>3</sub> ( $r_{O^{2-}/SiO_2} = 1.5$ ), and (iii) 1.0 mol% of CaO and 1.0  |

|           |   |     |
|-----------|---|-----|
|           | mol% of CaSiO <sub>3</sub> ( $r_{O^{2-}/SiO_2} = 2.0$ ) at 1023 K. ....   | 83  |
| Table 4-2 | Standard Gibbs energies for the decomposition reactions of CaSiO <sub>3</sub> (s) and Ca <sub>2</sub> SiO <sub>4</sub> (s) to Si(s), CaO(l), and O <sub>2</sub> (g) at 1023 K. ....   | 91  |
| Table 4-3 | XRD results for the samples obtained in molten NaCl–CaCl <sub>2</sub> with the addition of (i) 1.0 mol% of CaSiO <sub>3</sub> ( $r_{O^{2-}/SiO_2} = 1.0$ ), (ii) 0.5 mol% of CaO and 1.0 mol% of CaSiO <sub>3</sub> ( $r_{O^{2-}/SiO_2} = 1.5$ ), and (iii) 1.0 mol% of CaO and 1.0 mol% of CaSiO <sub>3</sub> ( $r_{O^{2-}/SiO_2} = 2.0$ ) at 1023 K. Charge density: $-14 \text{ C cm}^{-2}$ . ....   | 92  |
| Table 4-4 | XRD results for the samples obtained in molten NaCl–CaCl <sub>2</sub> with the addition of (i) 1.0 mol% of CaSiO <sub>3</sub> ( $r_{O^{2-}/SiO_2} = 1.0$ ), (ii) 0.5 mol% of CaO and 1.0 mol% of CaSiO <sub>3</sub> ( $r_{O^{2-}/SiO_2} = 1.5$ ), and (iii) 1.0 mol% of CaO and 1.0 mol% of CaSiO <sub>3</sub> ( $r_{O^{2-}/SiO_2} = 2.0$ ) at 1123 K. Charge density: $-14 \text{ C cm}^{-2}$ . ....   | 97  |
| Table 5-1 | Weight of the recovered Si particles and the current efficiency calculated from Si weight after the electrolysis conducted in molten NaCl–CaCl <sub>2</sub> with the addition of (i) 1.0 mol% of CaSiO <sub>3</sub> ( $r_{O^{2-}/SiO_2} = 1.0$ ), (ii) 0.5 mol% of CaO and 1.0 mol% of CaSiO <sub>3</sub> ( $r_{O^{2-}/SiO_2} = 1.5$ ), and (iii) 1.0 mol% of CaO and 1.0 mol% of CaSiO <sub>3</sub> ( $r_{O^{2-}/SiO_2} = 2.0$ ) at 1023 K. Charge: $-413.2 \text{ C}$ (theoretical formation of 1.0 mol% Si–Zn alloy). .. | 110 |
| Table 5-2 | Concentrations of Ca and Na in the Zn electrodes after the electrolysis conducted in molten NaCl–CaCl <sub>2</sub> with the addition of (i) 1.0 mol% of CaSiO <sub>3</sub> ( $r_{O^{2-}/SiO_2} = 1.0$ ), (ii) 0.5 mol% of CaO and 1.0 mol% of CaSiO <sub>3</sub> ( $r_{O^{2-}/SiO_2} = 1.5$ ), and (iii) 1.0 mol% of CaO and 1.0 mol% of CaSiO <sub>3</sub> ( $r_{O^{2-}/SiO_2} = 2.0$ ) at 1023 K. Charge: $-413.2 \text{ C}$ (theoretical formation of 1.0 mol% Si–Zn alloy). ....  | 111 |
| Table 5-3 | Weight of the recovered Si particles and the current efficiency calculated from Si weight after the electrolysis conducted in molten NaCl–CaCl <sub>2</sub> with the addition of (i) 1.0 mol% of CaSiO <sub>3</sub> ( $r_{O^{2-}/SiO_2} = 1.0$ ), (ii) 0.5 mol% of CaO and 1.0 mol% of CaSiO <sub>3</sub> ( $r_{O^{2-}/SiO_2} = 1.5$ ), and (iii) 1.0 mol% of CaO and 1.0 mol% of CaSiO <sub>3</sub> ( $r_{O^{2-}/SiO_2} = 2.0$ ) at 1123 K. Charge: $-590.3 \text{ C}$ (theoretical formation of 1.0 mol% Si–Zn alloy). .. | 116 |
| Table 5-4 | Concentrations of Ca and Na in the Zn electrodes after the electrolysis conducted in molten NaCl–CaCl <sub>2</sub> with the addition of (i) 1.0 mol% of CaSiO <sub>3</sub> ( $r_{O^{2-}/SiO_2} = 1.0$ ), (ii) 0.5 mol% of CaO and 1.0 mol% of CaSiO <sub>3</sub> ( $r_{O^{2-}/SiO_2} = 1.5$ ), and (iii) 1.0 mol% of CaO and 1.0 mol% of CaSiO <sub>3</sub> ( $r_{O^{2-}/SiO_2} = 2.0$ ) at 1123 K. Charge: $-590.3 \text{ C}$ (theoretical formation of 1.0 mol% Si–Zn alloy). ....  | 116 |
| Table 6-1 | Equilibrated phases with saturated solid Si or liquid Zn at 923 K and their standard Gibbs energy of formation at 923 K. ....   | 125 |
| Table 6-2 | Solubility of each impurity element in solid Si and liquid Zn at 923 K. ....  | 127 |
| Table 6-3 | Activity coefficient of each impurity element at infinite dilution in the solid Si and the liquid Zn with the standard states of their stable phase and distribution coefficient between the solid Si and the liquid Zn at 923 K. ....  | 129 |



|             |  |     |
|-------------|--|-----|
| Table 6-4   | Impurity contents in Si samples with removal fractions and acceptable impurity levels for SOG-Si. ....   | 133 |
| Table A.1-1 | Previous studies on the formation of Si nanomaterials using electrochemical reduction of SiO <sub>2</sub> in molten salts. ....  | 146 |
| Table A.1-2 | Previous studies on the formation of Si compounds using electrochemical reduction of SiO <sub>2</sub> in molten salts. ....  | 148 |
| Table A.2-1 | Impurity contents with removal fractions in the precipitated Si with different particle sizes at the cooling rate of 10 K h <sup>-1</sup> . ....   | 153 |
| Table A.2-2 | Impurity contents with removal fractions in the precipitated Si (>2 mm) obtained at different cooling rates, target impurity levels for primary Si, and acceptable impurity levels for solar-grade Si (SOG-Si). .... | 155 |
| Table A.3-1 | Size of graphite crucible and weight of used materials.....  | 157 |
| Table A.3-2 | Impurity contents with removal fractions in the precipitated Si recovered from the Si rod obtained in Experiment 2, and the target impurity levels for primary Si. ....  | 160 |

# List of Figures

|             |  |    |
|-------------|--|----|
| Figure 1-1  | World primary energy consumption from 1971 to 2019 by power sources (TWh) [1].<br>.....  | 1  |
| Figure 1-2  | Global solar PV and wind power capacity additions from 2010 to 2020 [4].   | 3  |
| Figure 1-3  | Total primary energy changes in Stated Policies Scenario (STEPS) and Sustainable Development Scenario (SDS) from 2019 to 2030 [5].   | 4  |
| Figure 1-4  | Ratio of solar photovoltaic cells production by type of cells in 2020 [9].   | 5  |
| Figure 1-5  | Flowchart of the SOG-Si production containing the Siemens process [11, 12].  | 6  |
| Figure 1-6  | Flowchart of the DuPont process [104–108].   | 13 |
| Figure 1-7  | Flowchart of the metallothermic reduction of $\text{SiCl}_4$ with the recycling of $\text{ZnCl}_2$ [111, 112].   | 13 |
| Figure 1-8  | Optical images of the contacting electrode (a) before and (b) after the electrochemical reduction [134].   | 16 |
| Figure 1-9  | Schematic drawing of SOG-Si production process using electrochemical reduction of solid $\text{SiO}_2$ at a liquid Zn cathode [185, 186].  | 23 |
| Figure 1-10 | Phase diagram for the NaCl–CaCl <sub>2</sub> system [188].   | 25 |
| Figure 2-1  | Schematic illustration of the electrolysis cell for the investigation of $\text{SiO}_2$ reduction behavior at a liquid Zn electrode. (a) $\text{Ag}^+/\text{Ag}$ reference electrode, (b) $\text{Ca}^{2+}/\text{Ca}$ dynamic reference electrode on a Mo wire, (c) liquid Zn electrode with $\text{Al}_2\text{O}_3/\text{SiO}_2$ tube, (d) graphite counter electrode, (e) $\text{Al}_2\text{O}_3$ crucible, (f) molten $\text{CaCl}_2$ , (g) small $\text{Al}_2\text{O}_3$ crucible, and (h) liquid Zn. | 39 |
| Figure 2-2  | Schematic illustrations of the liquid Zn electrodes for (a) cyclic voltammetry, and (b) electrochemical reduction of $\text{SiO}_2$ plate.   | 40 |
| Figure 2-3  | Schematic illustration of the electrolysis cell for the electrochemical reduction of $\text{SiO}_2$ particles. (a) $\text{Ag}^+/\text{Ag}$ reference electrode, (b) $\text{Ca}^{2+}/\text{Ca}$ dynamic reference electrode on a Mo wire, (c) W lead wire, (d) graphite counter electrode, (e) $\text{Al}_2\text{O}_3$ crucible, (f) molten $\text{CaCl}_2$ , (g) $\text{SiO}_2$ particle, and (h) liquid Zn.   | 41 |
| Figure 2-4  | Cyclic voltammograms at liquid Zn electrodes with an $\text{Al}_2\text{O}_3$ tube or a $\text{SiO}_2$ tube (left axis) and at a Si plate electrode (right axis) in molten $\text{CaCl}_2$ at 1123 K. Scan rate: $100 \text{ mV s}^{-1}$ .  | 42 |
| Figure 2-5  | Optical images of the $\text{SiO}_2$ plates after electrolysis at the liquid Zn electrode or immersion into liquid Zn for 30 min in molten $\text{CaCl}_2$ at 1123 K. (a) potentiostatic electrolysis at 0.9 V, (b) immersion after electrolysis (a), (c) potentiostatic electrolysis at 0.6 V, and (d) immersion after electrolysis (c).  | 44 |
| Figure 2-6  | (a) Optical image and (b) XRD pattern of the Si granules obtained after acid leaching  |    |

|            |   |    |
|------------|---|----|
|            | of Zn ingot. The electrochemical reduction of SiO <sub>2</sub> particles was conducted at a liquid Zn electrode at 0.6 V for 50 h in molten CaCl <sub>2</sub> at 1123 K. ....   | 46 |
| Figure 3-1 | Schematic drawing of experimental apparatus for Raman spectroscopy of molten salt. ....   | 52 |
| Figure 3-2 | Schematic drawing of the electrolysis cell. (a) Si quasi-reference electrode, (b) Ca <sup>2+</sup> /Ca dynamic reference electrode on a Mo wire, (c) flag-shaped graphite working electrode, (d) liquid Zn working electrode, (e) glass-like carbon counter electrode, (f) graphite counter electrode, (g) graphite holder, (h) graphite crucible, and (i) molten CaCl <sub>2</sub> containing CaO and CaSiO <sub>3</sub> . ....  | 53 |
| Figure 3-3 | Raman spectra for the salts (a) immediately after heated to 1123 K, and (b) kept at 1123 K for 1 day beforehand for the dissolution of silicate-ion sources. Salts (1): molten CaCl <sub>2</sub> containing 1.0 mol% CaO and 1.0 mol% SiO <sub>2</sub> ( $r_{O^{2-}/SiO_2} = 1.0$ ), and (2): molten CaCl <sub>2</sub> containing 1.0 mol% CaSiO <sub>3</sub> ( $r_{O^{2-}/SiO_2} = 1.0$ ). ....                                  | 55 |
| Figure 3-4 | Original and deconvolved Raman spectra for molten CaCl <sub>2</sub> with the addition of (a) 4.0 mol% of CaSiO <sub>3</sub> ( $r_{O^{2-}/SiO_2} = 1.0$ ), (b) 2.0 mol% of CaO and 4.0 mol% of CaSiO <sub>3</sub> ( $r_{O^{2-}/SiO_2} = 1.5$ ), and (c) 4.0 mol% of CaO and 4.0 mol% of CaSiO <sub>3</sub> ( $r_{O^{2-}/SiO_2} = 2.0$ ) at 1123 K. ....  | 56 |
| Figure 3-5 | Cyclic voltammograms at a graphite electrode in molten CaCl <sub>2</sub> before and after the addition of (a) 4.0 mol% of CaSiO <sub>3</sub> ( $r_{O^{2-}/SiO_2} = 1.0$ ), (b) 2.0 mol% of CaO and 4.0 mol% of CaSiO <sub>3</sub> ( $r_{O^{2-}/SiO_2} = 1.5$ ), and (c) 4.0 mol% of CaO and 4.0 mol% of CaSiO <sub>3</sub> ( $r_{O^{2-}/SiO_2} = 2.0$ ) at 1123 K. Scan rate: 50 mV s <sup>-1</sup> . R. P.: Rest potential. .... | 59 |
| Figure 3-6 | Current transient curves during the potentiostatic electrolysis at graphite plates in molten CaCl <sub>2</sub> with the addition of (a) 4.0 mol% of CaSiO <sub>3</sub> ( $r_{O^{2-}/SiO_2} = 1.0$ ), (b) 2.0 mol% of CaO and 4.0 mol% of CaSiO <sub>3</sub> ( $r_{O^{2-}/SiO_2} = 1.5$ ), and (c) 4.0 mol% of CaO and 4.0 mol% of CaSiO <sub>3</sub> ( $r_{O^{2-}/SiO_2} = 2.0$ ) at 1123 K. ....                                 | 62 |
| Figure 3-7 | Optical images of the samples obtained by electrolysis at graphite plates in molten CaCl <sub>2</sub> with the addition of (i) 4.0 mol% of CaSiO <sub>3</sub> ( $r_{O^{2-}/SiO_2} = 1.0$ ), (ii) 2.0 mol% of CaO and 4.0 mol% of CaSiO <sub>3</sub> ( $r_{O^{2-}/SiO_2} = 1.5$ ), and (iii) 4.0 mol% of CaO and 4.0 mol% of CaSiO <sub>3</sub> ( $r_{O^{2-}/SiO_2} = 2.0$ ) at 1123 K. ....                                       | 63 |
| Figure 3-8 | XRD patterns of the samples obtained by electrolysis at graphite plates in molten CaCl <sub>2</sub> with the addition of (i) 4.0 mol% of CaSiO <sub>3</sub> ( $r_{O^{2-}/SiO_2} = 1.0$ ), (ii) 2.0 mol% of CaO and 4.0 mol% of CaSiO <sub>3</sub> ( $r_{O^{2-}/SiO_2} = 1.5$ ), and (iii) 4.0 mol% of CaO and 4.0 mol% of CaSiO <sub>3</sub> ( $r_{O^{2-}/SiO_2} = 2.0$ ) at 1123 K. ....   | 64 |
| Figure 3-9 | SEM images of the samples obtained by electrolysis at graphite plates in molten CaCl <sub>2</sub> with the addition of (i) 4.0 mol% of CaSiO <sub>3</sub> ( $r_{O^{2-}/SiO_2} = 1.0$ ), (ii) 2.0 mol% of CaO and 4.0 mol% of CaSiO <sub>3</sub> ( $r_{O^{2-}/SiO_2} = 1.5$ ), and (iii) 4.0 mol% of CaO and 4.0 mol% of CaSiO <sub>3</sub> ( $r_{O^{2-}/SiO_2} = 2.0$ ) at 1123 K. ....   | 66 |

|             |   |    |
|-------------|---|----|
| Figure 3-10 | Cyclic voltammograms at a liquid Zn electrode in molten CaCl <sub>2</sub> before and after the addition of (a) 4.0 mol% of CaSiO <sub>3</sub> ( $r_{O^{2-}/SiO_2} = 1.0$ ), (b) 2.0 mol% of CaO and 4.0 mol% of CaSiO <sub>3</sub> ( $r_{O^{2-}/SiO_2} = 1.5$ ), and (c) 4.0 mol% of CaO and 4.0 mol% of CaSiO <sub>3</sub> ( $r_{O^{2-}/SiO_2} = 2.0$ ) at 1123 K. Scan rate: 100 mV s <sup>-1</sup> . R. P.: Rest potential.....  | 68 |
| Figure 3-11 | Current transient curves during the potentiostatic electrolysis at the liquid Zn electrode in molten CaCl <sub>2</sub> with the addition of (a) 4.0 mol% of CaSiO <sub>3</sub> ( $r_{O^{2-}/SiO_2} = 1.0$ ), (b) 2.0 mol% of CaO and 4.0 mol% of CaSiO <sub>3</sub> ( $r_{O^{2-}/SiO_2} = 1.5$ ), and (c) 4.0 mol% of CaO and 4.0 mol% of CaSiO <sub>3</sub> ( $r_{O^{2-}/SiO_2} = 2.0$ ) at 1123 K. Charge: -590.3 C (theoretical formation of 1.0 mol% Si-Zn alloy).....          | 70 |
| Figure 3-12 | Optical images of Si particles recovered from the Zn electrodes after the electrolysis conducted in molten CaCl <sub>2</sub> with the addition of (i) 4.0 mol% of CaSiO <sub>3</sub> ( $r_{O^{2-}/SiO_2} = 1.0$ ), (ii) 2.0 mol% of CaO and 4.0 mol% of CaSiO <sub>3</sub> ( $r_{O^{2-}/SiO_2} = 1.5$ ), and (iii) 4.0 mol% of CaO and 4.0 mol% of CaSiO <sub>3</sub> ( $r_{O^{2-}/SiO_2} = 2.0$ ) at 1123 K. Charge: -590.3 C (theoretical formation of 1.0 mol% Si-Zn alloy)..... | 71 |
| Figure 3-13 | SEM images of Si particles recovered from the Zn electrodes after the electrolysis conducted in molten CaCl <sub>2</sub> with the addition of (i) 4.0 mol% of CaSiO <sub>3</sub> ( $r_{O^{2-}/SiO_2} = 1.0$ ), (ii) 2.0 mol% of CaO and 4.0 mol% of CaSiO <sub>3</sub> ( $r_{O^{2-}/SiO_2} = 1.5$ ), and (iii) 4.0 mol% of CaO and 4.0 mol% of CaSiO <sub>3</sub> ( $r_{O^{2-}/SiO_2} = 2.0$ ) at 1123 K. Charge: -590.3 C (theoretical formation of 1.0 mol% Si-Zn alloy).....     | 72 |
| Figure 3-14 | (a) Current transient curve during the electrolysis in molten CaCl <sub>2</sub> , (b) optical image and (c) surface SEM image of the Si particles recovered from the Zn electrode after the slow cooling in molten CaCl <sub>2</sub> with the addition of 4.0 mol% of CaO and 4.0 mol% of CaSiO <sub>3</sub> ( $r_{O^{2-}/SiO_2} = 2.0$ ). Charge: -590.3 C (theoretical formation of 2.0 mol% Ca-Zn alloy). .....  | 74 |
| Figure 4-1  | Original and deconvolved Raman spectra for molten eutectic NaCl-CaCl <sub>2</sub> containing different amounts of CaO and SiO <sub>2</sub> at 1023 K.....   | 80 |
| Figure 4-2  | Original and deconvolved Raman spectra for molten NaCl-CaCl <sub>2</sub> containing (a) 1.0 mol% of CaSiO <sub>3</sub> ( $r_{O^{2-}/SiO_2} = 1.0$ ), (b) 0.5 mol% of CaO and 1.0 mol% of CaSiO <sub>3</sub> ( $r_{O^{2-}/SiO_2} = 1.5$ ), and (c) 1.0 mol% of CaO and 1.0 mol% of CaSiO <sub>3</sub> ( $r_{O^{2-}/SiO_2} = 2.0$ ) at 1023 K.....  | 82 |
| Figure 4-3  | Cyclic voltammograms at a Mo electrode and a glass-like carbon electrode in molten NaCl-CaCl <sub>2</sub> at (a) 1023 K and (b) 1123 K. Scan rate: 100 mV s <sup>-1</sup> . R. P.: Rest potential. ....   | 84 |
| Figure 4-4  | Cyclic voltammograms at a graphite electrode in molten NaCl-CaCl <sub>2</sub> before and after the addition of (a) 1.0 mol% of CaSiO <sub>3</sub> ( $r_{O^{2-}/SiO_2} = 1.0$ ), (b) 0.5 mol% of CaO and 1.0 mol% of CaSiO <sub>3</sub> ( $r_{O^{2-}/SiO_2} = 1.5$ ), and (c) 1.0 mol% of CaO and 1.0 mol% of CaSiO <sub>3</sub> ( $r_{O^{2-}/SiO_2} = 2.0$ ) at 1023 K. Scan rate: 50 mV s <sup>-1</sup> . R. P.: Rest potential.....   | 86 |

|             |  |     |
|-------------|--|-----|
| Figure 4-5  | Current transient curves during the potentiostatic electrolysis at graphite electrodes in molten NaCl–CaCl <sub>2</sub> with the addition of (a) 1.0 mol% of CaSiO <sub>3</sub> ( $r_{O^{2-}/SiO_2} = 1.0$ ), (b) 0.5 mol% of CaO and 1.0 mol% of CaSiO <sub>3</sub> ( $r_{O^{2-}/SiO_2} = 1.5$ ), and (c) 1.0 mol% of CaO and 1.0 mol% of CaSiO <sub>3</sub> ( $r_{O^{2-}/SiO_2} = 2.0$ ) at 1023 K. Charge density: $-14 \text{ C cm}^{-2}$ .<br>..... | 88  |
| Figure 4-6  | Optical images of an original graphite plate and the samples obtained in molten NaCl–CaCl <sub>2</sub> with the addition of (i) 1.0 mol% of CaSiO <sub>3</sub> ( $r_{O^{2-}/SiO_2} = 1.0$ ), (ii) 0.5 mol% of CaO and 1.0 mol% of CaSiO <sub>3</sub> ( $r_{O^{2-}/SiO_2} = 1.5$ ), and (iii) 1.0 mol% of CaO and 1.0 mol% of CaSiO <sub>3</sub> ( $r_{O^{2-}/SiO_2} = 2.0$ ) at 1023 K. Charge density: $-14 \text{ C cm}^{-2}$ .                        | 89  |
| Figure 4-7  | XRD patterns of the original graphite plate and the samples obtained in molten NaCl–CaCl <sub>2</sub> with the addition of (a) 1.0 mol% of CaSiO <sub>3</sub> ( $r_{O^{2-}/SiO_2} = 1.0$ ), (b) 0.5 mol% of CaO and 1.0 mol% of CaSiO <sub>3</sub> ( $r_{O^{2-}/SiO_2} = 1.5$ ), and (c) 1.0 mol% of CaO and 1.0 mol% of CaSiO <sub>3</sub> ( $r_{O^{2-}/SiO_2} = 2.0$ ) at 1023 K. Charge density: $-14 \text{ C cm}^{-2}$ .....                        | 90  |
| Figure 4-8  | SEM images of the samples obtained in molten NaCl–CaCl <sub>2</sub> with the addition of (i) 1.0 mol% of CaSiO <sub>3</sub> ( $r_{O^{2-}/SiO_2} = 1.0$ ), (ii) 0.5 mol% of CaO and 1.0 mol% of CaSiO <sub>3</sub> ( $r_{O^{2-}/SiO_2} = 1.5$ ), and (iii) 1.0 mol% of CaO and 1.0 mol% of CaSiO <sub>3</sub> ( $r_{O^{2-}/SiO_2} = 2.0$ ) at 1023 K. Charge density: $-14 \text{ C cm}^{-2}$ . ....  | 92  |
| Figure 4-9  | Current transient curves during the potentiostatic electrolysis at graphite plates in molten NaCl–CaCl <sub>2</sub> with the addition of (a) 1.0 mol% of CaSiO <sub>3</sub> ( $r_{O^{2-}/SiO_2} = 1.0$ ), (b) 0.5 mol% of CaO and 1.0 mol% of CaSiO <sub>3</sub> ( $r_{O^{2-}/SiO_2} = 1.5$ ), and (c) 1.0 mol% of CaO and 1.0 mol% of CaSiO <sub>3</sub> ( $r_{O^{2-}/SiO_2} = 2.0$ ) at 1123 K. Charge density: $-14 \text{ C cm}^{-2}$ .              | 94  |
| Figure 4-10 | Optical images of the samples obtained in molten NaCl–CaCl <sub>2</sub> with the addition of (i) 1.0 mol% of CaSiO <sub>3</sub> ( $r_{O^{2-}/SiO_2} = 1.0$ ), (ii) 0.5 mol% of CaO and 1.0 mol% of CaSiO <sub>3</sub> ( $r_{O^{2-}/SiO_2} = 1.5$ ), and (iii) 1.0 mol% of CaO and 1.0 mol% of CaSiO <sub>3</sub> ( $r_{O^{2-}/SiO_2} = 2.0$ ) at 1123 K. Charge density: $-14 \text{ C cm}^{-2}$ .....   | 95  |
| Figure 4-11 | XRD patterns of the samples obtained in molten NaCl–CaCl <sub>2</sub> with the addition of (a) 1.0 mol% of CaSiO <sub>3</sub> ( $r_{O^{2-}/SiO_2} = 1.0$ ), (b) 0.5 mol% of CaO and 1.0 mol% of CaSiO <sub>3</sub> ( $r_{O^{2-}/SiO_2} = 1.5$ ), and (c) 1.0 mol% of CaO and 1.0 mol% of CaSiO <sub>3</sub> ( $r_{O^{2-}/SiO_2} = 2.0$ ) at 1123 K. ....   | 96  |
| Figure 4-12 | SEM images of the samples obtained in molten NaCl–CaCl <sub>2</sub> with the addition of (i) 1.0 mol% of CaSiO <sub>3</sub> ( $r_{O^{2-}/SiO_2} = 1.0$ ), (ii) 0.5 mol% of CaO and 1.0 mol% of CaSiO <sub>3</sub> ( $r_{O^{2-}/SiO_2} = 1.5$ ), and (iii) 1.0 mol% of CaO and 1.0 mol% of CaSiO <sub>3</sub> ( $r_{O^{2-}/SiO_2} = 2.0$ ) at 1123 K. Charge density: $-14 \text{ C cm}^{-2}$ . ....  | 97  |
| Figure 5-1  | Schematic illustration of the liquid Zn electrode. ....  | 101 |
| Figure 5-2  | Cyclic voltammograms at a liquid Zn electrode in molten NaCl–CaCl <sub>2</sub> before and after the addition of (a) 1.0 mol% of CaSiO <sub>3</sub> ( $r_{O^{2-}/SiO_2} = 1.0$ ), (b) 0.5 mol% of CaO and 1.0 mol% of CaSiO <sub>3</sub> ( $r_{O^{2-}/SiO_2} = 1.5$ ), and (c) 1.0 mol% of CaO and 1.0 mol% of  |     |

|             |  |
|-------------|--|
|             | CaSiO <sub>3</sub> ( $r_{O^{2-}/SiO_2} = 2.0$ ) at 1023 K. Scan rate: 100 mV s <sup>-1</sup> . R. P.: Rest potential... 103  |
| Figure 5-3  | Cyclic voltammograms at a liquid Zn electrode in molten NaCl–CaCl <sub>2</sub> before and after the addition of (a) 1.0 mol% of CaSiO <sub>3</sub> ( $r_{O^{2-}/SiO_2} = 1.0$ ), (b) 0.5 mol% of CaO and 1.0 mol% of CaSiO <sub>3</sub> ( $r_{O^{2-}/SiO_2} = 1.5$ ), and (c) 1.0 mol% of CaO and 1.0 mol% of CaSiO <sub>3</sub> ( $r_{O^{2-}/SiO_2} = 2.0$ ) at 1123 K. Scan rate: 100 mV s <sup>-1</sup> . R. P.: Rest potential... 105  |
| Figure 5-4  | Current transient curves during the potentiostatic electrolysis at the liquid Zn electrode in molten NaCl–CaCl <sub>2</sub> with the addition of (a) 1.0 mol% of CaSiO <sub>3</sub> ( $r_{O^{2-}/SiO_2} = 1.0$ ), (b) 0.5 mol% of CaO and 1.0 mol% of CaSiO <sub>3</sub> ( $r_{O^{2-}/SiO_2} = 1.5$ ), and (c) 1.0 mol% of CaO and 1.0 mol% of CaSiO <sub>3</sub> ( $r_{O^{2-}/SiO_2} = 2.0$ ) at 1023 K. Charge: –413.2 C (theoretical formation of 1.0 mol% Si–Zn alloy)..... 107                |
| Figure 5-5  | Optical images of the Si particles recovered from the Zn electrodes after the electrolysis conducted in molten NaCl–CaCl <sub>2</sub> with the addition of (i) 1.0 mol% of CaSiO <sub>3</sub> ( $r_{O^{2-}/SiO_2} = 1.0$ ), (ii) 0.5 mol% of CaO and 1.0 mol% of CaSiO <sub>3</sub> ( $r_{O^{2-}/SiO_2} = 1.5$ ), and (iii) 1.0 mol% of CaO and 1.0 mol% of CaSiO <sub>3</sub> ( $r_{O^{2-}/SiO_2} = 2.0$ ) at 1023 K. Charge: –413.2 C (theoretical formation of 1.0 mol% Si–Zn alloy). ..... 108 |
| Figure 5-6  | SEM images of the Si particles recovered from the Zn electrodes after the electrolysis conducted in molten NaCl–CaCl <sub>2</sub> with the addition of (i) 1.0 mol% of CaSiO <sub>3</sub> ( $r_{O^{2-}/SiO_2} = 1.0$ ), (ii) 0.5 mol% of CaO and 1.0 mol% of CaSiO <sub>3</sub> ( $r_{O^{2-}/SiO_2} = 1.5$ ), and (iii) 1.0 mol% of CaO and 1.0 mol% of CaSiO <sub>3</sub> ( $r_{O^{2-}/SiO_2} = 2.0$ ) at 1023 K. Charge: –413.2 C (theoretical formation of 1.0 mol% Si–Zn alloy)..... 109       |
| Figure 5-7  | (a) Current transient curves during the electrolysis at liquid Zn electrode in molten NaCl–CaCl <sub>2</sub> , (b) optical image and (c) surface SEM image of the Si particles recovered from the Zn electrode after the slow cooling in molten NaCl–CaCl <sub>2</sub> with the addition of 1.0 mol% of CaO and 1.0 mol% of CaSiO <sub>3</sub> ( $r_{O^{2-}/SiO_2} = 2.0$ ) at 1023 K. .... 112  |
| Figure 5-8  | Current transient curves during the potentiostatic electrolysis at the liquid Zn electrode in molten NaCl–CaCl <sub>2</sub> with the addition of (a) 1.0 mol% of CaSiO <sub>3</sub> ( $r_{O^{2-}/SiO_2} = 1.0$ ), (b) 0.5 mol% of CaO and 1.0 mol% of CaSiO <sub>3</sub> ( $r_{O^{2-}/SiO_2} = 1.5$ ), and (c) 1.0 mol% of CaO and 1.0 mol% of CaSiO <sub>3</sub> ( $r_{O^{2-}/SiO_2} = 2.0$ ) at 1123 K. Charge: –590.3 C (theoretical formation of 1.0 mol% Si–Zn alloy)..... 113                |
| Figure 5-9  | Optical images of the Si particles recovered from the Zn electrodes after the electrolysis conducted in molten NaCl–CaCl <sub>2</sub> with the addition of (i) 1.0 mol% of CaSiO <sub>3</sub> ( $r_{O^{2-}/SiO_2} = 1.0$ ), (ii) 0.5 mol% of CaO and 1.0 mol% of CaSiO <sub>3</sub> ( $r_{O^{2-}/SiO_2} = 1.5$ ), and (iii) 1.0 mol% of CaO and 1.0 mol% of CaSiO <sub>3</sub> ( $r_{O^{2-}/SiO_2} = 2.0$ ) at 1123 K. Charge: –590.3 C (theoretical formation of 1.0 mol% Si–Zn alloy). ..... 114 |
| Figure 5-10 | SEM images of the Si particles recovered from the Zn electrodes after the electrolysis conducted in molten NaCl–CaCl <sub>2</sub> with the addition of (i) 1.0 mol% of CaSiO <sub>3</sub>  |

|              |   |     |
|--------------|---|-----|
|              | ( $r_{O^{2-}/SiO_2} = 1.0$ ), (ii) 0.5 mol% of CaO and 1.0 mol% of CaSiO <sub>3</sub> ( $r_{O^{2-}/SiO_2} = 1.5$ ), and (iii) 1.0 mol% of CaO and 1.0 mol% of CaSiO <sub>3</sub> ( $r_{O^{2-}/SiO_2} = 2.0$ ) at 1123 K. Charge: -590.3 C (theoretical formation of 1.0 mol% Si-Zn alloy).....  | 115 |
| Figure 5-11  | (a) Current transient curves during the electrolysis at liquid Zn electrode in molten NaCl-CaCl <sub>2</sub> , (b) optical image and (c) surface SEM image of the Si particles recovered from the Zn electrode after the slow cooling in molten NaCl-CaCl <sub>2</sub> with the addition of 1.0 mol% of CaO and 1.0 mol% of CaSiO <sub>3</sub> ( $r_{O^{2-}/SiO_2} = 2.0$ ) at 1123 K. .... | 117 |
| Figure 6-1   | Schematic drawing of the experimental apparatus for the precipitation of solid Si from a liquid Si-Zn alloy. (a) Thermocouple, (b) graphite crucible, (c) carbon tube (Exp. (1)), (d) funnel (Exp. (2)), (e) molten CaCl <sub>2</sub> , (f) liquid Zn, and (g) MG-Si. ....  | 121 |
| Figure 6-2   | Temperature changes during the cooling step. ....   | 122 |
| Figure 6-3   | Schematic drawing of the floating zone (FZ) melting method. ....  | 123 |
| Figure 6-4   | (a) Optical image of a top view and (b) SEM image of a cross section of the Zn lump obtained after the precipitation experiment (1) in molten CaCl <sub>2</sub> , and (c) optical image of the Si granules recovered after acid leaching of the Zn lump. ....   | 130 |
| Figure 6-5   | SEM image of a cross section of the Zn lump obtained after the precipitation experiment (2) in molten CaCl <sub>2</sub> . ....  | 131 |
| Figure 6-6   | Optical images of (a) Si powder for Si ingot and (b) Si ingot obtained by FZ melting. ....  | 131 |
| Figure A.2-1 | Schematic of the experimental apparatus for the precipitation of solid Si from a liquid Si-Zn alloy. (a) Thermocouple, (b) graphite crucible, (c) funnel, (d) molten CaCl <sub>2</sub> , (e) liquid Zn, and (f) MG-Si.....  | 149 |
| Figure A.2-2 | Temperature changes during the cooling step. ....   | 150 |
| Figure A.2-3 | Optical images of (a) Zn metal lump after the removal of salt and (b) precipitated Si granules with different particle sizes obtained at the cooling rate of 10 K h <sup>-1</sup> . ....  | 151 |
| Figure A.2-4 | Weight distribution of precipitated Si granules by particle size obtained at different cooling rate.....  | 152 |
| Figure A.2-5 | Phase diagram for the Zn-Si-P system [32]. ....   | 153 |
| Figure A.3-1 | Schematic of the experimental apparatus for the Si precipitation on a Si rod from liquid Si-Zn alloy. (a) Thermocouple, (b) 10-N Si rod, (c) graphite crucible, (d) molten NaCl-CaCl <sub>2</sub> , and (e) Si-saturated liquid Si-Zn alloy. ....   | 156 |
| Figure A.3-2 | Temperature changes during the cooling step. ....   | 158 |
| Figure A.3-3 | (a) Surface and (b) cross-sectional images of the Si rod obtained in Experiment 1. ....   | 158 |
| Figure A.3-4 | Optical images of the Si rod (a) recovered from liquid Si-Zn alloy, (b) during the  |     |

removal of residual Zn, and (c) after the removal of Zn..... 159



# Chapter 1

## General Introduction

### 1.1 Energy Trend and Situation of Solar Photovoltaic Power

With the growth of population in the world, the energy consumption has been significantly increasing year by year. Figure 1-1 shows the trend of world primary energy consumption from 1971 to 2019 by power source [1]. Although the nuclear power and renewable energies show increases in recent years, fossil fuels (coal, oil and natural gas) have been dominant in primary energy resource even now. However, conventional resources not only emit a large amount of carbon dioxide (CO<sub>2</sub>) which leads to the global warming, but also have the problem of emitting harmful gases such as SO<sub>x</sub> and NO<sub>x</sub>.

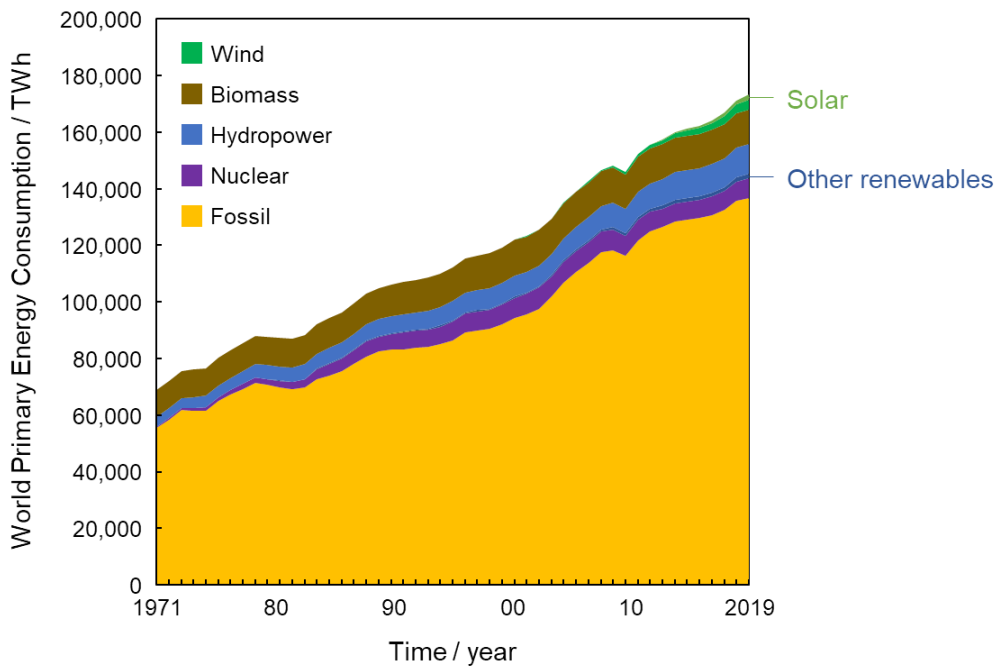


Figure 1-1 World primary energy consumption from 1971 to 2019 by power sources (TWh) [1].

Table 1-1 shows the lifecycle CO<sub>2</sub> emission by electricity supply technology [2]. The conventional fossil fuels and biomass show large CO<sub>2</sub> emissions per 1 kWh power generation. If the fossil fuels continue to be the dominant energy source, the impact on climate change will be more serious. The Intergovernmental Panel on Climate Change (IPCC) have highlighted the importance of reaching net-zero CO<sub>2</sub> emission globally by mid-century or sooner to avoid the worst impacts of climate change in the recent report on “Climate Change 2021” [3]. As an alternative energy source to fossil fuels, nuclear power has been attracting attention because of its low CO<sub>2</sub>

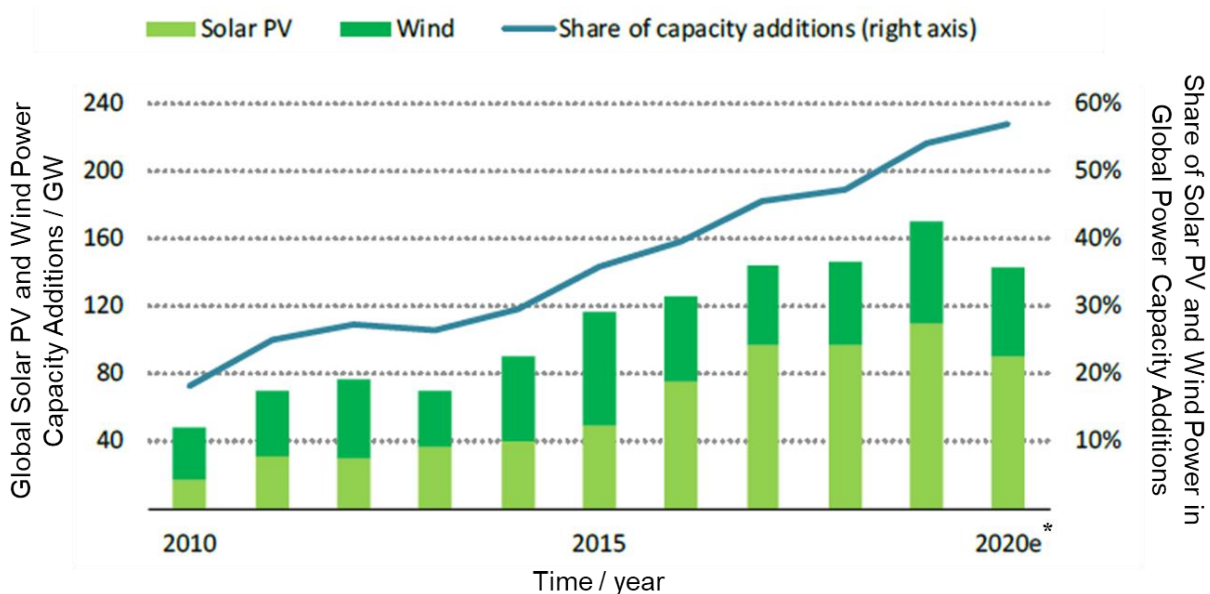
**Table 1-1 Lifecycle CO<sub>2</sub> emissions by electricity supply technologies (gCO<sub>2</sub>-eq kWh<sup>-1</sup>) [2].**

| Technology   | Lifecycle CO <sub>2</sub> emissions |        |      |
|--|-------------------------------------|--------|------|
|  | Min.                                | Median | Max. |
| <b>Currently commercially available technologies</b> |                                     |        |      |
| Coal–pulverized coal                                 | 740                                 | 820    | 910  |
| Gas–combined cycle                                   | 410                                 | 490    | 650  |
| Biomass–cofiring with coal                           | 620                                 | 740    | 890  |
| Biomass–dedicated                                    | 130                                 | 230    | 420  |
| Solar PV–rooftop                                     | 26                                  | 41     | 60   |
| Solar PV–utility scale                               | 18                                  | 48     | 180  |
| Concentrated solar power                             | 9                                   | 27     | 63   |
| Wind offshore  | 8                                   | 12     | 35   |
| Geothermal   | 6                                   | 38     | 79   |
| Hydropower   | 1                                   | 24     | 2200 |
| Nuclear  | 4                                   | 12     | 110  |
| <b>Pre-commercial technologies</b>                   |                                     |        |      |
| CCS *–Coal–pulverized coal                           | 190                                 | 220    | 250  |
| CCS–Coal–integrated gasification combined cycle      | 170                                 | 200    | 230  |
| CCS–Coal–oxyfuel                                     | 100                                 | 160    | 200  |
| CCS–Gas–combined cycle                               | 94                                  | 170    | 340  |
| Ocean (tidal and wave)                               | 6                                   | 17     | 28   |

\* CCS is the abbreviation of “Carbon Dioxide Capture and Storage”.

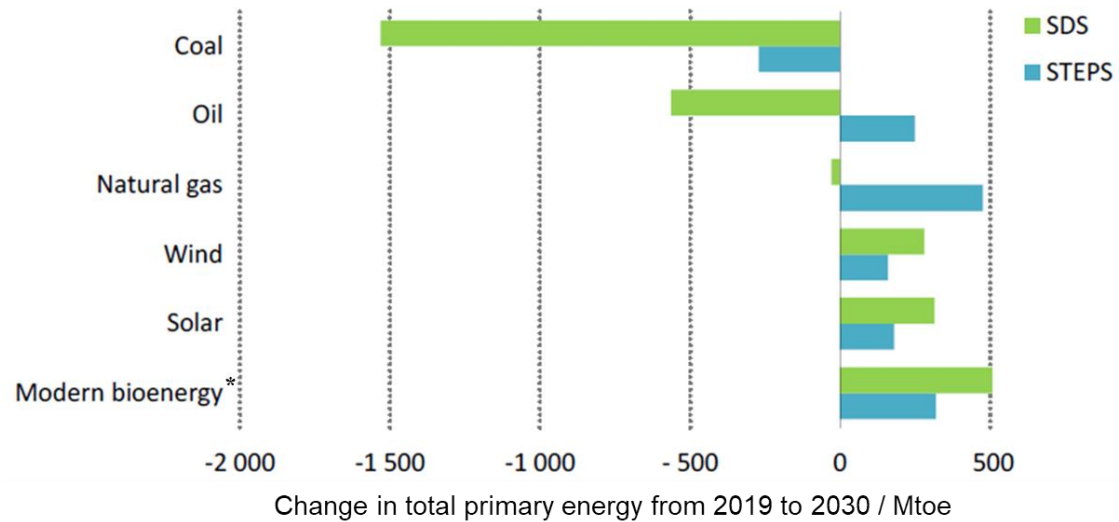
emission. However, the radioactive waste disposal and nuclear security are still the issues of nuclear power. Therefore, the establishment of zero-CO<sub>2</sub>-emission power supply system with the promotion of renewable energies that can substitute the conventional fossil-based energy is required.

According to “Sustainable Recovery” by International Energy Agency (IEA), solar photovoltaic (PV) and wind power have rapidly become the most favored technologies around the world [4]. In 2019, solar and wind capital expenditures accounted for almost half of all power plant investments. Figure 1-2 shows the global solar PV and wind power capacity additions from 2010 to 2020 [4]. From 2016, solar PV and wind power accounted more than 30% of global power capacity additions, with solar power growing twice as fast as wind power. Compared with wind power, solar PV is quiet during power generation and could be constructed to any size based on energy requirement. IEA also predicted the primary energy change with Sustainable Development Scenario (SDS) and Stated Policies Scenario (STEPS) in World Energy Outlook 2020 (Figure 1-3). The SDS and STEPS show 4.2 and 6.5 times increase in solar power generation, respectively [5]. Therefore, further cost reduction is necessary for the widespread use of solar power in the future.



\* 2020e: estimated values for 2020.

Figure 1-2 Global solar PV and wind power capacity additions from 2010 to 2020 [4].



\* Modern bioenergy includes biogas, biofuel and modern biomass.

**Figure 1-3 Total primary energy changes in Stated Policies Scenario (STEPS) and Sustainable Development Scenario (SDS) from 2019 to 2030 [5].**

## 1.2 Solar Photovoltaic Power Generation

In general, solar photovoltaic cells could be broadly categorized into Si-based crystalline (monocrystalline and polycrystalline Si), compound semiconductor (CdTe and CIGS) and organic. The highest conversion efficiency [6] and features [7] for each solar photovoltaic cell technology were summarized in Table 1-2. Si, the raw material of Si crystalline solar photovoltaic cell, is considered as a nontoxic and environment-friendly element, which also has an abundance of 27.2 wt.% in the earth crust [8], so that there is no concern about resource depletion. III–V compound semiconductor cells, which consist of materials such as GaAs on the Ge substrates, are typically used in concentrator PV (CPV) systems or for space applications because of their high conversion efficiencies and high cost. With the advantage of cost reduction, thin-film cells, which are formed by depositing extremely thin layers of photovoltaic semiconductor materials onto a backing material, has attracted attentions. Currently, CdTe and CIGS (copper-indium-gallium-diselenide) are commercially used as thin-film materials. Organic thin-film cells, which use dye or organic semiconductors, achieved a relatively high efficiency but have not yet resulted in stable market

products [7]. According to the Photovoltaic Market 2021 report by RTS corporation, since crystalline Si solar cells accounted for 96% of the worldwide production in 2020, they are expected to remain mainstream in the PV industry for the time being (Figure 1-4) [9]. Thus, the global demand for high-purity crystalline Si, which is known as solar-grade Si (SOG-Si), will continue to increase in the future.

**Table 1-2 Highest conversion efficiencies and features of solar photovoltaic cell technologies [6, 7].**

| Technology           | Highest efficiency / %<br>[6] | Features [7]  |   |
|----------------------|-------------------------------|---|---|
|                      |                               | Advantage   | Disadvantage                                  |
| Monocrystalline Si   | 27.6                          | High conversion efficiency<br>High durability       | High cost                                     |
| Polycrystalline Si   | 23.3                          | Lower cost than monocrystalline Si cell             | Lower efficiency than monocrystalline Si cell |
| GaAs III-V           | 30.5                          | Highest efficiency<br>Less loss at high temperature | High cost<br>Use of toxic element             |
| CIGS                 | 23.4                          | Less material use                                   | Use of In with low reserves                   |
| CdTe                 | 22.1                          | Less material use                                   | Use of toxic Cd                               |
| Organic (perovskite) | 25.5                          | Less material use<br>High flexibility               | Low durability                                |

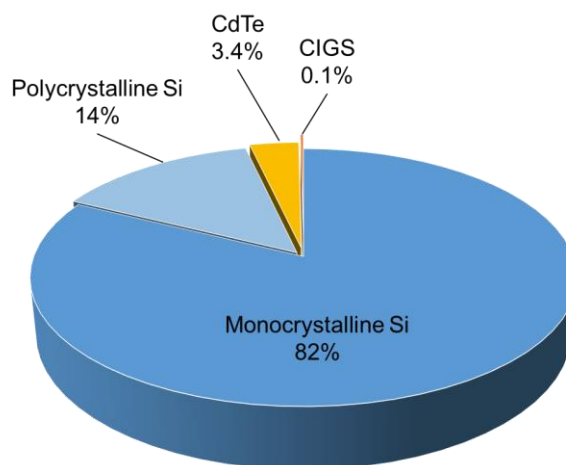


**Figure 1-4 Ratio of solar photovoltaic cells production by type of cells in 2020 [9].**

### 1.3 Current Commercial Production Processes of Solar-grade Silicon

The high-purity Si used in crystalline Si solar cells is called solar-grade Si (SOG-Si) and requires a purity of 6–7N (99.9999–99.99999%). Recently, SOG-Si is commercially produced by the steps shown below [10]. Figure 1-5 shows the flowchart corresponding to steps (1)–(4) [11, 12]. Here, steps (2)–(4) are referred to as the Siemens process [12–14]. Then, the solar module is fabricated in steps (5)–(9).

- (1) Production of metallurgical-grade Si (MG-Si, 2N purity) from SiO<sub>2</sub> by carbothermal reduction
- (2) Synthesis of SiHCl<sub>3</sub> by hydrochlorination of MG-Si with SiCl<sub>4</sub> byproduct
- (3) Purification of SiHCl<sub>3</sub> by distillation

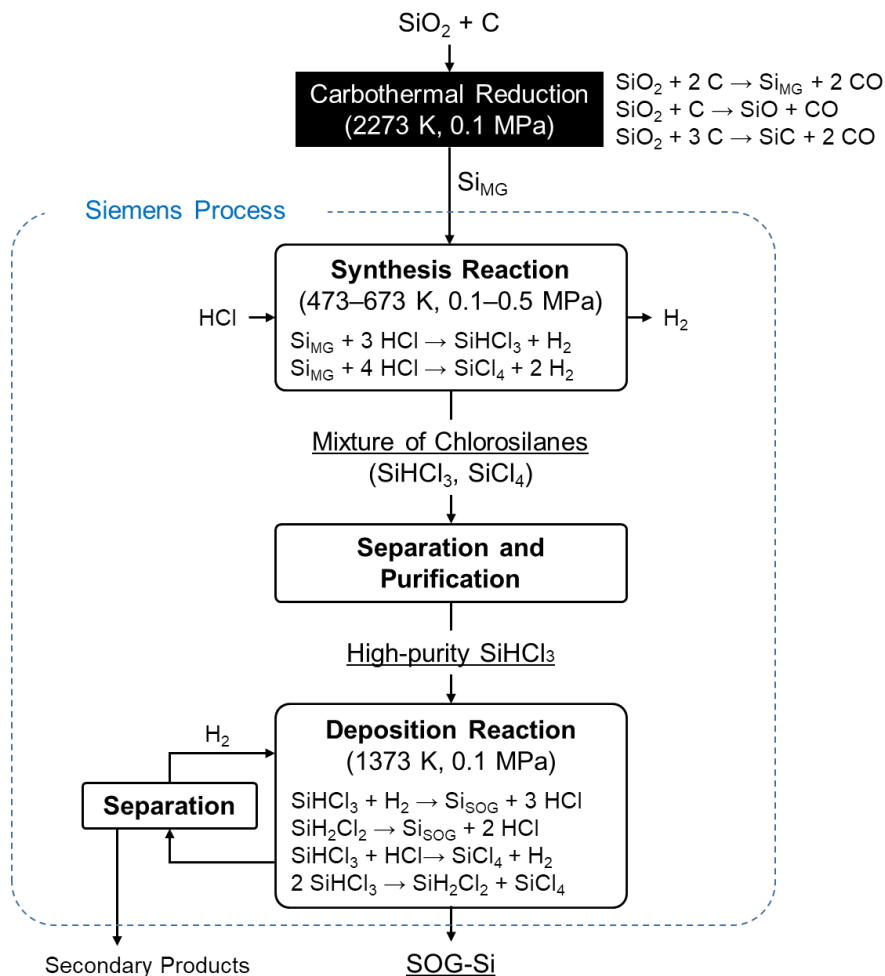


Figure 1-5 Flowchart of the SOG-Si production containing the Siemens process [11, 12].

- (4) Production of high-purity polycrystalline Si by chemical vapor deposition (CVD) using  $\text{SiHCl}_3$
- (5) Production of monocrystalline Si ingot by CZ (Czochralski) method [15] or polycrystalline Si ingot by casting method
- (6) Production of Si wafers by slicing Si ingot
- (7) Production of p-n junction by thermal diffusion method or ion implantation
- (8) Cell fabrication by electrical contacts connection and anti-reflective film coating
- (9) Module fabrication by cell encapsulation into resin and assembly into a frame with backsheet and glass or plastic cover

The Siemens process is used all over the world because it produces high quality Si. However, it has several safety and environmental problems, such as large energy consumption and extreme operating conditions. In addition, the production of  $\text{SiHCl}_3$ , which is toxic, corrosive and explosive, presents safety and environmental problems [11].

## 1.4 Studies on Next-generation SOG-Si Production Processes

To develop a next-generation production process for SOG-Si, experimental studies on the purification of MG-Si, metallothermic reduction of silicon halides and electrochemical reduction of  $\text{SiO}_2$  have been conducted.

### 1.4.1 Purification of MG-Si

The purification of MG-Si is considered as an alternative for the production of SOG-Si with many advantages, such as low energy consumption and environment-friendly operating conditions. The energy consumption for the production of SOG-Si using the purification of MG-Si (metallurgical route) is  $20 \text{ kWh (kg-Si)}^{-1}$ , which is one-third lower than that for the Siemens process [12, 16]. Compared to the Siemens process with  $30\text{--}70 \text{ gCO}_2\text{-eq kWh}^{-1}$  of global warming potential, the metallurgical route in China has  $20 \text{ gCO}_2\text{-eq kWh}^{-1}$  [17] and the Elkem solar metallurgical

process route shows the similar value of 23 gCO<sub>2</sub>-eq kWh<sup>-1</sup> [16]. Various purification processes using MG-Si as the raw material have been investigated [16, 18, 19] such as slag treatment [20–33], electron beam or plasma melting [34–45], acid leaching [29, 31, 46–52], directional solidification [40, 53–55], electrorefining of MG-Si in molten salt [56–69], and solvent refining [70–103].

#### 1.4.1.1 Electrorefining of MG-Si in Molten Salts

Table 1-3 shows the previous studies on electrorefining of MG-Si in molten salts. The idea was firstly introduced by Monnier *et al.*, who investigated the electrorefining of MG-Si and liquid Cu–Si alloy in molten Na<sub>3</sub>AlF<sub>6</sub>(–NaF)–SiO<sub>2</sub> and achieved highest purity of 99.9% [56–58]. In 1981, Olson and Carleton lowered the operating temperature to 1023 K with the use of molten LiF–KF–K<sub>2</sub>SiF<sub>6</sub> [59]. Later, Sharma and Mukherjee investigated the direct refining of MG-Si without the alloying step [60]. Similar studies were conducted in molten fluoride or fluoride–chloride mixture salts [61–63]. In 2007, Kongstein *et al.* are the first to study the electrorefining of MG-Si in molten chloride-based salts [64]. Then, Cai *et al.* added SiO<sub>2</sub> or Si into molten salt and used liquid Cu–Si alloy as the anode which proved advantageous for B and P removal [65, 66]. However, the powdery or porous Si products obtained by these studies is difficult to be separated from the molten salt, especially the fluoride salts with a low solubility in water, which leads to the contamination of impurities into Si. Several studies on liquid Si products were conducted to solve this problem. Olson *et al.* developed a three-layered refining process of MG-Si, which is used commercially in the production of superpure aluminum [67, 68]. Liquid Si was obtained in the refining process conducted at 1773 K, which is higher than the melting point of Si. The result shows a good promise in the removal of metallic elements and P. However, the removal of B was not ideal, because the thermodynamic properties of B are similar to Si. As an another approach, Lai *et al.* proposed a three-layered process using liquid Al as the cathode [69]. Although not mentioned in this study, contamination of Al, the alloying element, is considered to be a problem in the production of SOG-



**Table 1-3 Previous studies on electrorefining of MG-Si in molten salts.**

| Molten salt  | Si source  | Temperature / K | Purity of refined Si / % | Authors, Year [Ref.]   |
|--|--|-----------------|--------------------------|--|
| Na <sub>3</sub> AlF <sub>6</sub> (-NaF)-SiO <sub>2</sub>             | MG-Si anode, liquid Cu-Si alloy anode <sup>1</sup> | 1173–1273       | 99.99                    | Monnier and Giacometti, 1964 [56]<br>Monnier and Barakat, 1965 [57]<br>Monnier <i>et al.</i> , 1966 [58] |
| K <sub>3</sub> AlF <sub>6</sub> -LiF-K <sub>2</sub> SiF <sub>6</sub> | liquid Cu-Si alloy anode <sup>1</sup>              | 1223            | <99.98 <sup>a</sup>      | Lai <i>et al.</i> , 2010 [69]  |
| LiF-KF-K <sub>2</sub> SiF <sub>6</sub>                               | Si in Cu <sub>3</sub> Si anode                     | 1023            | >99.999                  | Olson and Carleton, 1981 [59]  |
| LiF-KF-K <sub>2</sub> SiF <sub>6</sub>                               | MG-Si anode  | 1023            | 99.99                    | Sharma and Mukherjee, 1986 [60]  |
| LiF-KF-K <sub>2</sub> SiF <sub>6</sub>                               | MG-Si anode  | 973             | 99.98 <sup>a</sup>       | Ryu <i>et al.</i> , 2012 [61]  |
| NaF-KF   | MG-Si anode  | 1073–1173       | <99.999 <sup>b</sup>     | Zou <i>et al.</i> , 2013 [63]  |
| CaF <sub>2</sub> -BaF <sub>2</sub> -K <sub>2</sub> SiF <sub>6</sub>  | liquid Cu-Si alloy anode <sup>1</sup>              | 1773            | - <sup>c</sup>           | Olson and Rolseth, 2010 [67]<br>Olson <i>et al.</i> , 2010 [68]  |
| NaF-KCl  | MG-Si anode  | 1073            | 99.99                    | Zou <i>et al.</i> , 2012 [62]  |
| NaCl-CaCl <sub>2</sub> -CaO  | MG-Si powder                                       | 1123            | -                        | Kongstein <i>et al.</i> , 2007 [64]  |
| NaCl-CaCl <sub>2</sub> -CaO-SiO <sub>2</sub>                         | liquid Cu-Si alloy anode <sup>1</sup>              | 1123–1223       | 99.96 <sup>a</sup>       | Cai <i>et al.</i> , 2012 [65]  |
| NaCl-CaCl <sub>2</sub> -CaO-Si                                       | liquid Cu-Si alloy anode <sup>1</sup>              | 973–1223        | 99.98 <sup>a</sup>       | Cai <i>et al.</i> , 2012 [66]  |

<sup>1</sup> Liquid Cu-Si alloy was prepared from MG-Si.

<sup>a</sup> Analyzed by ICP-AES.

<sup>b</sup> Analyzed by ICP-MS.

<sup>c</sup> Only several target elements analyzed by GD-MS.

Si, considering the reports mentioned in section 1.4.1.2.

#### 1.4.1.2 Solvent Refining of MG-Si

Over past years, the solidification refining of MG-Si using a metallic solvent at low temperature, which is named “solvent refining”, has attracted attention. This method focused on the enhanced solid/liquid segregation tendency of impurity at low temperature, so that impurities even with high segregation coefficient in Si (such as P and B) can be more effectively removed compared with the ordinary directional solidification. Obinata and Komatsu are the first who

focused on the Si refining using Al solvent [70, 71]. Then, Kotval and Strok refined MG-Si using Al solvent and showed that metallic impurities could be effectively removed, suggesting the possibility of SOG-Si production [72–74]. Since 2003, refining of MG-Si using the Si–Al solvent has been intensively investigated by Morita’s group [75–87]. Several other groups have also studied the Si–Al solvent with the aim of effective removal of B [88–91]. Although a high removal fraction of B was achieved, the residual of solvent element, Al, in Si with several hundred ppm is the issue for the production of SOG-Si.

Cu was considered as a candidate which has lower solid solubility in Si compared with Al. Juneja and Mukherjee reported that the metallic impurities were partially removed with the Si–Cu solvent [92]. However, the removal of B did not succeed. In 2010s, the additive of Ca and acid leaching were studied for the efficient removal of B, but the removal fraction of B was only approximately 60% at maximum [93, 94].

With the aim of massive precipitation of Si with temperature drop, the refining using Si–Sn solvent, which has a moderate liquid slop, was proposed by Morita’s group [95–98]. The Si–Sn solvent shows a high removal fraction of B and P after the treatment of  $\text{CaF}_2\text{–CaO–SiO}_2$  slag [96, 97]. The concentration of solvent element, Sn, was reduced by moving the melt during solidification to enrich Si crystals [98]. However, this study also reported that the solid solubility of Sn in Si is 10–15 ppma [98], which suggests further removal of Sn is difficult. Several different solvents were also studied such as Si–Na [99], Si–Fe [100, 101], Si–Ga [102], and Si–Al–Sn [103]. Although the concentration of solvent element was not reported in several studies, similar issue can be considered for the residual of solvent element. For the studies on Si–Fe alloy [100, 101], the low Fe concentration was achieved by hot HF solution leaching, while this leads to safety and environmental issues. Table 1-4 summarizes the best data for the removal of solvent and non-metallic (B and P) elements using the solvent refining method.

**Table 1-4 Previous studies on solvent refining with various Si–metal solvent.**

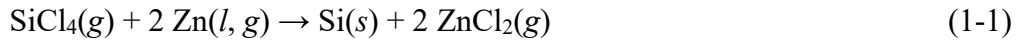
| Alloy  | Concentration (Removal fraction / %) of impurity elements |  | Authors, Year [Ref.]                |
|--|---|--|-------------------------------------|
|  | Solvent element   | B and P                                      |                                     |
| Si–Al  | Al: 453 ppmw (63.1)                                       | B: 0.81 ppmw (98.6)<br>P: 0.42 ppmw (98.8)   | Morita and Yoshikawa, 2011 [83]     |
| Si–Al  | –   | B: 3.8 ppmw (74.3)                           | Li <i>et al.</i> , 2015 [88]        |
| Si–Al<br>(with rotating magnetic field)      | Al: 327 ppmw (87.01)                                      | B: 4.67 ppmw (92.67)<br>P: 13.3 ppmw (77.33) | Zou <i>et al.</i> , 2015 [89]       |
| Si–Al<br>(additive: Ti)                      | Al: 835 ppma<br>Ti: 116 ppma                              | B: 12 ppma<br>P: 32 ppma                     | Ban <i>et al.</i> , 2016 [90]       |
| Si–Al<br>(additive: V)                       | Al: –<br>V: 1021 ppma (66)                                | B: 74 ppma (86)                              | Chen <i>et al.</i> , 2018 [91]      |
| Si–Al<br>(additive: Zn)                      | Al: 446.6 ppmw<br>Zn: 98.9 ppmw                           | B: 2.4 ppmw                                  | Li <i>et al.</i> , 2014 [85]        |
| Si–Al<br>(additive: Zr)                      | Al: 329 ppmw (79.5)<br>Zr: 0.6 ppmw (99.998)              | B: 1.2 ppmw (90)<br>P: 7.5 ppmw (85.6)       | Lei <i>et al.</i> , 2018 [87]       |
| Si–Al<br>(additive: Hf)                      | Al: 611 ppma<br>Hf: 66.8 ppma                             | B: 2.7 ppma                                  | Lei <i>et al.</i> , 2016 [86]       |
| Si–Cu<br>(additive: Ca)                      | Cu: –<br>Ca: – (91.95)                                    | B: – (44.4)<br>P: – (60.2)                   | Fang <i>et al.</i> , 2013 [93]      |
| Si–Cu<br>(with acid leaching)                | –   | B: – (58.7)<br>P: – (42.2)                   | Huang <i>et al.</i> , 2016 [94]     |
| Si–Sn  | Sn: 3310 ppmw   | B: 9.2 ppmw (75.1)<br>P: 9.6 ppmw (73.5)     | Ma <i>et al.</i> , 2013 [95]        |
| Si–Sn<br>(with 2 times of slag treatment)    | Sn: 5206 ppmw   | B: 0.3 ppmw (99.1)<br>P: 5.8 ppmw (84.3)     | Ma <i>et al.</i> , 2014 [97]        |
| Si–Sn<br>(with moving during solidification) | Sn: 13.2 ppma   | –  | Ren <i>et al.</i> , 2018 [98]       |
| Si–Na  | Na: 85 ppmw   | B: 120 ppmw<br>P: 3.4 ppmw                   | Morito <i>et al.</i> , 2012 [99]    |
| Si–Fe  | Fe: 1 ppmw (99.97)  | B: 2 ppmw (92.6)<br>P: 29 ppmw (57.4)        | Esfahani <i>et al.</i> , 2011 [100] |
| Si–Ga  | –   | B: 4.18 ppmw (83.3)<br>P: 36.6 ppmw (14.8)   | Li <i>et al.</i> , 2017 [102]       |
| Si–Al–Sn                                     | –   | B: 5.1 ppmw (63.3)                           | Li <i>et al.</i> , 2014 [103]       |

### 1.4.2 Metallothermic Reduction of Silicon Halides

The metallothermic reduction of silicon halides has been applied for the production of SOG-Si using reducing agents of Zn [104–117], Al [117–121], alkali metals such as Na [122–130] and K [122, 131], and alkaline earth metals such as Mg [124, 129].

### 1.4.2.1 Zincothermic reduction

The production of high-purity Si by zincothermic reduction of SiCl<sub>4</sub> was the commercial production method before the Siemens process. As shown in the following reaction, SiCl<sub>4</sub> was reduced by liquid Zn or Zn gas.



The use of Zn as a reductant provides the advantages of no intermetallic compound formation with Si and easy removal of Zn and ZnCl<sub>2</sub> due to their high vapor pressure.

The zincothermic reduction process was first proposed by DuPont company in 1950s [104–108]. Figure 1-6 shows a flowchart of the DuPont process, in which the SiCl<sub>4</sub> was reduced by Zn gas at 1223 K. While the high-purity Si was obtained, the impurity of BCl<sub>3</sub> was also reduced by Zn at the same time, so that the contamination of B into Si was the issue of DuPont process. Also, the generation of massive byproduct, ZnCl<sub>2</sub>, hindered the application for the large-scale production.

Since 1970s, a semi-continuous process using the fluidized bed reaction was investigated by Battelle Columbus Laboratories [111, 112]. This process proposed a closed recycle method of ZnCl<sub>2</sub>, which consists of 4 main steps: chlorination, distillation, reduction, and electrolysis (Figure 1-7). The byproduct of ZnCl<sub>2</sub> produced in the reduction step was recovered and electrolyzed into Zn and Cl<sub>2</sub> in the electrolysis step. The reduced Zn was recycled to the reduction step and the Cl<sub>2</sub> to the chlorination step. Recently, several other groups have also investigated the zincothermic reduction of SiCl<sub>4</sub> [109, 110, 113–117]. However, there are still issues of Zn recycling and its purity control, as well as the challenge in energy efficiency. Table 1-5 summarizes the Si production based on zincothermic reduction of SiCl<sub>4</sub> [132].

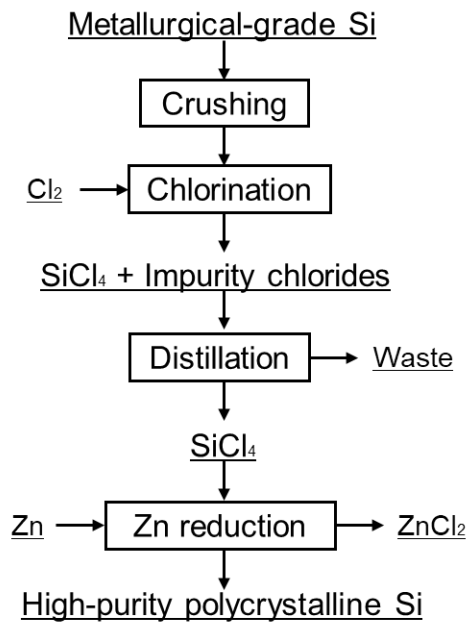


Figure 1-6 Flowchart of the DuPont process [104–108].

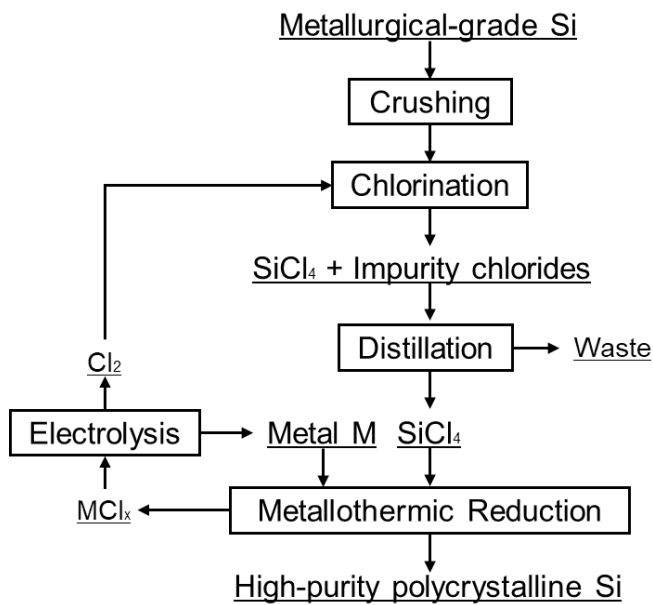


Figure 1-7 Flowchart of the metallothermic reduction of  $\text{SiCl}_4$  with the recycling of  $\text{ZnCl}_2$  [111, 112].

**Table 1-5 Si production process based on zincothermic reduction of SiCl<sub>4</sub> [132].**

| Phase of Zn    | Temperature / K | Feature   | Morphology of Si  | Authors, Year [Ref.]  |
|----------------|-----------------|---|-------------------|---|
| gas            | 1223            | batch process, Si with 99.97% purity  | fiber             | Lyon <i>et al.</i> , 1949 [104]   |
| gas            | 1173–1523       | continuous process, fluidized bed reaction, Si with 99.9+% purity   | powder            | Butler and Marcus, 1956 [105]<br>Olson, 1957 [106, 107]<br>Bertrand, 1961 [108] |
| gas            | 1073–1273       | SiCl <sub>4</sub> diluted with carrier gas  | fiber             | Johnson and Amick, 1954 [109]   |
| gas,<br>liquid | 773–1423        | pressure evaluated during the reaction  | deposit           | Ishino <i>et al.</i> , 1965 [110]   |
| gas            | 1100–1300       | semi-continuous process, fluidized bed reaction, ZnCl <sub>2</sub> electrolyzed into Zn and Cl <sub>2</sub> in molten KCl–ZnCl <sub>2</sub> | powder            | Blocher <i>et al.</i> , 1981 [111]<br>Seifer and Browning, 1982 [112]           |
| liquid         | ≤1073           | ZnCl <sub>2</sub> electrolyzed into Zn and Cl <sub>2</sub>  | deposit           | Natsume <i>et al.</i> , 1999 [113]  |
| gas            | 1183–1473       | Reaction occurred on the Si seed crystal  | epitaxial deposit | Shimamune and Yoshikawa, 2003 [114]   |
| gas            | 1073–1473       | continuous process  | fiber             | Honda <i>et al.</i> , 2005 [115]  |
| liquid         | 1005–1180       | Si purified at a temperature above the melting point of Zn  | deposit           | Robert and Zijlema, 2006 [116]  |
| gas,<br>liquid | ≥1073           | Zn supplied as fine particles   | deposit           | Sakaguchi, 2007 [117]   |

#### 1.4.2.2 Aluminothermic reduction

The production of high-purity Si by aluminothermic reduction of SiCl<sub>4</sub> has also been proposed. Similar with Zn, the formation of intermetallic compounds does not occur between Al and Si. On the other hand, the vapor pressure of Al is low even at 1300 K, which is different from Zn, so that the Al reductant is used in solid or liquid phase. In addition, the byproduct of AlCl<sub>3</sub> can be removed as a gas due to its high vapor pressure. Si production processes by aluminothermic reduction of SiCl<sub>4</sub> are summarized in Table 1-6 [132]. Since the solid solubility of Al in Si is about several hundred ppm, contamination of Si with Al is a problem, and an effective Al removal method is a challenge.

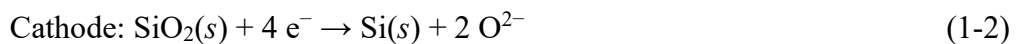
**Table 1-6 Si production process based on aluminothermic reduction of SiCl<sub>4</sub> [132].**

| Phase of Al | Temperature / K | Feature  | Morphology of Si        | Authors, Year [Ref.]                 |
|-------------|-----------------|--|-------------------------|--------------------------------------|
| liquid      | 1173–1473       | –  | –                       | Weaver, 1917 [118]                   |
| liquid      | 1023–1273       | Si with 99.9% purity                                       | powder, fiber, dendrite | Yoshizawa <i>et al.</i> , 1961 [119] |
| solid       | 200–850         | liquid and SiCl <sub>4</sub> gas used                      | –                       | Terry <i>et al.</i> , 1977 [120]     |
| solid       | 823–923         | AlCl <sub>3</sub> electrolyzed into Al and Cl <sub>2</sub> | cake                    | Woditsch <i>et al.</i> , 1985 [121]  |
| liquid      | 673–1473        | AlCl <sub>3</sub> electrolyzed into Al and Cl <sub>2</sub> | deposit                 | Saegusa and Yamabayashi, 2007 [133]  |
| liquid      | ≥1073           | Al supplied as fine particles                              | deposit                 | Sakaguchi, 2007 [117]                |

### 1.4.3 Electrochemical Reduction of SiO<sub>2</sub> in Molten Salts

#### 1.4.3.1 Electrochemical Reduction of Solid SiO<sub>2</sub>

For the past two decades, the electrochemical reduction of solid SiO<sub>2</sub> in molten salts for the production of SOG-Si has been investigated, especially for CaCl<sub>2</sub>-based salts [134–162]. Nohira *et al.* reported the electrochemical reduction of SiO<sub>2</sub> to Si in molten CaCl<sub>2</sub> using the contacting electrodes in 2003 [134]. SiO<sub>2</sub> is known as an insulator even at high temperature. However, with the use of the contacting electrode shown in Figure 1-8, the electrochemical reduction of SiO<sub>2</sub> is realized at the three-phase zone of conductor/SiO<sub>2</sub>/CaCl<sub>2</sub> with the supply of electrons by the contacting material.



The reduced Si has a high electronic conductivity (50 Ω<sup>-1</sup> cm<sup>-1</sup> [163]) at high temperature, which makes new electron paths, so that a new three-phase zone of conductive Si/SiO<sub>2</sub>/CaCl<sub>2</sub> is produced. As the reduction proceeds, the reduced area spreads until all SiO<sub>2</sub> is reduced. The CaCl<sub>2</sub>-base electrolytes were selected because of the high solubility of O<sup>2-</sup> ions [164].

Since then, many approaches have been conducted by not only Nohira's group, but other researchers. Table 1-7 summarizes the previous studies on the electrochemical reduction of solid

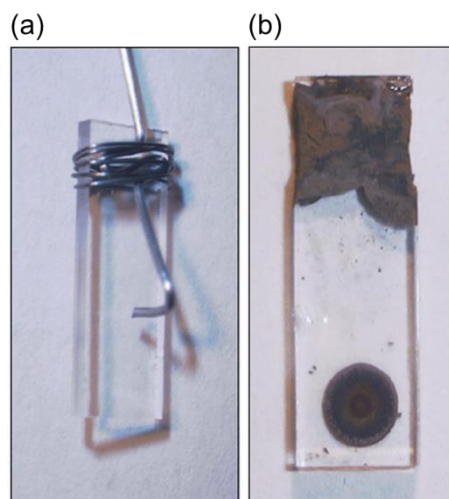


**Figure 1-8** Optical images of the contacting electrode (a) before and (b) after the electrochemical reduction [134].

SiO<sub>2</sub> in chloride-based molten salts. The highest purity was achieved 99.6 % for the reduced Si from solid SiO<sub>2</sub> and >99.995 % for the Si ingot made from the reduced Si by directional solidification [156]. Several studies in molten chlorides at lower temperatures [134, 158–160] and oxide-added salts [161, 162] were also conducted, but the purity of produced Si was not analyzed. One of the challenges faced in the industrial application of electrochemical reduction of solid SiO<sub>2</sub> is the efficient recovery and separation of the powdery Si product from unreacted SiO<sub>2</sub> and molten salt in order to prevent the contamination of impurities into Si.



**Table 1-7 Previous studies on the electrochemical reduction of solid SiO<sub>2</sub> in chloride-based molten salts.**

| Molten salt       | Si precursor   | Temperature / K | Contacting electrode | Counter electrode                    | (Pseudo) Reference electrode   | Purity of produced Si / %                       | Authors, Year [Ref.]   |
|-------------------|--|-----------------|----------------------|--------------------------------------|--|---|--|
| CaCl <sub>2</sub> | quartz plate   | 1123            | Mo                   | graphite                             | Pt, Mo–Ca <sup>2+</sup> /Ca  | –   | Nohira <i>et al.</i> , 2003 [134]  |
| CaCl <sub>2</sub> | quartz tube, SiO <sub>2</sub> pellet                       | 1123            | W, Ni                | graphite                             | Pt (for CV) <sup>1</sup>   | –   | Jin <i>et al.</i> , 2004 [135]   |
| CaCl <sub>2</sub> | quartz plate   | 1123            | Mo                   | graphite                             | Ag <sup>+</sup> /Ag in CaCl <sub>2</sub> ,<br>Mo–Ca <sup>2+</sup> /Ca              | –   | Yasuda <i>et al.</i> , 2005 [136, 137]   |
| CaCl <sub>2</sub> | SiO <sub>2</sub> pellet,<br>(SiO <sub>2</sub> + Si) pellet | 1123            | Mo                   | graphite                             | Ag <sup>+</sup> /Ag in CaCl <sub>2</sub> ,<br>Mo–Ca <sup>2+</sup> /Ca              | –   | Yasuda <i>et al.</i> , 2005 [138]  |
| CaCl <sub>2</sub> | SiO <sub>2</sub> tube                                      | 1123            | W                    | graphite                             | quartz sealed<br>Ag/AgCl <sup>[165]</sup> , Pt                                     | –   | Deng <i>et al.</i> , 2005 [139]  |
| CaCl <sub>2</sub> | quartz pellet  | 1173            | Ni                   | graphite                             | quartz sealed<br>Ag/AgCl <sup>[165]</sup>  | –   | Xiao <i>et al.</i> , 2006 [140]  |
| CaCl <sub>2</sub> | SiO <sub>2</sub> plate                                     | 1123            | <i>p</i> -Si (100)   | glass-like<br>carbon                 | Ag <sup>+</sup> /Ag in CaCl <sub>2</sub> ,<br>Mo–Ca <sup>2+</sup> /Ca              | 99.80 <sup>ii, a</sup>                          | Yasuda <i>et al.</i> , 2007 [141]  |
| CaCl <sub>2</sub> | SiO <sub>2</sub> plate,<br>SiO <sub>2</sub> tube           | 1123            | Si plate<br>Si rod   | glass-like<br>carbon,<br>Ca–Ni alloy | Ag <sup>+</sup> /Ag in CaCl <sub>2</sub> ,<br>Mo–Ca <sup>2+</sup> /Ca              | >99.5 <sup>i, a</sup>                           | Nohira <i>et al.</i> , 2009 [142]  |
| CaCl <sub>2</sub> | SiO <sub>2</sub> pellet                                    | 1123            | Si                   | glass-like<br>carbon                 | Ag <sup>+</sup> /Ag in CaCl <sub>2</sub> ,<br>Mo–Ca <sup>2+</sup> /Ca <sup>1</sup> | >99.7 <sup>i, a</sup>                           | Kobayashi <i>et al.</i> , 2010 [143]   |
| CaCl <sub>2</sub> | amorphous SiO <sub>2</sub> pellet                          | 1123            | Mo                   | graphite                             | Ag <sup>+</sup> /Ag in CaCl <sub>2</sub> ,<br>Mo–Ca <sup>2+</sup> /Ca              | –   | Nishimura <i>et al.</i> , 2010 [144]   |
| CaCl <sub>2</sub> | SiO <sub>2</sub> layer (~2.0 μm) on<br><i>p</i> -Si (100)  | 1123            | Mo                   | graphite                             | graphite,<br>Mo–Ca <sup>2+</sup> /Ca   | –   | Juzeliunas <i>et al.</i> , 2010 [145]<br>Juzeliunas <i>et al.</i> , 2012 [146] |
| CaCl <sub>2</sub> | quartz tube, SiO <sub>2</sub> pellet                       | 1173            | W                    | graphite                             | Ag <sup>+</sup> /Ag in NaCl–KCl  | –   | Xiao <i>et al.</i> , 2010 [147]  |
| CaCl <sub>2</sub> | SiO <sub>2</sub> pellet                                    | 1123            | Ni                   | graphite                             | Ag <sup>+</sup> /Ag in NaCl–KCl,<br>Mo–Ca <sup>2+</sup> /Ca <sup>1</sup>           | –   | Xiao <i>et al.</i> , 2012 [148]  |
| CaCl <sub>2</sub> | SiO <sub>2</sub> granule                                   | 1123            | <i>n</i> -Si (100)   | graphite                             | Ag <sup>+</sup> /Ag in NaCl–KCl,<br>Mo–Ca <sup>2+</sup> /Ca                        | –   | Toba <i>et al.</i> , 2013 [149]  |
| CaCl <sub>2</sub> | SiO <sub>2</sub> granule                                   | 1123            | <i>n</i> -Si (100)   | glass-like<br>carbon                 | Ag <sup>+</sup> /Ag in CaCl <sub>2</sub> ,<br>Mo–Ca <sup>2+</sup> /Ca              | >99.1 <sup>i, a</sup><br>>99.8 <sup>ii, a</sup> | Yasuda <i>et al.</i> , 2013 [150]  |

**Table 1-7 (continue) Previous studies on the electrochemical reduction of solid SiO<sub>2</sub> in chloride-based molten salts.**

| Molten salt                | Si precursor  | Temperature / K | Contacting electrode         | Counter electrode | (Pseudo) Reference electrode   | Purity of produced Si / %                        | Authors, Year [Ref.]   |
|----------------------------|---|-----------------|------------------------------|-------------------|--|--|--|
| CaCl <sub>2</sub>          | quartz, porous SiO <sub>2</sub> pellet                | 1173            | Mo                           | graphite          | quartz sealed Ag/AgCl <sup>[165]</sup>   | –  | Xiao <i>et al.</i> , 2013 [151]  |
| CaCl <sub>2</sub>          | SiO <sub>2</sub> granule                              | 1123            | graphite, <i>n</i> -Si (100) | glass-like carbon | Ag <sup>+</sup> /Ag in CaCl <sub>2</sub> , Mo–Ca <sup>2+</sup> /Ca                               | –  | Yang <i>et al.</i> , 2014 [152, 153]                                   |
| CaCl <sub>2</sub>          | SiO <sub>2</sub> layer (100 nm) on <i>p</i> -Si (100) | 1123            | Mo                           | graphite          | graphite   | –  | Juzeliunas <i>et al.</i> , 2016 [154] †                                |
| CaCl <sub>2</sub>          | SiO <sub>2</sub> granule                              | 1123            | <i>n</i> -Si (100)           | glass-like carbon | Ag <sup>+</sup> /Ag in CaCl <sub>2</sub> , Mo–Ca <sup>2+</sup> /Ca                               | –  | Yang <i>et al.</i> , 2016 [155]  |
| CaCl <sub>2</sub>          | SiO <sub>2</sub> granule                              | 1123            | graphite                     | glass-like carbon | Ag <sup>+</sup> /Ag in CaCl <sub>2</sub> , Mo–Ca <sup>2+</sup> /Ca                               | 99.6 <sup>i, a</sup><br>>99.995 <sup>ii, a</sup> | Yang <i>et al.</i> , 2016 [156]  |
| CaCl <sub>2</sub>          | SiO <sub>2</sub> granule                              | 1123            | Si                           | glass-like carbon | Ag <sup>+</sup> /Ag in CaCl <sub>2</sub> , Mo–Ca <sup>2+</sup> /Ca                               | 98.6 <sup>i, a</sup><br>>99.93 <sup>ii, a</sup>  | Zhong <i>et al.</i> , 2018 [157]                                       |
| NaCl–CaCl <sub>2</sub>     | SiO <sub>2</sub> pellet                               | 1023–1123       | stainless steel, Ni          | graphite          | – <sup>2</sup>   | –  | Ergül <i>et al.</i> , 2011 [158]                                       |
| NaCl–CaCl <sub>2</sub>     | SiO <sub>2</sub> pellet                               | 1023            | Si                           | graphite          | – <sup>2</sup>   | –  | Akpinar <i>et al.</i> , 2017 [159]                                     |
| LiCl–KCl–CaCl <sub>2</sub> | quartz plate  | 773             | Mo                           | graphite          | Ag <sup>+</sup> /Ag in LiCl–KCl–CaCl <sub>2</sub> , Mo–Li <sup>+</sup> , Ca <sup>2+</sup> /Li–Ca | –  | Nohira <i>et al.</i> , 2003 [134]<br>Yasuda <i>et al.</i> , 2005 [160] |
| LiCl–Li <sub>2</sub> O     | SiO <sub>2</sub> powder                               | 923             | stainless steel              | Pt                | Pt   | –  | Lee <i>et al.</i> , 2008 [161]   |
| CaCl <sub>2</sub> –CaO     | SiO <sub>2</sub> pellet                               | 1173            | Ni                           | graphite          | graphite, Mo–Ca <sup>2+</sup> /Ca  | –  | Pistorius and Fray, 2006 [162]   |

<sup>1</sup> Electrolysis was conducted by both 2-electrode constant voltage and 3-electrode manner.

<sup>2</sup> Electrolysis was conducted by 2-electrode constant voltage manner.

<sup>i</sup> Si product formed by electrolysis.

<sup>ii</sup> Si ingot produced by floating zone method.

<sup>a</sup> Analyzed by GD-MS.

### 1.4.3.2 Electrodeposition of Si from Dissolved SiO<sub>2</sub>

As another approach, the electrodeposition of Si from dissolved SiO<sub>2</sub> in molten salts has also been investigated. The electrodeposition was conducted in chloride-based [148, 166–175], fluoride-based [176–181] and fluoride–chloride [182–184] mixture salts.

Table 1-8 summarizes the previous studies in chloride-based molten salts. Bard's group has reported the formation of relatively smooth film in molten CaCl<sub>2</sub>-based salts at 1123 K [168, 169, 172–174], in which the highest purity of electrodeposited Si achieved 99.99989% [174]. In several reports, the photovoltaic behavior [167–169, 172–174] and the formation of *p-n* junction [173, 174] were confirmed. However, a pre-electrolysis for ~120 h was conducted to remove the impurities in electrolyte in Zou *et al.*'s report [174], which means the low tolerance of impurities in this process. Moreover, this method is not suitable for the continuous production due to its batch process nature.

The electrodeposition of Si was also confirmed in fluoride-based [178–181] and fluoride–chloride mixture [182] melts; Table 1-9 summarizes the previous studies. Suzuki *et al.* obtained polycrystalline Si films in molten LiF–NaF–KF–Li<sub>2</sub>O at 873 K [181]. In addition, the electrodeposition of Si using SiO<sub>2</sub>–K<sub>2</sub>SiF<sub>6</sub> mixture as the Si precursor was also investigated [176, 183], in which only powdery Si was obtained. However, the purity of deposited Si and the photovoltaic behavior have not been reported in any of the studies.

**Table 1-8 Previous studies on the electrodeposition of Si from SiO<sub>2</sub> in chloride-based molten salts.**

| Molten salt                               | Si precursor                               | Temperature / K | Substrate                      | Counter electrode | (Pseudo) Reference electrode                                     | Morphology of deposited Si | Purity of produced Si / % | Authors, Year [Ref.]                |
|---|--|-----------------|--------------------------------|-------------------|--|----------------------------|---------------------------|-------------------------------------|
| CaCl <sub>2</sub>                         | CaSiO <sub>3</sub>                         | 1123            | Ni                             | graphite          | Ag <sup>+</sup> /Ag in NaCl–KCl, Mo–Ca <sup>2+</sup> /Ca         | granular                   | –                         | Xiao <i>et al.</i> , 2012 [148]     |
| CaCl <sub>2</sub>                         | SiO <sub>2</sub> NP (nanopowder)           | 1123            | Mo, <i>n</i> -Si (100)         | glass-like carbon | Mo–Ca <sup>2+</sup> /Ca  | granular                   | –                         | Cho <i>et al.</i> , 2012 [166]      |
| CaCl <sub>2</sub>                         | SiO <sub>2</sub> NP                        | 1123            | Ag                             | graphite          | graphite   | granular                   | –                         | Cho <i>et al.</i> , 2012 [167] †    |
| CaCl <sub>2</sub>                         | SiO <sub>2</sub> NP                        | 1123            | graphite                       | graphite          | – <sup>1</sup>   | smooth film                | –                         | Zhao <i>et al.</i> , 2016 [168] †   |
| CaCl <sub>2</sub>                         | SiO <sub>2</sub> NP                        | 1123            | graphite                       | graphite          | – <sup>2</sup>   | smooth film                | –                         | Xie <i>et al.</i> , 2018 [169] †, # |
| CaCl <sub>2</sub>                         | SiO <sub>2</sub> NP                        | 1128            | Ag, Ni                         | graphite          | graphite   | nanocrystalline film       | –                         | Islam <i>et al.</i> , 2018 [170]    |
| NaCl–CaCl <sub>2</sub> –BaCl <sub>2</sub> | SiO <sub>2</sub>                           | 923             | Ag                             | glass-like carbon | Ag <sup>+</sup> /Ag in NaCl–CaCl <sub>2</sub> –BaCl <sub>2</sub> | porous film                | –                         | Sakanaka <i>et al.</i> , 2017 [171] |
| CaCl <sub>2</sub> –CaO                    | SiO <sub>2</sub> NP                        | 1123            | graphite                       | graphite          | Ag <sup>+</sup> /Ag in CaCl <sub>2</sub> (for CV) <sup>2</sup>   | smooth film                | >99.96 <sup>a</sup>       | Yang <i>et al.</i> , 2017 [172] †   |
| CaCl <sub>2</sub> –CaO                    | SiO <sub>2</sub> NP and CaSiO <sub>3</sub> | 1123            | graphite, <i>p</i> -Si deposit | graphite          | – <sup>1, 2, 3</sup>   | smooth film                | ~99.996 <sup>a</sup>      | Zou <i>et al.</i> , 2017 [173] †, ‡ |
| CaCl <sub>2</sub> –CaO                    | SiO <sub>2</sub> NP, CaSiO <sub>3</sub>    | 1123            | graphite, <i>p</i> -Si deposit | graphite          | – <sup>3</sup>   | smooth film                | 99.99989 <sup>a</sup>     | Zou <i>et al.</i> , 2019 [174] †, ‡ |
| CaCl <sub>2</sub> –CaO                    | SiO <sub>2</sub> NP                        | 1123            | graphite                       | graphite          | – <sup>1</sup>   | film                       | –                         | Zou <i>et al.</i> , 2020 [175]      |

<sup>1</sup> Electrodeposition was conducted by 2-electrode constant current density manner.

<sup>2</sup> Electrodeposition was conducted by 2-electrode constant voltage manner.

<sup>3</sup> Electrodeposition was conducted by 2-electrode pulse manner.

<sup>a</sup> Analyzed by GD-MS.

† Photovoltaic behavior of electrodeposited Si was confirmed.

‡ Formation of *p*–*n* junction by electrolysis was confirmed.

# Electrochemical performance was confirmed as the anode material of Li-ion battery.

**Table 1-9 Previous studies on the electrodeposition of Si from SiO<sub>2</sub> in fluoride-based and fluoride–chloride mixture molten salts.**

| Molten salt                              | Si precursor   | Temperature / K | Substrate     | Counter electrode | (Pseudo) Reference electrode  | Morphology of deposited Si | Purity of produced Si / % | Authors, Year [Ref.]   |
|--|--|-----------------|---------------|-------------------|---|----------------------------|---------------------------|--|
| NaF–KF                                   | K <sub>2</sub> SiF <sub>6</sub> and SiO <sub>2</sub> | 983–1053        | Mo, W, Ni, Cu | graphite          | –   | powder                     | 98.0–99.0 <sup>a</sup>    | Boiko <i>et al.</i> , 1982 [176]                                   |
| NaF–CaF <sub>2</sub>                     | SiO <sub>2</sub>                                     | 1423            | graphite      | graphite          | – <sup>1</sup>  | powder                     | –                         | Elwell, 1981 [177]   |
| CaF <sub>2</sub> –BaF <sub>2</sub>       | SiO <sub>2</sub>                                     | 1573            | Mo            | graphite          | MoSi <sub>2</sub> ,<br>glass-like carbon–<br>CO <sub>2</sub> /O <sup>2-</sup> | film                       | –                         | Hu <i>et al.</i> , 2013 [178]                                      |
| LiF–NaF–KF                               | SiO <sub>2</sub> powder                              | 873             | Ag            | glass-like carbon | Ni–K <sup>+</sup> /K  | film                       | –                         | Sakanaka and Goto, 2015 [179]<br>Suzuki <i>et al.</i> , 2017 [180] |
| LiF–NaF–KF–Li <sub>2</sub> O             | SiO <sub>2</sub> powder                              | 873             | Ag            | glass-like carbon | Ni–K <sup>+</sup> /K  | film                       | –                         | Suzuki <i>et al.</i> , 2019 [181]                                  |
| NaF–NaCl–KCl                             | SiO <sub>2</sub>                                     | 1073            | Mo            | graphite          | Pt  | film                       | –                         | Cai <i>et al.</i> , 2010 [182]                                     |
| KF–KCl                                   | K <sub>2</sub> SiF <sub>6</sub> and SiO <sub>2</sub> | 893–973         | W             | graphite          | – <sup>2</sup>  | powder                     | –                         | Andriiko <i>et al.</i> , 1997 [183]                                |
| CaF <sub>2</sub> –CaCl <sub>2</sub> –CaO | SiO <sub>2</sub> powder                              | 1023            | Mo            | W                 | Pt  | <i>unknown</i>             | –                         | Li <i>et al.</i> , 2019 [184]                                      |

<sup>1</sup> Electrodeposition was conducted by 2-electrode constant voltage manner.

<sup>2</sup> Electrodeposition was conducted by 2-electrode constant current manner.

<sup>a</sup> Analyzed by spectral emission method.

## 1.5 Background and Purposes of This Study

### 1.5.1 Background

#### 1.5.1.1 Issues of the Conventional Electrochemical Reduction of SiO<sub>2</sub>

As described in the previous section, the electrochemical reductions of solid and dissolved SiO<sub>2</sub> in molten salts have been extensively investigated. For the electrochemical reduction of solid SiO<sub>2</sub>, there are quite a few of previous studies, including the reaction mechanism, and the research has progressed considerably. The challenge of using solid SiO<sub>2</sub> as the raw material is that the separation of the powdery Si product from unreacted SiO<sub>2</sub> and molten salt is difficult, which leads to the contamination of impurities into Si. Such contamination can be avoided by the electrochemical reduction of dissolved SiO<sub>2</sub>. In fact, the electrodeposition of high-purity Si film was achieved in CaCl<sub>2</sub>-based molten salt. However, a long-time pre-electrolysis is necessary before the electrodeposition, which means the low tolerance of impurities in this process.

#### 1.5.1.2 A New SOG-Si Production Process Using Electrochemical Reduction of Solid SiO<sub>2</sub> at a Liquid Zn Cathode

In order to solve the issues mentioned above, electrochemical reduction process using a liquid Zn cathode was proposed [185, 186]. Since the electrolysis product is liquid Si–Zn alloy, its separation from unreacted SiO<sub>2</sub> and molten salts is expected to be easier than conventional solid cathode. The selection of Zn as the alloying element stems from the very factors that render the DuPont process advantageous, i.e., ensures the formation of no intermetallic compounds with Si, and facilitates easy removal of both Zn and ZnCl<sub>2</sub>. In addition, the evaporation of Zn is efficiently suppressed by sinking it into molten salt even at 1123 K. Figure 1-9 schematically illustrates the proposed process [185, 186]. The overall process consists of three major steps: electrolysis, precipitation, and refining. In the electrolysis step, solid SiO<sub>2</sub> is reduced to form liquid Si–Zn alloy at liquid Zn cathode.

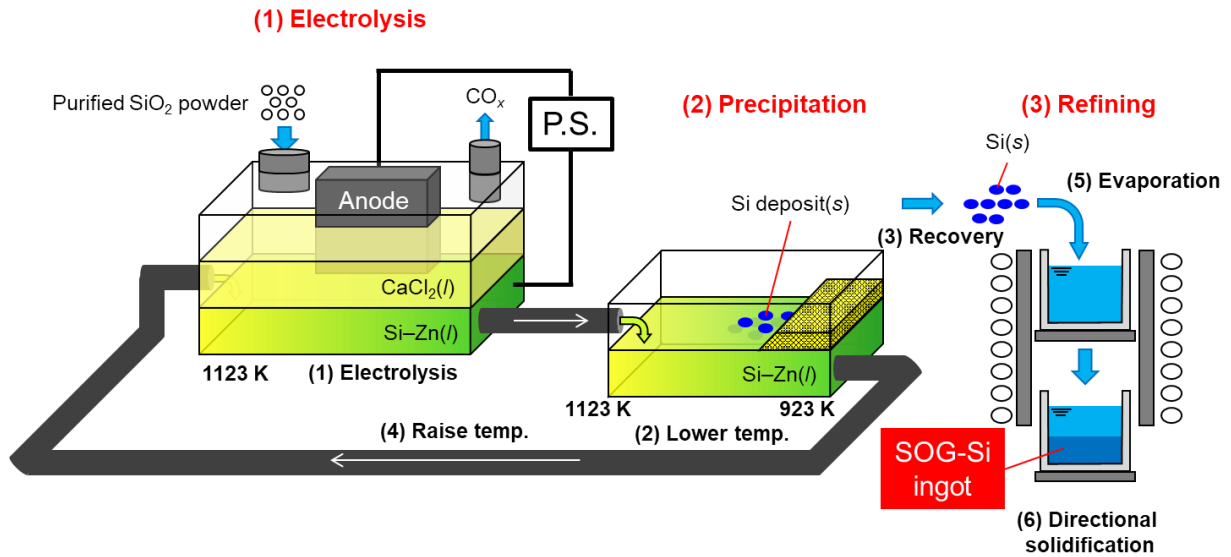
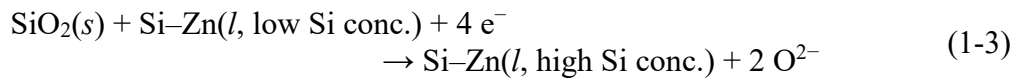
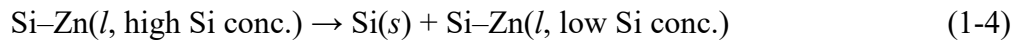


Figure 1-9 Schematic drawing of SOG-Si production process using electrochemical reduction of solid  $\text{SiO}_2$  at a liquid Zn cathode [185, 186].



In the precipitation step, solid Si is recovered by lowering the temperature of the liquid Si-Zn alloy.

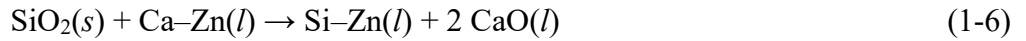
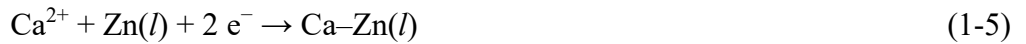


Since the solubility of Si in liquid Zn is 6 at.% at 1123 K and 1 at.% at 923 K [187], 5 at.% of solid Si with reference to Zn is theoretically recovered when the temperature is lowered from 1123 K to 923 K. Si is purified with the precipitation from liquid Si-Zn alloy because of the small distribution coefficient of impurities between solid Si and liquid Zn. After the precipitation step, the Si-Zn alloy with a low concentration of Si is reused as the cathode in the electrolysis step. The Si recovered is then subjected to the refining step: that entails vacuum refining to remove residual Zn and directional solidification to manufacture SOG-Si ingots.

## 1.5.2 Purposes of This Study

### 1.5.2.1 Electrochemical Reduction of Solid SiO<sub>2</sub> at a Liquid Zn Electrode in Molten CaCl<sub>2</sub>

The electrochemical reduction of solid SiO<sub>2</sub> at a liquid Zn electrode was confirmed (reaction (1-3)) in the previous study [186]. Also, the formation of liquid Ca–Zn alloy (reaction (1-5)) was suggested by cyclic voltammogram, so that the possibility of indirect reduction of SiO<sub>2</sub> by liquid Ca–Zn alloy (reaction (1-6)) could be considered. However, the evidence for the indirect reduction was not confirmed. Therefore, in this study, the author investigated indirect reduction by liquid Ca–Zn alloy and the contribution of direct electrochemical reduction and indirect reduction, which is described in Chapter 2.



### 1.5.2.2 Electrochemical Reduction of Dissolved SiO<sub>2</sub> at a Liquid Zn Electrode in Molten CaCl<sub>2</sub>

According to the results of Chapter 2, the reduction of SiO<sub>2</sub> at 0.60 V (vs. Ca<sup>2+</sup>/Ca) was confirmed as a mixed reduction mechanism of direct electrochemical reduction and indirect reduction by liquid Ca–Zn alloy. However, the current efficiency was only 28% due to the low reduction rate of Ca–Zn alloy; a part of it contributed to the indirect reduction of SiO<sub>2</sub> and the rest remained as Ca–Zn alloy.

To improve the productivity of the electrolysis step, the author focused on the electrochemical reduction of dissolved SiO<sub>2</sub>, that is, silicate ions such as SiO<sub>3</sub><sup>2-</sup>, SiO<sub>4</sub><sup>4-</sup>, *etc.* When O<sup>2-</sup> ion is added to the molten salt, the dissolution of SiO<sub>2</sub> can be expressed as follows:



In this study, the ionic species of silicates in molten CaCl<sub>2</sub> was investigated before the



electrochemical measurement because various ionic species of silicates exists. Then, electrochemical reduction of silicate ions at a liquid Zn electrode was conducted in molten CaCl<sub>2</sub> because of its high solubility of O<sup>2-</sup> ion [164]. The results are described in Chapter 3.

### 1.5.2.3 Electrochemical Reduction of Dissolved SiO<sub>2</sub> at a Liquid Zn Electrode in Molten NaCl–CaCl<sub>2</sub>

As mentioned above, CaCl<sub>2</sub> was selected in the electrolysis step because of its high solubility of O<sup>2-</sup> ion. On the other hand, CaCl<sub>2</sub> is not suitable for the suppression of Zn evaporation in the precipitation step, because its melting point is higher than the temperature for Si recovery from liquid Si–Zn alloy, i.e., 923 K. Therefore, a molten salt with a melting point lower than 923 K is required to suppress the evaporation of Zn. The author selected eutectic NaCl–CaCl<sub>2</sub> because of its relatively low melting point in binary chloride molten salts. Figure 1-10 shows a phase diagram for the NaCl–CaCl<sub>2</sub> system, in which the melting point is 777 K at the eutectic composition; NaCl:CaCl<sub>2</sub> = 47.9:52.1 mol% [188]. Since the process is considered to be simplified if both electrolysis and precipitation steps can be conducted in the same molten salt, the electrochemical reduction of dissolved SiO<sub>2</sub> in NaCl–CaCl<sub>2</sub> system was investigated (Chapter 5). Before the electrochemical measurement, ionic species of silicates in molten NaCl–CaCl<sub>2</sub> was investigated (Chapter 4).

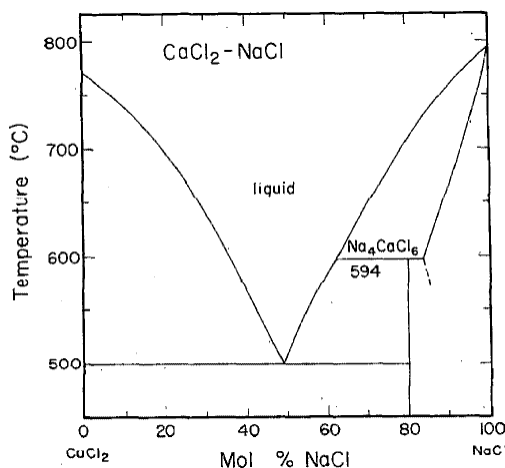


Figure 1-10 Phase diagram for the NaCl–CaCl<sub>2</sub> system [188].

#### 1.5.2.4 Silicon Refining by Solidification from Liquid Si–Zn Alloy and Floating Zone Method

To establish the process shown in [Figure 1-9](#), the solvent refining using the liquid Si–Zn alloy should be investigated. Due to the experimental difficulty caused by the high vapor pressure of Zn, there is no report so far. In this study, the distribution behavior of impurity elements was investigated using a liquid Si–Zn alloy prepared from low-purity MG-Si, which is described in Chapter 6. As the pre-study for the precipitation and refining steps, the author used the MG-Si instead of electrochemically reduced Si in the electrolysis step.

### 1.6 Overview of This Study

For the establishment of the SOG-Si production process using a liquid Zn cathode in molten salts, the electrochemical reduction of solid and dissolved SiO<sub>2</sub> was investigated in chloride-based molten salts in this study. The distribution behavior of impurity elements during the solidification of Si from liquid Si–Zn alloy and liquid Si was also investigated.

In Chapter 2, the electrochemical reduction of solid SiO<sub>2</sub> at a liquid Zn electrode was studied in molten CaCl<sub>2</sub> at 1123 K. The direct electrochemical reduction and the indirect reduction by liquid Ca–Zn alloy were investigated by a series of electrolysis and immersion experiments. The obtained Si particles were analyzed by X-ray diffractometry (XRD). Also, the impurity analysis for the Si particles was conducted by inductively coupled plasma atomic emission spectroscopy (ICP-AES).

In Chapter 3, the electrochemical reduction of dissolved SiO<sub>2</sub> at solid graphite and liquid Zn electrodes was conducted in molten CaCl<sub>2</sub>–CaO at 1123 K. Before the electrochemical investigation, the ionic species of dissolved SiO<sub>2</sub>, i.e., silicate ions, with different ratio of O<sup>2-</sup>/SiO<sub>2</sub> was investigated by Raman spectroscopy. The electrochemical reduction of silicate ions with different O<sup>2-</sup>/SiO<sub>2</sub> ratios was analyzed by cyclic voltammetry. Potentiostatic electrolysis was conducted at different potentials at solid graphite and liquid Zn electrodes. The surfaces of

deposited Si at graphite electrodes were observed by scanning electron microscopy (SEM) and analyzed by XRD. The Si particles obtained at the liquid Zn electrode were observed by optical microscopy and SEM. Furthermore, Ca concentration in the Zn electrode was analyzed by ICP-AES for the confirmation of Ca–Zn alloy formation.

In Chapter 4, the electrochemical reduction of silicate ions at graphite electrodes was investigated in molten NaCl–CaCl<sub>2</sub>–CaO at 1023 K and 1123 K, as the pre-study for the liquid Zn electrode. The ionic species of silicate ions with different O<sup>2-</sup>/SiO<sub>2</sub> ratios at 1023 K was also investigated by Raman spectroscopy before the electrochemical investigation. The electrochemical reduction of silicate ions in molten NaCl–CaCl<sub>2</sub>–CaO was also investigated in a similar manner as described in Chapter 3.

In Chapter 5, the electrochemical reduction of silicate ions at a liquid Zn electrode was investigated in molten NaCl–CaCl<sub>2</sub>–CaO at 1023 K and 1123 K. Cyclic voltammetry and potentiostatic electrolysis were conducted for the electrochemical investigation. The Si particles obtained from the electrolysis at the liquid Zn electrode were observed by optical microscopy and SEM. Also, concentrations of Ca and Na in the Zn electrode were analyzed by ICP-AES to confirm the formation of Ca–Zn and/or Na–Zn alloy.

In Chapter 6, the distribution behavior of impurity elements during the precipitation of solid Si from a liquid Si–Zn alloy was studied by thermodynamic calculations and precipitation experiments. The refining ability was evaluated from the results of impurity analysis for the precipitated Si. As the post-processing, a Si ingot was produced from the precipitated Si granules by the floating zone method. Based on the results of impurity analysis of the Si ingot, the overall refining ability of the precipitation and refining steps was discussed.

Finally, Chapter 7 summarizes the electrochemical reduction behavior of solid and dissolved SiO<sub>2</sub> at solid graphite and liquid Zn electrodes in chloride-based molten salts. Also, the distribution behavior of impurity elements during the Si precipitation from liquid Si–Zn alloy and solidification of liquid Si were investigated. Considering the above results, the prospects and

challenges for the establishment of the production process of SOG-Si using a liquid Zn cathode were discussed.

## 1.7 Reference List

- [1] Global Change Data Lab from University of Oxford, Energy Production and Consumption, <https://ourworldindata.org/energy-production-consumption#primary-energy-consumption> (01/07/2022 accessed).
- [2] *Climate Change 2014-Mitigation of Climate Change, Annex III: Technology-Specific Cost and Performance Parameters*, Intergovernmental Panel on Climate Change (IPCC) Working Group III (2014).
- [3] *Climate Change 2021: The Physical Science Basis*, Intergovernmental Panel on Climate Change (IPCC) (2021).
- [4] *Sustainable Recovery: World Energy Outlook 2020 Special Report*, International Energy Agency (IEA) (2020).
- [5] *World Energy Outlook 2020*, International Energy Agency (IEA) (2020).
- [6] National Renewable Energy Laboratory transforming ENERGY, Best Research-Cell Efficiency Chart, <https://www.nrel.gov/pv/cell-efficiency.html> (01/07/2022 accessed).
- [7] *Trends 2018 in Photovoltaic Applications*, International Energy Agency Photovoltaic Power System Programme (IEA PVPS) (2018).
- [8] *Kagaku Binran Kisoheh, 5th ed.*, Maruzen Co., Ltd. (2004). [in Japanese]
- [9] *Photovoltaic Market 2021*, RTS Corp. (2021). [in Japanese]
- [10] T. Abe, *Advanced Electronics I-5, Si-Crystal Growth and Wafer Manufacturing*, Baifukan Co., Ltd. (1994). [in Japanese]
- [11] C. Ramírez-Márquez, G. Contreras-Zarazúa, M. Martín and J. G. Segovia-Hernández, *ACS Sustain. Chem. Eng.*, **7**, 5355 (2019).
- [12] C. Bye and B. Ceccaroli, *Sol. Energ. Mater. Sol. C.*, **130**, 634 (2014).

- [13] H. Schweickert, K. Reusche and H. Gustsche, U.S. Patent 3011877 (1961).
- [14] H. Gustsche, U.S. Patent 3011877 (1962).
- [15] J. Czochralski, *Z. Phys. Chem.*, **92**, 219 (1918). [in German]
- [16] H. Chen, K. Morita, X. Ma, Z. Chen and Y. Wang, *Sol. Energ. Mater. Sol. C.*, **203**, 110169 (2019).
- [17] Z. Yu, W. Ma, K. Xie, G. Lv, Z. Chen, J. Wu and J. Yu, *Appl. Energy*, **185**, 68 (2017).
- [18] M. D. Johnston, L. T. Khajavi, M. Li, S. Sokhanvaran and M. Barati, *JOM*, **64**, 935 (2012).
- [19] F. Chigondo, *Silicon*, **10**, 789 (2018).
- [20] H. Momokawa and N. Sano, *Metall. Mater. Trans. B*, **13B**, 643 (1982).
- [21] K. Suzuki, T. Sugiyama, K. Takano and N. Sano, *J. Jpn. Inst. Met. Mater.*, **54**, 168 (1990).  
[in Japanese]
- [22] S. Anders, European Patent 0699625 (1996).
- [23] L. A. V. Teixeira and K. Morita, *ISIJ Int.*, **49**, 783 (2009).
- [24] L. Teixeira and K. Morita, *ISIJ Int.*, **49**, 783 (2009).
- [25] M. D. Johnston and M. Barati, *Sol. Energ. Mater. Sol. C.*, **94**, 2085 (2010).
- [26] J. Cai, J. Li, W. Chen, C. Chen and X. Luo, *Trans. Nonfer. Metal Soc. Chn.*, **21**, 1402 (2011).
- [27] E. Jung, B. Moon and D. Min, *Sol. Energ. Mater. Sol. C.*, **95**, 1779 (2011).
- [28] C. Yin, B. Hu and X. Huang, *J. Semicond.*, **32**, 092003/1 (2011).
- [29] Y. V. Meteleva-Fischer, Y. Yang, R. Boom, B. Kraaijveld and H. Kuntzel, *JOM*, **64**, 957 (2012).
- [30] Y. Wang, X. Ma and K. Morita, *Metall. Mater. Trans. B*, **45**, 334 (2014).
- [31] H. Lai, L. Huang, C. Lu, M. Fang, W. Ma, P. Xing, J. Li and X. Luo, *JOM*, **68**, 2371 (2016).
- [32] F. Wang, J. Wu, W. Ma, M. Xu, Y. Lei and B. Yang, *Sep. Purif. Technol.*, **170**, 248 (2016).
- [33] J. Wu, F. Wang, W. Ma, Y. Lei and B. Yang, *Metall. Mater. Trans. B*, **47**, 1796 (2016).
- [34] H. C. Theurer, *J. Mech. Eng. Technol.*, **8**, 1316 (1956).
- [35] K. Suzuki, K. Sakaguchi, T. Nakagiri and N. Sano, *J. Jpn. Inst. Met. Mater.*, **54**, 161 (1990).

- [36] T. Ikeda and M. Maeda, *ISIJ Int.*, **32**, 635 (1992). [in Japanese]
- [37] K. Suzuki, T. Kumagai and N. Sano, *ISIJ Int.*, **32**, 630 (1992). [in Japanese]
- [38] N. Yuge, H. Baba and F. Aratani, U.S. Patent 5182091 (1993).
- [39] N. Yuge, H. Baba, Y. Sakaguchi, K. Nishikawa, H. Terashima and F. Aratani, *Sol. Energ. Mater. Sol. C.*, **34**, 243 (1994).
- [40] N. Yuge, M. Abe, K. Hanazawa, H. Baba, N. Nakamura, Y. Kato, Y. Sakaguchi, S. Hiwasa and F. Aratani, *Prog. Photovolt. Res. Appl.*, **9**, 203 (2001).
- [41] Y. Delannoy, C. Alemany, K. I. Li, P. Proulx and C. Trassy, *Sol. Energ. Mater. Sol. C.*, **72**, 69 (2002).
- [42] J. C. S. Pires, A. F. B. Braga and P. R. Mei, *Sol. Energ. Mater. Sol. C.*, **79**, 347 (2003).
- [43] K. Hanazawa, N. Yuge and Y. Kato, *Mater. Trans.*, **45**, 844 (2004).
- [44] J. C. S. Pires, J. Otubo, A. F. B. Braga and P. R. Mei, *J. Mater. Process. Technol.*, **169**, 16 (2005).
- [45] J. Safarian, G. Tranell and M. Tangstad, *Energy Procedia*, **20**, 88 (2012).
- [46] S. Pizzini, *Sol. Energy Mater.*, **6**, 253 (1982).
- [47] J. Dietl, *Solar Cells*, **10**, 145 (1983).
- [48] I. C. Santos, A. P. Gonçalves, C. S. Santos, M. Almeida, M. H. Afonso and M. J. Cruz, *Hydrometallurgy*, **23**, 237 (1990).
- [49] T. Shimpo, T. Yoshikawa and K. Morita, *Metall. Mater. Trans. B*, **35**, 277 (2004).
- [50] M. Dueñas Díez, M. Fjeld, E. Andersen and B. Lie, *Chem. Eng. Sci.*, **61**, 229 (2006).
- [51] X. Ma, J. Zhang, T. Wang and T. Li, *Rare Metals*, **28**, 221 (2009).
- [52] Y. Sun, Q. Ye, C. Guo, H. Chen, X. Lang, F. David, Q. Luo and C. Yang, *Hydrometallurgy*, **139**, 64 (2013).
- [53] P. Keck and M. Golay, *Phys. Rev.*, **89**, 1297 (1953).
- [54] P. R. Mei, S. P. Moreira, E. Cardoso, A. D. S. Côrtes and F. C. Marques, *Sol. Energ. Mater. Sol. C.*, **98**, 233 (2012).

- [55] S. Hu, Y. Dai, A. Gagnoud, Y. Fautrelle, R. Moreau, Z. Ren, K. Deng, C. Li and X. Li, *J. Alloy. Compd.*, **722**, 108 (2017).
- [56] R. Monnier and J. C. Giacometti, *Helv. Chim. Acta.*, **47**, 345 (1964).
- [57] R. Monnier and D. Barakat, U.S. Patent 3219561 (1965).
- [58] R. Monnier, D. Barakat and J. C. Giacometti, U.S. Patent 3254010 (1966).
- [59] J. M. Olson and K. L. Carleton, *J. Electrochem. Soc.*, **128**, 2698 (1981).
- [60] I. G. Sharma and T. K. Mukherjee, *Metallurgical Transactions B*, **17**, 395 (1986).
- [61] H. Ryu, Y. An, B. Jang, J. Lee, H. H. Nersisyan, M. Han, J. Noh and J. Lee, *Mater. Chem. Phys.*, **137**, 160 (2012).
- [62] X. Zou, H. Xie, Y. Zhai, X. Lang and J. Zhang, *Adv. Mater. Res.*, **391-392**, 697 (2012).
- [63] X. Zou, H. Xie, Y. Zhai and X. Lang, *Chin. J. Chem. Phys.*, **26**, 88 (2013).
- [64] O. E. Kongstein, C. Wollan, S. Sultana and G. M. Haarberg, *ECS Trans.*, **3**, 357 (2007).
- [65] J. Cai, X. Luo, G. M. Haarberg, O. E. Kongstein and S. Wang, *J. Electrochem. Soc.*, **159**, D155 (2012).
- [66] J. Cai, X. Luo, C. Lu, G. M. Haarberg, A. Laurent, O. E. Kongstein and S. Wang, *Trans. Nonfer. Metal Soc. Chn.*, **22**, 3103 (2012).
- [67] E. Olsen and S. Rolseth, *Metall. Mater. Trans. B*, **41**, 295 (2010).
- [68] E. Olsen, S. Rolseth and J. Thonstad, *Metall. Mater. Trans. B*, **41**, 752 (2010).
- [69] Y. Lai, M. Jia, Z. Tian, J. Li, J. Yan, J. Yi, Z. Wang and Y. Liu, *Metall. Mater. Trans. A*, **41**, 929 (2010).
- [70] I. Obinata and N. Komatsu, *J. Jpn. Inst. Met. Mater.*, **18**, 279 (1954). [in Japanese]
- [71] I. Obinata and N. Komatsu, *J. Jpn. Inst. Met. Mater.*, **18**, 283 (1954). [in Japanese]
- [72] P. S. Kotval and H. B. Strock, U.S. Patent 4124410 (1978).
- [73] P. S. Kotval and H. B. Strock, U.S. Patent 4193975 (1980).
- [74] P. S. Kotval and H. B. Strock, U.S. Patent 4195067 (1980).
- [75] T. Yoshikawa and K. Morita, *STAM*, **4**, 531 (2003).

- [76] T. Yoshikawa and K. Morita, *J. Electrochem. Soc.*, **150**, G465 (2003).
- [77] T. Yoshikawa, K. Arimura and K. Morita, *Metall. Mater. Trans. B*, **36**, 837 (2005).
- [78] T. Yoshikawa and K. Morita, *ISIJ Int.*, **45**, 967 (2005).
- [79] T. Yoshikawa and K. Morita, *Metall. Mater. Trans. B*, **36**, 731 (2005).
- [80] T. Yoshikawa and K. Morita, *J. Phys. Chem. Solids*, **66**, 261 (2005).
- [81] T. Yoshikawa and K. Morita, *J. Cryst. Growth.*, **311**, 776 (2009).
- [82] T. Yoshikawa, K. Morita, S. Kawanishi and T. Tanaka, *J. Alloy. Compd.*, **490**, 31 (2010).
- [83] K. Morita and T. Yoshikawa, *Trans. Nonfer. Metal Soc. Chn.*, **21**, 685 (2011).
- [84] T. Yoshikawa and K. Morita, *JOM*, **64**, 946 (2012).
- [85] Y. Li, Y. Tan, J. Li and K. Morita, *J. Alloy. Compd.*, **611**, 267 (2014).
- [86] Y. Lei, W. Ma, L. Sun, J. Wu, Y. Dai and K. Morita, *STAM*, **17**, 12 (2016).
- [87] Y. Lei, W. Ma, J. Wu, K. Wei, S. Li and K. Morita, *J. Alloy. Compd.*, **734**, 250 (2018).
- [88] Y. Li, Y. Tan, P. Cao, J. Li, P. Jia and Y. Liu, *Mater. Res. Innov.*, **19**, 81 (2015).
- [89] Q. Zou, J. Jie, J. Sun, T. Wang, Z. Cao and T. Li, *Sep. Purif. Technol.*, **142**, 101 (2015).
- [90] B. Ban, J. Li, X. Bai, Q. He, J. Chen and S. Dai, *J. Alloy. Compd.*, **672**, 489 (2016).
- [91] K. Chen, X. Chen, Y. Lei, W. Ma, J. Han and Z. Yang, *Sep. Purif. Technol.*, **203**, 168 (2018).
- [92] J. M. Juneja and T. K. Mukherjee, *Hydrometallurgy*, **16**, 69 (1986).
- [93] M. Fang, C. Lu, H. Lai, L. Huang, J. Chen, W. Ma, Z. Sheng, J. Shen, J. Li and X. Luo, *Mater. Sci. Technol.*, **29**, 861 (2013).
- [94] L. Huang, H. Lai, C. Lu, M. Fang, W. Ma, P. Xing, J. Li and X. Luo, *Hydrometallurgy*, **161**, 14 (2016).
- [95] X. Ma, T. Yoshikawa and K. Morita, *J. Cryst. Growth.*, **377**, 192 (2013).
- [96] X. Ma, T. Yoshikawa and K. Morita, *Metall. Mater. Trans. B*, **44**, 528 (2013).
- [97] X. Ma, T. Yoshikawa and K. Morita, *Sep. Purif. Technol.*, **125**, 264 (2014).
- [98] Y. Ren, H. Wang and K. Morita, *Vacuum*, **158**, 86 (2018).
- [99] H. Morito, T. Karahashi, M. Uchikoshi, M. Isshiki and H. Yamane, *Silicon*, **4**, 121 (2012).



- [100] S. Esfahani and M. Barati, *Metals Mater. Int.*, **17**, 1009 (2011).
- [101] S. Esfahani and M. Barati, *Metals Mater. Int.*, **17**, 823 (2011).
- [102] J. Li, B. Ban, Y. Li, X. Bai, T. Zhang and J. Chen, *Silicon*, **9**, 77 (2017).
- [103] Y. Li, Y. Tan, J. Li, Q. Xu and Y. Liu, *J. Alloy. Compd.*, **583**, 85 (2014).
- [104] D. W. Lyon, C. M. Olson and E. D. Lewis, *J. Electrochem. Soc.*, **96**, 359 (1949).
- [105] K. H. Butler and C. M. Olson, U.S. Patent 2773745 (1956).
- [106] C. M. Olson, U.S. Patent 2804377 (1957).
- [107] C. M. Olson, U.S. Patent 2805133 (1957).
- [108] L. Bertrand and C. M. Olson, U.S. Patent 3012862 (1961).
- [109] E. R. Johnson and J. A. Amick, *J. Appl. Phys.*, **25**, 1204 (1954).
- [110] T. Ishino, A. Matsumoto and S. Yamagishi, *The Journal of Chemical Industry (Kogyo Kagaku Zasshi)*, **68**, 262 (1965). [in Japanese]
- [111] J. M. Blocher, Jr., M. F. Browning and D. A. Seifert, DOE/JPL Report 954339-81/21, Battelle Columbus Lab. (1981).
- [112] D. A. Seifert and M. F. Browning, *ACS Symp. Ser.*, **78**, 104 (1982).
- [113] Y. Natsume, K. Kaneko and T. Ogasawara, Japanese Patent 1997-169127 (1999).
- [114] T. Shimamune and A. Yoshikawa, Japanese Patent 2002-186872 (2003).
- [115] S. Honda, M. Yasueda, S. Hayashida, M. Yamaguchi and T. Tanaka, Japanese Patent 2005-344004 (2005).
- [116] E. Robert and T. Zijlema, PCT International Patent 2006-EP2937 (2006).
- [117] S. Sakaguchi, PCT International Patent 2007-JP57044 (2007). [in Japanese]
- [118] V. M. Weaver, U.S. Patent 1241796 (1917).
- [119] S. Yoshizawa, T. Hatano and S. Sakaguchi, *The Journal of Chemical Industry (Kogyo Kagaku Zasshi)*, **64**, 1347 (1961). [in Japanese]
- [120] J. C. Terry, A. Lippman, R. F. Sebenik and H. G. Harris, Jr., U.S. Patent 3900312 (1975).
- [121] P. Woditsch, M. Abels and B. Brazel, U.S. Patent 4525334 (1985).

- [122] R. S. Aries, U.S. Patent 3041145 (1962).
- [123] B. Kamenar and D. Grdenić, *Z. Anorg. Allg. Chem.*, **321**, 113 (1963).
- [124] M. G. Fey, F. J. Harvey, II and J. McDonald, U.S. Patent 4102765 (1978).
- [125] R. A. Frosch, C. B. Wolf and T. N. Meyer, U.S. Patent 4188368 (1980).
- [126] J. Eringer, U.S. Patent 2172969 (1939).
- [127] A. Sanjurjo, L. Nanis, K. Sancier, R. Bartlett and V. Kapur, *J. Electrochem. Soc.*, **128**, 179 (1981).
- [128] A. Sanjurjo, PCT International Patent 1982-US1795 (1982).
- [129] F. A. Schmidt, D. Rehbein and P. Chiotti, U.S. Patent 4446120 (1984).
- [130] N. Auner, PCT International Patent 2003-DE115 (2003).
- [131] A. C. Voubnasos, *Z. Anorg. Chem.*, **81**, 364 (1913). [in German]
- [132] K. Yasuda and T. H. Okabe, *J. Jpn. Inst. Met. Mater.*, **74**, 1 (2010). [in Japanese]
- [133] K. Saegusa and T. Yamabayashi, PCT International Patent 2006-JP313363 (2007).
- [134] T. Nohira, K. Yasuda and Y. Ito, *Nat. Mater.*, **2**, 397 (2003).
- [135] X. Jin, P. Gao, D. Wang, X. Hu and G. Z. Chen, *Angew. Chem. Int. Ed.*, **43**, 733 (2004).
- [136] K. Yasuda, T. Nohira, K. Amezawa, Y. H. Ogata and Y. Ito, *J. Electrochem. Soc.*, **152**, D69 (2005).
- [137] K. Yasuda, T. Nohira and Y. Ito, *J. Phys. Chem. Solids*, **66**, 443 (2005).
- [138] K. Yasuda, T. Nohira, K. Takahashi, R. Hagiwara and Y. H. Ogata, *J. Electrochem. Soc.*, **152**, D232 (2005).
- [139] Y. Deng, D. Wang, W. Xiao, X. Jin, X. Hu and G. Z. Chen, *J. Phys. Chem. B*, **109**, 14043 (2005).
- [140] W. Xiao, X. Jin, Y. Deng, D. Wang, X. Hu and G. Z. Chen, *ChemPhysChem*, **7**, 1750 (2006).
- [141] K. Yasuda, T. Nohira, R. Hagiwara and Y. H. Ogata, *Electrochim. Acta*, **53**, 106 (2007).
- [142] T. Nohira, N. Kani and R. Hagiwara, *ECS Trans.*, **16**, 239 (2009).

- [143] K. Kobayashi, T. Nohira, R. Hagiwara, K. Ichitsubo and K. Yamada, *ECS Trans.*, **33**, 239 (2010).
- [144] Y. Nishimura, T. Nohira, K. Yasuda, Y. Fukunaka and R. Hagiwara, *TMRS-J*, **35**, 47 (2010).
- [145] E. Juzeliunas, A. Cox and D. J. Fray, *Electrochem. Commun.*, **12**, 1270 (2010).
- [146] E. Juzeliunas, A. Cox and D. J. Fray, *Electrochim. Acta*, **68**, 123 (2012).
- [147] W. Xiao, X. Jin, Y. Deng, D. Wang and G. Z. Chen, *J. Electroanal. Chem.*, **639**, 130 (2010).
- [148] W. Xiao, X. Wang, H. Yin, H. Zhu, X. Mao and D. Wang, *RSC Adv.*, **2**, 7588 (2012).
- [149] T. Toba, K. Yasuda, T. Nohira, X. Yang, R. Hagiwara, K. Ichitsubo, K. Masuda and T. Homma, *Electrochemistry*, **81**, 559 (2013).
- [150] K. Yasuda, T. Nohira, K. Kobayashi, N. Kani, T. Tsuda and R. Hagiwara, *Energy Tech.*, **1**, 245 (2013).
- [151] W. Xiao, X. Jin and G. Z. Chen, *J. Mater. Chem. A*, **1**, 10243 (2013).
- [152] X. Yang, K. Yasuda, T. Nohira, R. Hagiwara and T. Homma, *Metall. Mater. Trans. B*, **45**, 1337 (2014).
- [153] X. Yang, K. Yasuda, T. Nohira, R. Hagiwara and T. Homma, *J. Electrochem. Soc.*, **161**, D3116 (2014).
- [154] E. Juzeliunas, P. Coxon, D. J. Fray, P. Kalinauskas, I. Valsiunas and P. Miečinskas, *CHEMIJA*, **27**, 11 (2016).
- [155] X. Yang, K. Yasuda, T. Nohira, R. Hagiwara and T. Homma, *Metall. Mater. Trans. B*, **47**, 788 (2016).
- [156] X. Yang, K. Yasuda, T. Nohira, R. Hagiwara and T. Homma, *Metall. Mater. Trans. E*, **3**, 145 (2016).
- [157] M. Zhong, K. Yasuda, T. Homma and T. Nohira, *Electrochemistry*, **86**, 77 (2018).
- [158] E. Ergül, İ. Karakaya and M. Erdoğan, *J. Alloy. Compd.*, **509**, 899 (2011).
- [159] B. Akpınar, M. Erdogan, B. Akduman and I. Karakaya, *ECS Trans.*, **77**, 2011 (2017).
- [160] K. Yasuda, T. Nohira, Y. H. Ogata and Y. Ito, *J. Electrochem. Soc.*, **152**, D208 (2005).

- [161] S. Lee, J. Hur and C. Seo, *J. Ind. Eng. Chem.*, **14**, 651 (2008).
- [162] P. C. Pistorius and D. J. Fray, *J. South. Afr. Inst. Min. Metall.*, **106**, 31 (2006).
- [163] G. L. Pearson and J. Bardeen, *Phys. Rev.*, **75**, 865 (1949).
- [164] D. A. Wenz, I. Johnson and R. D. Wolson, *J. Chem. Eng. Data*, **14**, 250 (1969).
- [165] P. Gao, X. Jin, D. Wang, X. Hu and G. Z. Chen, *J. Electroanal. Chem.*, **579**, 321 (2005).
- [166] S. Cho, F. F. Fan and A. J. Bard, *Electrochim. Acta*, **65**, 57 (2012).
- [167] S. Cho, F. F. Fan and A. J. Bard, *Angew. Chem. Int. Ed.*, **51**, 12740 (2012).
- [168] J. Zhao, H. Yin, T. Lim, H. Xie, H. Hsu, F. Forouzan and A. J. Bard, *J. Electrochem. Soc.*, **163**, D506 (2016).
- [169] H. Xie, H. Zhao, J. Liao, H. Yin and A. J. Bard, *Electrochim. Acta*, **269**, 610 (2018).
- [170] M. M. Islam, I. Abdellaoui, C. Moslah, T. Sakurai, M. Ksibi, S. Hamzaoui and K. Akimoto, *Thin Solid Films*, **654**, 1 (2018).
- [171] Y. Sakanaka, A. Murata, T. Goto and K. Hachiya, *J. Alloy. Compd.*, **695**, 2131 (2017).
- [172] X. Yang, L. Ji, X. Zou, T. Lim, J. Zhao, E. T. Yu and A. J. Bard, *Angew. Chem. Int. Ed.*, **56**, 15078 (2017).
- [173] X. Zou, L. Ji, X. Yang, T. Lim, E. T. Yu and A. J. Bard, *J. Am. Chem. Soc.*, **139**, 16060 (2017).
- [174] X. Zou, L. Ji, J. Ge, D. R. Sadoway, E. T. Yu and A. J. Bard, *Nat. Commun.*, **10**, 5772 (2019).
- [175] X. Zou, L. Ji, Z. Pang, Q. Xu and X. Lu, *J. Energy Chem.*, **44**, 147 (2020).
- [176] O. I. Boiko, Y. K. Delimarskii and R. V. Chernov, *Institute of General and Inorganic Chemistry*, **6**, 1 (1982).
- [177] D. Elwell, *Sol. Energy Mater.*, **5**, 205 (1981).
- [178] Y. Hu, X. Wang, J. Xiao, J. Hou, S. Jiao and H. Zhu, *J. Electrochem. Soc.*, **160**, D81 (2013).
- [179] Y. Sakanaka and T. Goto, *Electrochim. Acta*, **164**, 139 (2015).
- [180] Y. Suzuki, M. Yokota, Y. Sakanaka, Y. Fukunaka and T. Goto, *ECS Trans.*, **80**, 823 (2017).
- [181] Y. Suzuki, Y. Inoue, M. Yokota and T. Goto, *J. Electrochem. Soc.*, **166**, D564 (2019).

- [182] Z. Cai, Y. Li, X. He and J. Liang, *Metall. Mater. Trans. B*, **41B**, 1033 (2010).
- [183] A. A. Andriiko, E. V. Panov, O. I. Boiko, B. V. Yakovlev and O. Y. Borovik, *Russ. J. Electrochem.*, **33**, 1343 (1997).
- [184] J. Li, H. Ren, X. Yin, J. Lu and J. Li, *Russ. J. Electrochem.*, **55**, 392 (2019).
- [185] T. Nohira, A. Ido, T. Shima, X. Yang, K. Yasuda, R. Hagiwara and T. Homma, *ECS Trans.*, **75**, 17 (2016).
- [186] K. Yasuda, T. Shima, R. Hagiwara, T. Homma and T. Nohira, *J. Electrochem. Soc.*, **164**, H5049 (2017).
- [187] R. W. Olesinski and G. J. Abbaschian, *Bull. Alloy Phase Diagrams*, **6**, 545 (1985).
- [188] G. J. Janz, R. P. T. Tomkins, C. B. Allen, J. R. Downey, G. L. Garner, U. Krebs and S. K. Singer, *J. Phys. Chem. Ref. Data*, **4**, 871 (1975).

## Chapter 2

# Mechanism of Electrochemical Reduction of SiO<sub>2</sub> at a Liquid Zn Electrode in Molten CaCl<sub>2</sub>

### 2.1 Introduction

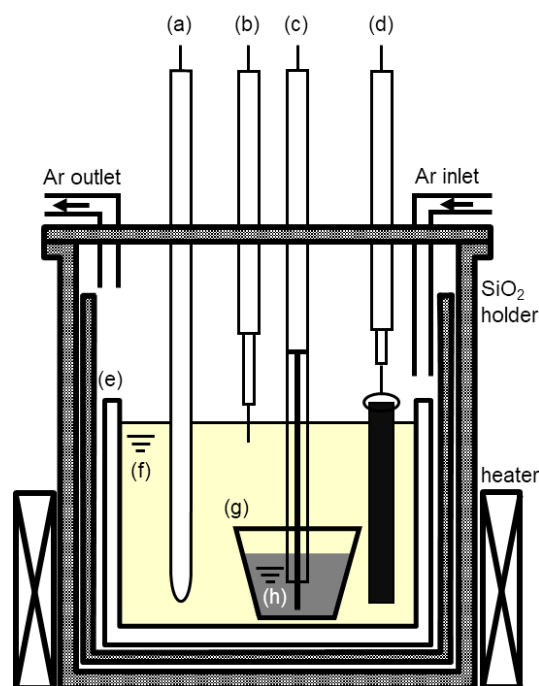
In this chapter, the mechanism of electrochemical reduction of SiO<sub>2</sub> at a liquid Zn electrode in the electrolysis step (Figure 1-9) was investigated. Since direct electrolysis reduction of SiO<sub>2</sub> and indirect reduction of SiO<sub>2</sub> by liquid Ca–Zn alloy were suggested in previous study [1, 2], a series of electrolysis and immersion experiments were conducted to investigate the contributions of direct and indirect reductions of SiO<sub>2</sub>. Then, the mixed reduction mechanism was discussed in terms of reduction rate. Finally, Si particles were produced at the liquid Zn electrode by potentiostatic electrolysis; they were analyzed by ICP-AES for the impurity analysis.

### 2.2 Experimental

All the experiments were performed in a dry Ar atmosphere at 1123 K. An Ag<sup>+</sup>/Ag electrode was used as a reference electrode in the experiments. The experimental conditions for (a) cyclic voltammetry, (b) electrochemical reduction of SiO<sub>2</sub> plates, and (c) electrochemical reduction of SiO<sub>2</sub> particles are described as follows.

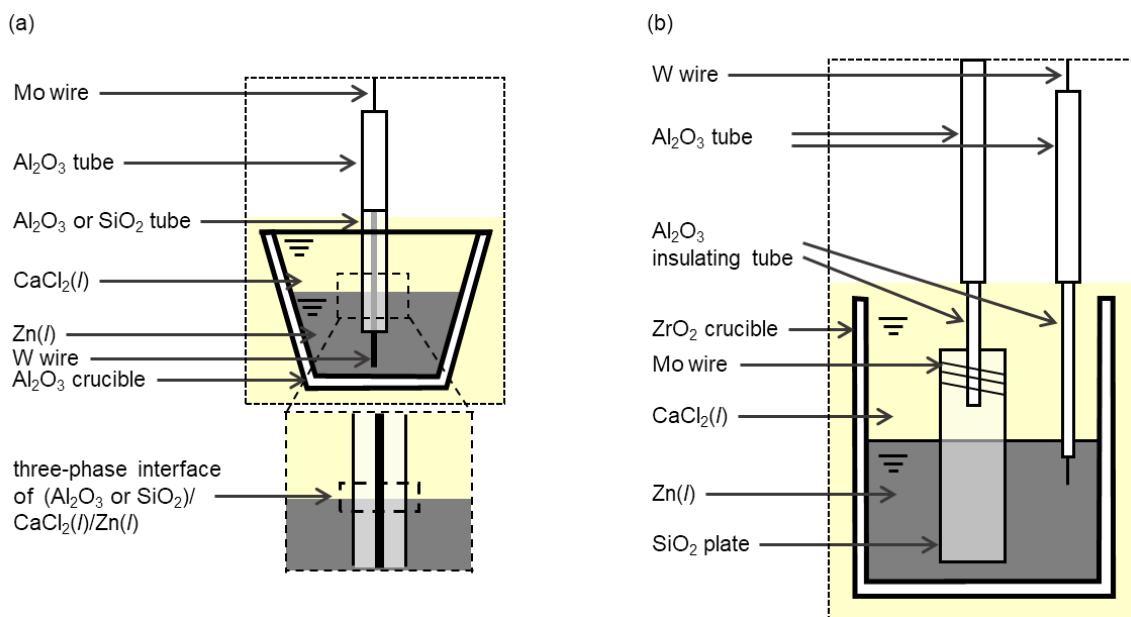
#### 2.2.1 Cyclic Voltammetry

Figure 2-1 shows a schematic illustration of the electrolysis cell for the investigation of the reduction behavior of SiO<sub>2</sub> at a liquid Zn electrode. Figure 2-2(a) schematically illustrates the



**Figure 2-1** Schematic illustration of the electrolysis cell for the investigation of SiO<sub>2</sub> reduction behavior at a liquid Zn electrode. (a) Ag<sup>+</sup>/Ag reference electrode, (b) Ca<sup>2+</sup>/Ca dynamic reference electrode on a Mo wire, (c) liquid Zn electrode with Al<sub>2</sub>O<sub>3</sub>/SiO<sub>2</sub> tube, (d) graphite counter electrode, (e) Al<sub>2</sub>O<sub>3</sub> crucible, (f) molten CaCl<sub>2</sub>, (g) small Al<sub>2</sub>O<sub>3</sub> crucible, and (h) liquid Zn.

structure of the liquid Zn working electrode for cyclic voltammetry. Approximately 70 g of Zn (FUJIFILM Wako Pure Chemical Corp., reagent grade, granule) was charged into a small Al<sub>2</sub>O<sub>3</sub> crucible (AS ONE, o.d. 45 mm × height 36 mm, >99%). The small Al<sub>2</sub>O<sub>3</sub> crucible was placed at the bottom of another Al<sub>2</sub>O<sub>3</sub> crucible (AS ONE, o.d. 90 mm × i.d. 80 mm × height 140 mm, >99%), and approximately 500 g of CaCl<sub>2</sub> (Kojundo Chemical Laboratory Co., Ltd., >99%) was charged. A W wire (Nilaco Corp., diameter 2.0 mm, 99.95%) threaded into an Al<sub>2</sub>O<sub>3</sub> tube (Nikkato Corp., SSA-S grade, o.d. 6.0 mm × i.d. 4.0 mm) or a SiO<sub>2</sub> tube (Soei Riken Corp., o.d. 6.0 mm × i.d. 2.0 mm) was used as the current lead and immersed in the liquid Zn in the small Al<sub>2</sub>O<sub>3</sub> crucible. The direct electrochemical reduction of SiO<sub>2</sub> occurs at the three-phase interface of (Al<sub>2</sub>O<sub>3</sub> or SiO<sub>2</sub>)/CaCl<sub>2</sub>(l)/Zn(l), as shown in Figure 2-2(a). For comparison, a square-shaped plate of single-crystal Si (30 mm × 5 mm × thickness 0.5 mm, *p*-type, (100), 1.5–3.0 × 10<sup>-3</sup> Ω cm at 298 K) was also used as the working electrode. The counter electrode was a square graphite bar (Toyo Tanso



**Figure 2-2** Schematic illustrations of the liquid Zn electrodes for (a) cyclic voltammetry, and (b) electrochemical reduction of SiO<sub>2</sub> plate.

Co., Ltd., 5 mm × 5 mm).

## 2.2.2 Electrochemical Reduction of SiO<sub>2</sub> Plates

Figure 2-2(b) shows a schematic illustration of the liquid Zn electrode for the investigation of the effect of indirect reduction of SiO<sub>2</sub> by liquid Ca–Zn alloy. Approximately 125 g of Zn was charged into a small ZrO<sub>2</sub> crucible (AS ONE, ZrO<sub>2</sub> 91.5%, Y<sub>2</sub>O<sub>3</sub> 8%, o.d. 60 mm × i.d. 52 mm × height 35 mm). The ZrO<sub>2</sub> crucible was placed in a graphite crucible (Toyo Tanso Co., Ltd., IG-110 grade, o.d. 100 mm × i.d. 90 mm × height 120 mm) to which a graphite rod (Toyo Tanso Co., Ltd., IG-110 grade, diameter 9 mm) was fixed using a stainless-steel screw. Approximately 500 g of CaCl<sub>2</sub> was charged into the graphite crucible. A SiO<sub>2</sub> plate (Soei Riken Corp., 25 mm × 10 mm × thickness 1 mm), fixed to an insulating tube of Al<sub>2</sub>O<sub>3</sub> (Nikkato Corp., SSA-S grade, o.d. 2.5 mm × i.d. 1.5 mm) by winding a Mo wire (Nilaco Corp., diameter 0.20 mm, 99.95%), was immersed into the liquid Zn in the small ZrO<sub>2</sub> crucible. The counter electrode was the graphite crucible, and the graphite rod was used as the current lead. The test piece prepared by electrolysis or immersion of



SiO<sub>2</sub> plate was washed with distilled water to remove the salt, and then immersed in HCl solution (3 wt.%, prepared from FUJIFILM Wako Pure Chemical Corp., reagent grade, 36 wt.%) overnight to dissolve the Zn metal on the surface of the plate. An optical microscope (Thanko Inc., DILITE30) was used for surface observation, and the weight change of the SiO<sub>2</sub> plates were measured.

### 2.2.3 Electrochemical Reduction of SiO<sub>2</sub> Particles

Figure 2-3 schematically illustrates a cell for the electrochemical reduction of SiO<sub>2</sub> particles. A total of 335 g of Zn and 349 g of CaCl<sub>2</sub> were charged into an Al<sub>2</sub>O<sub>3</sub> crucible. After the temperature was raised to 1123 K, a total of 16.2 g of SiO<sub>2</sub> particles (Kojundo Chemical Laboratory Co., Ltd., 0.25–1.00 mm, 99.995%) was charged into molten salt uniformly using a quartz funnel. The SiO<sub>2</sub> particles floated on the surface of liquid Zn in molten CaCl<sub>2</sub> because the densities of liquid CaCl<sub>2</sub>, solid SiO<sub>2</sub>, and liquid Zn are 2.05 g cm<sup>-3</sup> [6], 2.2 g cm<sup>-3</sup> [7], and 5.9 g cm<sup>-3</sup> [8], respectively, at 1123 K. A W wire (Nilaco Corp., diameter 1.0 mm, 99.95%) threaded into an

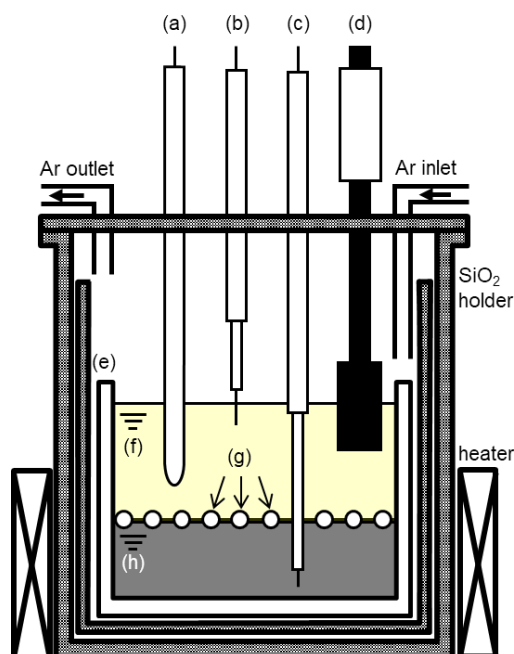


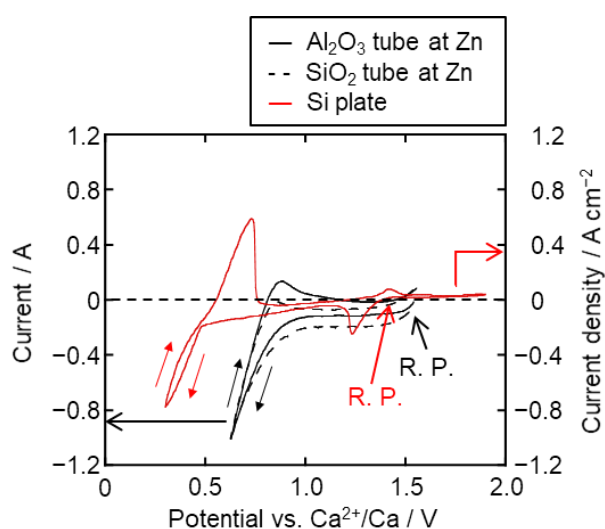
Figure 2-3 Schematic illustration of the electrolysis cell for the electrochemical reduction of SiO<sub>2</sub> particles. (a) Ag<sup>+</sup>/Ag reference electrode, (b) Ca<sup>2+</sup>/Ca dynamic reference electrode on a Mo wire, (c) W lead wire, (d) graphite counter electrode, (e) Al<sub>2</sub>O<sub>3</sub> crucible, (f) molten CaCl<sub>2</sub>, (g) SiO<sub>2</sub> particle, and (h) liquid Zn.

alumina tube was used as the current lead for liquid Zn. The counter electrode was a graphite rod (Toyo Tanso Co., Ltd., IG-110 grade, diameter 20 mm) fixed to a thinner graphite rod (Toyo Tanso Co., Ltd., IG-110 grade, diameter 9 mm). The sample obtained after electrolysis was cooled from 1123 K to 773 K over 35 h, then maintained at 773 K for 10 h, and further cooled to 298 K over 5 h. The ingot of Zn metal was recovered after the removal of  $\text{CaCl}_2$  by flowing water. The Zn metal ingot was dissolved in HCl solution (20 wt.%). The particles recovered after the dissolution of HCl were further washed; they were alternately immersed in HCl solution (10 wt.%) twice and in HF solution (5 wt.%, prepared from Tama Chemicals Co., Ltd., AA-100 grade, 38 wt.%) once overnight. The analysis was conducted using X-ray diffraction (XRD, Rigaku, Ultima 4,  $\text{Cu-K}\alpha$ ,  $\lambda = 1.5418 \text{ \AA}$ , 40 kV, 40 mA) and inductively coupled plasma atomic emission spectroscopy (ICP-AES; AMETEK, Inc., SPECTROBLUE).

## 2.3 Results and Discussion

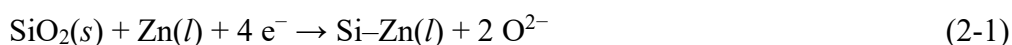
### 2.3.1 Cyclic Voltammetry

Figure 2-4 shows the cyclic voltammograms obtained at liquid Zn electrodes with an  $\text{Al}_2\text{O}_3$  tube or a  $\text{SiO}_2$  tube (left axis) and at a Si plate electrode (right axis) in molten  $\text{CaCl}_2$  at 1123 K. Scan rate:  $100 \text{ mV s}^{-1}$ .



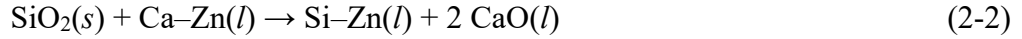
**Figure 2-4** Cyclic voltammograms at liquid Zn electrodes with an  $\text{Al}_2\text{O}_3$  tube or a  $\text{SiO}_2$  tube (left axis) and at a Si plate electrode (right axis) in molten  $\text{CaCl}_2$  at 1123 K. Scan rate:  $100 \text{ mV s}^{-1}$ .

plate (red color) electrodes. As for the Si electrode, the cathodic and anodic current peaks at around 1.3–1.4 V (vs.  $\text{Ca}^{2+}/\text{Ca}$ ) corresponded to the reduction of surface  $\text{SiO}_2$  film to metallic Si and the oxidation of Si into  $\text{SiO}_2$  layer, respectively [9, 10]. The smaller anodic current compared with the cathodic current was due to the passivation effect of the formed  $\text{SiO}_2$  layer. The redox at 0.5 V was attributed to  $\text{CaSi}_2/\text{Si}$  [9, 10]. The solid and broken black lines show the voltammograms at Zn electrodes using  $\text{Al}_2\text{O}_3$  and  $\text{SiO}_2$  tubes, respectively. A sharp increase in cathodic current at 0.85 V was seen at both the Zn electrodes. Since the electrochemical reduction of  $\text{Al}_2\text{O}_3$  did not occur in the potential range measured [11], the cathodic current was attributed to the formation of liquid Ca–Zn alloy, which was already confirmed by potentiostatic electrolysis at potentials more negative than 0.85 V [2]. In the case of the Zn electrode with  $\text{SiO}_2$ , the rest potential was 1.55 V, which was more positive than that of the Si plate electrode (1.47 V), and the cathodic current was observed from the rest potential in the negative scan even at potentials more positive than 1.3 V. These results suggested the formation of liquid Si–Zn alloy with Si activity lower than unity with respect to pure solid Si. The cathodic current at the Zn electrode with  $\text{SiO}_2$  was 80 mA larger than that with  $\text{Al}_2\text{O}_3$ , which also suggested electrochemical reduction of  $\text{SiO}_2$ .



### 2.3.2 Electrochemical Reduction of $\text{SiO}_2$ Plates

On the basis of the voltammetry results, potentiostatic electrolysis was first conducted at 0.60 V and then at 0.90 V. Specifically, the experiments were conducted in the following order: [A1] electrolysis of a  $\text{SiO}_2$  plate at 0.90 V for 30 min, [B1] immersion of a new  $\text{SiO}_2$  plate for 30 min, [A2] electrolysis of a new  $\text{SiO}_2$  plate at 0.60 V for 30 min, and [B2] immersion of a new  $\text{SiO}_2$  plate for 30 min. Here, same Zn electrode was used in each step. As the result, four samples, A1, B1, A2 and B2, were prepared. Since electrolysis was not conducted for the samples B1 and B2, the reduction of  $\text{SiO}_2$  could be advanced only due to the indirect reduction by liquid Ca–Zn alloy.



On the other hand, the reduction of the samples A1 and A2 could proceed by a mixed reduction mechanism comprising direct electrochemical reaction (reaction (2-1)) and indirect reduction by liquid Ca-Zn alloy (reaction (2-2)).

Figure 2-5 shows the optical images of the samples A1, B1, A2, and B2. For the sample A1, which was electrolyzed at 0.90 V, a change in color from transparent, i.e., no color to dark brown was observed in a portion lower than the Zn/CaCl<sub>2</sub> interface (8 mm from the bottom of the SiO<sub>2</sub> plate). Also, a decrease in plate thickness was clearly observed. In the case of the sample A2, which was electrolyzed at 0.60 V, the entire area below the Zn/CaCl<sub>2</sub> interface changed to dark brown in color. In this case, the plate became thinner, showing that a larger amount of the Si-Zn liquid alloy was produced. The thickness was more decreased near the three-phase interface of

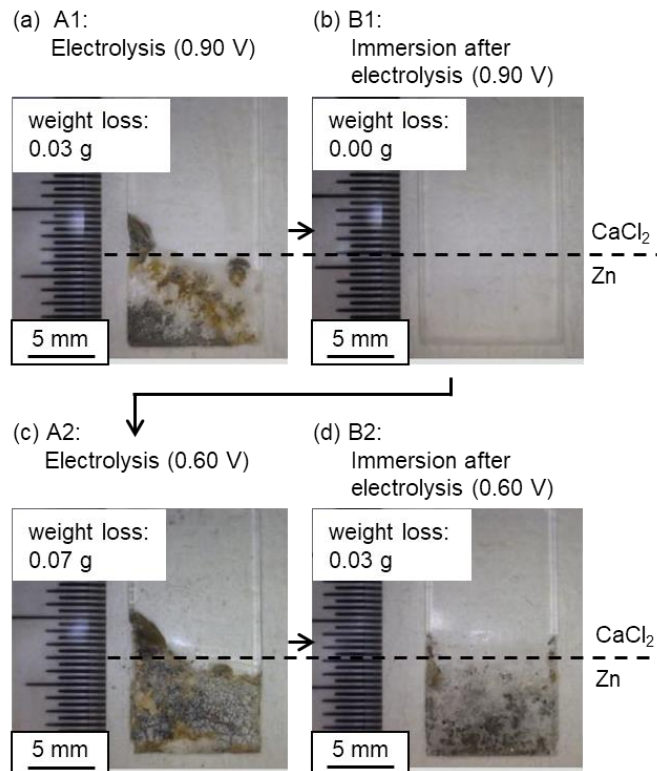


**Figure 2-5** Optical images of the SiO<sub>2</sub> plates after electrolysis at the liquid Zn electrode or immersion into liquid Zn for 30 min in molten CaCl<sub>2</sub> at 1123 K. (a) potentiostatic electrolysis at 0.9 V, (b) immersion after electrolysis (a), (c) potentiostatic electrolysis at 0.6 V, and (d) immersion after electrolysis (c).

Zn/SiO<sub>2</sub>/CaCl<sub>2</sub> than that at the two-phase interface of Zn/SiO<sub>2</sub> in liquid Zn. This is explained by higher solubility and faster diffusion of O<sup>2-</sup> ions in molten CaCl<sub>2</sub> compared with those in liquid Zn. As for the immersion sample B1, no dark brown part was observed, indicating no progress of indirect reduction. Concerning the sample B2, which was immersed after electrolysis at 0.60 V, the color of the immersed portion changed to dark brown. This is explained by the indirect reduction of SiO<sub>2</sub> by Ca–Zn alloy. The weight losses of the samples were 0.03 g (A1), 0.07 g (A2), 0.00 g (B1), and 0.03 g (B2).

By comparing the samples A1 and B1, it can be inferred that only the direct reduction of SiO<sub>2</sub> (reaction (2-1)) occurs at 0.90 V. On the other hand, the results for sample A2 and B2 conclude that comparable amount of reduction proceeded in the indirect reaction, i.e., reduction by liquid Ca–Zn alloy (reaction (2-2)), in the electrolysis at 0.60 V to the direct reduction.

### 2.3.3 Electrochemical Reduction of SiO<sub>2</sub> Particles

To prepare a sample for impurity analysis, potentiostatic electrolysis of SiO<sub>2</sub> particles was conducted at 0.60 V for 50 h. Figure 2-6(a) shows a photograph of the granules recovered after the dissolution of Zn by HCl solution and the treatment of acid washing. The XRD analysis confirmed that the granules are crystalline Si (Figure 2-6(b)). The current efficiency ( $\eta$ ) was calculated by the following equations:

$$\eta = \frac{W_{\text{act.}}}{W_{\text{theo.}}} \times 100 \quad (2-3)$$

$$W_{\text{theo.}} = \frac{Q}{4F} \times M_{\text{Si}} \quad (2-4)$$

where  $W_{\text{act.}}$  is the actual weight of the Si recovered,  $W_{\text{theo.}}$  is the theoretical weight of Si produced according to Faraday's law in reaction (2-1),  $Q$  is the quantity of electric charge during electrolysis,  $F$  is Faraday's constant (96485 C mol<sup>-1</sup>), and  $M_{\text{Si}}$  is the molar weight of Si (28.1 g mol<sup>-1</sup>). From the values of  $W_{\text{act.}} = 3.02$  g and  $Q = 1.48 \times 10^5$  C,  $\eta$  was calculated to be 28%. One of the reasons

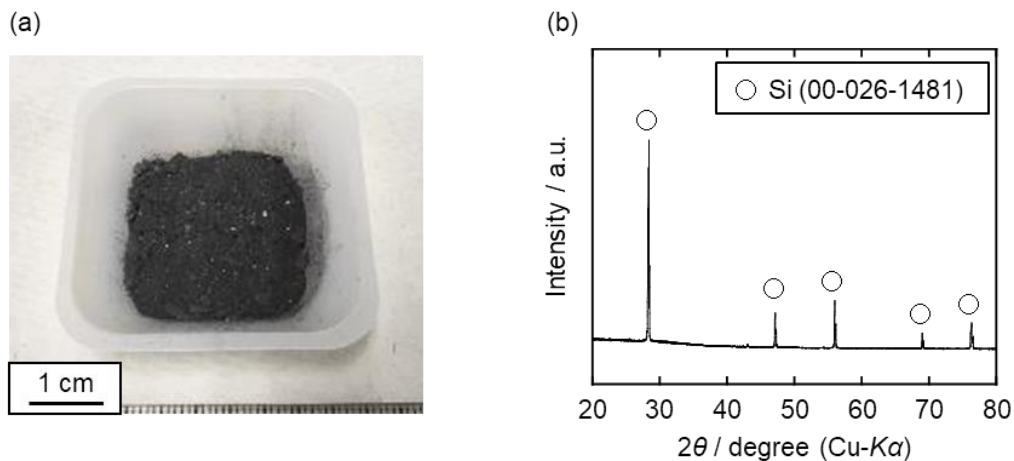


**Figure 2-6 (a) Optical image and (b) XRD pattern of the Si granules obtained after acid leaching of Zn ingot. The electrochemical reduction of SiO<sub>2</sub> particles was conducted at a liquid Zn electrode at 0.6 V for 50 h in molten CaCl<sub>2</sub> at 1123 K.**

for the low current efficiency is the loss during acid washing. Another reason is the formation of liquid Ca–Zn alloy as a side reaction; a part of which contributes to the indirect reduction of SiO<sub>2</sub> and the rest remains as Ca–Zn alloy.

Table 2-1 lists the impurity contents of the Si granules after the treatment of acid washing. It also lists the acceptable levels for SOG-Si [3], segregation coefficients [4], and target levels for primary Si for directional solidification. For comparison, the impurity contents of the Si sample obtained by electrochemical reduction at (0.60 V, 5 h) in molten CaCl<sub>2</sub> [5] are also shown. The impurity levels of the metallic elements (Al, Ca, Fe, and Ti) in the Si granules met the target levels for the primary Si that is to be further purified by unidirectional solidification according to the process proposed in Figure 1-9. The content of P was also lower than the target level for the primary Si, and this is noteworthy because the removal of P from elemental Si is known to be difficult. The content of B was higher than the target level, and this needs to be improved in the future. Overall, a comparison between the impurity concentrations in the Si products obtained by electrolysis at a liquid Zn electrode and at a solid electrode indicates that higher purity is achieved by the use of the liquid Zn electrode. The main reason for the higher purity is the solidification refining during the precipitation of Si from the Si–Zn alloy wherein most impurities remain in the liquid Zn phase. It

**Table 2-1 Impurity contents of Si granules obtained after acid leaching, and target levels for primary Si of SOG-Si. The electrochemical reduction of SiO<sub>2</sub> particles was conducted at 0.6 V for 50 h at a liquid Zn electrode in molten CaCl<sub>2</sub> at 1123 K.**

| Impurity element, A | Acceptable level for SOG-Si [3], $x_A(\text{SOG-Si}) / \text{ppmw}$ | Segregation coefficient [4], $k_A^\circ$ | Target level for primary Si <sup>a</sup> , $x_A(\text{primary}) / \text{ppmw}$ | Impurity content of Si granules by electrochemical reduction at a liquid Zn electrode, $x_A / \text{ppmw}$ <sup>b</sup> | Impurity content of Si by electrochemical reduction at a solid electrode [5], $x_A / \text{ppmw}$ <sup>c</sup> |
|---------------------|---|--|--|---|--|
| B                   | 0.1–0.3   | 0.8                                      | 0.13–0.38  | 1.5   | 2.6  |
| P                   | 0.03–0.04   | 0.35                                     | 0.086–0.4  | <0.2  | 6.4  |
| Al                  | <0.1  | $2.0 \times 10^{-3}$                     | <50  | 8   | 600  |
| Ca                  | <0.2  | $1.6 \times 10^{-3}$                     | <125   | 85  | 5800   |
| Fe                  | <0.1  | $8.0 \times 10^{-6}$                     | <12500   | 110   | 30   |
| Ti                  | < $10^{-3}$   | $9.0 \times 10^{-6}$                     | <100   | 25  | 19   |
| Zn                  | – <sup>d</sup>  | – <sup>d</sup>                           | – <sup>d</sup>   | 6055  | 2.1  |

<sup>a</sup>  $x_{A(\text{primary})} = x_{A(\text{SOG-Si})} / k_A^\circ$

<sup>b</sup> Analyzed by ICP-AES.

<sup>c</sup> Analyzed by glow discharge-mass spectrometry (GD-MS).

should be mentioned that the Ca concentration was lower than the target level for the primary Si in spite of the use of indirect reduction by liquid Ca–Zn at 0.60 V. Ca is also expected to be removed to the Zn phase during precipitation. Although a relatively large amount of Zn (6055 ppmw) remained in the Si granules, this can be easily removed in the gas phase during the refining process owing to its high vapor pressure.

## 2.4 Conclusion

The reaction mechanism of electrochemical reduction of SiO<sub>2</sub> at a liquid Zn electrode was investigated in molten CaCl<sub>2</sub> at 1123 K. Cyclic voltammetry suggested that electrochemical

reduction of SiO<sub>2</sub> started from the rest potential (1.55 V), and liquid Ca–Zn alloy was formed at potentials more negative than 0.85 V. The progress of the indirect reduction of SiO<sub>2</sub> by liquid Ca–Zn alloy was confirmed by electrolysis and immersion experiments. The reduction at 0.60 V proceeded by a mixed reduction mechanism of direct electrochemical reaction and indirect reduction by Ca–Zn alloy. Impurity analysis confirmed that the concentrations of the metal elements and P were lower than the target levels for primary Si. The indirect reduction of SiO<sub>2</sub> by liquid Ca–Zn did not increase the Ca content of the Si product because it remained in the Zn phase during precipitation.

## 2.5 Reference List

- [1] T. Nohira, A. Ido, T. Shima, X. Yang, K. Yasuda, R. Hagiwara and T. Homma, *ECS Trans.*, **75**, 17 (2016).
- [2] K. Yasuda, T. Shima, R. Hagiwara, T. Homma and T. Nohira, *J. Electrochem. Soc.*, **164**, H5049 (2017).
- [3] N. Yuge, M. Abe, K. Hanazawa, H. Baba, N. Nakamura, Y. Kato, Y. Sakaguchi, S. Hiwasa and F. Aratani, *Prog. Photovolt. Res. Appl.*, **9**, 203 (2001).
- [4] F. A. Trumbore, *The Bell System Technical Journal*, **39**, 205 (1960).
- [5] X. Yang, K. Yasuda, T. Nohira, R. Hagiwara and T. Homma, *Metall. Mater. Trans. B*, **47**, 788 (2016).
- [6] G. J. Janz, R. P. T. Tomkins, C. B. Allen, J. R. Downey, G. L. Garner, U. Krebs and S. K. Singer, *J. Phys. Chem. Ref. Data*, **4**, 871 (1975).
- [7] A. Hayashi, *Product and Application of High-Purity Silica*, CMC Press (1999). [in Japanese]
- [8] R. Kubo, S. Nagakura, H. Iguchi and H. Ezawa, *Rikagaku Jiten*, 4th ed., Iwanami Shoten (1987). [in Japanese]
- [9] T. Toba, K. Yasuda, T. Nohira, X. Yang, R. Hagiwara, K. Ichitsubo, K. Masuda and T. Homma, *Electrochemistry*, **81**, 559 (2013).



[10] K. Yasuda, T. Nohira and Y. Ito, *J. Phys. Chem. Solids*, **66**, 443 (2005).

[11] H. Kadowaki, Y. Katasho, K. Yasuda and T. Nohira, *J. Electrochem. Soc.*, **165**, D83 (2018).

## Chapter 3

# Raman Analysis and Electrochemical Reduction of Silicate Ions in Molten CaCl<sub>2</sub>

### 3.1 Introduction

In previous chapter, the reduction of solid SiO<sub>2</sub> at 0.60 V was confirmed as a mixed reduction mechanism of direct electrochemical reduction and indirect reduction by liquid Ca–Zn alloy. However, the current efficiency was only 28%. To improve the productivity, in this chapter, the electrochemical reduction of dissolved SiO<sub>2</sub>, i.e., silicate ions, was investigated in molten CaCl<sub>2</sub> at 1123 K. Firstly, the ionic species of silicates in molten CaCl<sub>2</sub> with various ratios of O<sup>2-</sup>/SiO<sub>2</sub> ( $r_{\text{O}^{2-}/\text{SiO}_2}$ ) was investigated by Raman spectroscopy at 1123 K. CaO was used as the source of O<sup>2-</sup> ion. Since the concentrations of CaO used in this study were lower than its solubility (34.7 mol%) [1], it is considered to be completely dissociated into Ca<sup>2+</sup> and O<sup>2-</sup>. Then, the electrochemical reduction of silicate ions was investigated at a solid graphite electrode to find the optimal silicate ion for the production of liquid Si–Zn alloy. The surfaces of Si deposited at the graphite electrodes were observed by SEM and analyzed by XRD. Based on the results obtained at a graphite electrode, the electrochemical investigation was conducted at a liquid Zn electrode. The precipitated Si particles obtained from the Zn electrode were recovered by the dissolution of Zn in HCl solution. The current efficiency was calculated from the weight of recovered Si. Furthermore, Ca concentration in the Zn electrode was analyzed by ICP-AES.

## 3.2 Experimental

All the experiments were conducted in a dry Ar atmosphere at 1123 K. The experimental procedures for Raman spectroscopy and electrochemical reduction of silicate ions are described as follows.

### 3.2.1 Raman Spectroscopy of Silicate Ions

Salt preparation was conducted in a dry Ar-filled glove box (less than 1 ppm O<sub>2</sub> and 1 ppm H<sub>2</sub>O). To confirm the dissolution rate of SiO<sub>2</sub> and CaSiO<sub>3</sub>, half of the samples were (a) analyzed by Raman spectroscopy immediately after heated to 1123 K, and other half were (b) melted in a graphite crucible for 1 day beforehand and then analyzed by Raman spectroscopy.

As the salt preparation for (a), CaCl<sub>2</sub> powder (FUJIFILM Wako Pure Chemical Corp., reagent grade) with 0 and 1.0 mol% of CaO (FUJIFILM Wako Pure Chemical Corp., 98.0%), 0 and 1.0 mol% of SiO<sub>2</sub> (Sigma-Aldrich, 10–20 nm, 99.5%), and 0 and 1.0 mol% of CaSiO<sub>3</sub> (Sigma-Aldrich, 200 mesh, 99%) powders were charged into a mortar and mixed for 2 min. Before mixing, CaO was dried at 1273 K and CaSiO<sub>3</sub> at 773 K for 10 h, respectively. The mixture was then loaded into a Pt pan (Rigaku Corp., o.d. 5 mm × height 2.5 mm) in an airtight high-temperature stage (Japan High Tech Co., Ltd., 10042) and heated to 1123 K.

For samples used in (b), salts with the same compositions as in (a) were mixed and loaded into graphite crucibles (Toyo Tanso Co., Ltd., IG-110 grade, o.d. 55 mm × i.d. 49 mm × height 150 mm). The mixtures were dried under vacuum at 453 K for 2 days and then at 773 K for 1 day. After the temperature was increased to 1123 K and maintained for 1 day to sufficiently dissolve the silicate-ion sources, the salts were quickly sampled using a borosilicate glass tube (Pyrex<sup>®</sup>, o.d. 6 mm × i.d. 4 mm). The sampled salts were then loaded into a Pt pan in an airtight high-temperature stage and heated to 1123 K, which was same as in (a).

The salts with various ratios of O<sup>2-</sup>/SiO<sub>2</sub> were prepared in the same method as in (b). CaCl<sub>2</sub> powder with pre-determined amounts of CaO and CaSiO<sub>3</sub> powders were prepared. The

added amounts were 0, 2.0 and 4.0 mol% for CaO, and 4.0 mol% for CaSiO<sub>3</sub>.

Figure 3-1 shows a schematic drawing of the experimental apparatus used for Raman spectroscopy. After the mixture was heated to 1123 K, the ionic species of silicates was investigated using a micro-Raman spectrometer (Tokyo Instruments, Nanofinder 30) using a laser source with an excitation wavelength of 532 nm. Origin 2021 software was used to deconvolve the spectra using the Voigtian function.

### 3.2.2 Electrochemical Reduction of Silicate Ions at a Solid Graphite Electrode

CaCl<sub>2</sub> powder was loaded into a graphite crucible (Toyo Tanso Co., Ltd., IG-110 grade, o.d. 100 mm × i.d. 95 mm × height 120 mm). The crucible was placed at the bottom of a graphite vessel in an airtight Kanthal container. The powder was dried under vacuum at 453 K for 2 days and at 773 K for 1 day. After the temperature was raised to 1123 K, pre-determined amounts of CaO (0, 2.0 or 4.0 mol%) and CaSiO<sub>3</sub> (4.0 mol%) powders were added to the melt. The temperature was maintained at 1123 K for 1 day to sufficiently dissolve the silicate-ion sources. Ar bubbling was also conducted at 50 ml min<sup>-1</sup> to promote the dissolution.

Figure 3-2 shows a schematic drawing of the experimental apparatus for the electrochemical reduction of silicate ions. All electrochemical measurements were conducted by a three-electrode method using an electrochemical measurement system (Hokuto Denko Corp., HZ-

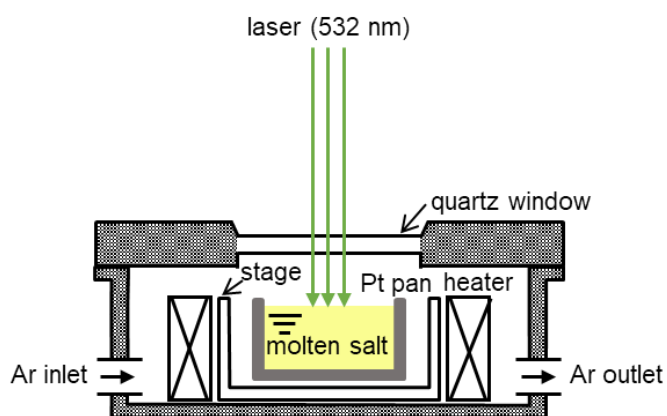
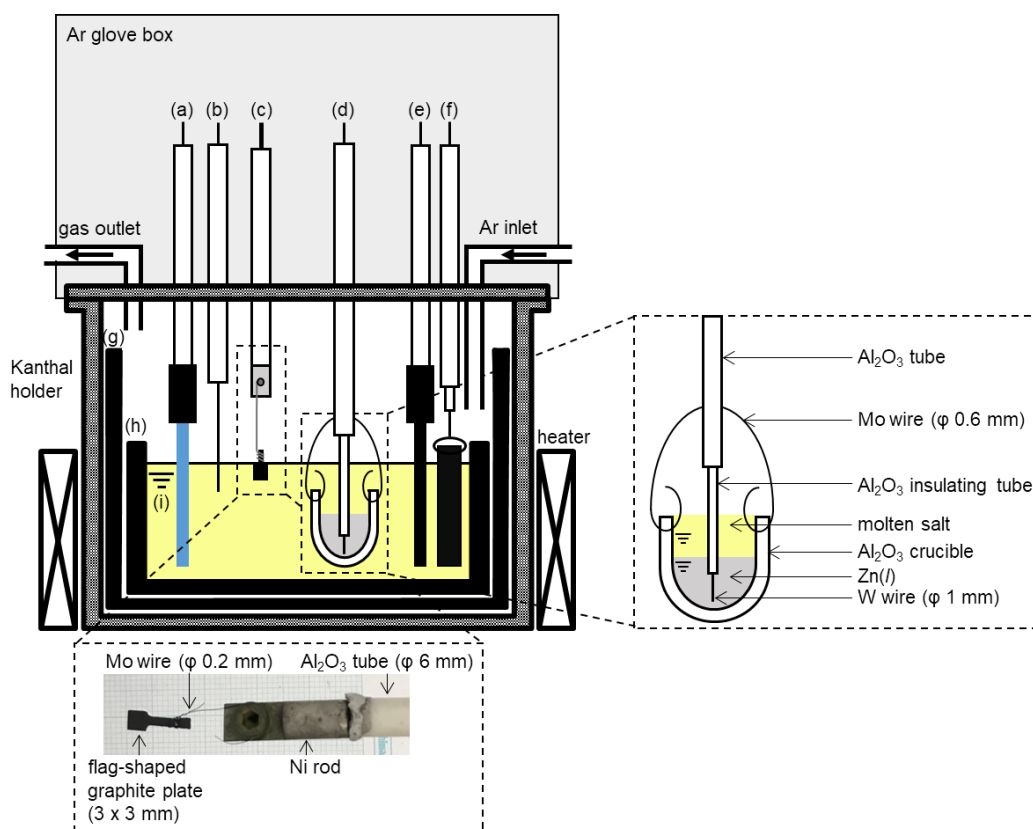


Figure 3-1 Schematic drawing of experimental apparatus for Raman spectroscopy of molten salt.



**Figure 3-2** Schematic drawing of the electrolysis cell. (a) Si quasi-reference electrode, (b)  $\text{Ca}^{2+}/\text{Ca}$  dynamic reference electrode on a Mo wire, (c) flag-shaped graphite working electrode, (d) liquid Zn working electrode, (e) glass-like carbon counter electrode, (f) graphite counter electrode, (g) graphite holder, (h) graphite crucible, and (i) molten  $\text{CaCl}_2$  containing  $\text{CaO}$  and  $\text{CaSiO}_3$ .

7000) in the glove box. As the working electrodes, a flag-shaped graphite plate (Toyo Tanso Co., Ltd., 3 mm × 3 mm × thickness 0.5 mm) was used for cyclic voltammetry and a graphite plate (Toyo Tanso Co., Ltd., 10 mm × 10 mm × thickness 0.5 mm) was used for electrolysis. The counter electrodes were a glass-like carbon (Tokai Carbon Co., Ltd., diameter: 3.0 mm) for cyclic voltammetry and a graphite square bar (Toyo Tanso Co., Ltd., 5 mm × 5 mm) for electrolysis. A Pt wire (Nilaco Corp., diameter 1.0 mm, 99.98%) was used as the quasi-reference electrode for blank melt. For melts containing silicate ions, a Si rod (Furuuchi Chemical Corp., diameter 7.3 mm, 10 N purity) was used as the reference electrode. The potentials of the quasi-reference and reference electrodes were calibrated with respect to a dynamic  $\text{Ca}^{2+}/\text{Ca}$  potential, determined by cyclic voltammetry on a Mo wire (Nilaco Corp., diameter 1.0 mm, 99.95%) electrode.

After the electrolysis, the salt adhered to the sample surfaces were removed by washing in an 1 M HCl solution prepared by diluting of 36 wt.% solution at 333 K for 15 min. The surfaces of the samples were observed using optical microscopy and SEM. The deposits were also characterized by XRD.

### 3.2.3 Electrochemical Reduction of Silicate Ions at a Liquid Zn Electrode

The salt preparation was almost the same as described in 3.2.2. Schematic illustration of the liquid Zn electrode is shown in [Figure 3-2](#). A small Al<sub>2</sub>O<sub>3</sub> crucible (Nikkato Corp., SSA-S grade, o.d. 21 mm × i.d. 15 mm × height 25 mm) was fixed to an Al<sub>2</sub>O<sub>3</sub> tube (Nikkato Corp., SSA-S grade, o.d. 6.0 mm × i.d. 4.0 mm) by a Mo wire (Nilaco Corp., diameter 0.6 mm, 99.95%). A W wire (Nilaco Corp., diameter 1.0 mm, 99.95%) threaded into the Al<sub>2</sub>O<sub>3</sub> insulating tube was used as the current lead. A total of 10.0 g of Zn grains (Kojundo Chemical Laboratory Co., Ltd., 99.99%, 3–7 mm) was charged into small Al<sub>2</sub>O<sub>3</sub> crucible and melted in the molten salt. The counter and reference electrodes are the same as those described in 3.2.2.

After the electrolysis, several Zn electrodes were taken out of the molten salt and cooled by natural heat dissipation (approximately 10–20 s). Other Zn electrodes were cooled at a rate of 20 K h<sup>-1</sup> from 1123 K to 823 K and then cooled to room temperature by natural heat dissipation in the salt. Hereafter, the cooling by natural heat dissipation alone is referred to as "rapid cooling" and the cooling at 20 K h<sup>-1</sup> as "slow cooling". The Si granules in the Zn metal lumps were recovered by dissolving Zn in a 20 wt.% HCl solution prepared from a 36 wt.% solution. The solutions of dissolved Zn were analyzed by ICP-AES to determine the Ca concentration in the Zn lumps.

## 3.3 Results and Discussion

### 3.3.1 Ionic Species of Silicates

As the source of silicate ions, CaO–SiO<sub>2</sub> and CaSiO<sub>3</sub> are candidates. With the aim of fast preparation of the melts with target compositions, the dissolution rates of CaO–SiO<sub>2</sub> and CaSiO<sub>3</sub>

were investigated by Raman spectroscopy. Figure 3-3 shows Raman spectra for the salts (a) immediately (approximately 2–3 min) after heated to 1123 K, and (b) kept at 1123 K for 1 day beforehand for the dissolution of silicate-ion sources (CaO–SiO<sub>2</sub> and CaSiO<sub>3</sub>). The compositions of the molten salts were (1) CaCl<sub>2</sub> containing 1.0 mol% CaO and 1.0 mol% SiO<sub>2</sub>, and (2) CaCl<sub>2</sub> containing 1.0 mol% CaSiO<sub>3</sub>. The spectra are shown with background subtracted. For molten salt (1) in Figure 3-3(a), a strong band near 950 cm<sup>-1</sup> and medium bands at approximately 830 and 1040 cm<sup>-1</sup> were observed. On the other hand, for molten salt (2), only a strong band were detected near 970 cm<sup>-1</sup>. In addition, weak bands were observed at about 830 and 1050 cm<sup>-1</sup>. For both molten salts (1) and (2) in Figure 3-3(b), strong bands were detected near 970 cm<sup>-1</sup> and weak bands at approximately 830 and 1050 cm<sup>-1</sup>. Since the spectrum of the molten salt (2) immediately after heated to 1123 K was similar to that of the one dissolved for 1 day, the dissolution rate of CaSiO<sub>3</sub> is considered to be much higher than that of CaO–SiO<sub>2</sub>. Therefore, CaSiO<sub>3</sub> was suggested to be

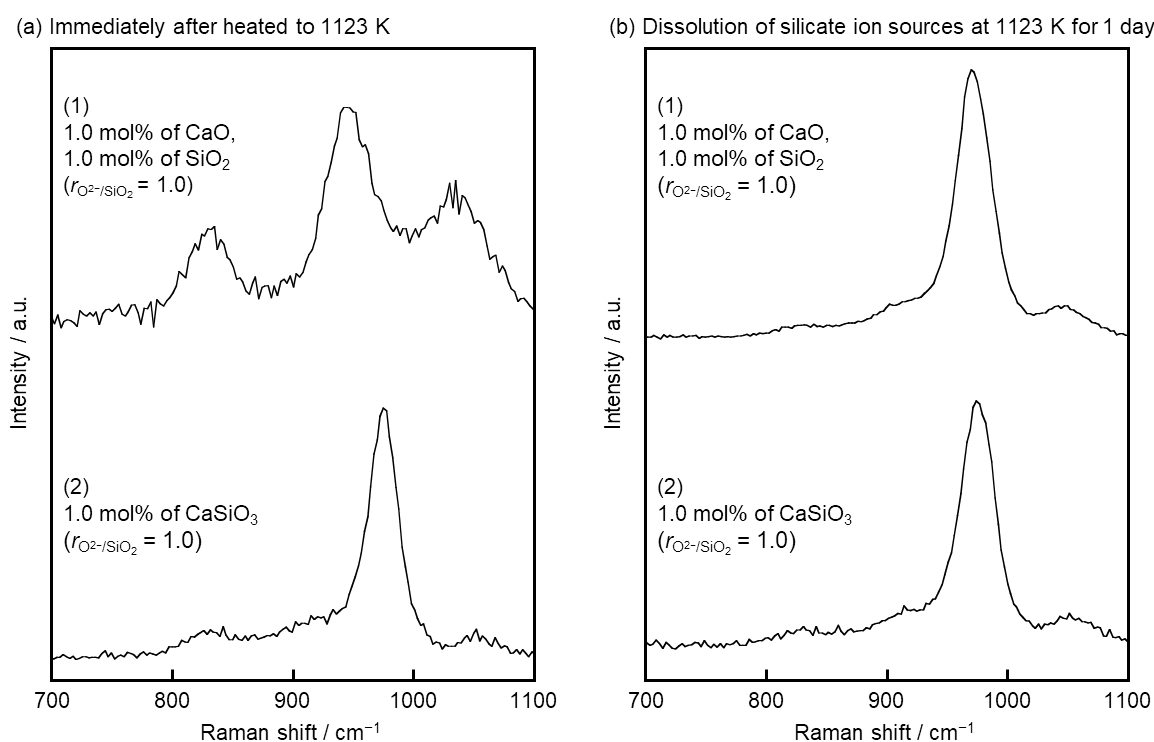


**Figure 3-3** Raman spectra for the salts (a) immediately after heated to 1123 K, and (b) kept at 1123 K for 1 day beforehand for the dissolution of silicate-ion sources. Salts (1): molten CaCl<sub>2</sub> containing 1.0 mol% CaO and 1.0 mol% SiO<sub>2</sub> ( $r_{O^{2-}/SiO_2} = 1.0$ ), and (2): molten CaCl<sub>2</sub> containing 1.0 mol% CaSiO<sub>3</sub> ( $r_{O^{2-}/SiO_2} = 1.0$ ).

suitable for the fast preparation of the melts with target compositions.

The ionic species of silicate ions in molten  $\text{CaCl}_2$  with  $r_{\text{O}^{2-}/\text{SiO}_2} = 1.0, 1.5,$  and  $2.0$  were investigated, using  $\text{CaSiO}_3$  as the source of silicate ions. Figure 3-4 shows the original and deconvoluted Raman spectra for those molten salts. The original spectra are shown with background subtracted and deconvoluted using the Voigtian function. For the melts containing 4.0 mol%  $\text{CaSiO}_3$  ( $r_{\text{O}^{2-}/\text{SiO}_2} = 1.0$ , Figure 3-4(a)), a strong band was deconvoluted at  $978 \text{ cm}^{-1}$  and weak bands at 834,

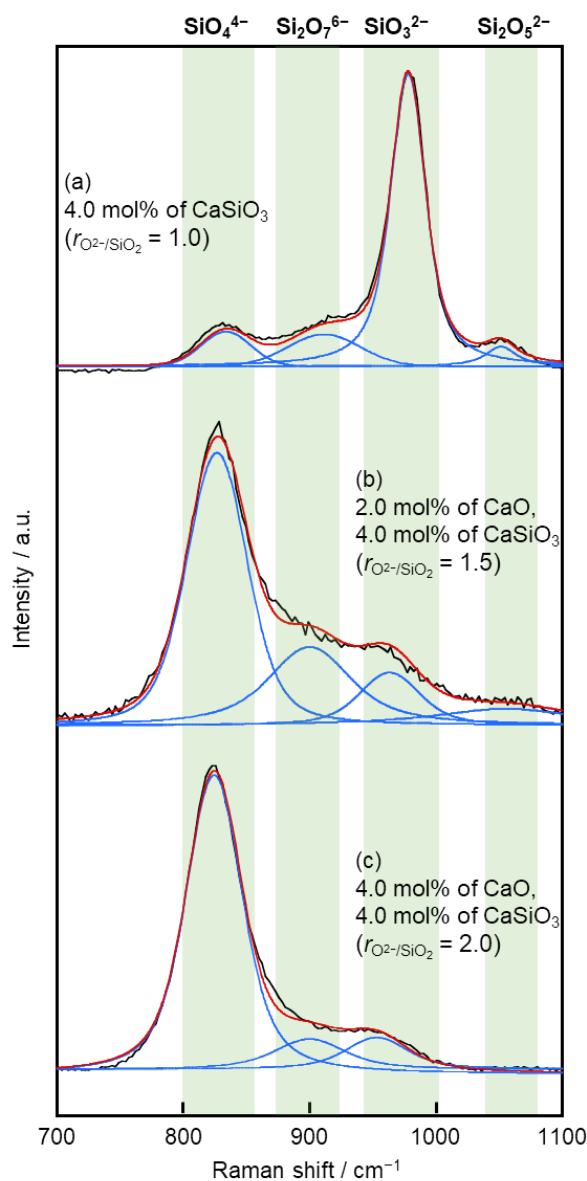


**Figure 3-4** Original and deconvoluted Raman spectra for molten  $\text{CaCl}_2$  with the addition of (a) 4.0 mol% of  $\text{CaSiO}_3$  ( $r_{\text{O}^{2-}/\text{SiO}_2} = 1.0$ ), (b) 2.0 mol% of  $\text{CaO}$  and 4.0 mol% of  $\text{CaSiO}_3$  ( $r_{\text{O}^{2-}/\text{SiO}_2} = 1.5$ ), and (c) 4.0 mol% of  $\text{CaO}$  and 4.0 mol% of  $\text{CaSiO}_3$  ( $r_{\text{O}^{2-}/\text{SiO}_2} = 2.0$ ) at 1123 K.



911 and 1051  $\text{cm}^{-1}$ . The symmetric stretch vibrations of  $\text{SiO}_4^{4-}$ ,  $\text{Si}_2\text{O}_7^{6-}$ ,  $\text{SiO}_3^{2-}$  and  $\text{Si}_2\text{O}_5^{2-}$  were reported at 850–880, 900–920, 950–980, and 1050–1100  $\text{cm}^{-1}$ , respectively [2–4]. Therefore, the bands at 911, 978, and 1051  $\text{cm}^{-1}$  were assigned to  $\text{Si}_2\text{O}_7^{6-}$ ,  $\text{SiO}_3^{2-}$  and  $\text{Si}_2\text{O}_5^{2-}$ , respectively. According to the report by Wang *et al.*, the Raman spectra for CaO–SiO<sub>2</sub>–CaCl<sub>2</sub> slags gradually shift to lower wavenumber with the increase of chlorine content, and that chlorine atoms can also be substituted with oxygen atoms [5]. Thus, in this study, the weak band at 834  $\text{cm}^{-1}$  is considered to be assigned to  $\text{SiO}_4^{4-}$  with oxygen ions partially substituted for chloride ions as follows:



As described in Figure 3-4(b) and (c), similar fitting results were obtained for the molten salts with  $r_{\text{O}^{2-}/\text{SiO}_2} = 1.5$  and 2.0. The deconvolution results of the Raman spectra are presented in Table 3-1. For the molten salt with  $r_{\text{O}^{2-}/\text{SiO}_2} = 1.0$ , the dominant silicate ion was  $\text{SiO}_3^{2-}$ . The weak bands of other silicate ions are considered to be due to the equilibrium reactions of  $\text{SiO}_3^{2-}$  and  $\text{Si}_2\text{O}_7^{6-}$ .



**Table 3-1** Deconvolved wavenumbers of Raman spectra for samples obtained in molten CaCl<sub>2</sub> with the addition of (i) 4.0 mol% of CaSiO<sub>3</sub> ( $r_{\text{O}^{2-}/\text{SiO}_2} = 1.0$ ), (ii) 2.0 mol% of CaO and 4.0 mol% of CaSiO<sub>3</sub> ( $r_{\text{O}^{2-}/\text{SiO}_2} = 1.5$ ), and (iii) 4.0 mol% of CaO and 4.0 mol% of CaSiO<sub>3</sub> ( $r_{\text{O}^{2-}/\text{SiO}_2} = 2.0$ ) at 1123 K.

| Ratio of $\text{O}^{2-}/\text{SiO}_2$<br>in molten salt<br>( $r_{\text{O}^{2-}/\text{SiO}_2}$ ) | Wavenumber / $\text{cm}^{-1}$<br>(Band intensity fraction † / %) |                              |                     |                              |
|---|--|------------------------------|---------------------|------------------------------|
|   | $\text{SiO}_4^{4-}$  | $\text{Si}_2\text{O}_7^{6-}$ | $\text{SiO}_3^{2-}$ | $\text{Si}_2\text{O}_5^{2-}$ |
| (i) 1.0   | 834vw<br>(9.3)   | 911w<br>(12.5)               | 978s<br>(73.4)      | 1051vw<br>(4.8)              |
| (ii) 1.5  | 827s<br>(48.3)   | 900m<br>(24.4)               | 953w<br>(13.8)      | 1056w<br>(13.5)              |
| (iii) 2.0   | 824s<br>(79.5)   | 900w<br>(10.9)               | 953vw<br>(9.6)      | —                            |

Abbreviations: vw, very weak; w, weak; m, medium; s, strong.

† Calculated from fitted band area.



When  $r_{\text{O}^{2-}/\text{SiO}_2}$  increased to 1.5, the dominant silicate species was attributed to  $\text{SiO}_4^{4-}$ , secondary dominant species to  $\text{Si}_2\text{O}_7^{6-}$ , and minor species to  $\text{SiO}_3^{2-}$  and  $\text{Si}_2\text{O}_5^{2-}$ . Although the ratio of  $\text{O}^{2-}/\text{SiO}_2 = 1.5$  corresponds to  $\text{Si}_2\text{O}_7^{6-}$ , it is considered to change to the ionic species with simpler structures (reaction (3-3)) due to the poor stability of  $\text{Si}_2\text{O}_7^{6-}$  in the molten salt. With respect to the melt with  $r_{\text{O}^{2-}/\text{SiO}_2} = 2.0$ ,  $\text{SiO}_4^{4-}$  was the dominant silicate ion, which is consistent with the composition calculated from the  $\text{O}^{2-}/\text{SiO}_2$  ratio.

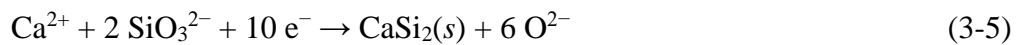
### 3.3.2 Electrochemical Reduction of Silicate Ions at a Solid Graphite Electrode

#### 3.3.2.1 Cyclic Voltammetry

Figure 3-5 shows the cyclic voltammograms at a graphite electrode in molten  $\text{CaCl}_2$  containing different amounts of  $\text{CaO}$  and  $\text{CaSiO}_3$ . The black curves show the voltammograms before the addition of  $\text{CaSiO}_3$  and  $\text{CaO}$  (blank). The small cathodic current observed around 0.5 V (vs.  $\text{Ca}^{2+}/\text{Ca}$ ) is likely due to the intercalation of  $\text{Ca}^{2+}$  into graphite. After the addition of 4.0 mol%  $\text{CaSiO}_3$  ( $r_{\text{O}^{2-}/\text{SiO}_2} = 1.0$ ), as shown in Figure 3-5(a), cathodic current increased from 1.35 V, suggesting the electrochemical reduction of dominant  $\text{SiO}_3^{2-}$  that observed in the Raman spectra.



The cathodic current peaks at 0.40 V and 0.49 V are considered as the formation of Ca–Si alloys. According to the phase diagram of the Ca–Si system [6], the first intermediate phase in the Si-rich region is  $\text{CaSi}_2$ . Therefore, the cathodic current peak at 0.40 V and 0.49 V are likely due to the formation of  $\text{CaSi}_2$  from  $\text{SiO}_3^{2-}$  and solid Si.



A voltammogram of the melt containing 2.0 mol%  $\text{CaO}$  and 4.0 mol%  $\text{CaSiO}_3$  ( $r_{\text{O}^{2-}/\text{SiO}_2} = 1.5$ ) is

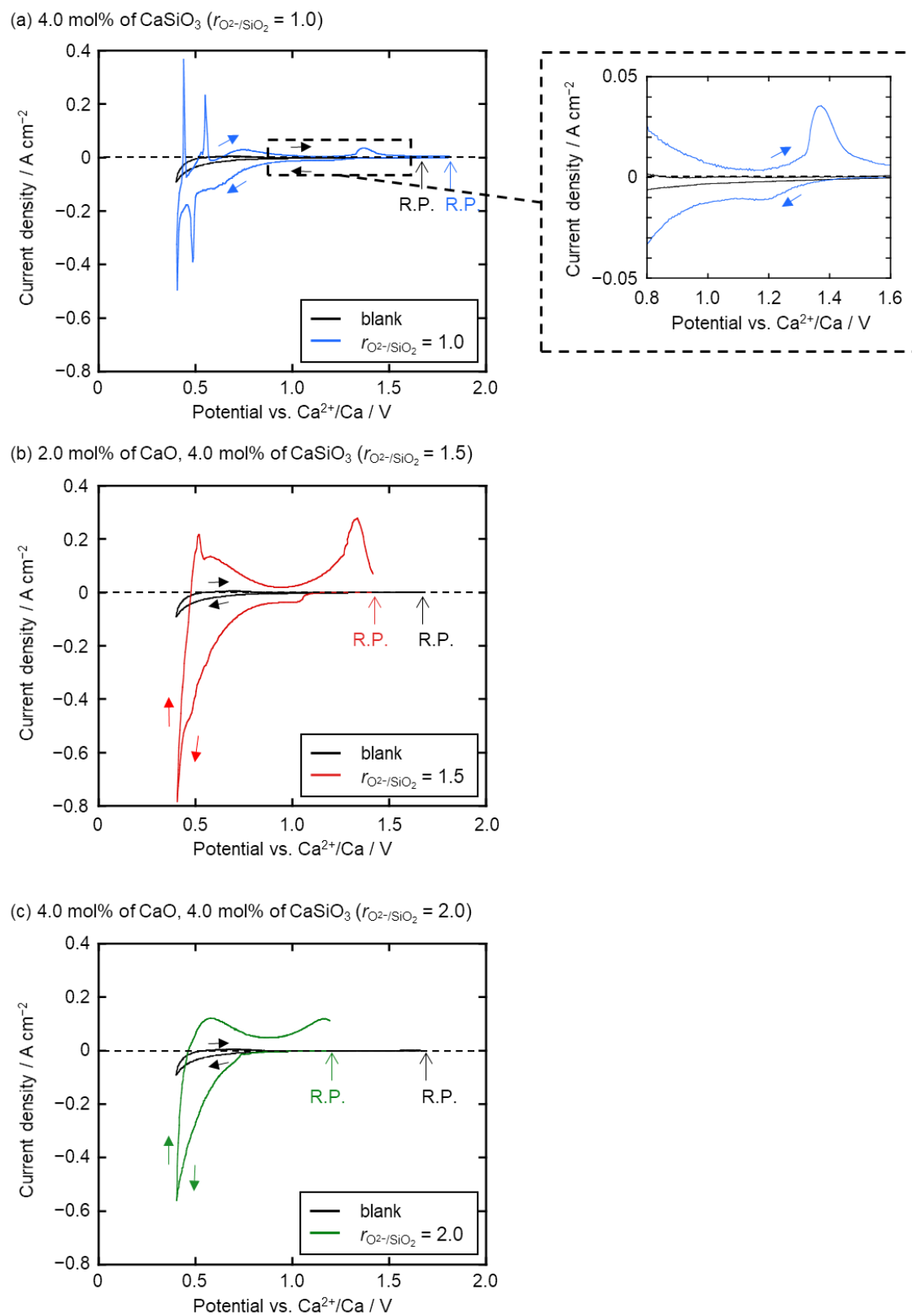


**Figure 3-5** Cyclic voltammograms at a graphite electrode in molten  $\text{CaCl}_2$  before and after the addition of (a) 4.0 mol% of  $\text{CaSiO}_3$  ( $r_{\text{O}^{2-}/\text{SiO}_2} = 1.0$ ), (b) 2.0 mol% of  $\text{CaO}$  and 4.0 mol% of  $\text{CaSiO}_3$  ( $r_{\text{O}^{2-}/\text{SiO}_2} = 1.5$ ), and (c) 4.0 mol% of  $\text{CaO}$  and 4.0 mol% of  $\text{CaSiO}_3$  ( $r_{\text{O}^{2-}/\text{SiO}_2} = 2.0$ ) at 1123 K. Scan rate:  $50 \text{ mV s}^{-1}$ . R. P.: Rest potential.

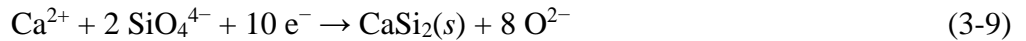
shown in Figure 3-5(b). Cathodic current increased from 1.12 V was likely attributed to the electrochemical reduction of secondary dominant  $\text{Si}_2\text{O}_7^{6-}$ .



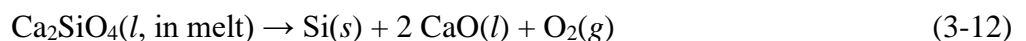
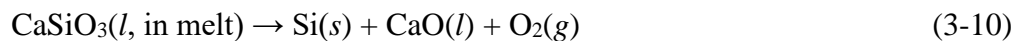
The rapid increase of cathodic current from 0.75 V is considered to be due to the electrochemical reduction of dominant  $\text{SiO}_4^{4-}$ .



Figure 3-5(c) shows the voltammogram measured after the addition of 4.0 mol% CaO and 4.0 mol%  $\text{CaSiO}_3$  ( $r_{\text{O}^{2-}/\text{SiO}_2} = 2.0$ ). A rapid increase of cathodic current was observed from 0.75 V, suggesting the electrochemical reduction of dominant  $\text{SiO}_4^{4-}$  (reaction (3-8)). According to the potential– $p\text{O}^{2-}$  diagram for Si in molten  $\text{CaCl}_2$  at 1123 K, the boundary between  $\text{Ca}_2\text{SiO}_4(s)$  and  $\text{CaSi}_2(s)$  exists in the high- $p\text{O}^{2-}$  region and its equilibrium potential shifts to negative with the increase of  $\text{O}^{2-}$  concentration [7]. Therefore, the cathodic current peaks observed at 0.40 V in molten salt (ii) and (iii) are considered to be the formation of  $\text{CaSi}_2$  from  $\text{SiO}_4^{4-}$ .



In order to confirm the results shown above, thermodynamic data associated with the electrochemical reduction of  $\text{SiO}_3^{2-}$ ,  $\text{Si}_2\text{O}_7^{6-}$  and  $\text{SiO}_4^{4-}$  were calculated. Generally, the difference in reduction potential of  $\text{SiO}_3^{2-}$ ,  $\text{Si}_2\text{O}_7^{6-}$  and  $\text{SiO}_4^{4-}$  can be calculated from the Gibbs energies for the decomposition reactions,  $\Delta G_d(l, \text{ in melt})$ .



Here,  $\text{CaSiO}_3(l, \text{ in melt})$ ,  $\text{Ca}_3\text{Si}_2\text{O}_7(l, \text{ in melt})$  and  $\text{Ca}_2\text{SiO}_4(l, \text{ in melt})$  are  $\text{CaSiO}_3$ ,  $\text{Ca}_3\text{Si}_2\text{O}_7$  and  $\text{Ca}_2\text{SiO}_4$  dissolved into molten salt. However, these Gibbs energies can not be calculated from the

reported data. On the other hand, the Gibbs energies for the decomposition reactions for solid  $\text{CaSiO}_3$ ,  $\text{Ca}_3\text{Si}_2\text{O}_7$  and  $\text{Ca}_2\text{SiO}_4$ ,  $\Delta G_d(s)$ , can be calculated from the data in literatures [8, 9]. Here, we assumed that the difference of the Gibbs energy,  $\Delta G_d(l, \text{ in melt}) - \Delta G_d(s)$ , is almost the same for  $\text{CaSiO}_3$ ,  $\text{Ca}_3\text{Si}_2\text{O}_7$  and  $\text{Ca}_2\text{SiO}_4$ , so that  $\Delta G_d(s)$  could be used to estimate the difference in reduction potential of  $\text{SiO}_3^{2-}$ ,  $\text{Si}_2\text{O}_7^{6-}$  and  $\text{SiO}_4^{4-}$ . The calculated data are shown in Table 3-2. Since the standard Gibbs energy decreases in the order of  $\text{CaSiO}_3(s)$ ,  $\text{Ca}_3\text{Si}_2\text{O}_7(s)$  and  $\text{Ca}_2\text{SiO}_4(s)$ , the potential for the electrochemical reduction of silicate ions would shift to negative values in the order of  $\text{SiO}_3^{2-}$ ,  $\text{Si}_2\text{O}_7^{6-}$  and  $\text{SiO}_4^{4-}$ , which is corresponded to the results of cyclic voltammetry.

### 3.3.2.2 Potentiostatic Electrolysis

Based on the voltammetry results, potentiostatic electrolysis was conducted at 0.50, 0.60, 0.70, 0.90 and 1.1 V in molten  $\text{CaCl}_2$  containing (i) 4.0 mol%  $\text{CaSiO}_3$  ( $r_{\text{O}^{2-}/\text{SiO}_2} = 1.0$ ), (ii) 2.0 mol%  $\text{CaO}$  and 4.0 mol%  $\text{CaSiO}_3$  ( $r_{\text{O}^{2-}/\text{SiO}_2} = 1.5$ ), and (iii) 4.0 mol%  $\text{CaO}$  and 4.0 mol%  $\text{CaSiO}_3$  ( $r_{\text{O}^{2-}/\text{SiO}_2} = 2.0$ ). The current transient curves during the electrolysis are shown in Figure 3-6. The charge densities during the electrolysis were fixed at  $-14 \text{ C cm}^{-2}$ . However, the electrolysis at 0.70, 0.90 and 1.1 V in molten salt (iii) were intentionally stopped in 1 hour before reaching  $-14 \text{ C cm}^{-2}$  because the currents were less than 1 mA. The low current densities proved that the electrochemical reduction of  $\text{SiO}_4^{4-}$  starts from a more negative potential than that of  $\text{SiO}_3^{2-}$ , which is consistent with the voltammograms.

**Table 3-2 Standard Gibbs energies for the decomposition reactions of  $\text{CaSiO}_3(s)$ ,  $\text{Ca}_3\text{Si}_2\text{O}_7(s)$  and  $\text{Ca}_2\text{SiO}_4(s)$  to  $\text{Si}(s)$ ,  $\text{CaO}(l)$ , and  $\text{O}_2(g)$  at 1123 K.**

| Reaction   | Standard Gibbs energy, $\Delta G_d^\circ / \text{kJ mol}^{-1}$ |
|--|--|
| $\text{CaSiO}_3(s) \rightarrow \text{Si}(s) + \text{CaO}(l) + \text{O}_2(g)$                             | 849.5  |
| $0.5 \text{ Ca}_3\text{Si}_2\text{O}_7(s) \rightarrow \text{Si}(s) + 1.5 \text{ CaO}(l) + \text{O}_2(g)$ | 913.8  |
| $\text{Ca}_2\text{SiO}_4(s) \rightarrow \text{Si}(s) + 2 \text{ CaO}(l) + \text{O}_2(g)$                 | 947.5  |

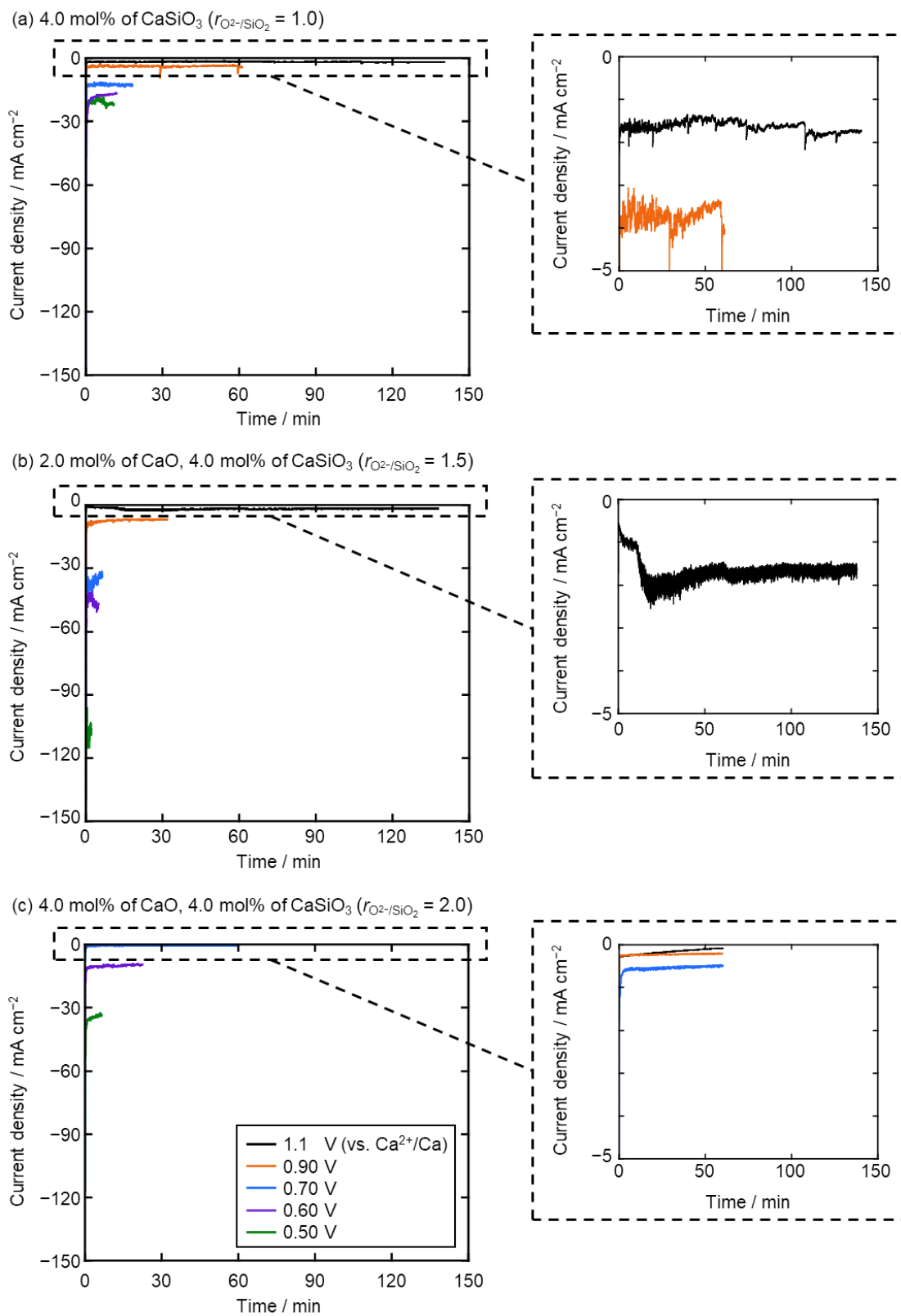


**Figure 3-6** Current transient curves during the potentiostatic electrolysis at graphite plates in molten  $\text{CaCl}_2$  with the addition of (a) 4.0 mol% of  $\text{CaSiO}_3$  ( $r_{\text{O}^{2-}/\text{SiO}_2} = 1.0$ ), (b) 2.0 mol% of  $\text{CaO}$  and 4.0 mol% of  $\text{CaSiO}_3$  ( $r_{\text{O}^{2-}/\text{SiO}_2} = 1.5$ ), and (c) 4.0 mol% of  $\text{CaO}$  and 4.0 mol% of  $\text{CaSiO}_3$  ( $r_{\text{O}^{2-}/\text{SiO}_2} = 2.0$ ) at 1123 K.

Optical images of the electrolyzed samples are shown in Figure 3-7. Deposits in gray or dark brown color were observed except the samples obtained at 0.90 V and 1.1 V in molten salt (iii). No deposit was observed at these samples. For the sample obtained at 0.90 V in molten salt (ii), the deposits in dark brown color fell off during the removal of residual salt.

Figure 3-8 shows XRD patterns of the electrolyzed samples. In Figure 3-8(a), the existence of Si was confirmed in all samples obtained in molten salt (i). Thus, the increase of cathodic current from 1.35 V in Figure 3-5(a) was confirmed to be the electrochemical reduction of  $\text{SiO}_3^{2-}$  to solid Si (reaction (3-4)). For the sample obtained at 0.50 V,  $\text{CaSi}_2$  was identified before removing the residual salt, indicating that the cathodic current peak at 0.49 V was the formation of  $\text{CaSi}_2$  from solid Si. In molten salt (ii), Si was also confirmed at all samples, which suggested the increase of cathodic current from 1.12 V as the electrochemical reduction of  $\text{Si}_2\text{O}_7^{6-}$  (reaction (3-7)). For samples obtained in molten salt (iii), the existence of Si was only confirmed at 0.50 and 0.60 V. Therefore, the cathodic current increased from 0.75 V, as shown in Figure 3-5(b) and (c),

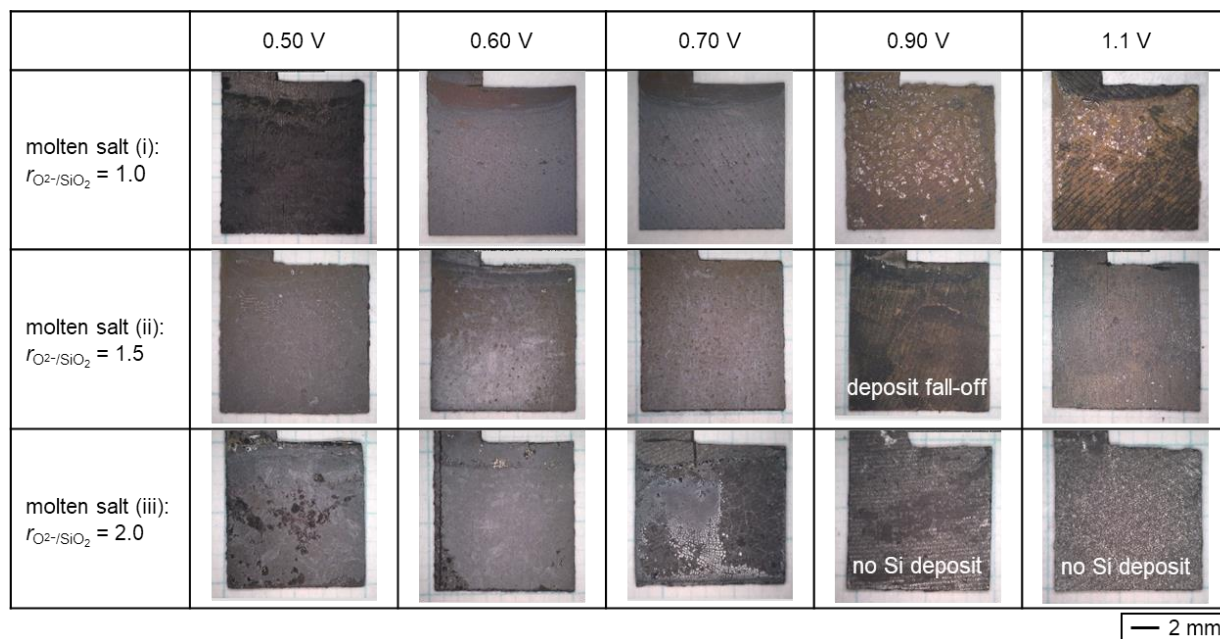


**Figure 3-7** Optical images of the samples obtained by electrolysis at graphite plates in molten  $\text{CaCl}_2$  with the addition of (i) 4.0 mol% of  $\text{CaSiO}_3$  ( $r_{\text{O}^{2-}/\text{SiO}_2} = 1.0$ ), (ii) 2.0 mol% of  $\text{CaO}$  and 4.0 mol% of  $\text{CaSiO}_3$  ( $r_{\text{O}^{2-}/\text{SiO}_2} = 1.5$ ), and (iii) 4.0 mol% of  $\text{CaO}$  and 4.0 mol% of  $\text{CaSiO}_3$  ( $r_{\text{O}^{2-}/\text{SiO}_2} = 2.0$ ) at 1123 K.

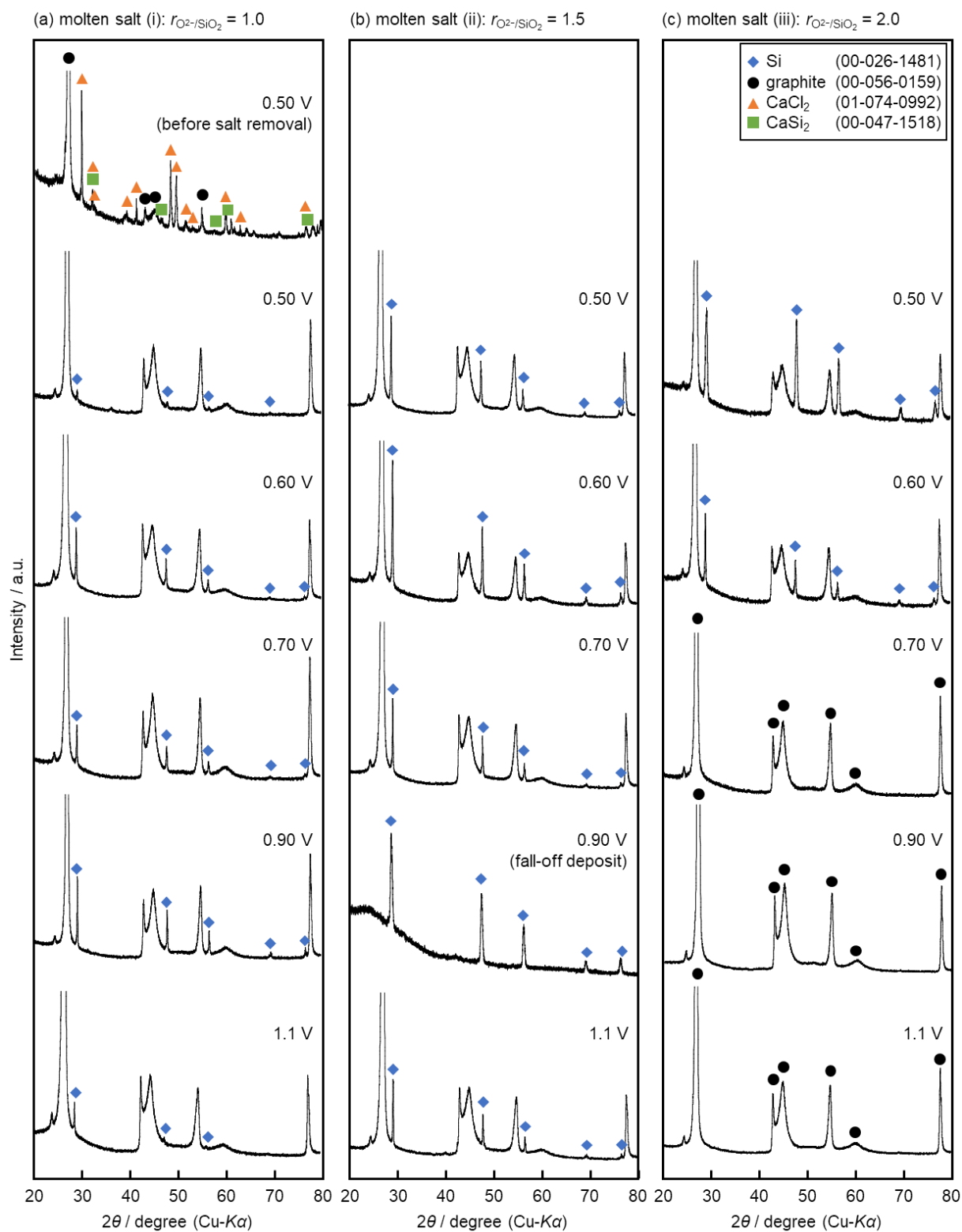


**Figure 3-8** XRD patterns of the samples obtained by electrolysis at graphite plates in molten  $CaCl_2$  with the addition of (i) 4.0 mol% of  $CaSiO_3$  ( $r_{O^{2-}/SiO_2} = 1.0$ ), (ii) 2.0 mol% of  $CaO$  and 4.0 mol% of  $CaSiO_3$  ( $r_{O^{2-}/SiO_2} = 1.5$ ), and (iii) 4.0 mol% of  $CaO$  and 4.0 mol% of  $CaSiO_3$  ( $r_{O^{2-}/SiO_2} = 2.0$ ) at 1123 K.



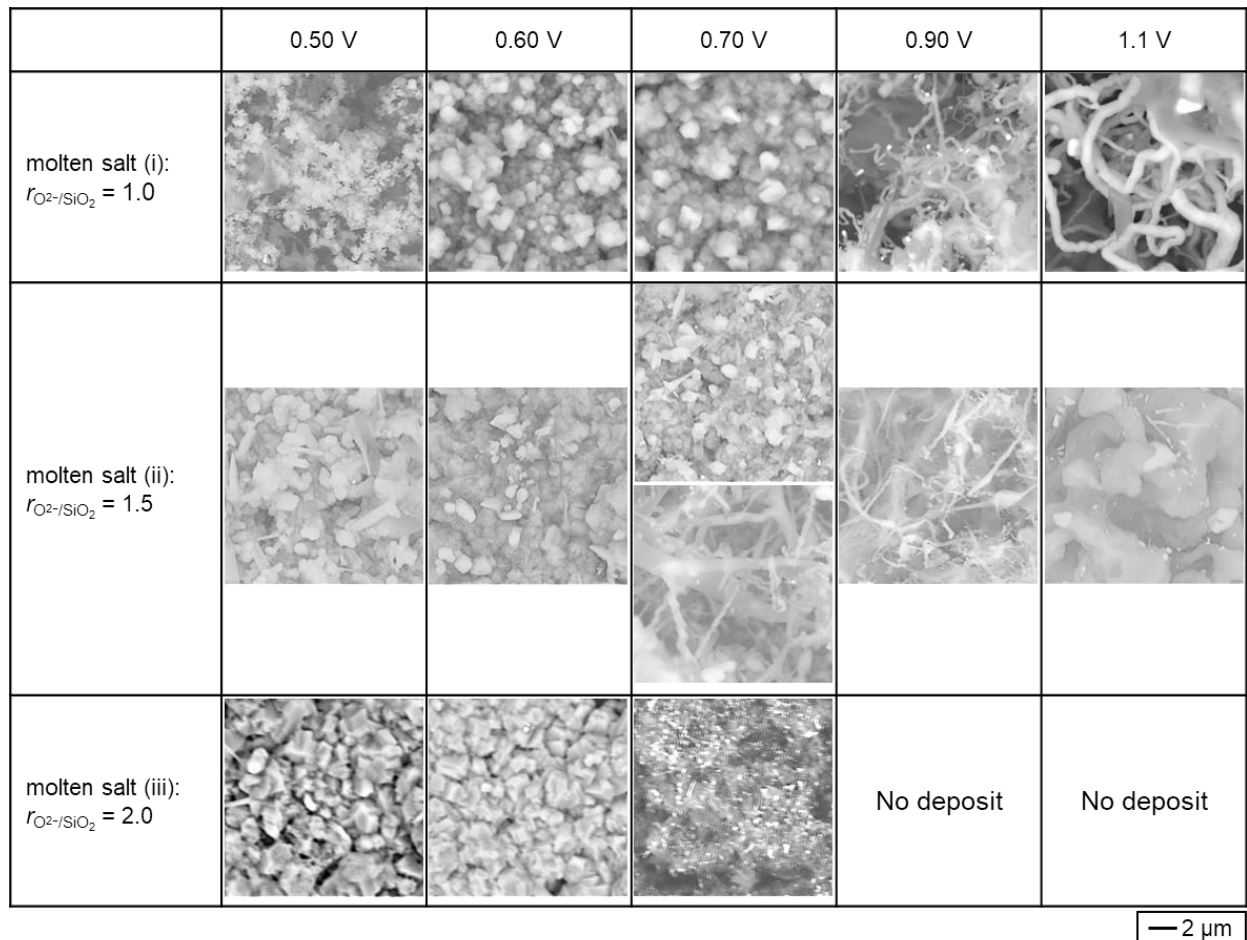
corresponding to the electrochemical reduction of dominant  $\text{SiO}_4^{4-}$  to solid Si (reaction (3-8)). The identified phases are summarized in Table 3-3.

Figure 3-9 shows the SEM images of the deposits. For samples obtained in molten salt (i), wire-like Si with different shapes were obtained at 0.90 V and 1.1 V, and particle Si was obtained at 0.50, 0.60 and 0.70 V, respectively. In molten salt (ii), wire-like Si was observed at 0.70, 0.90 and 1.10 V, and particle Si at 0.50, 0.60 and 0.70 V. In molten salt (iii), particle Si was formed at 0.50 V and 0.60 V. For the sample obtained at 0.70 V, deposits were observed in the gray-color region of the optical image, where 44.5 at.% of Si and 55.5 at.% of O was detected by EDX analysis. The change in morphology of reduced Si is considered to be due to the change of overpotential and current density. According to the research by Winand [10], electrodeposits become field-oriented isolated crystals type such as wires when the overpotential and current density are low. On the other hand, when the overpotential and current density are higher, the electrodeposits shift to unoriented dispersion type, such as particles. In molten salt (i) with dominant  $\text{SiO}_3^{2-}$ , the potential of more positive than 0.90 V would correspond to the low overpotential and current density, which results in the formation of wire-like Si. The potential of 0.70 V is likely to be classified as higher overpotential and current density, resulting in the formation of particle Si. For molten salt (iii), the

**Table 3-3 XRD results for the samples obtained in molten  $\text{CaCl}_2$  with the addition of (i) 4.0 mol% of  $\text{CaSiO}_3$  ( $r_{\text{O}^{2-}/\text{SiO}_2} = 1.0$ ), (ii) 2.0 mol% of CaO and 4.0 mol% of  $\text{CaSiO}_3$  ( $r_{\text{O}^{2-}/\text{SiO}_2} = 1.5$ ), and (iii) 4.0 mol% of CaO and 4.0 mol% of  $\text{CaSiO}_3$  ( $r_{\text{O}^{2-}/\text{SiO}_2} = 2.0$ ) at 1123 K.**

| Ratio of $\text{O}^{2-}/\text{SiO}_2$<br>in molten salt<br>( $r_{\text{O}^{2-}/\text{SiO}_2}$ ) | Identified phase of electrolyzed samples |        |               |               |               |
|---|--|--------|---------------|---------------|---------------|
|   | 0.50 V                                   | 0.60 V | 0.70 V        | 0.90 V        | 1.1 V         |
| (i) 1.0   | $\text{CaSi}_2$ *, Si                    | Si     | Si            | Si            | Si            |
| (ii) 1.5  | Si                                       | Si     | Si            | Si            | Si            |
| (iii) 2.0   | Si                                       | Si     | no Si deposit | no Si deposit | no Si deposit |

\* Detected before removing the residual salt.



**Figure 3-9** SEM images of the samples obtained by electrolysis at graphite plates in molten  $\text{CaCl}_2$  with the addition of (i) 4.0 mol% of  $\text{CaSiO}_3$  ( $r_{\text{O}^{2-}/\text{SiO}_2} = 1.0$ ), (ii) 2.0 mol% of  $\text{CaO}$  and 4.0 mol% of  $\text{CaSiO}_3$  ( $r_{\text{O}^{2-}/\text{SiO}_2} = 1.5$ ), and (iii) 4.0 mol% of  $\text{CaO}$  and 4.0 mol% of  $\text{CaSiO}_3$  ( $r_{\text{O}^{2-}/\text{SiO}_2} = 2.0$ ) at 1123 K.

dominant ion is  $\text{SiO}_4^{4-}$  and its electrochemical reduction starts from a more negative potential than  $\text{SiO}_3^{2-}$ . Then, the potential of 0.60 V is classified as higher overpotential and current density, resulting in the formation of particle Si. In molten salt (ii),  $\text{SiO}_4^{4-}$  and  $\text{Si}_2\text{O}_7^{6-}$  were dominant and second dominant species, respectively. Therefore, wire-like Si is considered to be formed from  $\text{Si}_2\text{O}_7^{6-}$  and particle Si from  $\text{SiO}_4^{4-}$  at 0.70 V. Then, particle Si was electrodeposited from 0.60 V, which is classified as higher overpotential.

From all the results shown above, in the terms of available potential range for electrolysis, molten salt (i) with dominant  $\text{SiO}_3^{2-}$  is suggested to be suitable for producing Si–Zn alloy, because the electrodeposition of Si starts from a more positive potential than other silicate ions. Since the

formation of Ca–Zn alloy during the electrolysis, which leads to low efficiency of Si–Zn alloy production, has been confirmed in the electrochemical reduction of solid SiO<sub>2</sub> that described in Chapter 2, the SiO<sub>3</sub><sup>2-</sup>, of which the electrochemical reduction is further apart from the Ca–Zn alloy formation, is considered to be advantageous for the efficient Si production.

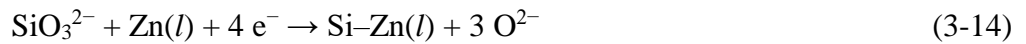
### 3.3.3 Electrochemical Reduction of Silicate Ions at a Liquid Zn Electrode

#### 3.3.3.1 Cyclic Voltammetry

Figure 3-10 shows the cyclic voltammograms at a liquid Zn electrode in molten salts (i), (ii) and (iii). The black curves show the voltammograms in blank melt. The small cathodic current observed around 0.85 V is likely due to the formation of Ca–Zn alloy.

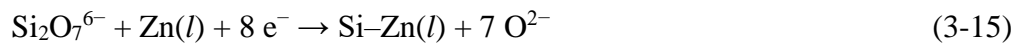


After the addition of 4.0 mol% CaSiO<sub>3</sub> ( $r_{\text{O}^{2-}/\text{SiO}_2} = 1.0$ ), as shown in Figure 3-10(a), cathodic current increase was observed from the rest potential (1.46 V), which suggested the electrochemical reduction of dominant SiO<sub>3</sub><sup>2-</sup>.



A sharp increase in cathodic current from 0.85 V is considered to correspond to the simultaneous reactions of the electrochemical reduction of SiO<sub>3</sub><sup>2-</sup> (reaction (3-14)) and the formation of Ca–Zn alloy (reaction (3-13)).

Figure 3-10(b) shows the voltammogram measured after the addition of 2.0 mol% CaO and 4.0 mol% CaSiO<sub>3</sub> ( $r_{\text{O}^{2-}/\text{SiO}_2} = 1.5$ ). Cathodic current increased rapidly from the rest potential, i.e., 1.25 V, which seems to be attributed to the electrochemical reduction of secondary dominant Si<sub>2</sub>O<sub>7</sub><sup>6-</sup>.



A plateau of cathodic current observed at around 1.0 V is likely due to the electrochemical

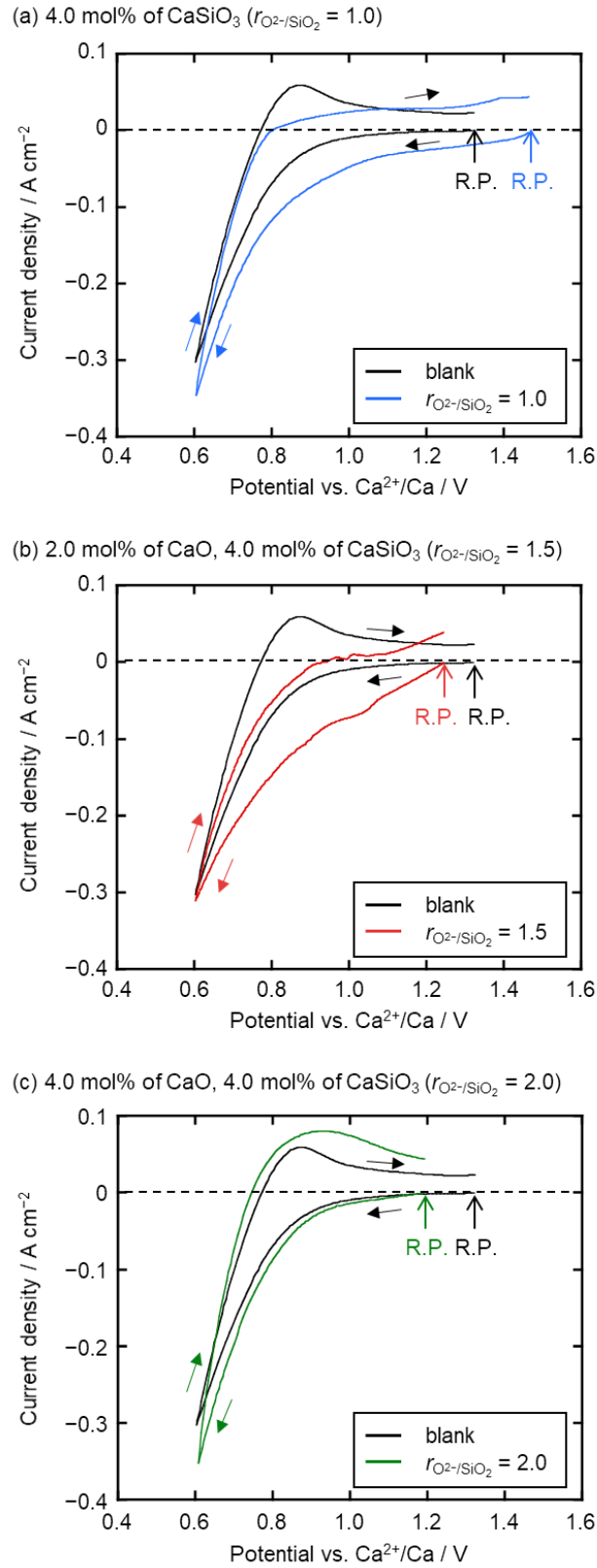
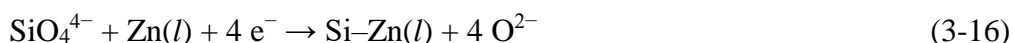


**Figure 3-10** Cyclic voltammograms at a liquid Zn electrode in molten  $\text{CaCl}_2$  before and after the addition of (a) 4.0 mol% of  $\text{CaSiO}_3$  ( $r_{\text{O}^{2-}/\text{SiO}_2} = 1.0$ ), (b) 2.0 mol% of  $\text{CaO}$  and 4.0 mol% of  $\text{CaSiO}_3$  ( $r_{\text{O}^{2-}/\text{SiO}_2} = 1.5$ ), and (c) 4.0 mol% of  $\text{CaO}$  and 4.0 mol% of  $\text{CaSiO}_3$  ( $r_{\text{O}^{2-}/\text{SiO}_2} = 2.0$ ) at 1123 K. Scan rate:  $100 \text{ mV s}^{-1}$ . R. P.: Rest potential.

reduction of dominant  $\text{SiO}_4^{4-}$ .

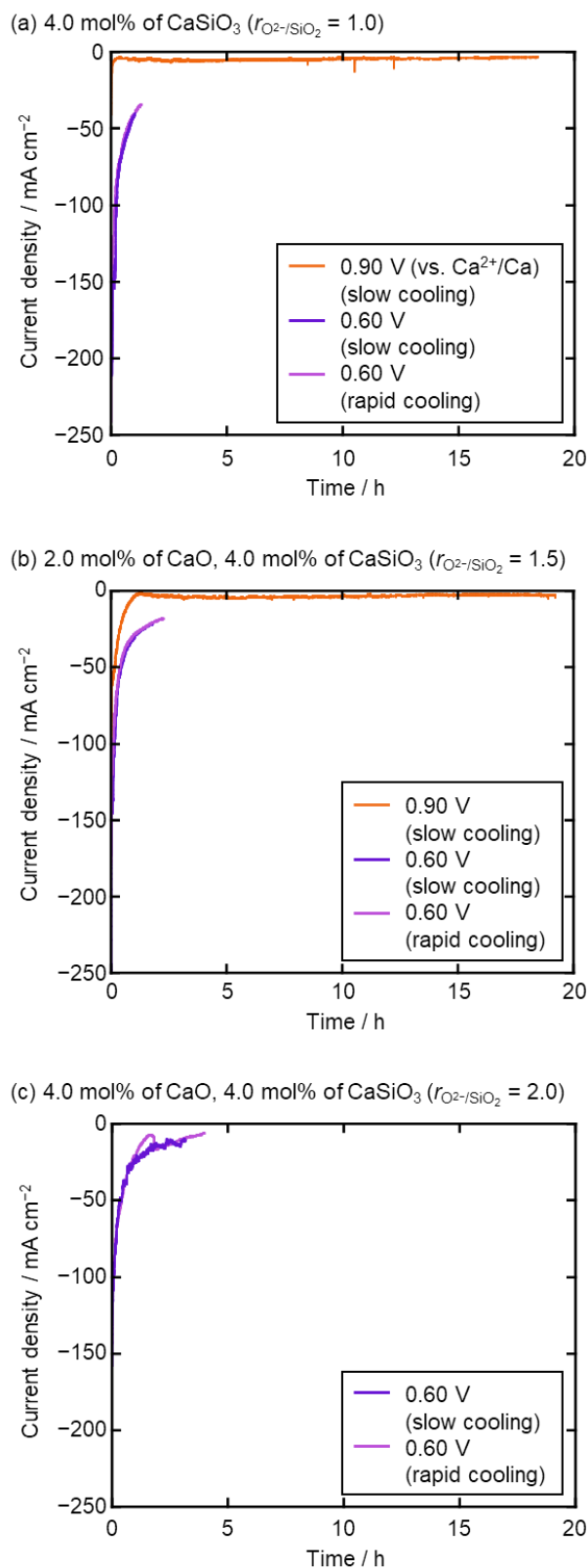


The sharp increase in cathodic current from 0.85 V was regarded as the simultaneous reactions of the electrochemical reduction of silicate ions and the Ca–Zn alloy formation, which was similar to that observed in [Figure 3-10\(a\)](#).

A voltammogram conducted in the melt containing 4.0 mol% CaO and 4.0 mol%  $\text{CaSiO}_3$  ( $r_{\text{O}^{2-}/\text{SiO}_2} = 2.0$ ) is shown in [Figure 3-10\(c\)](#). Rapid increase in cathodic current from the rest potential (1.15 V) was likely attributed to the electrochemical reduction of dominant  $\text{SiO}_4^{4-}$ . The rest potential in molten salt (iii) with dominant  $\text{SiO}_4^{4-}$  was more negative than that in molten salt (i) with dominant  $\text{SiO}_3^{2-}$ , which is corresponded to voltammograms at the graphite electrode shown in [Figure 3-5](#). The sharp increase in cathodic current from 0.85 V was ascribed to the same simultaneous reactions, similar to the other two melts shown in [Figure 3-10\(a\)](#) and [\(b\)](#). Compared with the results of cyclic voltammetry conducted at the graphite electrode, the electrochemical reduction of silicate ions started from a more positive potential, which suggested the formation of liquid Si–Zn alloy with Si activity lower than unity with respect to pure solid Si.

### 3.3.3.2 Potentiostatic Electrolysis

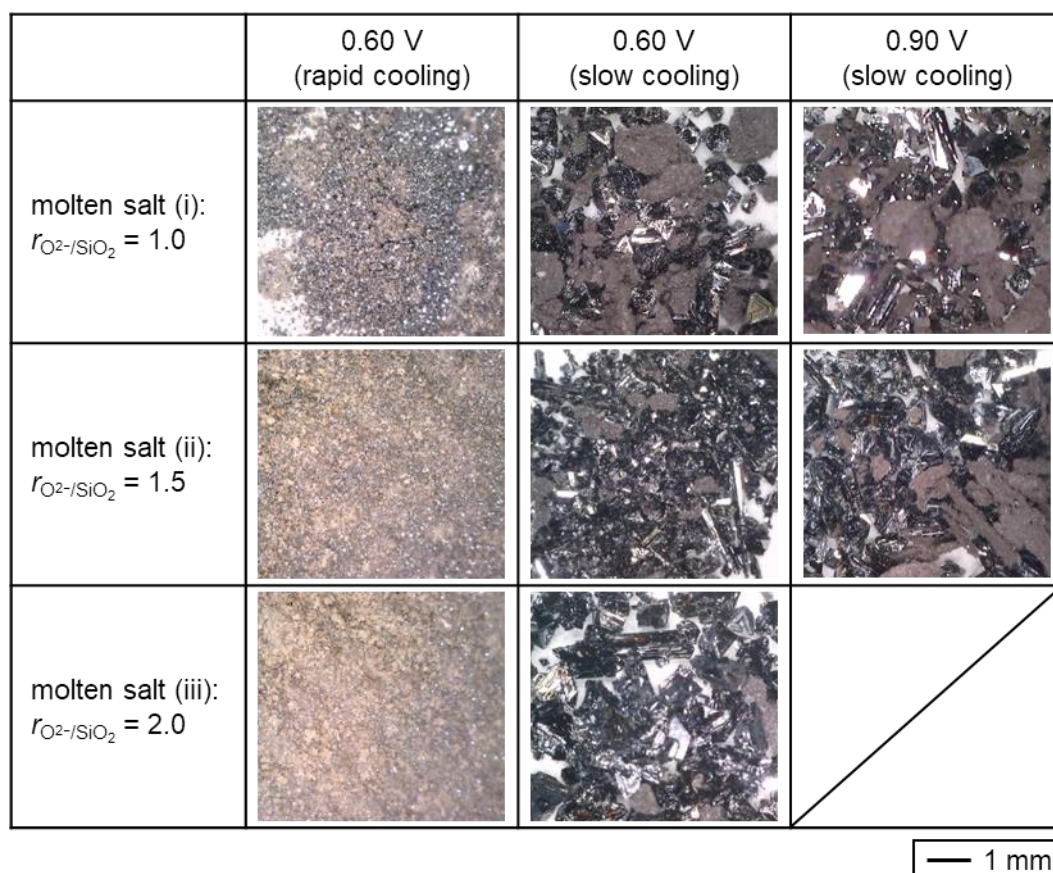
Potentiostatic electrolysis was conducted at 0.60 V and 0.90 V in molten salts (i) and (ii), and 0.60 V in molten salt (iii). Electrolysis at 0.90 V in molten salt (iii) was excluded because its current was too small to form Si–Zn alloy. All electrolysis was conducted with a constant charge of  $-590.3$  C, which corresponds to the theoretical quantity of charge for 1.0 mol% Si–Zn alloy formation. The current transient curves during the electrolysis are shown in [Figure 3-11](#). In molten salt (i), the large current density at 0.60 V is considered as the simultaneous reactions of the electrochemical reduction of  $\text{SiO}_3^{2-}$  ([reaction \(3-14\)](#)) and the formation of Ca–Zn alloy ([reaction \(3-13\)](#)), and only the electrochemical reduction of  $\text{SiO}_3^{2-}$  occurred at 0.90 V. Similarly, larger



**Figure 3-11** Current transient curves during the potentiostatic electrolysis at the liquid Zn electrode in molten  $\text{CaCl}_2$  with the addition of (a) 4.0 mol% of  $\text{CaSiO}_3$  ( $r_{\text{O}^{2-}/\text{SiO}_2} = 1.0$ ), (b) 2.0 mol% of  $\text{CaO}$  and 4.0 mol% of  $\text{CaSiO}_3$  ( $r_{\text{O}^{2-}/\text{SiO}_2} = 1.5$ ), and (c) 4.0 mol% of  $\text{CaO}$  and 4.0 mol% of  $\text{CaSiO}_3$  ( $r_{\text{O}^{2-}/\text{SiO}_2} = 2.0$ ) at 1123 K. Charge:  $-590.3$  C (theoretical formation of 1.0 mol% Si-Zn alloy).

currents were observed at 0.60 V in molten salts (ii) and (iii), suggesting the simultaneous reactions of the electrochemical reduction of silicate ions (reactions (3-15) and (3-16)) and the formation of Ca–Zn alloy (reaction (3-13)).

After the electrolysis, half of the samples obtained at 0.60 V were cooled by natural heat dissipation (rapid cooling), and other half were cooled at  $20 \text{ K h}^{-1}$  (slow cooling) in the same molten salt (iii). The samples obtained at 0.90 V were cooled with the same slow cooling condition. Figure 3-12 shows the optical images of the Si particles recovered from the Zn electrodes. For the samples obtained at 0.60 V with rapid cooling, brown-color fine powders were mainly obtained, containing

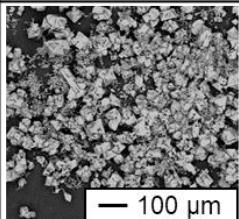
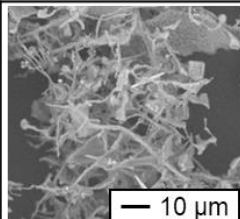
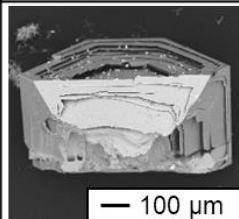
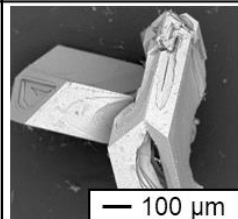
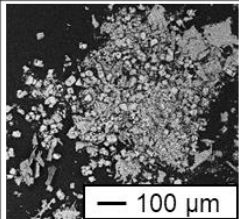
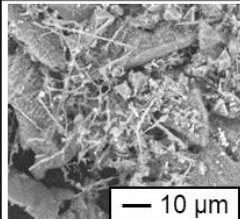
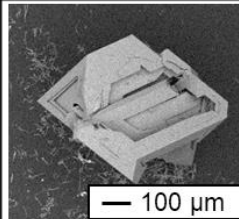
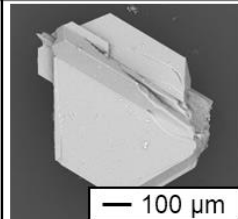
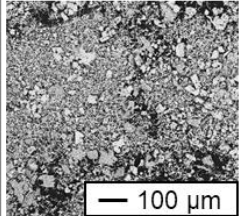
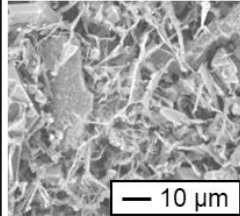
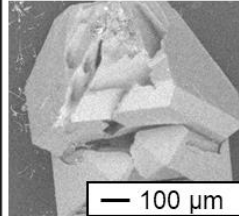


**Figure 3-12** Optical images of Si particles recovered from the Zn electrodes after the electrolysis conducted in molten  $\text{CaCl}_2$  with the addition of (i) 4.0 mol% of  $\text{CaSiO}_3$  ( $r_{\text{O}^{2-}/\text{SiO}_2} = 1.0$ ), (ii) 2.0 mol% of  $\text{CaO}$  and 4.0 mol% of  $\text{CaSiO}_3$  ( $r_{\text{O}^{2-}/\text{SiO}_2} = 1.5$ ), and (iii) 4.0 mol% of  $\text{CaO}$  and 4.0 mol% of  $\text{CaSiO}_3$  ( $r_{\text{O}^{2-}/\text{SiO}_2} = 2.0$ ) at 1123 K. Charge:  $-590.3 \text{ C}$  (theoretical formation of 1.0 mol% Si–Zn alloy).



some small Si granules with a metallic luster. In contrast, for the samples obtained after the slow cooling, larger granules with a metallic luster were mainly precipitated, suggesting the crystal growth at the slow cooling step. SEM images of the samples are shown in Figure 3-13. For the samples obtained at 0.60 V with rapid cooling, the brown-color fine powders were found to be the aggregates of entangled wires with a diameter of 0.5–2  $\mu\text{m}$ . The small Si granules with metallic luster were found to be angular crystals with a size of 10–20  $\mu\text{m}$ . After the slow cooling, the granule size increased to approximately 700  $\mu\text{m}$ . Since all Si particles were precipitated from Zn electrodes with the same cooling condition, no significant difference in particle size or crystal shape was observed in all samples. From EDX analysis, only Si was detected in the granules and wires.

Table 3-4 lists the weight of the recovered Si and the current efficiency calculated from

|  | 0.60 V<br>(rapid cooling)   |   | 0.60 V<br>(slow cooling)   | 0.90 V<br>(slow cooling)  |
|--|---|---|--|---|
| molten salt (i):<br>$r_{\text{O}^{2-}/\text{SiO}_2} = 1.0$   |  |  |  |  |
| molten salt (ii):<br>$r_{\text{O}^{2-}/\text{SiO}_2} = 1.5$  |  |  |  |  |
| molten salt (iii):<br>$r_{\text{O}^{2-}/\text{SiO}_2} = 2.0$ |  |  |  |   |

**Figure 3-13** SEM images of Si particles recovered from the Zn electrodes after the electrolysis conducted in molten  $\text{CaCl}_2$  with the addition of (i) 4.0 mol% of  $\text{CaSiO}_3$  ( $r_{\text{O}^{2-}/\text{SiO}_2} = 1.0$ ), (ii) 2.0 mol% of  $\text{CaO}$  and 4.0 mol% of  $\text{CaSiO}_3$  ( $r_{\text{O}^{2-}/\text{SiO}_2} = 1.5$ ), and (iii) 4.0 mol% of  $\text{CaO}$  and 4.0 mol% of  $\text{CaSiO}_3$  ( $r_{\text{O}^{2-}/\text{SiO}_2} = 2.0$ ) at 1123 K. Charge:  $-590.3$  C (theoretical formation of 1.0 mol% Si–Zn alloy).



**Table 3-4 Weight of the recovered Si, current efficiency, and Ca concentration in the Zn electrodes after the electrolysis conducted in molten CaCl<sub>2</sub> with the addition of (i) 4.0 mol% of CaSiO<sub>3</sub> ( $r_{O^{2-}/SiO_2} = 1.0$ ), (ii) 2.0 mol% of CaO and 4.0 mol% of CaSiO<sub>3</sub> ( $r_{O^{2-}/SiO_2} = 1.5$ ), and (iii) 4.0 mol% of CaO and 4.0 mol% of CaSiO<sub>3</sub> ( $r_{O^{2-}/SiO_2} = 2.0$ ) at 1123 K. Charge: -590.3 C (theoretical formation of 1.0 mol% Si-Zn alloy).**

| Ratio of O <sup>2-</sup> /SiO <sub>2</sub><br>in molten salt<br>( $r_{O^{2-}/SiO_2}$ ) | Weight of recovered Si, $w_{act.}$ / g<br>(Current efficiency, $\eta$ / %) |                     |                     | Ca concentration in the liquid Zn<br>electrodes, $x_{Ca}$ / ppmw |                     |                     |
|--|--|---------------------|---------------------|--|---------------------|---------------------|
|  | 0.60 V <sup>a</sup>  | 0.60 V <sup>b</sup> | 0.90 V <sup>b</sup> | 0.60 V <sup>a</sup>  | 0.60 V <sup>b</sup> | 0.90 V <sup>b</sup> |
| (i) 1.0  | 0.0246<br>(57.2)   | 0.0352<br>(81.9)    | 0.0346<br>(80.5)    | 4233   | 210                 | 92                  |
| (ii) 1.5   | 0.0232<br>(54.0)   | 0.0334<br>(77.7)    | 0.0342<br>(79.6)    | 4709   | 217                 | 81                  |
| (iii) 2.0  | 0.0248<br>(57.7)   | 0.0340<br>(79.1)    | –                   | 4187   | 315                 | –                   |

<sup>a</sup> Cooled by natural heat dissipation (rapid cooling).

<sup>b</sup> Cooled at a rate of 20 K h<sup>-1</sup> (slow cooling).

the Si weight. The current efficiency was calculated by the following equations:

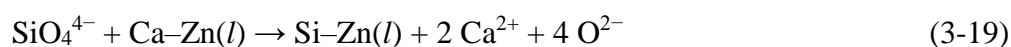
$$\eta = \frac{w_{act.}}{w_{theo.}} \times 100 \quad (3-17)$$

$$w_{theo.} = \frac{Q}{4F} \times M_{Si} \quad (3-18)$$

where  $w_{act.}$  is the actual weight of the recovered Si,  $w_{theo.}$  is the theoretical weight of Si produced according to Faraday's law,  $Q$  is the quantity of electric charge during electrolysis,  $F$  is Faraday's constant (96485 C mol<sup>-1</sup>), and  $M_{Si}$  is the molar weight of Si (28.1 g mol<sup>-1</sup>). Ca concentration in the liquid Zn electrodes is also listed in Table 3-4. The Ca concentration was calibrated by subtracting the Ca concentrations in raw Zn and HCl solution.

For samples obtained at 0.90 V, at which only direct electrochemical reduction of silicate ions is considered to proceed, the current efficiency was approximately 80% and near 100 ppmw

of Ca was detected. Residual silicate salt is considered as the reason for this increase of the Ca concentration because acid could not be used during the salt removal. The samples obtained at 0.60 V with rapid cooling showed current efficiencies of just under 60%. In these samples, more than 4000 ppmw of Ca was detected, suggesting the formation of Ca–Zn alloys. On the other hand, for the samples obtained at 0.60 V with slow cooling, the current efficiency increased to approximately 80% and the residual Ca concentrations were 200–300 ppmw, suggesting the indirect reduction of silicate ions by Ca–Zn alloy.



Similar reaction for solid  $\text{SiO}_2$ , i.e., indirect reduction by Ca–Zn alloy, has been confirmed at 0.60 V in molten  $\text{CaCl}_2$  at 1123 K, which was described in Chapter 2.

To confirm the indirect reduction mentioned above, two samples of Ca–Zn alloy were prepared at 0.60 V in molten  $\text{CaCl}_2$ . Figure 3-14(a) shows the current transient curve during the electrolysis when one of them was prepared. One Ca–Zn alloy sample was then analyzed by ICP-AES; the concentration of Ca was detected to be 5570 ppmw. The current efficiency for the formation of Ca–Zn alloy was calculated to be 87.3%. The other sample was placed in the molten

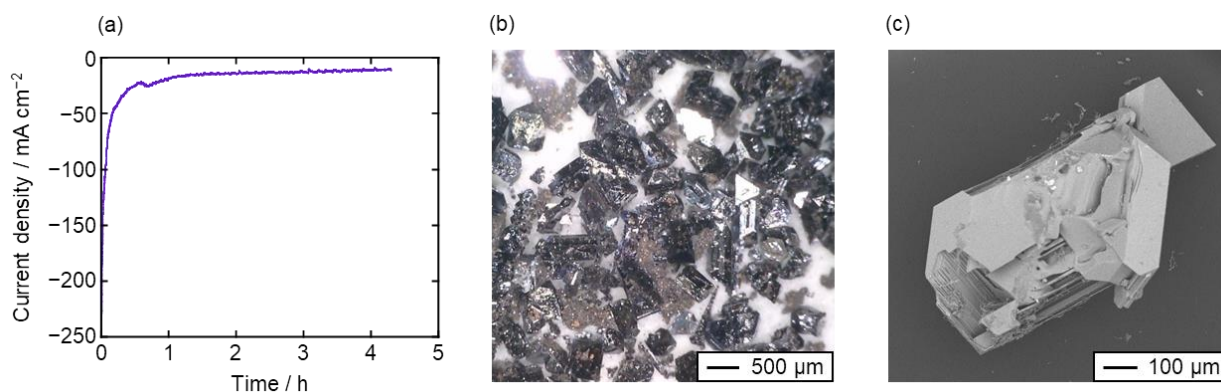


**Figure 3-14** (a) Current transient curve during the electrolysis in molten  $\text{CaCl}_2$ , (b) optical image and (c) surface SEM image of the Si particles recovered from the Zn electrode after the slow cooling in molten  $\text{CaCl}_2$  with the addition of 4.0 mol% of  $\text{CaO}$  and 4.0 mol% of  $\text{CaSiO}_3$  ( $r_{\text{O}^{2-}/\text{SiO}_2} = 2.0$ ). Charge:  $-590.3 \text{ C}$  (theoretical formation of 2.0 mol% Ca–Zn alloy).

salt (iii) and cooled with same slow cooling condition as described above. After the slow cooling, Si particles were recovered from the Zn electrode, indicating that the indirect reduction by Ca–Zn alloy proceeded during the slow cooling. Figure 3-14(b) and (c) show an optical image and a SEM image of the recovered Si particles, respectively. Similar with the samples obtained by electrolysis with slow cooling, the Si granules show metallic luster with a size of approximately 700  $\mu\text{m}$ . The concentration of Ca in the Zn electrode decreased to 259 ppmw, suggesting that almost all of the Ca was used for the indirect reduction of silicate ions. The current efficiency calculated from the weight of recovered Si was 76.1%. Both the residual Ca concentration and the current efficiency were similar with those for the samples obtained by electrolysis.

To summarize the results obtained at the liquid Zn electrode, in the term of available potential range for production of Si–Zn alloy, molten salt (i) with dominant  $\text{SiO}_3^{2-}$  is suitable, which is corresponded to the results obtained at the graphite electrode. In the potentiostatic electrolysis, the current densities were also largest in molten salt (i). On the other hand, current efficiency calculated from the weight of recovered Si did not show significant difference in all molten salts. Also, the formation of Ca–Zn alloy did not lead to a low current efficiency because of the indirect reduction of silicate ions by Ca–Zn alloy during the slow cooling period. Therefore, molten salt (i), which gives the largest current densities, is considered to be suitable for the production of Si–Zn alloy.

### 3.4 Conclusion

The ionic species and the electrochemical reduction of silicate ions at solid graphite and liquid Zn electrodes were investigated in molten  $\text{CaCl}_2$  at 1123 K. The ionic species of silicates in molten salts with  $r_{\text{O}^{2-}/\text{SiO}_2} = 1.0, 1.5, \text{ and } 2.0$  was investigated by Raman spectroscopy. The dominant silicate ion was found to be  $\text{SiO}_3^{2-}$  in molten salt (i) with  $r_{\text{O}^{2-}/\text{SiO}_2} = 1.0$ , and  $\text{SiO}_4^{4-}$  in molten salt (iii) with  $r_{\text{O}^{2-}/\text{SiO}_2} = 2.0$ , which is consistent with the  $r_{\text{O}^{2-}/\text{SiO}_2}$  value. Due to the poor stability of  $\text{Si}_2\text{O}_7^{6-}$ , the primary dominant species was detected as  $\text{SiO}_4^{4-}$  and secondary dominant

species as  $\text{Si}_2\text{O}_7^{6-}$  in molten salt (ii) with  $r_{\text{O}^{2-}/\text{SiO}_2} = 1.5$ .

Considering the results of cyclic voltammetry and potentiostatic electrolysis obtained at the graphite electrode, molten salt (i) with dominant  $\text{SiO}_3^{2-}$  is considered to be suitable for producing Si–Zn alloy, because its available potential range was widest, and apart from the formation of liquid Ca–Zn alloy which possibly leads to a low current efficiency.

For the cyclic voltammetry conducted at the liquid Zn electrode, the electrochemical reduction of silicate ions started from a more positive potential compared with that at the solid graphite electrode, which suggested the formation of liquid Si–Zn alloy with Si activity lower than unity with respect to pure solid Si. Also, molten salt (i) with dominant  $\text{SiO}_3^{2-}$  is considered to be suitable for the production of Si–Zn alloy in the term of available potential range, which is consistent to the results obtained at the graphite electrode. For the electrolysis conducted at 0.60 V, although the formation of Ca–Zn alloy proceeded, the current efficiency of approximately 80% was achieved because of the indirect reduction of silicate ions by Ca–Zn alloy during the slow cooling period.

### 3.5 Reference List

- [1] S. Wang, F. Zhang, X. Liu and L. Zhang, *Thermochimica Acta*, **470**, 105 (2008).
- [2] D. Virgo, B. O. Mysen and I. Kushiro, *Science*, **208**, 1371 (1980).
- [3] B. O. Mysen, D. Virgo and C. M. Scarfe, *Am. Mineral.*, **65**, 690 (1980).
- [4] B. O. Mysen, *Structure and Properties of Silicate Melts*, Elsevier (1988).
- [5] C. Wang, J. Zhang, Z. Liu, K. Jiao, G. Wang, J. Yang and K. Chou, *Metall. Mater. Trans. B*, **48**, 328 (2017).
- [6] P. Manfrinetti, M. L. Fornasini and A. Palenzona, *Intermetallics*, **8**, 223 (2000).
- [7] K. Yasuda, T. Nohira, R. Hagiwara and Y. H. Ogata, *J. Electrochem. Soc.*, **154**, E95 (2007).
- [8] L. B. Pankratz, *Thermodynamic Properties of Carbides, Nitrides, and Other Selected Substances*, U. S. Bureau of Mines (USBM) (1994).

- [9] M. W. Chase, *NIST-JANAF Thermochemical Tables, 4th ed., Part I Al-Co*, American Chemical Society, and the American Institute of Physics for the National Institute of Standards and Technology (1998).
- [10] R. Winand, *Electrochim. Acta*, **39**, 1091 (1994).

## Chapter 4

# Raman Analysis and Electrochemical Reduction of Silicate Ions in Molten NaCl–CaCl<sub>2</sub>

### 4.1 Introduction

In the previous chapters, the electrochemical reduction of SiO<sub>2</sub> was investigated in molten CaCl<sub>2</sub>. As described in Chapter 1, while CaCl<sub>2</sub> exhibits a high solubility of O<sup>2-</sup>, its high melting point renders it unsuitable for the use in the precipitation process. Therefore, the author selected the eutectic NaCl–CaCl<sub>2</sub> with a low melting point. The use of NaCl–CaCl<sub>2</sub> molten salt in the electrolysis step is expected to simplify the process (Figure 1-9) because the same salt can be used in the precipitation step.

In this chapter, the electrochemical reduction of silicate ions was investigated in molten eutectic NaCl–CaCl<sub>2</sub>. Before the electrochemical measurements, the ionic species of silicates in molten eutectic NaCl–CaCl<sub>2</sub> with various ratios of O<sup>2-</sup>/SiO<sub>2</sub> ( $r_{\text{O}^{2-}/\text{SiO}_2}$ ) was investigated by Raman spectroscopy. CaO was used as the source of O<sup>2-</sup> ion. Since the concentrations of CaO used in this study were lower than its solubility (7.6 mol% at 1023 K, and 8.1 mol% at 1123 K) [1], it is considered to be completely dissociated into Ca<sup>2+</sup> and O<sup>2-</sup>. Then, the electrochemical reduction of silicate ions was investigated at a solid graphite electrode as the pre-study for the liquid Zn electrode. The surface of electrodeposited Si was observed by SEM and analyzed by XRD.

### 4.2 Experimental

All the experiments were conducted in a dry Ar atmosphere at 1023 K and 1123 K. The

salt preparation, experimental apparatus and analysis methods are almost the same as those given in Chapter 3. Important and/or different points are described as follows.

#### 4.2.1 Raman Spectroscopy of Silicate Ions

NaCl and CaCl<sub>2</sub> powders (FUJIFILM Wako Pure Chemical Corp., reagent grade) were mixed in a eutectic composition (NaCl:CaCl<sub>2</sub> = 47.9:52.1 mol%). Pre-determined amounts of CaO (0, 0.5, and 1.0 mol%), SiO<sub>2</sub> (0 and 1.0 mol%), and CaSiO<sub>3</sub> (1.0 mol%) powders were added to the eutectic mixture before the melting. Raman spectroscopy was conducted at 1023 K.

#### 4.2.2 Electrochemical Window of Molten Eutectic NaCl–CaCl<sub>2</sub>

NaCl and CaCl<sub>2</sub> powders were mixed in the eutectic composition and loaded into a graphite crucible. After the mixture was heated to 1023 K or 1123 K, all electrochemical measurements were conducted by a three-electrode method. A Mo wire electrode was used as the working electrode and a glass-like carbon electrode as the counter electrode in the negative potential region. In the positive potential region, the glass-like carbon electrode was used as the working electrode and the Mo wire electrode as the counter electrode. A Si square bar was used as the quasi-reference electrode in both potential regions. The potentials of the quasi-reference and reference electrodes were calibrated with respect to a dynamic Na<sup>+</sup>/Na potential, determined by cyclic voltammetry on a Mo wire electrode.

#### 4.2.3 Electrochemical Reduction of Silicate Ions

After the investigation of electrochemical window, pre-determined amounts of CaO (0, 0.5 or 1.0 mol%) and CaSiO<sub>3</sub> (1.0 mol%) powders were added to the eutectic mixture. All electrochemical measurements were conducted by a three-electrode method. As the working electrodes, flag-shaped graphite plates with different size were used for cyclic voltammetry and potentiostatic electrolysis. A Si square bar was used as the quasi-reference and reference electrodes.

The potentials of the quasi-reference and reference electrodes were calibrated with respect to a dynamic  $\text{Na}^+/\text{Na}$  potential, determined by cyclic voltammetry on a Mo wire electrode. The counter electrodes were the same as those described in Chapter 3.

## 4.3 Results and Discussion

### 4.3.1 Ionic Species of Silicates

Figure 4-1 shows the original and deconvoluted Raman spectra for molten eutectic  $\text{NaCl}$ – $\text{CaCl}_2$  containing different amounts of  $\text{CaO}$  and  $\text{SiO}_2$  at 1023 K. The original spectra are shown with background subtracted. Within the wavenumber range of  $700$ – $1100\text{ cm}^{-1}$ , no band was

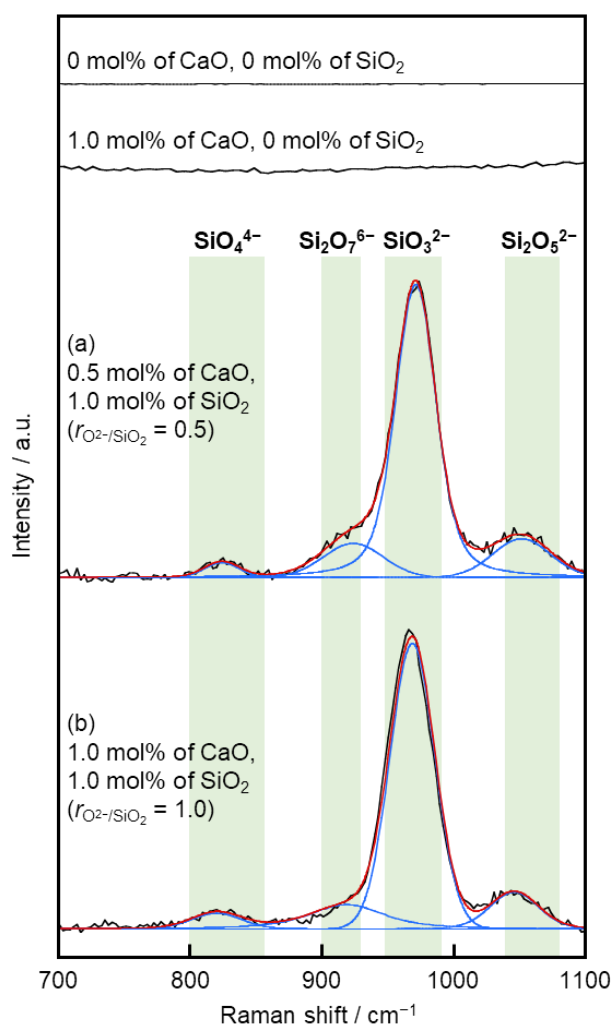


**Figure 4-1** Original and deconvoluted Raman spectra for molten eutectic  $\text{NaCl}$ – $\text{CaCl}_2$  containing different amounts of  $\text{CaO}$  and  $\text{SiO}_2$  at 1023 K.



observed for the molten salts without SiO<sub>2</sub>. For (a) molten NaCl–CaCl<sub>2</sub> containing 0.5 mol% CaO and 1.0 mol% SiO<sub>2</sub> ( $r_{\text{O}^{2-}/\text{SiO}_2} = 0.5$ ), and (b) molten NaCl–CaCl<sub>2</sub> containing 1.0 mol% CaO and 1.0 mol% SiO<sub>2</sub> ( $r_{\text{O}^{2-}/\text{SiO}_2} = 1.0$ ), strong bands were detected near 970 cm<sup>-1</sup> and several weak bands at about 820, 920, and 1050 cm<sup>-1</sup>. The spectra were deconvolved using the Voigtian function. For the molten salt with  $r_{\text{O}^{2-}/\text{SiO}_2} = 0.5$ , according to previous studies [2–4], the bands at 920, 972, and 1053 cm<sup>-1</sup> were assigned to Si<sub>2</sub>O<sub>7</sub><sup>6-</sup>, SiO<sub>3</sub><sup>2-</sup> and Si<sub>2</sub>O<sub>5</sub><sup>2-</sup>, respectively. The band at 825 cm<sup>-1</sup> was attributed to SiO<sub>4</sub><sup>4-</sup> vibration. As described in Chapter 3, the wavenumber for SiO<sub>4</sub><sup>4-</sup> lower than the reported value is considered to be due to the partial substitution of oxygen ions to chlorine ions according to the following reaction [5].



Similar fitting results were obtained for the molten salt with  $r_{\text{O}^{2-}/\text{SiO}_2} = 1.0$ ; there was a strong band at 968 cm<sup>-1</sup> for SiO<sub>3</sub><sup>2-</sup>, and three weak bands at 822, 920, and 1050 cm<sup>-1</sup> attributed to SiO<sub>4</sub><sup>4-</sup>, Si<sub>2</sub>O<sub>7</sub><sup>6-</sup>, and Si<sub>2</sub>O<sub>5</sub><sup>2-</sup>, respectively. Since the dominant silicate ion was SiO<sub>3</sub><sup>2-</sup> in the molten salts with  $r_{\text{O}^{2-}/\text{SiO}_2} \leq 1.0$ , the dissolution limit of SiO<sub>2</sub> is likely to be determined by the O<sup>2-</sup> content. In addition, the weak bands of SiO<sub>4</sub><sup>4-</sup>, Si<sub>2</sub>O<sub>7</sub><sup>6-</sup>, and Si<sub>2</sub>O<sub>5</sub><sup>2-</sup> were observed because of the equilibrium reactions of SiO<sub>3</sub><sup>2-</sup> and Si<sub>2</sub>O<sub>7</sub><sup>6-</sup>.



As mentioned above, the ionic species of SiO<sub>2</sub> in molten salts with  $r_{\text{O}^{2-}/\text{SiO}_2} \leq 1.0$  was mainly attributed to SiO<sub>3</sub><sup>2-</sup>. To further investigate the stable silicate ions in the melts with various  $r_{\text{O}^{2-}/\text{SiO}_2}$  values ( $\geq 1.0$ ), CaSiO<sub>3</sub> was used as the SiO<sub>2</sub> source. As described in Chapter 3, the dissolution rate of CaSiO<sub>3</sub> is significantly higher than that of SiO<sub>2</sub>, which enables the fast preparation of the melts with target compositions. By changing the concentration of CaO, molten salts with  $r_{\text{O}^{2-}/\text{SiO}_2} = 1.0, 1.5, \text{ and } 2.0$  were prepared and analyzed by Raman spectroscopy. Figure 4-2 shows the original and deconvolved Raman spectra of the molten salts. The spectrum in

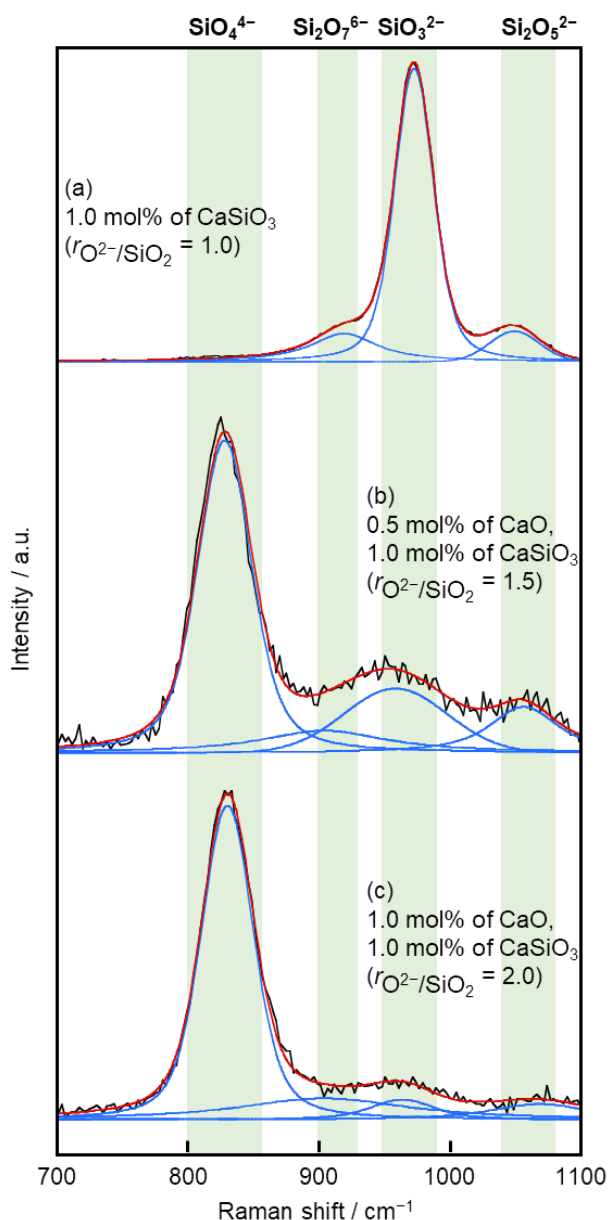


**Figure 4-2** Original and deconvoluted Raman spectra for molten NaCl–CaCl<sub>2</sub> containing (a) 1.0 mol% of CaSiO<sub>3</sub> ( $r_{\text{O}^{2-}/\text{SiO}_2} = 1.0$ ), (b) 0.5 mol% of CaO and 1.0 mol% of CaSiO<sub>3</sub> ( $r_{\text{O}^{2-}/\text{SiO}_2} = 1.5$ ), and (c) 1.0 mol% of CaO and 1.0 mol% of CaSiO<sub>3</sub> ( $r_{\text{O}^{2-}/\text{SiO}_2} = 2.0$ ) at 1023 K.

Figure 4-2(a) was deconvoluted to 3 bands at 920 for Si<sub>2</sub>O<sub>7</sub><sup>6-</sup>, 972 cm<sup>-1</sup> for SiO<sub>3</sub><sup>2-</sup>, and 1050 cm<sup>-1</sup> for Si<sub>2</sub>O<sub>5</sub><sup>2-</sup>. For the deconvolution in Figure 4-2(b), the band near 830 cm<sup>-1</sup> was added and the spectrum was deconvoluted to 4 bands. Although the band for Si<sub>2</sub>O<sub>7</sub><sup>6-</sup> was weak, the coefficient of determination,  $R^2$ , for 4 bands was 0.9909, which was higher than that for 3 bands without Si<sub>2</sub>O<sub>7</sub><sup>6-</sup> band ( $R^2 = 0.9842$ ). Therefore, Figure 4-2(b) and (c) were deconvoluted to 4 bands. The deconvolution results of the Raman spectra are presented in Table 4-1.

**Table 4-1** Deconvolved wavenumbers of Raman spectra for samples obtained in molten NaCl–CaCl<sub>2</sub> with the addition of (i) 1.0 mol% of CaSiO<sub>3</sub> ( $r_{\text{O}^{2-}/\text{SiO}_2} = 1.0$ ), (ii) 0.5 mol% of CaO and 1.0 mol% of CaSiO<sub>3</sub> ( $r_{\text{O}^{2-}/\text{SiO}_2} = 1.5$ ), and (iii) 1.0 mol% of CaO and 1.0 mol% of CaSiO<sub>3</sub> ( $r_{\text{O}^{2-}/\text{SiO}_2} = 2.0$ ) at 1023 K.

| Ratio of O <sup>2-</sup> /SiO <sub>2</sub><br>in molten salt<br>( $r_{\text{O}^{2-}/\text{SiO}_2}$ ) | Wavenumber / cm <sup>-1</sup><br>(Band intensity fraction † / %) |  |                                |  |
|--|--|--|--------------------------------|--|
|  | SiO <sub>4</sub> <sup>4-</sup>                                   | Si <sub>2</sub> O <sub>7</sub> <sup>6-</sup> | SiO <sub>3</sub> <sup>2-</sup> | Si <sub>2</sub> O <sub>5</sub> <sup>2-</sup> |
| (i) 1.0  | –  | 920w<br>(15.6)                               | 974s<br>(75.9)                 | 1050vw<br>(8.6)                              |
| (ii) 1.5   | 829s<br>(57.0)   | 905w<br>(11.9)                               | 960w<br>(18.7)                 | 1058w<br>(12.5)                              |
| (iii) 2.0  | 831s<br>(67.9)   | 905w<br>(18.7)                               | 965vw<br>(5.8)                 | 1070vw<br>(7.6)                              |

Abbreviations: vw, very weak; w, weak; s, strong.

† Calculated from fitted band area.

As the result, for the molten salt with  $r_{\text{O}^{2-}/\text{SiO}_2} = 1.0$ , the dominant silicate ion was SiO<sub>3</sub><sup>2-</sup>, which is consistent with the molten salt with the same  $r_{\text{O}^{2-}/\text{SiO}_2}$  prepared from CaO and SiO<sub>2</sub>. When  $r_{\text{O}^{2-}/\text{SiO}_2}$  increased to 1.5, the dominant silicate species was SiO<sub>4</sub><sup>4-</sup>, secondary dominant SiO<sub>3</sub><sup>2-</sup>, and minor Si<sub>2</sub>O<sub>7</sub><sup>6-</sup> and Si<sub>2</sub>O<sub>5</sub><sup>2-</sup>. Although the ratio of O<sup>2-</sup>/SiO<sub>2</sub> = 1.5 corresponds to Si<sub>2</sub>O<sub>7</sub><sup>6-</sup> ion, the equilibrium reaction of Si<sub>2</sub>O<sub>7</sub><sup>6-</sup> (reaction (4-3)) would occur because of its poor stability in the molten salt. With respect to the molten salt with  $r_{\text{O}^{2-}/\text{SiO}_2} = 2.0$ , SiO<sub>4</sub><sup>4-</sup> was the dominant silicate ion which is consistent with the composition calculated from the O<sup>2-</sup>/SiO<sub>2</sub> ratio.

### 4.3.2 Electrochemical Window of Molten Eutectic NaCl–CaCl<sub>2</sub>

The electrochemical window of molten eutectic NaCl–CaCl<sub>2</sub> was investigated by cyclic voltammetry at 1023 K and 1123 K. A Mo wire electrode was used as the working electrode in the negative potential region, because it does not form any alloy with Na or Ca at the experiment temperature [6]. In the positive potential region, a glass-like carbon rod was used as the working

electrode. Figure 4-3(a) shows the voltammograms obtained at 1023 K. In the negative potential region, a sharp increase in cathodic current and the corresponding anodic peak were observed at 0 V (vs. Na<sup>+</sup>/Na), which are attributed to Na deposition and dissolution.



Since Na metal is considered to dissolve into molten salt, the cathodic current observed at more negative than 0.2 V is likely due to the formation of Na metal with the activity smaller than unity. In the positive potential region, anodic current rapidly increased from about 3.3 V, which is due to the evolution of Cl<sub>2</sub> gas.

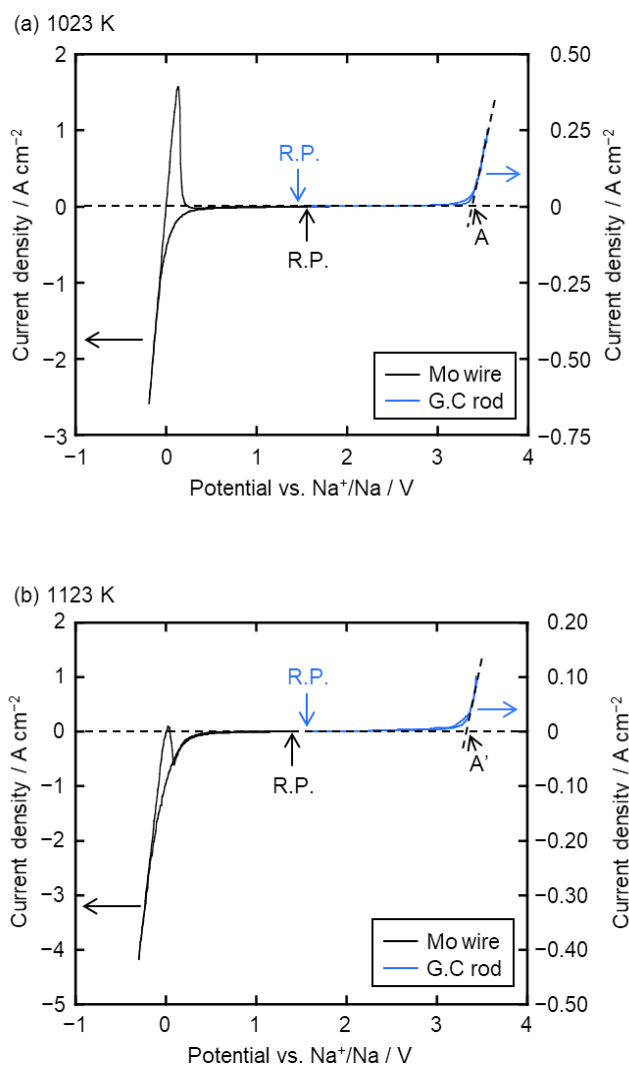


**Figure 4-3** Cyclic voltammograms at a Mo electrode and a glass-like carbon electrode in molten NaCl–CaCl<sub>2</sub> at (a) 1023 K and (b) 1123 K. Scan rate: 100 mV s<sup>-1</sup>. R. P.: Rest potential.



The potential of the anodic limit was 3.37 V, which was defined as the potential where the linear region of the anode current is extrapolated to zero current. This value was close to the theoretical decomposition voltage of NaCl in eutectic NaCl–CaCl<sub>2</sub> mixture, 3.33 V, that was calculated from the standard Gibbs energy of formation of NaCl (–315.4 kJ mol<sup>–1</sup> [7]) assuming the activity of NaCl to be 0.479.

The voltammograms obtained at 1123 K are shown in [Figure 4-3\(b\)](#). Similar to the voltammograms obtained at 1023 K, the sharp increase in cathodic current in the negative potential region and anodic current in the positive potential region were attributed to the deposition of Na metal ([reaction \(4-4\)](#)) and evolution of Cl<sub>2</sub> gas ([reaction \(4-5\)](#)), respectively. On the other hand, the anodic current for the dissolution of Na metal was smaller than that at 1023 K, which is considered to be due to the faster diffusion of Na metal into the molten salt at the higher temperature. The potential of the anodic limit was determined as 3.30 V at 1123 K, which was close to the theoretical decomposition voltage, 3.27 V, that was calculated from the standard Gibbs energy of NaCl (–309.3 kJ mol<sup>–1</sup> [7]).

### 4.3.3 Electrochemical Reduction of Silicate Ions

#### 4.3.3.1 Cyclic Voltammetry at 1023 K

[Figure 4-4](#) shows the cyclic voltammograms at a graphite electrode in molten NaCl–CaCl<sub>2</sub> containing different amounts of CaO and CaSiO<sub>3</sub> at 1023 K. The black curves show the voltammograms before the addition of CaSiO<sub>3</sub> and CaO (blank). The small cathodic current observed around 0.5 V (vs. Na<sup>+</sup>/Na) is likely due to the intercalation of Ca<sup>2+</sup> into graphite.

After the addition of 1.0 mol% CaSiO<sub>3</sub> ( $r_{\text{O}^{2-}/\text{SiO}_2} = 1.0$ ), as shown in [Figure 4-4\(a\)](#), cathodic currents increased from 1.0 V, suggesting the electrochemical reduction of dominant SiO<sub>3</sub><sup>2–</sup> that observed in the Raman spectrum ([Figure 4-2\(a\)](#)). A larger cathodic current peak at around 0.50 V

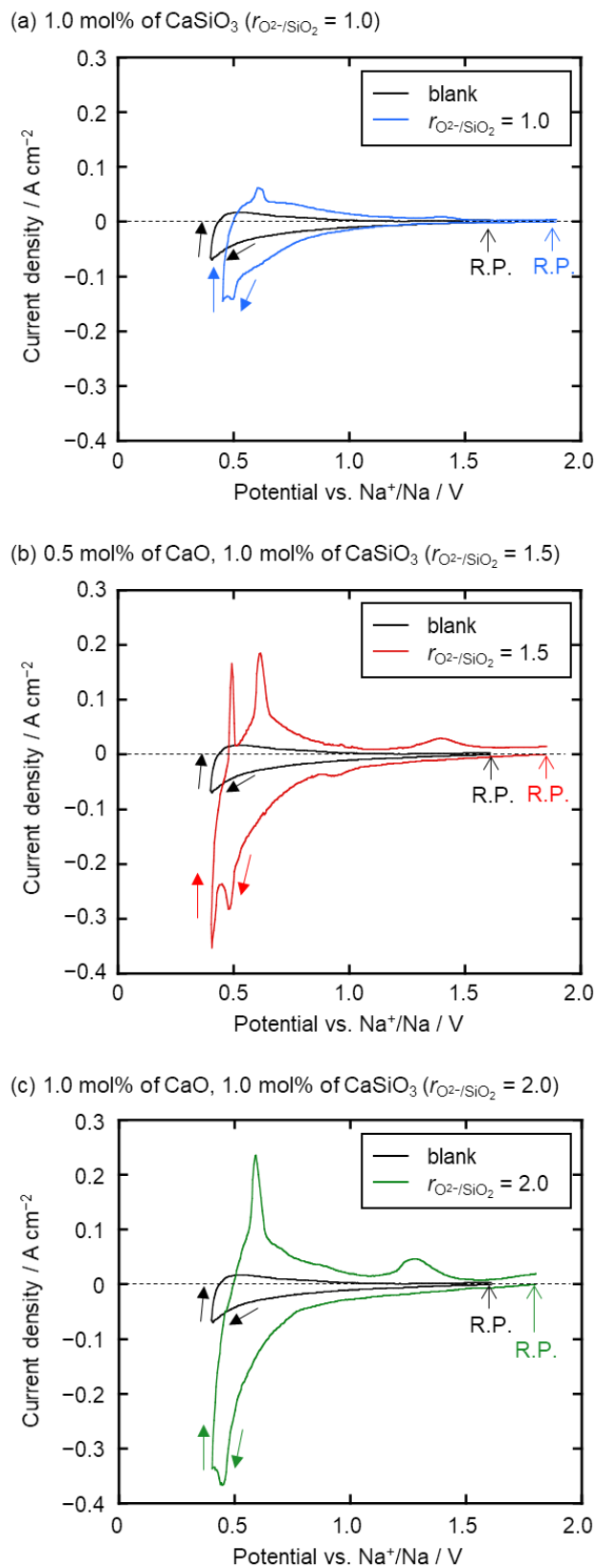


**Figure 4-4** Cyclic voltammograms at a graphite electrode in molten  $\text{NaCl-CaCl}_2$  before and after the addition of (a) 1.0 mol% of  $\text{CaSiO}_3$  ( $r_{\text{O}^{2-}/\text{SiO}_2} = 1.0$ ), (b) 0.5 mol% of  $\text{CaO}$  and 1.0 mol% of  $\text{CaSiO}_3$  ( $r_{\text{O}^{2-}/\text{SiO}_2} = 1.5$ ), and (c) 1.0 mol% of  $\text{CaO}$  and 1.0 mol% of  $\text{CaSiO}_3$  ( $r_{\text{O}^{2-}/\text{SiO}_2} = 2.0$ ) at 1023 K. Scan rate:  $50 \text{ mV s}^{-1}$ . R. P.: Rest potential.

is considered as the formation of Na–Si and/or Ca–Si alloys. [Figure 4-4\(b\)](#) shows the voltammogram measured after the addition of 0.50 mol% CaO and 1.0 mol% CaSiO<sub>3</sub> ( $r_{\text{O}^{2-}/\text{SiO}_2} = 1.5$ ). A small cathodic peak observed at 0.95 V is likely due to the electrochemical reduction of secondary dominant SiO<sub>3</sub><sup>2-</sup> that observed in the Raman spectrum ([Figure 4-2\(b\)](#)). Cathodic currents increased rapidly from 0.80 V, which seems to be due to the electrochemical reduction of dominant SiO<sub>4</sub><sup>4-</sup>. The larger currents compared to [Figure 4-4\(a\)](#) suggested that diffusion coefficient of SiO<sub>4</sub><sup>4-</sup> is larger than that of SiO<sub>3</sub><sup>2-</sup>. Since SiO<sub>4</sub><sup>4-</sup> ions are known to have weaker interaction each other than SiO<sub>3</sub><sup>2-</sup> ions [3], it is reasonable that the effective size of SiO<sub>4</sub><sup>4-</sup> is smaller than that of SiO<sub>3</sub><sup>2-</sup>. A cathodic current peak at around 0.50 V was regarded as the formation of Na–Si and/or Ca–Si alloys, which was similar to that observed in [Figure 4-4\(a\)](#).

A voltammogram of the melt containing 1.0 mol% CaO and 1.0 mol% CaSiO<sub>3</sub> ( $r_{\text{O}^{2-}/\text{SiO}_2} = 2.0$ ) is shown in [Figure 4-4\(c\)](#). A rapid increase of cathodic current from 0.75 V was likely attributed to the electrochemical reduction of dominant SiO<sub>4</sub><sup>4-</sup>. The current peak at around 0.50 V was ascribed to the same reaction of Na–Si and/or Ca–Si alloys formation, similar to the other two melts in [Figure 4-4\(a\)](#) and [\(b\)](#).

#### 4.3.3.2 Potentiostatic Electrolysis at 1023 K

Based on the voltammetry results, potentiostatic electrolysis was conducted at 0.50, 0.70, and 0.90 V with a constant charge density of  $-14 \text{ C cm}^{-2}$  in molten NaCl–CaCl<sub>2</sub> containing (i) 1.0 mol% CaSiO<sub>3</sub> ( $r_{\text{O}^{2-}/\text{SiO}_2} = 1.0$ ), (ii) 0.5 mol% CaO and 1.0 mol% CaSiO<sub>3</sub> ( $r_{\text{O}^{2-}/\text{SiO}_2} = 1.5$ ), and (iii) 1.0 mol% CaO and 1.0 mol% CaSiO<sub>3</sub> ( $r_{\text{O}^{2-}/\text{SiO}_2} = 2.0$ ). [Figure 4-5](#) shows the current transient curves during the electrolysis. The current densities increased in the order of molten salts (i), (ii), and (iii), which is consistent with the trend shown in cyclic voltammograms ([Figure 4-4](#)) that the diffusion coefficient of SiO<sub>4</sub><sup>4-</sup> is larger than that of SiO<sub>3</sub><sup>2-</sup>.

Optical images of an original graphite plate and the electrolyzed samples are shown in [Figure 4-6](#). Deposits in brown or dark brown color were observed at all samples except the sample

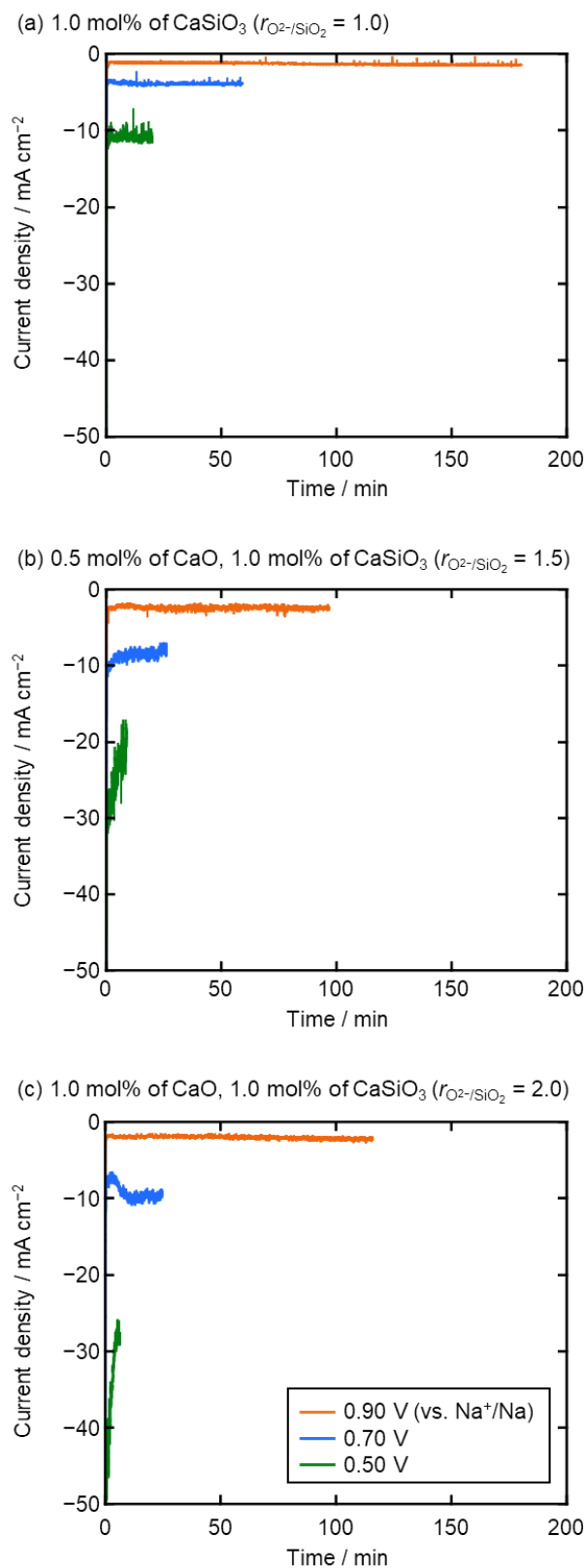


**Figure 4-5** Current transient curves during the potentiostatic electrolysis at graphite electrodes in molten  $\text{NaCl-CaCl}_2$  with the addition of (a) 1.0 mol% of  $\text{CaSiO}_3$  ( $r_{\text{O}^{2-}/\text{SiO}_2} = 1.0$ ), (b) 0.5 mol% of  $\text{CaO}$  and 1.0 mol% of  $\text{CaSiO}_3$  ( $r_{\text{O}^{2-}/\text{SiO}_2} = 1.5$ ), and (c) 1.0 mol% of  $\text{CaO}$  and 1.0 mol% of  $\text{CaSiO}_3$  ( $r_{\text{O}^{2-}/\text{SiO}_2} = 2.0$ ) at 1023 K. Charge density:  $-14 \text{ C cm}^{-2}$ .



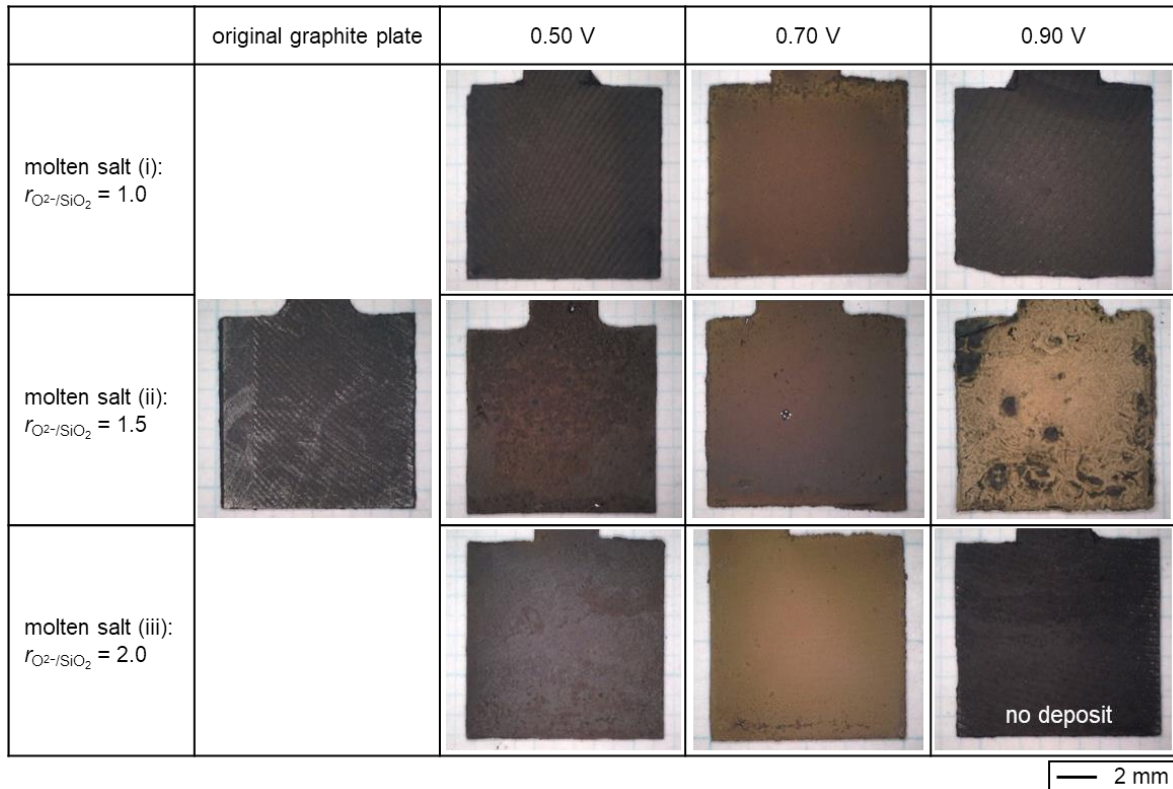


**Figure 4-6** Optical images of an original graphite plate and the samples obtained in molten NaCl–CaCl<sub>2</sub> with the addition of (i) 1.0 mol% of CaSiO<sub>3</sub> ( $r_{\text{O}^{2-}/\text{SiO}_2} = 1.0$ ), (ii) 0.5 mol% of CaO and 1.0 mol% of CaSiO<sub>3</sub> ( $r_{\text{O}^{2-}/\text{SiO}_2} = 1.5$ ), and (iii) 1.0 mol% of CaO and 1.0 mol% of CaSiO<sub>3</sub> ( $r_{\text{O}^{2-}/\text{SiO}_2} = 2.0$ ) at 1023 K. Charge density:  $-14 \text{ C cm}^{-2}$ .

obtained at 0.90 V in molten salt (iii). No significant deposit was observed at this sample.

Figure 4-7 shows XRD patterns of the original graphite plate and the electrolyzed samples. In Figure 4-7(a), the existence of Si was confirmed in the samples obtained at 0.70 V and 0.90 V in molten salt (i). Thus, the increase in cathodic current from 1.0 V in Figure 4-4(a) was confirmed to be the electrochemical reduction of  $\text{SiO}_3^{2-}$  to solid Si.



The XRD pattern at 0.50 V indicated the existence of CaSi<sub>2</sub>, which was identified by the strongest peak at 45.3 degree (relative intensity 100), and the second-strongest one at 46.8 degree (relative intensity 42). Since CaSi<sub>2</sub> was identified at 0.50 V, the cathodic current peak at 0.50 V corresponded to the formation of CaSi<sub>2</sub>.

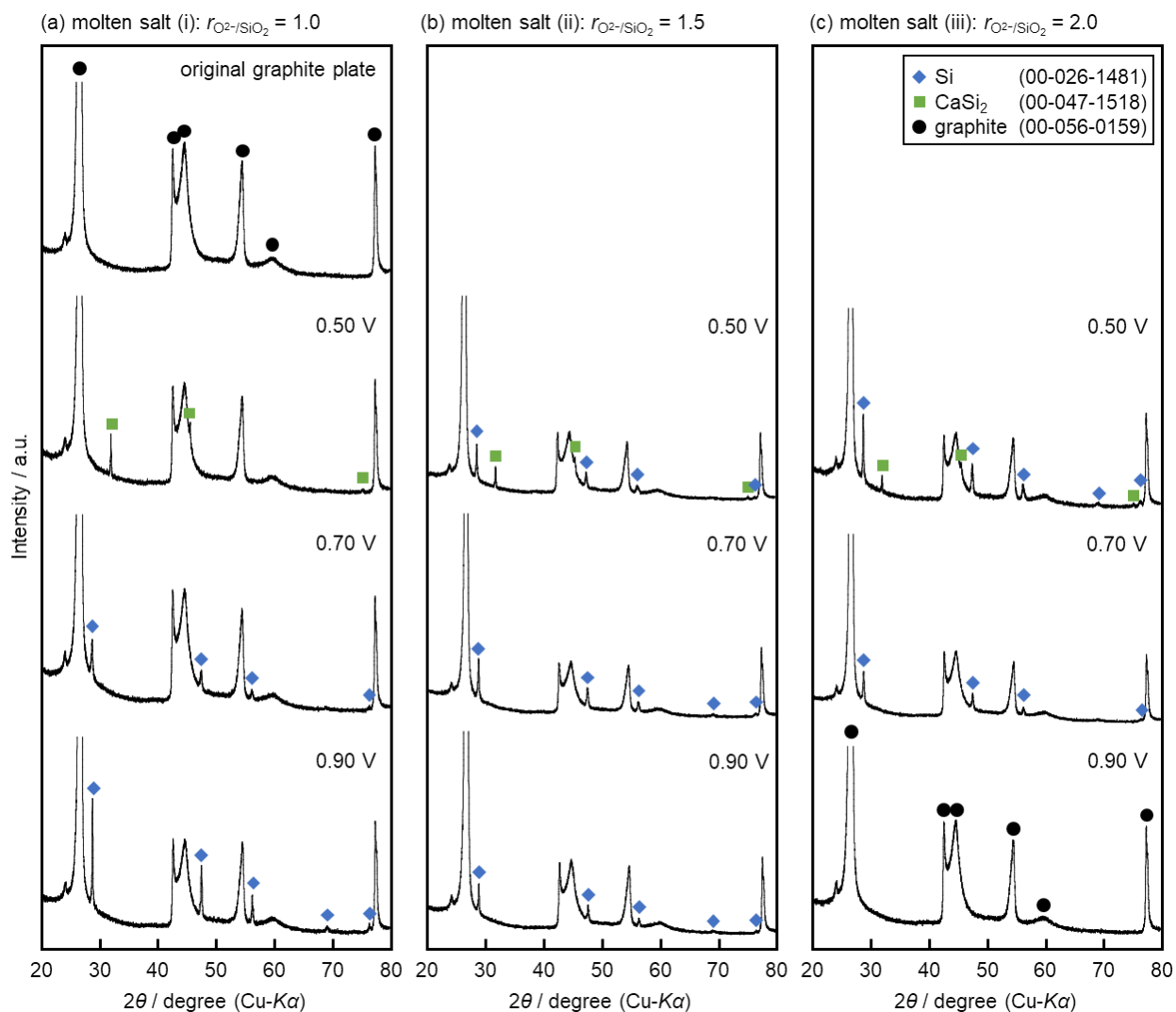
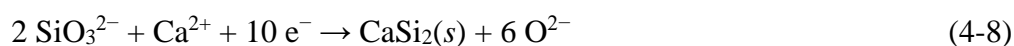


**Figure 4-7** XRD patterns of the original graphite plate and the samples obtained in molten NaCl–CaCl<sub>2</sub> with the addition of (a) 1.0 mol% of CaSiO<sub>3</sub> ( $r_{\text{O}^{2-}/\text{SiO}_2} = 1.0$ ), (b) 0.5 mol% of CaO and 1.0 mol% of CaSiO<sub>3</sub> ( $r_{\text{O}^{2-}/\text{SiO}_2} = 1.5$ ), and (c) 1.0 mol% of CaO and 1.0 mol% of CaSiO<sub>3</sub> ( $r_{\text{O}^{2-}/\text{SiO}_2} = 2.0$ ) at 1023 K. Charge density:  $-14 \text{ C cm}^{-2}$ .



In molten salt (ii), only Si deposits were confirmed for samples obtained at 0.70 V and 0.90 V. Since approximately 20% of  $\text{SiO}_3^{2-}$  was confirmed by Raman spectroscopy, as shown in Table 4-1, the small cathodic peak at 0.95 V is considered to be the electrochemical reduction of  $\text{SiO}_3^{2-}$  to solid Si (reaction (4-6)). The cathodic current increase from 0.80 V was attributed to the

electrochemical reduction of  $\text{SiO}_4^{4-}$ .



In order to confirm the results shown above, similar thermodynamic calculation as described in Chapter 3 was conducted from the data in literatures [8, 9]. The calculated data are shown in Table 4-2. Since the standard Gibbs energy for  $\text{CaSiO}_3(s)$  is smaller than that for  $\text{Ca}_2\text{SiO}_4(s)$ , the electrochemical reduction of  $\text{SiO}_3^{2-}$  would start from a more positive potential than  $\text{SiO}_4^{4-}$ . From the Nernst equation, the difference in the reduction potential of  $\text{CaSiO}_3(s)$  and  $\text{Ca}_2\text{SiO}_4(s)$  was calculated to be 0.26 V, which is consistent with the results of the voltammetry. Since the mixture of Si and  $\text{CaSi}_2$  was detected at 0.50 V, the cathodic current peak at 0.50 V was attributed to the formation of  $\text{CaSi}_2$  expressed in reactions (4-7) and (4-8).

For samples obtained in molten salt (iii), the existence of pure Si was confirmed at only 0.70 V and the mixture of Si and  $\text{CaSi}_2$  at 0.50 V. Since only graphite was detected at 0.90 V, the increase in cathodic current from 0.75 V would correspond to the electrochemical reduction of dominant  $\text{SiO}_4^{4-}$  to solid Si (reaction (4-9)), and the current peak at around 0.5 V was the formation of  $\text{CaSi}_2$  (reactions (4-7), (4-8)). The identified phases are summarized in Table 4-3.

Figure 4-8 shows the SEM images of the deposits. In molten salt (i), wire-like Si, particle Si and dense  $\text{CaSi}_2$  were obtained at 0.90, 0.70 and 0.50 V, respectively. In molten salt (ii), wire-like Si with different shapes were deposited at 0.70 V and 0.90 V, and particle Si was formed at 0.50 V. For samples obtained in molten salt (iii), wire-like Si was observed at 0.70 V and particle

**Table 4-2** Standard Gibbs energies for the decomposition reactions of  $\text{CaSiO}_3(s)$  and  $\text{Ca}_2\text{SiO}_4(s)$  to  $\text{Si}(s)$ ,  $\text{CaO}(l)$ , and  $\text{O}_2(g)$  at 1023 K.

| Reaction  | Standard Gibbs energy, $\Delta G_d^\circ / \text{kJ mol}^{-1}$ |
|---|--|
| $\text{CaSiO}_3(s) \rightarrow \text{Si}(s) + \text{CaO}(l) + \text{O}_2(g)$            | 869.4  |
| $\text{Ca}_2\text{SiO}_4(s) \rightarrow \text{Si}(s) + 2 \text{CaO}(l) + \text{O}_2(g)$ | 970.0  |

**Table 4-3** XRD results for the samples obtained in molten NaCl–CaCl<sub>2</sub> with the addition of (i) 1.0 mol% of CaSiO<sub>3</sub> ( $r_{O^{2-}/SiO_2} = 1.0$ ), (ii) 0.5 mol% of CaO and 1.0 mol% of CaSiO<sub>3</sub> ( $r_{O^{2-}/SiO_2} = 1.5$ ), and (iii) 1.0 mol% of CaO and 1.0 mol% of CaSiO<sub>3</sub> ( $r_{O^{2-}/SiO_2} = 2.0$ ) at 1023 K. Charge density:  $-14 \text{ C cm}^{-2}$ .

| Ratio of $O^{2-}/SiO_2$<br>in molten salt<br>( $r_{O^{2-}/SiO_2}$ ) | Identified phase of electrolyzed samples |        |            |
|---|--|--------|------------|
|   | 0.50 V                                   | 0.70 V | 0.90 V     |
| (i) 1.0   | CaSi <sub>2</sub>                        | Si     | Si         |
| (ii) 1.5  | Si, CaSi <sub>2</sub>                    | Si     | Si         |
| (iii) 2.0   | Si, CaSi <sub>2</sub>                    | Si     | no deposit |

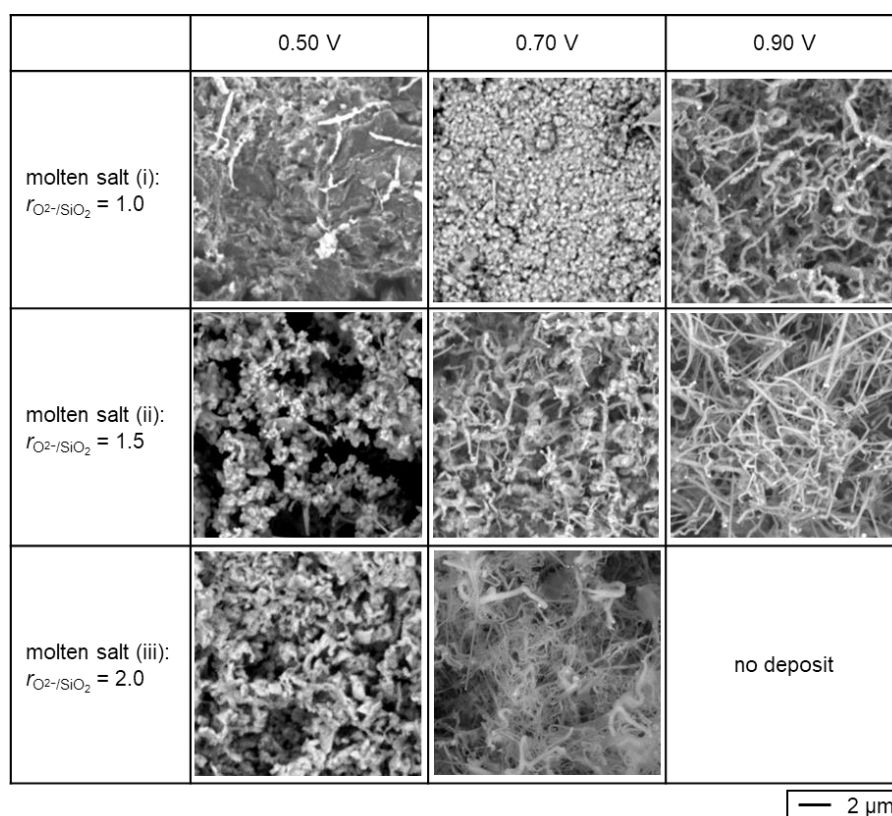


**Figure 4-8** SEM images of the samples obtained in molten NaCl–CaCl<sub>2</sub> with the addition of (i) 1.0 mol% of CaSiO<sub>3</sub> ( $r_{O^{2-}/SiO_2} = 1.0$ ), (ii) 0.5 mol% of CaO and 1.0 mol% of CaSiO<sub>3</sub> ( $r_{O^{2-}/SiO_2} = 1.5$ ), and (iii) 1.0 mol% of CaO and 1.0 mol% of CaSiO<sub>3</sub> ( $r_{O^{2-}/SiO_2} = 2.0$ ) at 1023 K. Charge density:  $-14 \text{ C cm}^{-2}$ .

Si at 0.50 V. The change in morphology of reduced Si is likely due to the change of overpotential and current density. As described in Chapter 3, electrodeposits become field-oriented isolated crystals type when the overpotential and current density are low. When the overpotential and current density are higher, the electrodeposits shift to unoriented dispersion type [10]. In molten salt (i), the potential of 0.90 V would correspond to the low overpotential and current density, which results in the formation of wire-like Si. The potential of 0.70 V is considered to be classified as higher overpotential and current density, resulting in the formation of particle Si. In molten salt (iii), the electrochemical reduction of  $\text{SiO}_4^{4-}$  starts from a more negative potential than  $\text{SiO}_3^{2-}$ . Then, the potential of 0.70 V corresponds to the low overpotential and current density, giving wire-like Si. The potential of 0.50 V is classified as higher overpotential and current density, resulting in the formation of particle Si. In molten salt (ii),  $\text{SiO}_4^{4-}$  and  $\text{SiO}_3^{2-}$  are dominant and second dominant ionic species, respectively. Therefore, wire-like Si is formed from  $\text{SiO}_3^{2-}$  at 0.90 V and from  $\text{SiO}_4^{4-}$  at 0.70 V. Then, particle Si is electrodeposited from  $\text{SiO}_4^{4-}$  at 0.50 V.

#### 4.3.3.3 Potentiostatic Electrolysis at 1123 K

To investigate the effect of temperature on the crystallinity of deposited Si, electrolysis was conducted in the same conditions at 1123 K. Figure 4-9 shows the current transient curves during the electrolysis. The charge densities during the electrolysis were fixed at  $-14 \text{ C cm}^{-2}$ . However, the electrolysis at 0.90 V in molten salt (iii) was intentionally stopped in 1 hour because the current density was less than  $1 \text{ mA cm}^{-2}$ . The low current density proved that the electrochemical reduction of  $\text{SiO}_4^{4-}$  starts from a more negative potential than that of  $\text{SiO}_3^{2-}$ , which is consistent with the voltammograms (Figure 4-4).

Optical images of the electrolyzed samples are shown in Figure 4-10. Deposits in brown or gray color were observed at all samples except samples obtained at 0.50 V in molten salt (i) and 0.90 V in molten salt (iii). In molten salt (i), deposits obtained at 0.50 V fell off during salt removal. No significant deposit was observed at the sample obtained at 0.90 V in molten salt (iii).

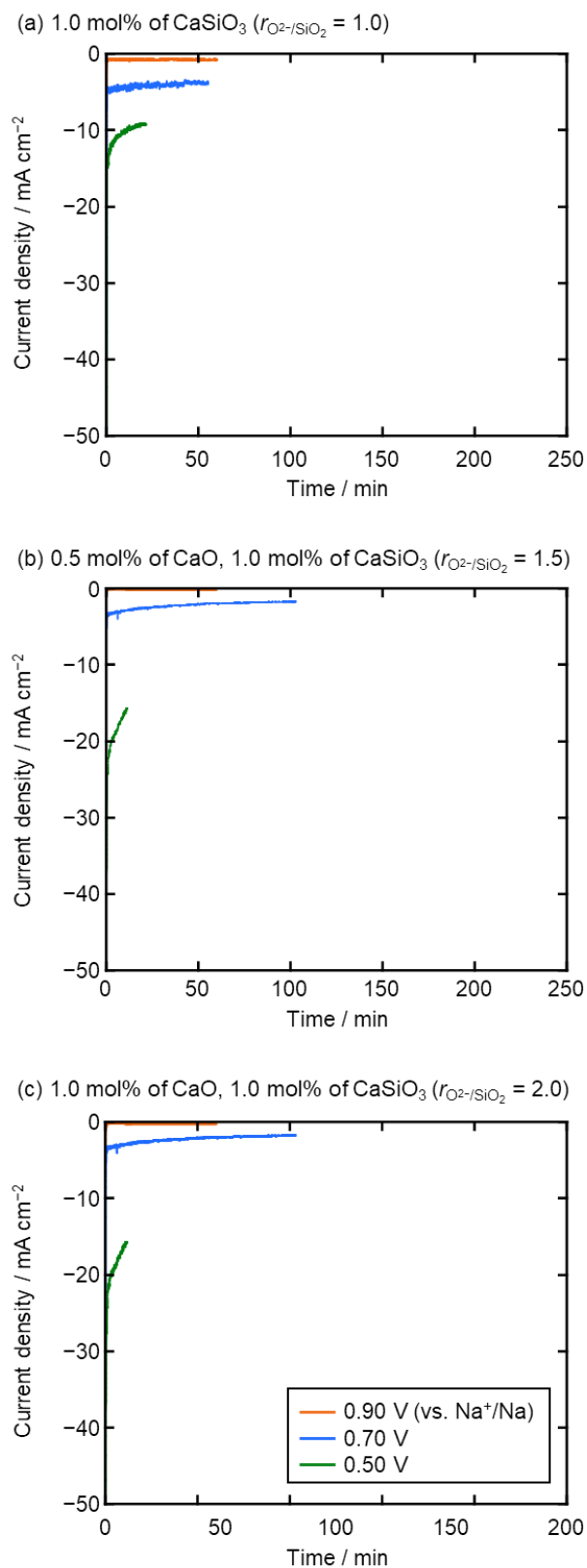


**Figure 4-9** Current transient curves during the potentiostatic electrolysis at graphite plates in molten NaCl–CaCl<sub>2</sub> with the addition of (a) 1.0 mol% of CaSiO<sub>3</sub> ( $r_{\text{O}^{2-}/\text{SiO}_2} = 1.0$ ), (b) 0.5 mol% of CaO and 1.0 mol% of CaSiO<sub>3</sub> ( $r_{\text{O}^{2-}/\text{SiO}_2} = 1.5$ ), and (c) 1.0 mol% of CaO and 1.0 mol% of CaSiO<sub>3</sub> ( $r_{\text{O}^{2-}/\text{SiO}_2} = 2.0$ ) at 1123 K. Charge density:  $-14 \text{ C cm}^{-2}$ .

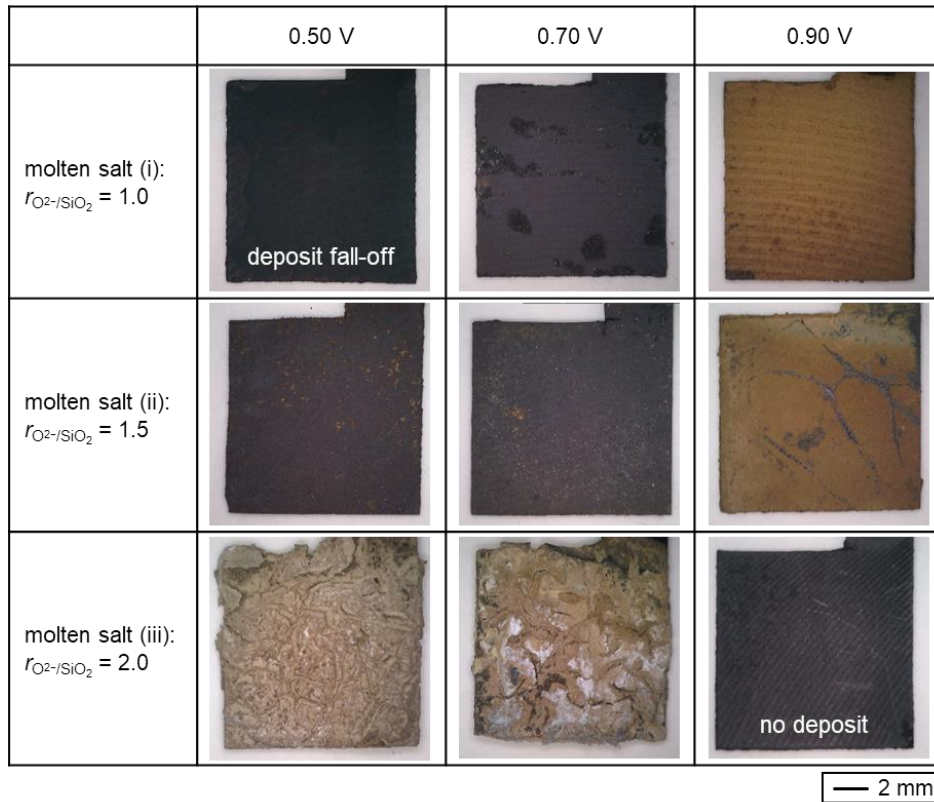


**Figure 4-10** Optical images of the samples obtained in molten NaCl–CaCl<sub>2</sub> with the addition of (i) 1.0 mol% of CaSiO<sub>3</sub> ( $r_{\text{O}^{2-}/\text{SiO}_2} = 1.0$ ), (ii) 0.5 mol% of CaO and 1.0 mol% of CaSiO<sub>3</sub> ( $r_{\text{O}^{2-}/\text{SiO}_2} = 1.5$ ), and (iii) 1.0 mol% of CaO and 1.0 mol% of CaSiO<sub>3</sub> ( $r_{\text{O}^{2-}/\text{SiO}_2} = 2.0$ ) at 1123 K. Charge density:  $-14 \text{ C cm}^{-2}$ .

Figure 4-11 shows XRD patterns of the electrolyzed samples. As shown in Figure 4-11(a), the existence of Si was confirmed at 0.70 and 0.90 V in molten salt (i). CaSi<sub>2</sub> was detected at the sample obtained at 0.50 V before the residual salts removed. Since deposits fell off during salt removal, only the substrate, i.e., graphite was detected. In molten salt (ii), Si was detected at all samples. For samples obtained in molten salt (iii), Si and Ca<sub>2</sub>SiO<sub>4</sub> were detected at 0.50 and 0.70 V. The white part on the brown-color deposits (Figure 4-10) is considered as the residual Ca<sub>2</sub>SiO<sub>4</sub>. At 0.90 V, only graphite substrate was detected. The identified phases are summarized in Table 4-4. The deposits were similar to that obtained at 1023 K.

Figure 4-12 shows the SEM images of the deposits. In molten salt (i), wire-like Si and particle Si were obtained at 0.90 V and 0.70 V, respectively. Compared with the samples obtained at 1023 K (Figure 4-8), larger crystal size and larger amount of wire were observed, which



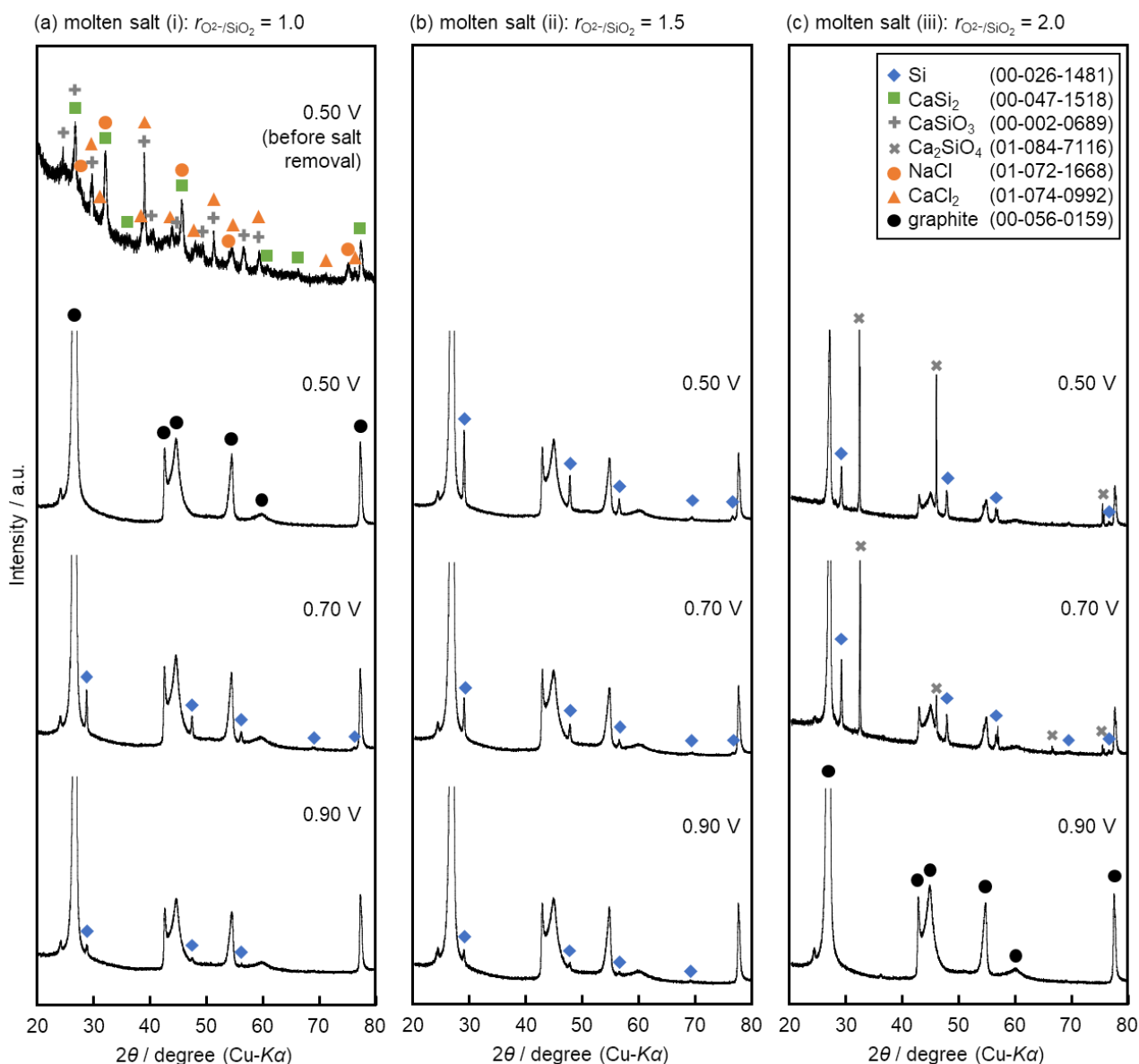


**Figure 4-11** XRD patterns of the samples obtained in molten NaCl–CaCl<sub>2</sub> with the addition of (a) 1.0 mol% of CaSiO<sub>3</sub> ( $r_{O^{2-}/SiO_2} = 1.0$ ), (b) 0.5 mol% of CaO and 1.0 mol% of CaSiO<sub>3</sub> ( $r_{O^{2-}/SiO_2} = 1.5$ ), and (c) 1.0 mol% of CaO and 1.0 mol% of CaSiO<sub>3</sub> ( $r_{O^{2-}/SiO_2} = 2.0$ ) at 1123 K.

suggested the crystal growth of Si deposits at the higher temperature. For the samples obtained in molten salt (ii), wire-like Si was observed at 0.90 V, and particle Si was observed at 0.50 V and 0.70 V. The crystal size and the amount of wire also increased, which was similar as in molten salt (i). In molten salt (iii), wire-like Si was observed at 0.70 V. The deposited Si wires showed a larger diameter than that obtained at 1023 K, which also suggested the crystal growth at the higher temperature. For the sample obtained at 0.50 V, leaf-shape deposits were observed. High



**Table 4-4** XRD results for the samples obtained in molten NaCl–CaCl<sub>2</sub> with the addition of (i) 1.0 mol% of CaSiO<sub>3</sub> ( $r_{\text{O}^{2-}/\text{SiO}_2} = 1.0$ ), (ii) 0.5 mol% of CaO and 1.0 mol% of CaSiO<sub>3</sub> ( $r_{\text{O}^{2-}/\text{SiO}_2} = 1.5$ ), and (iii) 1.0 mol% of CaO and 1.0 mol% of CaSiO<sub>3</sub> ( $r_{\text{O}^{2-}/\text{SiO}_2} = 2.0$ ) at 1123 K. Charge density:  $-14 \text{ C cm}^{-2}$ .

| Ratio of $\text{O}^{2-}/\text{SiO}_2$<br>in molten salt<br>( $r_{\text{O}^{2-}/\text{SiO}_2}$ ) | Identified phase of electrolyzed samples |                                      |            |
|---|--|--------------------------------------|------------|
|   | 0.50 V                                   | 0.70 V                               | 0.90 V     |
| (i) 1.0   | CaSi <sub>2</sub> *                      | Si                                   | Si         |
| (ii) 1.5  | Si                                       | Si                                   | Si         |
| (iii) 2.0   | Si, Ca <sub>2</sub> SiO <sub>4</sub>     | Si, Ca <sub>2</sub> SiO <sub>4</sub> | no deposit |

\* Detected before residual salt removal.

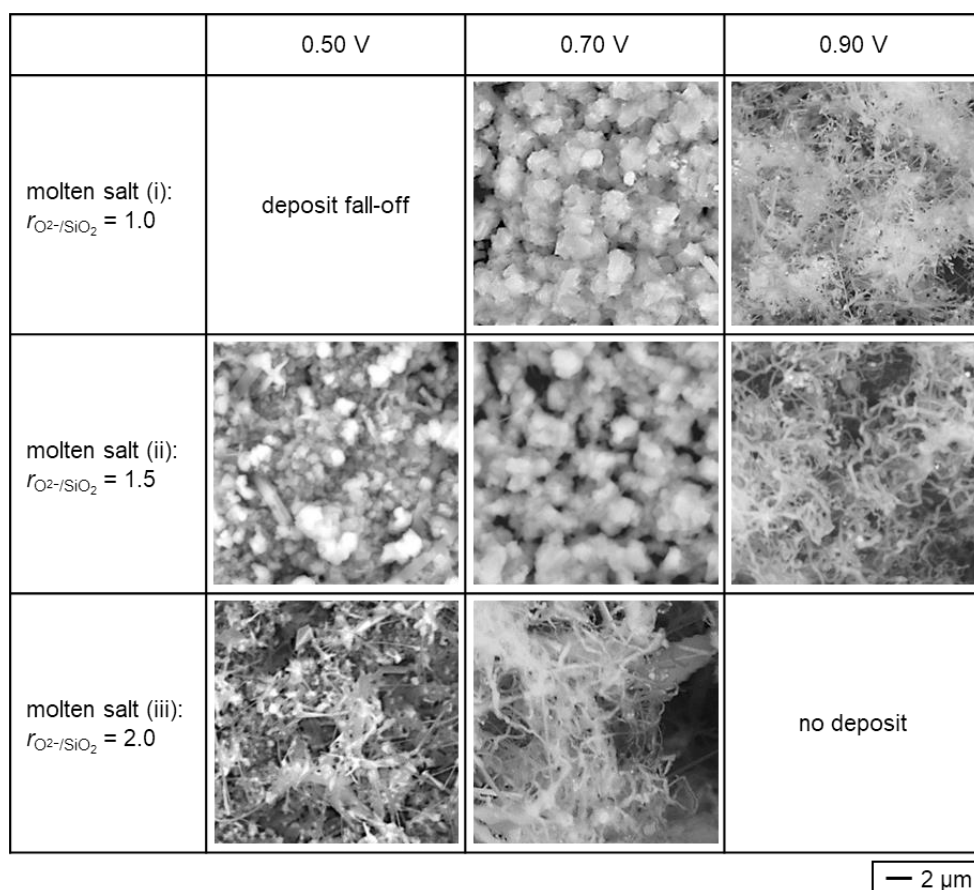


**Figure 4-12** SEM images of the samples obtained in molten NaCl–CaCl<sub>2</sub> with the addition of (i) 1.0 mol% of CaSiO<sub>3</sub> ( $r_{\text{O}^{2-}/\text{SiO}_2} = 1.0$ ), (ii) 0.5 mol% of CaO and 1.0 mol% of CaSiO<sub>3</sub> ( $r_{\text{O}^{2-}/\text{SiO}_2} = 1.5$ ), and (iii) 1.0 mol% of CaO and 1.0 mol% of CaSiO<sub>3</sub> ( $r_{\text{O}^{2-}/\text{SiO}_2} = 2.0$ ) at 1123 K. Charge density:  $-14 \text{ C cm}^{-2}$ .

concentrations of Ca (12.4 at.%) and O (39.0 at.%) were detected by EDX analysis in deposits. Concerning the result of XRD shown in Table 4-4, the leaf-shape deposits were suggested as the mixture of Si and Ca<sub>2</sub>SiO<sub>4</sub>.

From all the results shown above, SiO<sub>3</sub><sup>2-</sup> seems to be suitable for producing Si–Zn alloy. Since the electrochemical reduction of SiO<sub>3</sub><sup>2-</sup> starts from approximately 0.2 V more positive than SiO<sub>4</sub><sup>4-</sup>, the potential is apart from the formation of Ca–Zn alloy, which is considered to be advantageous because the formation of Ca–Zn which may lead to a low current efficiency of Si–Zn alloy production. Therefore, molten salt (i) with dominant SiO<sub>3</sub><sup>2-</sup> and molten salt (ii) with secondary dominant SiO<sub>3</sub><sup>2-</sup> that showed approximately the same potential range for the electrodeposition of Si, are considered to be suitable for the production of Si–Zn alloy at the liquid Zn electrode.

## 4.4 Conclusion

The ionic species and electrochemical reduction of silicate ions at a solid graphite electrode were investigated in molten eutectic NaCl–CaCl<sub>2</sub> with various ratios of O<sup>2-</sup>/SiO<sub>2</sub> as a pre-study for the liquid Zn electrode. The ionic species of silicates in molten salts containing (i) 1.0 mol% CaSiO<sub>3</sub> ( $r_{\text{O}^{2-}/\text{SiO}_2} = 1.0$ ), (ii) 0.5 mol% CaO and 1.0 mol% CaSiO<sub>3</sub> ( $r_{\text{O}^{2-}/\text{SiO}_2} = 1.5$ ), and (iii) 1.0 mol% CaO and 1.0 mol% CaSiO<sub>3</sub> ( $r_{\text{O}^{2-}/\text{SiO}_2} = 2.0$ ) were investigated by Raman spectroscopy at 1023 K. The dominant silicate ion was attributed to SiO<sub>3</sub><sup>2-</sup> ion in molten salt (i) and SiO<sub>4</sub><sup>4-</sup> ion in molten salt (iii), which is consistent with the  $r_{\text{O}^{2-}/\text{SiO}_2}$  in the melt. In molten salt (ii), the primary dominant species was detected as SiO<sub>4</sub><sup>4-</sup> and secondary dominant species as SiO<sub>3</sub><sup>2-</sup> due to the poor stability of Si<sub>2</sub>O<sub>7</sub><sup>6-</sup>.

In molten salt (i), electrodeposition of Si from 1.0 V was confirmed. In molten salt (ii), electrochemical reduction of SiO<sub>3</sub><sup>2-</sup> was indicated at 0.95 V and SiO<sub>4</sub><sup>4-</sup> from 0.80 V. Electrochemical reduction of SiO<sub>4</sub><sup>4-</sup> was indicated from 0.80 V in molten salt (iii). Formation of

CaSi<sub>2</sub> was confirmed at 0.50 V in all molten salts. Electrolysis was also conducted at 1123 K, and the crystal growth of deposited Si was suggested at the higher temperature. From all the results, molten salt (i) with dominant SiO<sub>3</sub><sup>2-</sup> and molten salt (ii) with secondary dominant SiO<sub>3</sub><sup>2-</sup> that showed approximately the same potential range for the electrodeposition of Si, are suggested to be suitable for the production of Si–Zn alloy at the liquid Zn electrode.

## 4.5 Reference List

- [1] S. Wang, F. Zhang, X. Liu and L. Zhang, *Thermochimica Acta*, **470**, 105 (2008).
- [2] D. Virgo, B. O. Mysen and I. Kushiro, *Science*, **208**, 1371 (1980).
- [3] B. O. Mysen, D. Virgo and C. M. Scarfe, *Am. Mineral.*, **65**, 690 (1980).
- [4] B. O. Mysen, *Structure and Properties of Silicate Melts*, Elsevier (1988).
- [5] C. Wang, J. Zhang, Z. Liu, K. Jiao, G. Wang, J. Yang and K. Chou, *Metall. Mater. Trans. B*, **48**, 328 (2017).
- [6] T. B. Massalski, H. Okamoto, P. R. Subramanian and L. Kacprzak, *Binary Alloy Phase Diagrams, 2nd ed.*, ASM International (1990).
- [7] M. W. Chase, C. A. Davies, J. R. Downey, D. J. Frurip, R. A. McDonald and A. N. Syverud, *JANAF Thermochemical Tables, 3rd ed.*, American Chemical Society (1985).
- [8] L. B. Pankratz, *Thermodynamic Properties of Carbides, Nitrides, and Other Selected Substances*, U. S. Bureau of Mines (USBM) (1994).
- [9] M. W. Chase, *NIST-JANAF Thermochemical Tables, 4th ed., Part I Al-Co*, American Chemical Society, and the American Institute of Physics for the National Institute of Standards and Technology (1998).
- [10] R. Winand, *Electrochim. Acta*, **39**, 1091 (1994).

## Chapter 5

# Electrochemical Reduction of Silicate Ions at a Liquid Zn Electrode in Molten NaCl–CaCl<sub>2</sub>

### 5.1 Introduction

In Chapter 4, the ionic species and the electrochemical reduction at a graphite electrode were investigated. As the result, molten salts containing dominant or secondary dominant  $\text{SiO}_3^{2-}$  were suggested to be suitable for the production of Si–Zn alloy. In the present chapter, the electrochemical reduction of silicate ions was investigated at a liquid Zn electrode in molten NaCl–CaCl<sub>2</sub> with various  $\text{O}^{2-}/\text{SiO}_2$  ratios at 1023 K and 1123 K. The precipitated Si particles obtained from the Zn electrode were recovered by the dissolution of Zn in HCl solution and observed by SEM. The current efficiency was calculated from the weight of recovered Si. Furthermore, to investigate the formation of Ca–Zn and/or Na–Zn alloys, the Na and Ca concentrations in the Zn electrode were analyzed by ICP-AES.

### 5.2 Experimental

All the experiments were conducted in a dry Ar atmosphere at 1023 and 1123 K. The salt preparation, experimental apparatus and analysis methods are almost the same as those given in Chapter 3. Important and/or different points are described as follows.

NaCl and CaCl<sub>2</sub> powders were mixed in the eutectic composition and loaded into a graphite crucible. After the temperature was raised to 1023 or 1123 K, pre-determined amounts of CaO (0, 0.5 or 1.0 mol%) and CaSiO<sub>3</sub> (1.0 mol%) powders were added to the eutectic mixture.

All electrochemical measurements were conducted by a three-electrode method. Schematic illustration of the liquid Zn electrode is shown in Figure 5-1. A small BN crucible (Denka Co. Ltd, NB-1000 grade, o.d. 20 mm  $\times$  i.d. 16 mm  $\times$  height 20 mm) was fixed to an Al<sub>2</sub>O<sub>3</sub> tube (Nikkato Corp., SSA-S grade, o.d. 6.0 mm  $\times$  i.d. 4.0 mm) by a Mo wire (Nilaco Corp., diameter 0.6 mm, 99.95%). A W wire (Nilaco Corp., diameter 1.0 mm, 99.95%) threaded into a BN tube (Denka Co. Ltd, NB-1000 grade, o.d. 6.0 mm  $\times$  i.d. 3.0 mm) fixed by a graphite tube, was used as the current lead. For electrolysis at 1023 K, 7.0 g of Zn grains was charged into a small BN crucible. For electrolysis at 1123 K, a crucible containing 10.0 g of Zn was used. As quasi-reference electrodes for the blank melt, a Pt wire was used at 1023 K and a Si rod at 1123 K. The same Si rod was used as the reference electrode in the melts containing silicate ions at 1023 K and 1123 K. The potentials of the quasi-reference and reference electrodes were calibrated with respect to a dynamic Na<sup>+</sup>/Na potential. The counter electrodes were the same as those described in Chapter 3.

After electrolysis, several Zn electrodes were taken out of the molten salt and cooled by natural heat dissipation (approximately 10–20 s). All other Zn electrodes were cooled at a rate of 20 K h<sup>-1</sup> from 1023 K or 1123 K to 823 K and then to room temperature by natural heat dissipation in the salt. Hereafter, we refer to cooling by natural heat dissipation alone to as “rapid cooling” and cooling at 20 K h<sup>-1</sup> as “slow cooling”. The Si granules in the Zn metal lumps were recovered by dissolving Zn in a 20 wt.% HCl solution. The solutions of dissolved Zn were analyzed by ICP-AES to determine the concentrations of Ca and Na in the Zn lumps.

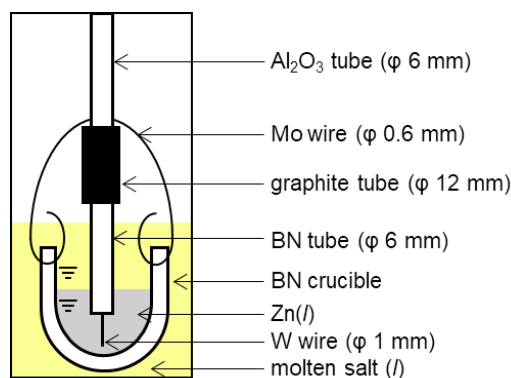


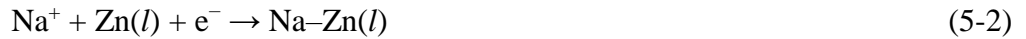
**Figure 5-1** Schematic illustration of the liquid Zn electrode.

## 5.3 Results and Discussion

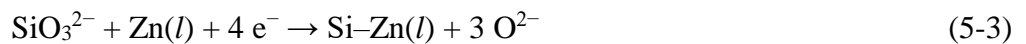
### 5.3.1 Cyclic Voltammetry

#### 5.3.1.1 Voltammetry at 1023 K

Figure 5-2 shows the cyclic voltammograms at a liquid Zn electrode at 1023 K in molten eutectic NaCl–CaCl<sub>2</sub> containing different amounts of CaO and CaSiO<sub>3</sub>: (i) 1.0 mol% CaSiO<sub>3</sub> ( $r_{\text{O}^{2-}/\text{SiO}_2} = 1.0$ ), (ii) 0.5 mol% CaO and 1.0 mol% CaSiO<sub>3</sub> ( $r_{\text{O}^{2-}/\text{SiO}_2} = 1.5$ ), and (iii) 1.0 mol% CaO and 1.0 mol% CaSiO<sub>3</sub> ( $r_{\text{O}^{2-}/\text{SiO}_2} = 2.0$ ). The black curves show the voltammograms before the addition of CaSiO<sub>3</sub> and CaO (blank). The rapid increase in cathodic current observed around 0.8 V (vs. Na<sup>+</sup>/Na) is likely due to the formation of Ca–Zn and/or Na–Zn alloys.



After the addition of 1.0 mol% CaSiO<sub>3</sub> ( $r_{\text{O}^{2-}/\text{SiO}_2} = 1.0$ ), as shown in Figure 5-2(a), the cathode current increased from around 1.1 V compared with the current in the blank melt. This suggested the electrochemical reduction of SiO<sub>3</sub><sup>2-</sup>, the dominant ionic species observed by Raman spectroscopy in Chapter 4 (Figure 4-2).



A sharp increase in cathodic current from around 0.80 V is considered to correspond to the simultaneous reactions of the electrochemical reduction of SiO<sub>3</sub><sup>2-</sup> (reaction (5-3)) and the formation of Ca–Zn and/or Na–Zn alloys (reaction (5-1), (5-2)).

A voltammogram conducted in the melt containing 0.5 mol% CaO and 1.0 mol% CaSiO<sub>3</sub> ( $r_{\text{O}^{2-}/\text{SiO}_2} = 1.5$ ) is shown in Figure 5-2(b). Cathodic current increased from 1.1 V was attributed to the electrochemical reduction of secondary dominant SiO<sub>3</sub><sup>2-</sup> (reaction (5-3)), of which the potential was the same as that shown in Figure 5-2(a). The sharp increase in cathodic current from 0.80 V was regarded as the simultaneous reactions, i.e., the electrochemical reduction of silicate ions and

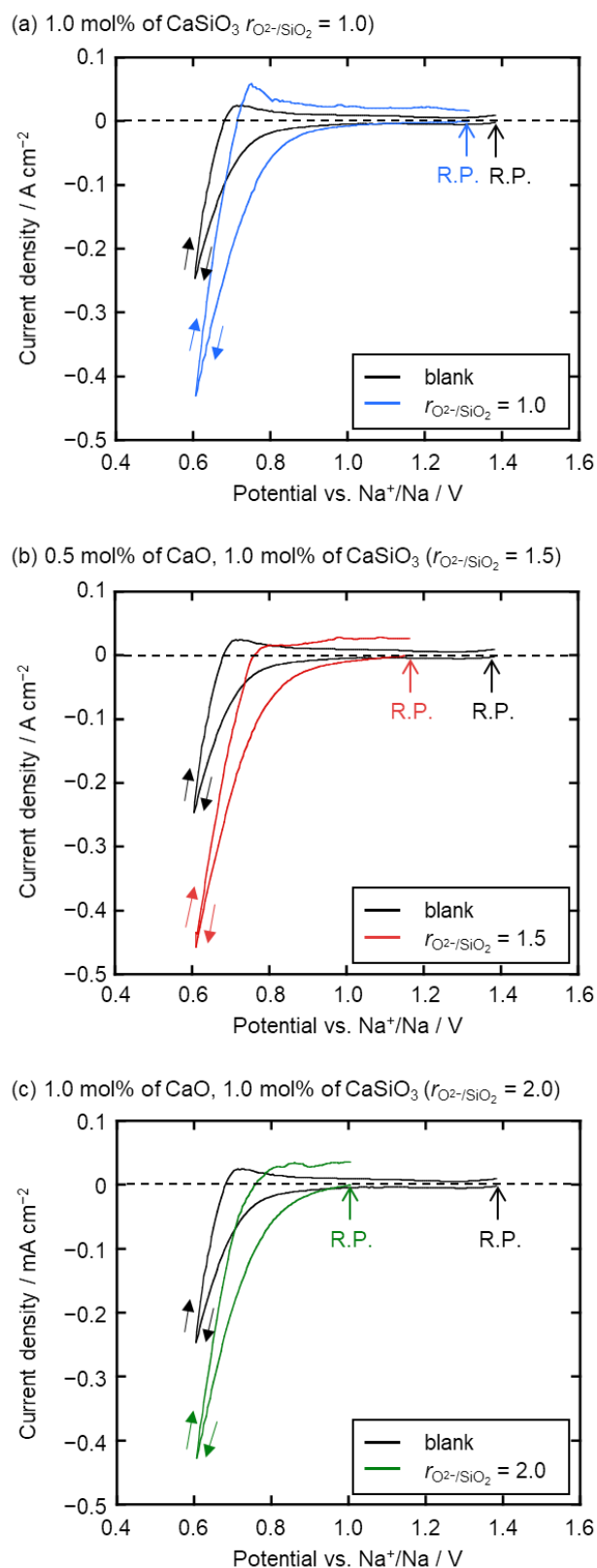
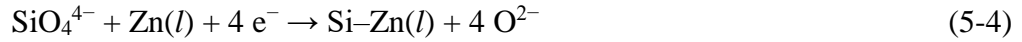


**Figure 5-2** Cyclic voltammograms at a liquid Zn electrode in molten  $\text{NaCl-CaCl}_2$  before and after the addition of (a) 1.0 mol% of  $\text{CaSiO}_3$  ( $r_{\text{O}^{2-}/\text{SiO}_2} = 1.0$ ), (b) 0.5 mol% of  $\text{CaO}$  and 1.0 mol% of  $\text{CaSiO}_3$  ( $r_{\text{O}^{2-}/\text{SiO}_2} = 1.5$ ), and (c) 1.0 mol% of  $\text{CaO}$  and 1.0 mol% of  $\text{CaSiO}_3$  ( $r_{\text{O}^{2-}/\text{SiO}_2} = 2.0$ ) at 1023 K. Scan rate:  $100 \text{ mV s}^{-1}$ . R. P.: Rest potential.

the formation of Ca–Zn and/or Na–Zn alloy, which was similar to that observed in [Figure 5-2\(a\)](#).

[Figure 5-2\(c\)](#) shows the voltammogram measured after the addition of 1.0 mol% CaO and 1.0 mol% CaSiO<sub>3</sub> ( $r_{\text{O}^{2-}/\text{SiO}_2} = 2.0$ ). The increase in cathodic current from 0.95 V is considered as the electrochemical reduction of dominant SiO<sub>4</sub><sup>4-</sup>.



The rapid increase in cathodic current from 0.80 V was ascribed to the same simultaneous reactions, similar to the other two melts shown in [Figure 5-2\(a\)](#) and [\(b\)](#). The rest potential in molten salt (iii) with dominant SiO<sub>4</sub><sup>4-</sup> was more negative than that in molten salt (i) with dominant SiO<sub>3</sub><sup>2-</sup>, which corresponds to the results obtained at the solid graphite electrodes in Chapter 4.

### 5.3.1.2 Voltammetry at 1123 K

Voltammograms obtained at 1123 K are shown in [Figure 5-3](#). The sharp increase in cathodic current observed at 0.85 V in blank melt (black curves) is considered as the formation of Ca–Zn and/or Na–Zn alloy ([reaction \(5-1\)](#), [\(5-2\)](#)).

[Figure 5-3\(a\)](#) shows the voltammogram after the addition of 1.0 mol% CaSiO<sub>3</sub> ( $r_{\text{O}^{2-}/\text{SiO}_2} = 1.0$ ). Cathodic current increased from 1.3 V suggested the same reaction at 1023 K, i.e., the electrochemical reduction of dominant SiO<sub>3</sub><sup>2-</sup> shown in [reaction \(5-3\)](#). As in the case of 1023 K, a sharp current increase was observed from 0.85 V, suggesting the same simultaneous reactions of the electrochemical reduction of SiO<sub>3</sub><sup>2-</sup> and the formation of Ca–Zn and/or Na–Zn alloys.

[Figure 5-3\(b\)](#) shows the voltammogram measured in molten salt (ii) with  $r_{\text{O}^{2-}/\text{SiO}_2} = 1.5$ . Cathodic current increased from 1.2 V was attributed to the electrochemical reduction of secondary dominant SiO<sub>3</sub><sup>2-</sup>. Similarly, cathodic current rapidly increased from 0.85 V, which suggested the same simultaneous reactions observed in [Figure 5-3\(a\)](#).

[Figure 5-3\(c\)](#) shows the voltammogram conducted in molten salt (iii) with  $r_{\text{O}^{2-}/\text{SiO}_2} = 2.0$ . Increase in cathodic current from 1.0 V was attributed to the electrochemical reduction of dominant



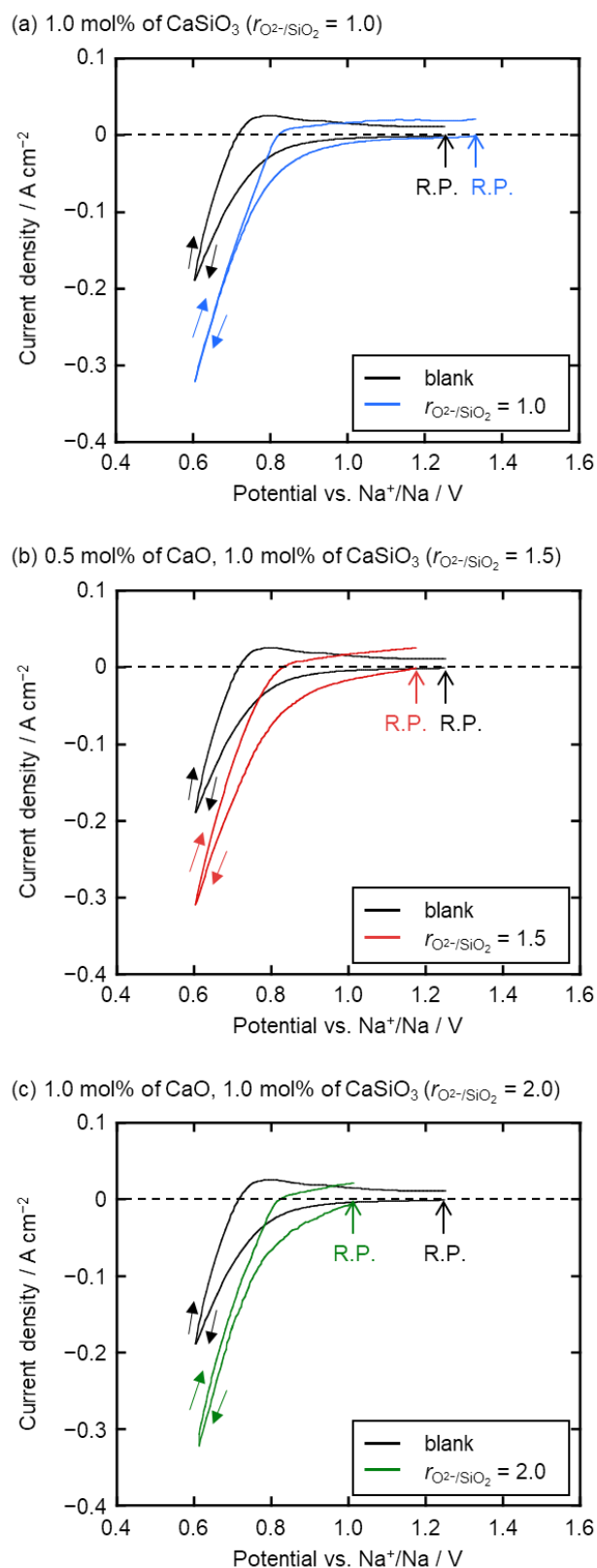


**Figure 5-3** Cyclic voltammograms at a liquid Zn electrode in molten  $\text{NaCl-CaCl}_2$  before and after the addition of (a) 1.0 mol% of  $\text{CaSiO}_3$  ( $r_{\text{O}^{2-}/\text{SiO}_2} = 1.0$ ), (b) 0.5 mol% of  $\text{CaO}$  and 1.0 mol% of  $\text{CaSiO}_3$  ( $r_{\text{O}^{2-}/\text{SiO}_2} = 1.5$ ), and (c) 1.0 mol% of  $\text{CaO}$  and 1.0 mol% of  $\text{CaSiO}_3$  ( $r_{\text{O}^{2-}/\text{SiO}_2} = 2.0$ ) at 1123 K. Scan rate:  $100 \text{ mV s}^{-1}$ . R. P.: Rest potential.

$\text{SiO}_4^{4-}$  (reaction (5-4)). The sharp increase in cathodic current from 0.85 V was ascribed to the same simultaneous reactions, similar to the other two melts shown in Figure 5-3(a) and (b). The potential for the electrochemical reduction of  $\text{SiO}_4^{4-}$  was more negative than that for  $\text{SiO}_3^{2-}$  in molten salt (i), which was same to the result obtained at 1023 K. Compared with the results of cyclic voltammetry conducted at the graphite electrode (described in Chapter 4), the electrochemical reduction of silicate ions at the liquid electrode started from a more positive potential, which suggested the formation of liquid Si–Zn alloy with Si activity lower than unity with respect to pure solid Si.

### 5.3.2 Potentiostatic Electrolysis

#### 5.3.2.1 Electrolysis at 1023 K

Potentiostatic electrolysis was conducted at 0.60 and 0.90 V in the same melts used for cyclic voltammetry measurement. Electrolysis at 0.90 V in molten salt (iii) was excluded because its current was too small to form Si–Zn alloy. All electrolysis was conducted with a constant charge of  $-413.2$  C, which corresponds to the theoretical quantity of charge for 1.0 mol% Si–Zn alloy formation. The current transient curves during the electrolysis are shown in Figure 5-4. In molten salt (i) with  $r_{\text{O}^{2-}/\text{SiO}_2} = 1.0$  (Figure 5-4(a)), small cathodic current of  $5\text{--}10$   $\text{mA cm}^{-2}$  was observed for 13 h at 0.90 V, which seems to be mainly attributed to the direct electrochemical reduction of  $\text{SiO}_3^{2-}$  (reaction (5-3)). At 0.60 V, large cathodic current of about  $50$   $\text{mA cm}^{-2}$  was observed at first, and then it gradually decreased to an average of  $15$   $\text{mA cm}^{-2}$  after 2.6 h. The larger current is considered to be the simultaneous reactions of the electrochemical reduction of  $\text{SiO}_3^{2-}$  and the formation of Ca–Zn and/or Na–Zn alloy (reaction (5-1), (5-2)). Similarly, in molten salt (ii) with  $r_{\text{O}^{2-}/\text{SiO}_2} = 1.5$  (Figure 5-4(b)), the current at 0.90 V was attributed to the direct electrochemical reduction of silicate ions (reactions (5-3) and (5-4)), and the larger current at 0.60 V to the simultaneous reactions. In molten salt (iii) with  $r_{\text{O}^{2-}/\text{SiO}_2} = 2.0$  (Figure 5-4(c)), considering the similar shape of the voltammogram to that in other two melts (Figure 5-2), the cathodic current at

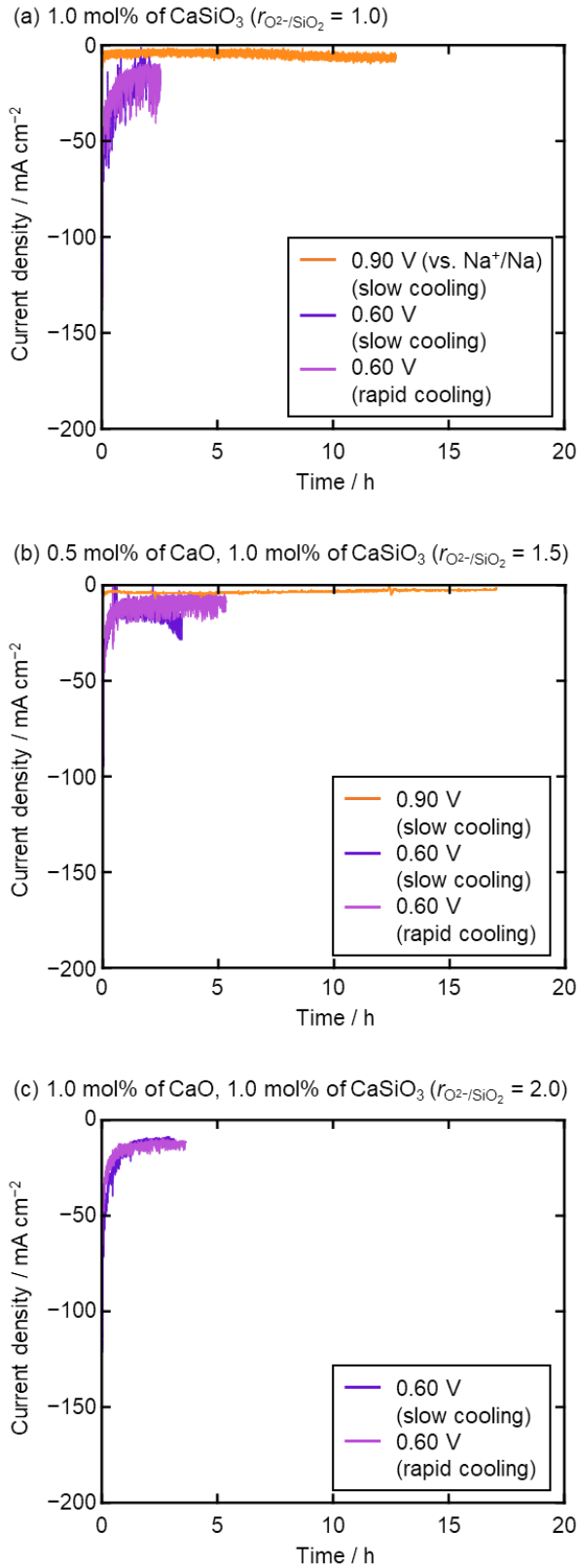


**Figure 5-4** Current transient curves during the potentiostatic electrolysis at the liquid Zn electrode in molten NaCl–CaCl<sub>2</sub> with the addition of (a) 1.0 mol% of CaSiO<sub>3</sub> ( $r_{\text{O}^{2-}/\text{SiO}_2} = 1.0$ ), (b) 0.5 mol% of CaO and 1.0 mol% of CaSiO<sub>3</sub> ( $r_{\text{O}^{2-}/\text{SiO}_2} = 1.5$ ), and (c) 1.0 mol% of CaO and 1.0 mol% of CaSiO<sub>3</sub> ( $r_{\text{O}^{2-}/\text{SiO}_2} = 2.0$ ) at 1023 K. Charge:  $-413.2$  C (theoretical formation of 1.0 mol% Si–Zn alloy).

0.60 V was also assigned to the simultaneous reactions of the direct electrochemical reduction and the alloy formation.

After the electrolysis, of the six samples obtained at 0.60 V, half were cooled by natural heat dissipation (rapid cooling) and the other half were cooled at  $20 \text{ K h}^{-1}$  (slow cooling) in the same molten salt (iii). The samples obtained at 0.90 V were cooled under the same slow-cooling conditions. Figure 5-5 shows the optical images of the Si particles recovered from the Zn electrodes after the electrolysis at 1023 K. For the samples obtained at 0.60 V with rapid cooling, brown-color fine powders and small Si granules with a metallic luster were obtained. In contrast, for the samples obtained after the slow cooling, larger granules with a metallic luster were mainly precipitated, suggesting the crystal growth at the slow cooling step. Figure 5-6 shows the SEM images of the samples. For the samples obtained at 0.60 V with rapid cooling, the brown-color fine powders were

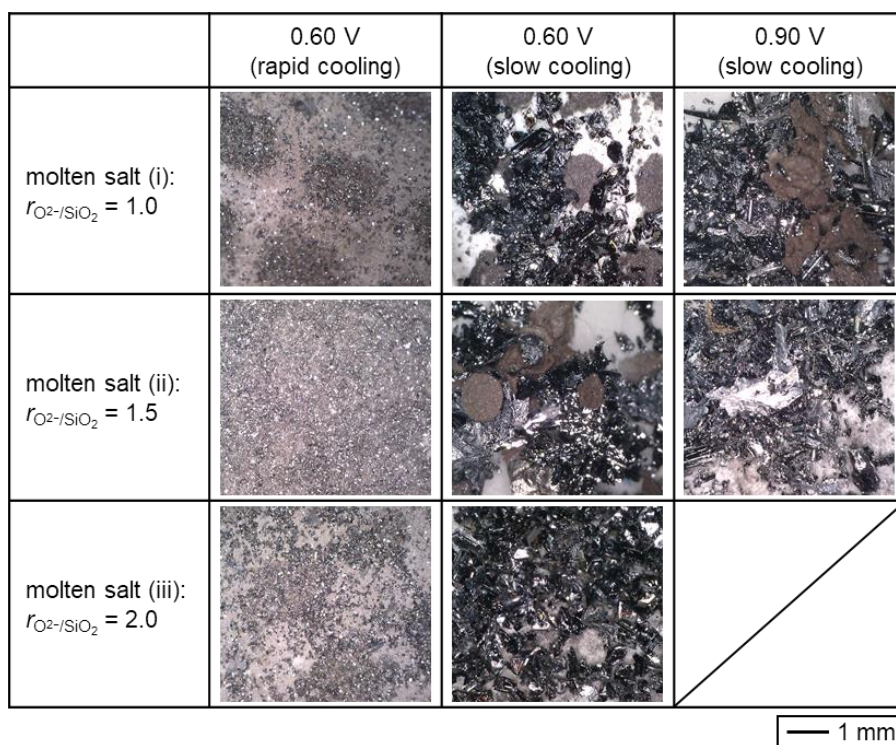


**Figure 5-5** Optical images of the Si particles recovered from the Zn electrodes after the electrolysis conducted in molten NaCl–CaCl<sub>2</sub> with the addition of (i) 1.0 mol% of CaSiO<sub>3</sub> ( $r_{\text{O}^{2-}/\text{SiO}_2} = 1.0$ ), (ii) 0.5 mol% of CaO and 1.0 mol% of CaSiO<sub>3</sub> ( $r_{\text{O}^{2-}/\text{SiO}_2} = 1.5$ ), and (iii) 1.0 mol% of CaO and 1.0 mol% of CaSiO<sub>3</sub> ( $r_{\text{O}^{2-}/\text{SiO}_2} = 2.0$ ) at 1023 K. Charge:  $-413.2 \text{ C}$  (theoretical formation of 1.0 mol% Si–Zn alloy).

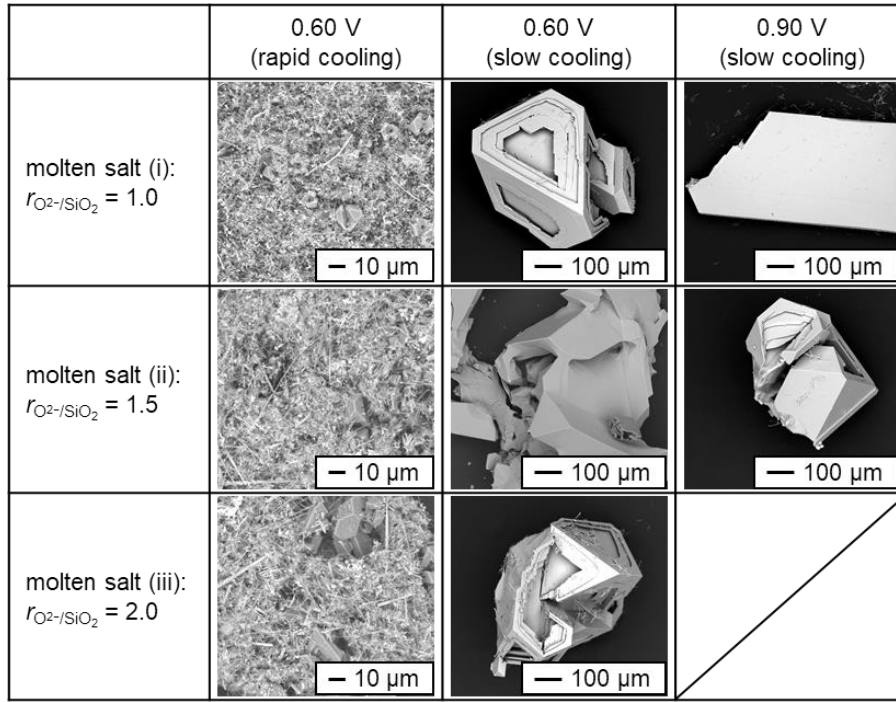


**Figure 5-6** SEM images of the Si particles recovered from the Zn electrodes after the electrolysis conducted in molten NaCl–CaCl<sub>2</sub> with the addition of (i) 1.0 mol% of CaSiO<sub>3</sub> ( $r_{\text{O}^{2-}/\text{SiO}_2} = 1.0$ ), (ii) 0.5 mol% of CaO and 1.0 mol% of CaSiO<sub>3</sub> ( $r_{\text{O}^{2-}/\text{SiO}_2} = 1.5$ ), and (iii) 1.0 mol% of CaO and 1.0 mol% of CaSiO<sub>3</sub> ( $r_{\text{O}^{2-}/\text{SiO}_2} = 2.0$ ) at 1023 K. Charge: –413.2 C (theoretical formation of 1.0 mol% Si–Zn alloy).

found to be the aggregates of entangled Si wires. The small Si granules with a metallic luster were found to be angular crystals with a size of 10–20 μm. In all samples with slow cooling, the granule size increased to several hundred micrometers. There was no significant difference in the particle size and crystal shape in all the samples with slow cooling. This can be reasonably explained by the fact that the Si particles precipitated from the Zn electrodes under the same cooling conditions.

Table 5-1 lists the weight of recovered Si and the current efficiency calculated from the Si weight. The current efficiency was calculated by the following equations:

$$\eta = \frac{w_{\text{act.}}}{w_{\text{theo.}}} \times 100 \quad (5-5)$$

$$w_{\text{theo.}} = \frac{Q}{4F} \times M_{\text{Si}} \quad (5-6)$$

**Table 5-1** Weight of the recovered Si particles and the current efficiency calculated from Si weight after the electrolysis conducted in molten NaCl–CaCl<sub>2</sub> with the addition of (i) 1.0 mol% of CaSiO<sub>3</sub> ( $r_{\text{O}^{2-}/\text{SiO}_2} = 1.0$ ), (ii) 0.5 mol% of CaO and 1.0 mol% of CaSiO<sub>3</sub> ( $r_{\text{O}^{2-}/\text{SiO}_2} = 1.5$ ), and (iii) 1.0 mol% of CaO and 1.0 mol% of CaSiO<sub>3</sub> ( $r_{\text{O}^{2-}/\text{SiO}_2} = 2.0$ ) at 1023 K. Charge: –413.2 C (theoretical formation of 1.0 mol% Si–Zn alloy).

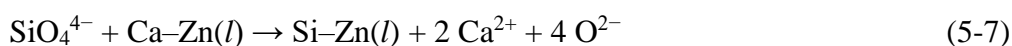
| Ratio of $\text{O}^{2-}/\text{SiO}_2$<br>in molten salt<br>( $r_{\text{O}^{2-}/\text{SiO}_2}$ ) | Weight of recovered Si, $w_{\text{act.}}$ / g |                     |                     | Current efficiency, $\eta$ / % |                     |                     |
|---|---|---------------------|---------------------|--------------------------------|---------------------|---------------------|
|   | 0.60 V <sup>a</sup>                           | 0.60 V <sup>b</sup> | 0.90 V <sup>b</sup> | 0.60 V <sup>a</sup>            | 0.60 V <sup>b</sup> | 0.90 V <sup>b</sup> |
| (i) 1.0   | 0.0202  | 0.0287              | 0.0193              | 67.1                           | 95.4                | 64.2                |
| (ii) 1.5  | 0.0199  | 0.0286              | 0.0121              | 66.1                           | 95.1                | 40.2                |
| (iii) 2.0   | 0.0203  | 0.0289              | –                   | 67.5                           | 96.1                | –                   |

<sup>a</sup> Cooled by natural heat dissipation (rapid cooling).

<sup>b</sup> Cooled at a rate of 20 K h<sup>–1</sup> (slow cooling).

where  $w_{\text{act.}}$  is the actual weight of the Si recovered, and  $w_{\text{theo.}}$  is the theoretical weight of Si produced according to Faraday’s law in reaction (5-3) or (5-4),  $Q$  is the quantity of electric charge during electrolysis,  $F$  is Faraday’s constant (96485 C mol<sup>–1</sup>), and  $M_{\text{Si}}$  is the molar weight of Si (28.1 g mol<sup>–1</sup>). Concentrations of Ca and Na in the liquid Zn electrodes are listed in Table 5-2. The Ca concentration was calibrated by subtracting the Ca concentrations in raw Zn and HCl solution.

As the result, no Na was detected in all samples, indicating that the alloy formed during electrolysis was Ca–Zn alloy only (reaction (5-1)). The samples obtained at 0.60 V with rapid cooling showed current efficiencies of just under 70%. In these samples, more than 3000 ppmw of Ca was detected, indicating the formation of Ca–Zn alloy during the electrolysis. On the other hand, for the samples obtained at 0.60 V with slow cooling, the current efficiencies increased to more than 95% and the residual Ca concentrations were approximately 200–300 ppmw, suggesting the indirect reduction of silicate ions by Ca–Zn alloy.



Similar reaction has been confirmed at 0.60 V in molten CaCl<sub>2</sub> at 1123 K, which was described in

**Table 5-2 Concentrations of Ca and Na in the Zn electrodes after the electrolysis conducted in molten NaCl–CaCl<sub>2</sub> with the addition of (i) 1.0 mol% of CaSiO<sub>3</sub> ( $r_{O^{2-}/SiO_2} = 1.0$ ), (ii) 0.5 mol% of CaO and 1.0 mol% of CaSiO<sub>3</sub> ( $r_{O^{2-}/SiO_2} = 1.5$ ), and (iii) 1.0 mol% of CaO and 1.0 mol% of CaSiO<sub>3</sub> ( $r_{O^{2-}/SiO_2} = 2.0$ ) at 1023 K. Charge: –413.2 C (theoretical formation of 1.0 mol% Si–Zn alloy).**

| Ratio of O <sup>2-</sup> /SiO <sub>2</sub><br>in molten salt<br>( $r_{O^{2-}/SiO_2}$ ) | Ca concentration in the Zn electrodes<br>after electrolysis, $x_{Ca}$ / ppmw |                     |                     | Na concentration in the Zn electrodes<br>after electrolysis, $x_{Na}$ / ppmw |                     |                     |
|--|--|---------------------|---------------------|--|---------------------|---------------------|
|  | 0.60 V <sup>a</sup>  | 0.60 V <sup>b</sup> | 0.90 V <sup>b</sup> | 0.60 V <sup>a</sup>  | 0.60 V <sup>b</sup> | 0.90 V <sup>b</sup> |
|  | (i) 1.0  | 3440                | 197                 | – †  | – †                 | – †                 |
| (ii) 1.5   | 3404   | – †                 | 44                  | – †  | – †                 | – †                 |
| (iii) 2.0  | 3439   | 268                 | –                   | – †  | – †                 | –                   |

<sup>a</sup> Cooled by natural heat dissipation (rapid cooling).

<sup>b</sup> Cooled at a rate of 20 K h<sup>-1</sup> (slow cooling).

† Not detected.

Chapter 3. For samples obtained at 0.90 V, at which only direct electrochemical reduction of silicate ions is considered to proceed, the current efficiencies were 64.2% in molten salt (i) and 40.2% in molten salt (ii). Considering almost no Ca was detected in the samples obtained at 0.90 V, the low current efficiencies are considered to be due to the small cathodic current observed in Figure 5-4. Namely, the reduction current of silicate ions is considered to be not sufficiently large compared to the background current.

To confirm the indirect reduction of silicate ions by Ca–Zn alloy, two samples of Ca–Zn alloy were prepared at 0.60 V in molten NaCl–CaCl<sub>2</sub> at 1023 K. Figure 5-7(a) shows the current transient curve during the electrolysis. One Ca–Zn alloy sample was then analyzed by ICP-AES; the concentration of Ca was detected to be 5962 ppmw. The current efficiency for the formation of Ca–Zn alloy was calculated to be 94.4%. The other sample was placed in the molten salt (iii) and cooled with the same slow cooling condition as described above. After the slow cooling, Si particles were recovered from the Zn electrode and the concentration of Ca in the Zn electrode decreased to



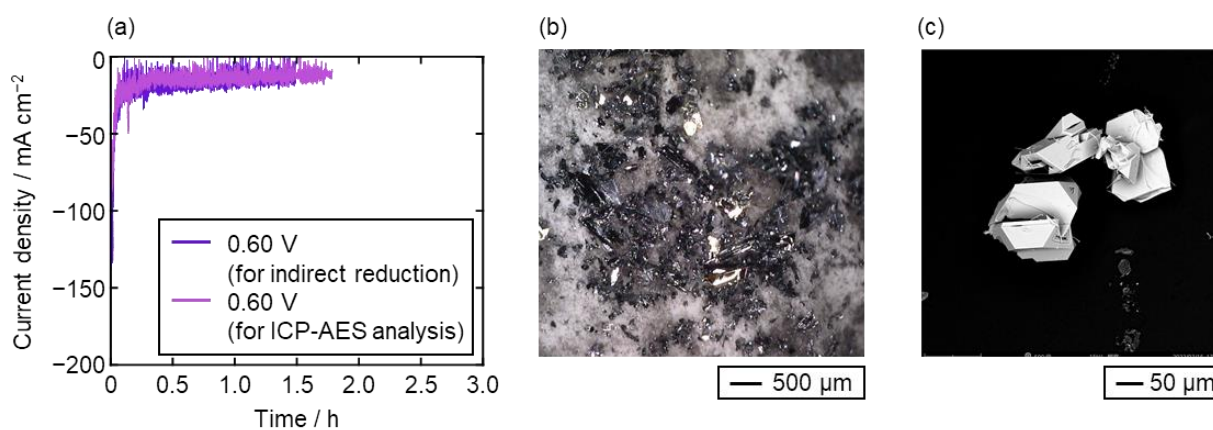


**Figure 5-7** (a) Current transient curves during the electrolysis at liquid Zn electrode in molten NaCl–CaCl<sub>2</sub>, (b) optical image and (c) surface SEM image of the Si particles recovered from the Zn electrode after the slow cooling in molten NaCl–CaCl<sub>2</sub> with the addition of 1.0 mol% of CaO and 1.0 mol% of CaSiO<sub>3</sub> ( $r_{\text{O}^{2-}/\text{SiO}_2} = 2.0$ ) at 1023 K.

666 ppmw, indicating that the indirect reduction by Ca–Zn alloy proceeded during the slow cooling. Figure 5-7(b) and (c) show optical and SEM images of the recovered Si particles, respectively. The Si granules showed a metallic luster with a size of approximately 100 μm, which was smaller than those obtained by electrolysis with slow cooling. Since the indirect reduction by Ca–Zn alloy only proceeded during slow cooling, Si concentration in Zn electrode is considered to be lower than that obtained by electrolysis. The current efficiency calculated from the weight of recovered Si was 75.2%, also indicating the lower Si concentration in the sample obtained by indirect reduction.

### 5.3.2.2 Electrolysis at 1123 K

Potentiostatic electrolysis was also conducted in the same conditions at 1123 K. Electrolysis at 0.90 V in molten salt (iii) was excluded because its current was too small to form Si–Zn alloy. All electrolysis was conducted with a constant charge of –590.3 C, which corresponds to the theoretical quantity of charge for 1.0 mol% Si–Zn alloy formation, except the sample obtained at 0.90 V in molten salt (i), of which electrolysis stopped after –369.7 C charged.

Figure 5-8 shows the current transient curves during the electrolysis. In molten salt (i) with  $r_{\text{O}^{2-}/\text{SiO}_2} = 1.0$  (Figure 5-8(a)), small cathodic current at 0.90 V was mainly attributed to the



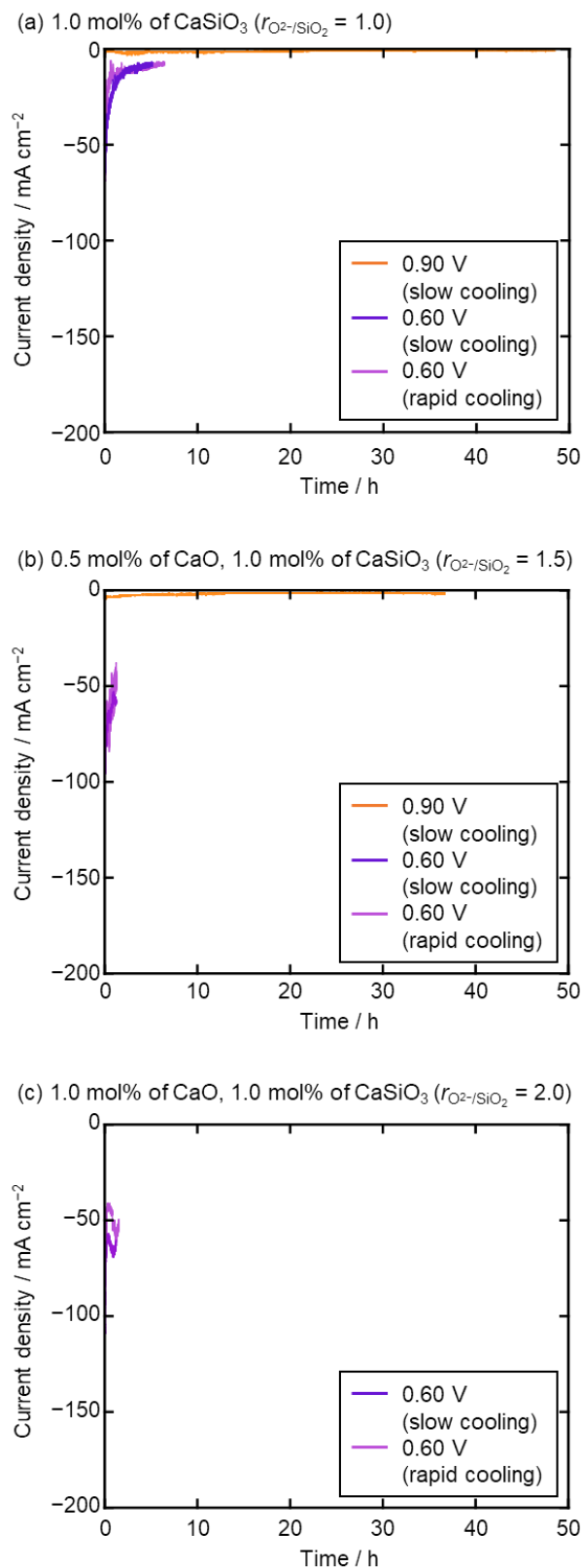


**Figure 5-8** Current transient curves during the potentiostatic electrolysis at the liquid Zn electrode in molten  $\text{NaCl-CaCl}_2$  with the addition of (a) 1.0 mol% of  $\text{CaSiO}_3$  ( $r_{\text{O}^{2-}/\text{SiO}_2} = 1.0$ ), (b) 0.5 mol% of  $\text{CaO}$  and 1.0 mol% of  $\text{CaSiO}_3$  ( $r_{\text{O}^{2-}/\text{SiO}_2} = 1.5$ ), and (c) 1.0 mol% of  $\text{CaO}$  and 1.0 mol% of  $\text{CaSiO}_3$  ( $r_{\text{O}^{2-}/\text{SiO}_2} = 2.0$ ) at 1123 K. Charge:  $-590.3$  C (theoretical formation of 1.0 mol% Si-Zn alloy).

direct electrochemical reduction of  $\text{SiO}_3^{2-}$  (reaction (5-3)). The larger current at 0.60 V is considered to correspond to the simultaneous reactions of the electrochemical reduction of  $\text{SiO}_3^{2-}$  and the formation of Ca–Zn alloy (reaction (5-1)), similar to the result obtained at 1023 K. In molten salt (ii) with  $r_{\text{O}^{2-}/\text{SiO}_2} = 1.5$  (Figure 5-8(b)), the current at 0.90 V was attributed to the direct electrochemical reduction of silicate ions and that at 0.60 V was the same simultaneous reactions proceeded in molten salt (i). Similarly, in molten salt(iii) with  $r_{\text{O}^{2-}/\text{SiO}_2} = 2.0$  (Figure 5-8(c)), the cathodic current at 0.60 V is also considered as the same simultaneous reactions.

Same as the experiment conducted at 1023 K, half of the samples obtained at 0.60 V were cooled by rapid cooling, and other half were cooled by slow cooling after the electrolysis. The samples obtained at 0.90 V were cooled under the same slow-cooling conditions. Figure 5-9 shows the optical images of the Si particle recovered from the Zn electrodes. For the samples obtained by

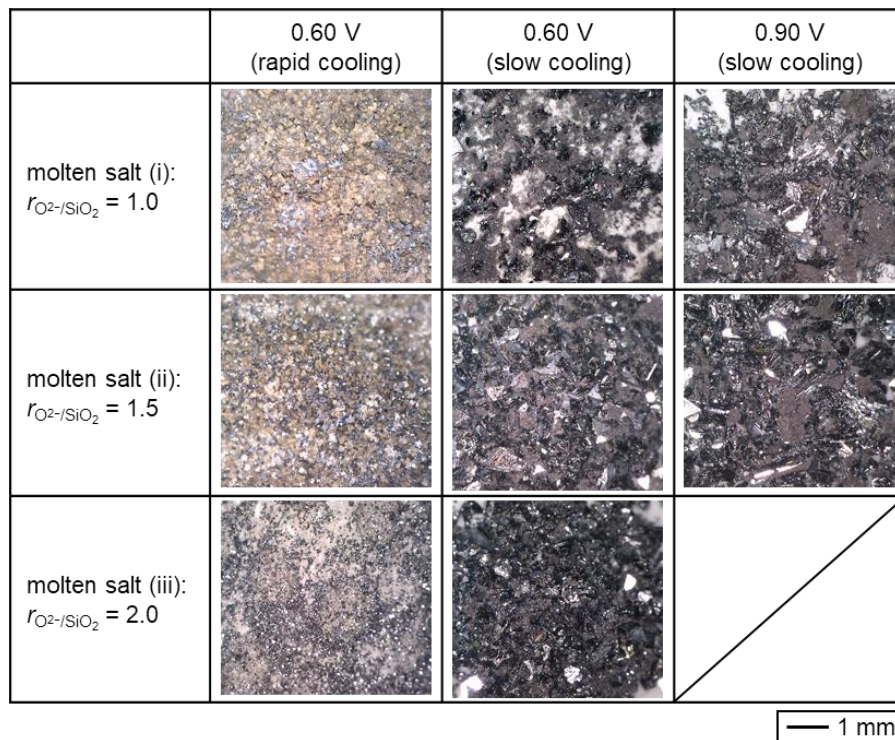


**Figure 5-9** Optical images of the Si particles recovered from the Zn electrodes after the electrolysis conducted in molten NaCl–CaCl<sub>2</sub> with the addition of (i) 1.0 mol% of CaSiO<sub>3</sub> ( $r_{\text{O}^{2-}/\text{SiO}_2} = 1.0$ ), (ii) 0.5 mol% of CaO and 1.0 mol% of CaSiO<sub>3</sub> ( $r_{\text{O}^{2-}/\text{SiO}_2} = 1.5$ ), and (iii) 1.0 mol% of CaO and 1.0 mol% of CaSiO<sub>3</sub> ( $r_{\text{O}^{2-}/\text{SiO}_2} = 2.0$ ) at 1123 K. Charge: –590.3 C (theoretical formation of 1.0 mol% Si–Zn alloy).

rapid cooling, brown-color fine powders and small Si granules with a metallic luster were obtained. Larger granules with a metallic luster were mainly precipitated with the slow cooling, which was same to the results obtained at 1023 K. Figure 5-10 shows the SEM images of the samples. The precipitated Si obtained by rapid cooling was the mixture of entangled Si wires and angular Si crystals with a size of several tens of micrometers. After the slow cooling, the size of Si granules increased to several hundred micrometers. Similar to the results obtained at 1023 K, no significant difference in particle size or crystal shape was observed in all samples, because all Si particles were precipitated from Zn electrodes with the same cooling condition.

The weight of the recovered Si and the current efficiency calculated from the Si weight are listed in Table 5-3. The current efficiency was calculated by equations (5-5) and (5-6). Table 5-4 lists the concentrations of Ca and Na in the liquid Zn electrodes. Similar to the result obtained at 1023 K, no Na was detected in all samples, indicating that the formed alloy was only Ca–Zn

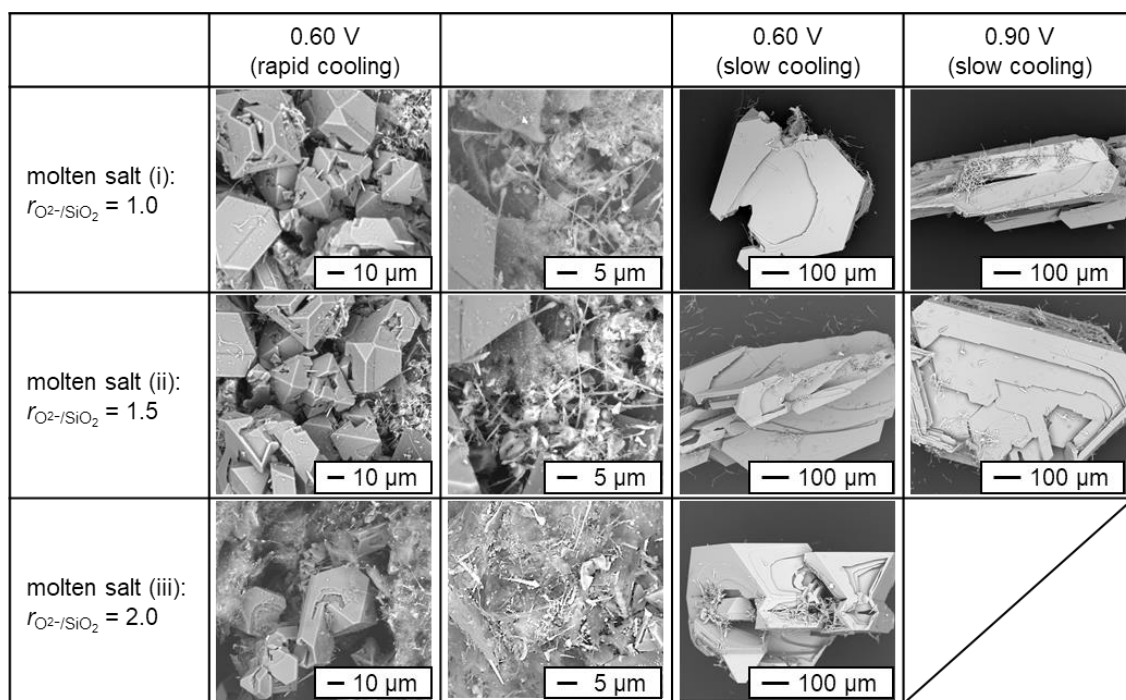


**Figure 5-10** SEM images of the Si particles recovered from the Zn electrodes after the electrolysis conducted in molten NaCl–CaCl<sub>2</sub> with the addition of (i) 1.0 mol% of CaSiO<sub>3</sub> ( $r_{\text{O}^{2-}/\text{SiO}_2} = 1.0$ ), (ii) 0.5 mol% of CaO and 1.0 mol% of CaSiO<sub>3</sub> ( $r_{\text{O}^{2-}/\text{SiO}_2} = 1.5$ ), and (iii) 1.0 mol% of CaO and 1.0 mol% of CaSiO<sub>3</sub> ( $r_{\text{O}^{2-}/\text{SiO}_2} = 2.0$ ) at 1123 K. Charge: –590.3 C (theoretical formation of 1.0 mol% Si–Zn alloy).

**Table 5-3** Weight of the recovered Si particles and the current efficiency calculated from Si weight after the electrolysis conducted in molten NaCl–CaCl<sub>2</sub> with the addition of (i) 1.0 mol% of CaSiO<sub>3</sub> ( $r_{O^{2-}/SiO_2} = 1.0$ ), (ii) 0.5 mol% of CaO and 1.0 mol% of CaSiO<sub>3</sub> ( $r_{O^{2-}/SiO_2} = 1.5$ ), and (iii) 1.0 mol% of CaO and 1.0 mol% of CaSiO<sub>3</sub> ( $r_{O^{2-}/SiO_2} = 2.0$ ) at 1123 K. Charge: –590.3 C (theoretical formation of 1.0 mol% Si–Zn alloy).

| Ratio of O <sup>2-</sup> /SiO <sub>2</sub><br>in molten salt<br>( $r_{O^{2-}/SiO_2}$ ) | Weight of recovered Si, $w_{act.}$ / g |                     |                     | Current efficiency, $\eta$ / % |                     |                     |
|--|--|---------------------|---------------------|--------------------------------|---------------------|---------------------|
|  | 0.60 V <sup>a</sup>                    | 0.60 V <sup>b</sup> | 0.90 V <sup>b</sup> | 0.60 V <sup>a</sup>            | 0.60 V <sup>b</sup> | 0.90 V <sup>b</sup> |
| (i) 1.0  | 0.0218                                 | 0.0350              | 0.0192 <sup>*</sup> | 50.7                           | 81.4                | 71.4                |
| (ii) 1.5   | 0.0216                                 | 0.0351              | 0.0286              | 50.3                           | 81.7                | 66.6                |
| (iii) 2.0  | 0.0220                                 | 0.0359              | –                   | 51.2                           | 83.6                | –                   |

<sup>a</sup> Cooled by natural heat dissipation (rapid cooling).

<sup>b</sup> Cooled at a rate of 20 K h<sup>-1</sup> (slow cooling).

<sup>\*</sup> Charge: –369.7 C

**Table 5-4** Concentrations of Ca and Na in the Zn electrodes after the electrolysis conducted in molten NaCl–CaCl<sub>2</sub> with the addition of (i) 1.0 mol% of CaSiO<sub>3</sub> ( $r_{O^{2-}/SiO_2} = 1.0$ ), (ii) 0.5 mol% of CaO and 1.0 mol% of CaSiO<sub>3</sub> ( $r_{O^{2-}/SiO_2} = 1.5$ ), and (iii) 1.0 mol% of CaO and 1.0 mol% of CaSiO<sub>3</sub> ( $r_{O^{2-}/SiO_2} = 2.0$ ) at 1123 K. Charge: –590.3 C (theoretical formation of 1.0 mol% Si–Zn alloy).

| Ratio of O <sup>2-</sup> /SiO <sub>2</sub><br>in molten salt<br>( $r_{O^{2-}/SiO_2}$ ) | Ca concentration in the Zn electrodes<br>after electrolysis, $x_{Ca}$ / ppmw |                     |                     | Na concentration in the Zn electrodes<br>after electrolysis, $x_{Na}$ / ppmw |                     |                     |
|--|--|---------------------|---------------------|--|---------------------|---------------------|
|  | 0.60 V <sup>a</sup>  | 0.60 V <sup>b</sup> | 0.90 V <sup>b</sup> | 0.60 V <sup>a</sup>  | 0.60 V <sup>b</sup> | 0.90 V <sup>b</sup> |
| (i) 1.0  | 5109   | 422                 | 27 <sup>*</sup>     | – <sup>†</sup>   | – <sup>†</sup>      | – <sup>†</sup>      |
| (ii) 1.5   | 5385   | 704                 | 18                  | – <sup>†</sup>   | – <sup>†</sup>      | – <sup>†</sup>      |
| (iii) 2.0  | 5133   | 629                 | –                   | – <sup>†</sup>   | – <sup>†</sup>      | –                   |

<sup>a</sup> Cooled by natural heat dissipation (rapid cooling).

<sup>b</sup> Cooled at a rate of 20 K h<sup>-1</sup> (slow cooling).

<sup>†</sup> Not detected.

<sup>\*</sup> Charge: –369.7 C

during the electrolysis at 1123 K. For the samples obtained at 0.60 V with rapid cooling, the current efficiencies were approximately 50% and the Ca concentrations were higher than 5000 ppmw. Compared with the samples obtained at 1023 K, the current efficiency was lower and the Ca concentration was higher, suggesting that the ratio of Ca–Zn alloy formation increased at 1123 K. With slow cooling, the current efficiencies increased from 50% to more than 80% and the Ca concentration decreased to 400–700 ppmw, indicating the indirect reduction of silicate ions by Ca–Zn alloy. For the samples obtained at 0.90 V, the current efficiencies were 71.4% in molten salt (i) and 66.6% in molten salt (ii). Approximately 30 ppmw of Ca was likely due to the residual silicate salt. Although the samples obtained at 0.90 V showed higher current efficiencies than those obtained at 1023 K, the efficiencies were still lower than those obtained at 0.60 V. As in the case of 1023 K, the reason is considered to be that the reduction current of silicate ions is considered to be not sufficiently large compared to the background current.

As in the case of 1023 K described in 5.3.2.1, experiments were conducted to confirm the indirect reduction by Ca–Zn alloy. Figure 5-11(a) shows the current transient curve during the electrolysis for the preparation of Ca–Zn alloy at 0.60 V. After two samples of Ca–Zn alloy were prepared, one sample was then analyzed by ICP-AES; the concentration of Ca was detected to be

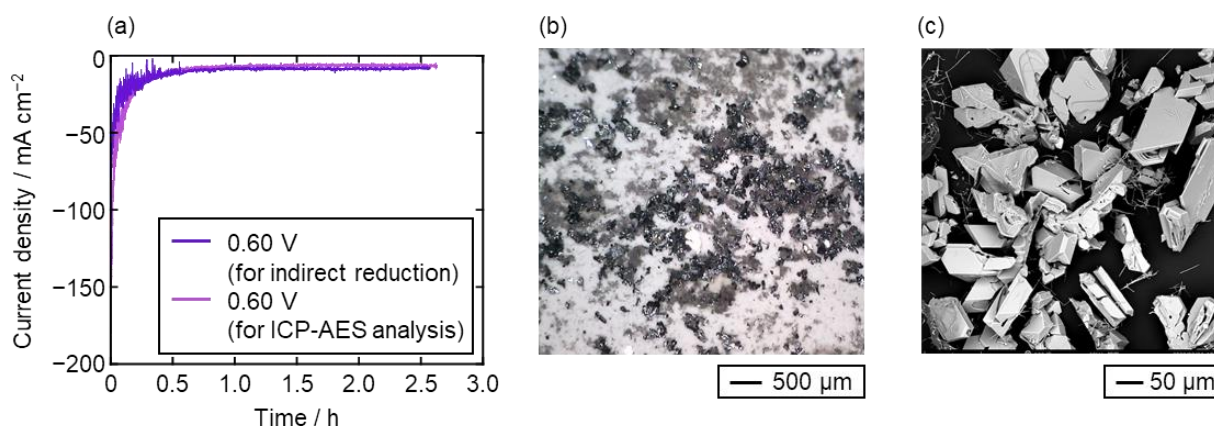


**Figure 5-11** (a) Current transient curves during the electrolysis at liquid Zn electrode in molten NaCl–CaCl<sub>2</sub>, (b) optical image and (c) surface SEM image of the Si particles recovered from the Zn electrode after the slow cooling in molten NaCl–CaCl<sub>2</sub> with the addition of 1.0 mol% of CaO and 1.0 mol% of CaSiO<sub>3</sub> ( $r_{O^{2-}/SiO_2} = 2.0$ ) at 1123 K.

4771 ppmw. The current efficiency for the formation of Ca–Zn alloy was calculated to be 74.9%. The other sample was placed in the molten salt (iii) and cooled with the same slow cooling condition. After the slow cooling, Si particles were recovered from the Zn electrode and Ca was not detected by ICP-AES. Optical and SEM images of the recovered Si particles are also shown in [Figure 5-11](#). Similar with the sample obtained at 1023 K, the Si granules showed a metallic luster with a size of approximately 100  $\mu\text{m}$ . The current efficiency calculated from the weight of recovered Si was 49.9%. The current efficiencies for both the Ca–Zn alloy formation and the indirect reduction by Ca–Zn alloy were lower than those obtained at 1023 K. Ca is known to dissolve in molten  $\text{CaCl}_2$ , and its solubility increases with increasing temperature [1–3]. Since the activity of Ca in Ca–Zn alloys is smaller than unity, the dissolved concentration is expected to be smaller than that of Ca metal; however, the dissolved concentration is expected to increase with increasing temperature, similar to that of Ca metal. Therefore, the lower current efficiencies at 1123 K are likely due to the higher dissolution rate of Ca into molten salt than that at 1023 K.

## 5.4 Conclusion

The electrochemical reduction of silicate ions at a liquid Zn electrode was conducted in molten  $\text{NaCl-CaCl}_2$  at 1023 K and 1123 K. From the cyclic voltammetry conducted at 1023 K, the electrochemical reduction of  $\text{SiO}_3^{2-}$  was observed from 1.1 V and  $\text{SiO}_4^{4-}$  from 0.95 V. The simultaneous reactions of the electrochemical reduction of silicate ions and the formation of Ca–Zn and/or Na–Zn alloy were suggested from 0.80 V. As the results of potentiostatic electrolysis, high current efficiencies of more than 95% were obtained in the samples obtained at 0.60 V with slow cooling. From the results of ICP-AES analysis, the formed alloy was confirmed to be Ca–Zn only. Although the formation of Ca–Zn alloy proceeded at 0.60 V, the high current efficiencies were achieved because of the indirect reduction of silicate ions by Ca–Zn alloy during the slow cooling period. The current efficiencies for samples obtained at 0.90 V were lower than that at 0.60 V; the reason is considered to be that the reduction current of silicate ions is considered to be not

sufficiently large compared to the background current. As the results of cyclic voltammetry at 1123 K, the electrochemical reduction of  $\text{SiO}_3^{2-}$  was observed from 1.3 V and that of  $\text{SiO}_4^{4-}$  from 1.0 V. The simultaneous reactions of the electrochemical reduction of silicate ions and the formation of Ca–Zn were suggested from 0.85 V. For the samples obtained at 0.60 V with slow cooling, the current efficiencies were lower than those obtained at 1023 K, suggesting higher dissolution rate of Ca from Ca–Zn into molten salt at higher temperature.

## 5.5 Reference List

- [1] D. D. Cubicciotti and C. D. Thurmond, *J. Am. Chem. Soc.*, **71**, 2149 (1949).
- [2] J. A. Sanchez and R. Monnier, *Rev. Int. Hautes Temper. Refract. Fr.*, **16**, 5 (1979).
- [3] S. Shaw and R. Watson, *ECS Trans.*, **16**, 301 (2009).



## Chapter 6

# Silicon Refining by Solidification from Liquid Si–Zn Alloy and Floating Zone Method

### 6.1 Introduction

In previous chapters, the author investigated the electrochemical reduction behavior of solid SiO<sub>2</sub> and dissolved SiO<sub>2</sub> in the electrolysis step. In this chapter, the author focused on the behavior of impurity elements in the precipitation and refining steps (Figure 1-9). Firstly, the distribution behavior of impurity elements between the solid Si and the liquid Zn was calculated from thermodynamic data at 923 K. Then, the behavior of impurity elements in the precipitation step was experimentally evaluated using a liquid Si–Zn alloy, which was prepared from low-purity metallurgical-grade Si (MG-Si). Finally, the precipitated Si was melted and refined using the floating zone (FZ) melting method to analyze the behavior of impurities in the refining step.

### 6.2 Experimental

#### 6.2.1 Si Refining by Solidification from Liquid Si–Zn Alloy

Figure 6-1 shows a schematic drawing of the experimental apparatus for the precipitation of solid Si from a liquid Si–Zn alloy. 885 g of metallic Zn (FUJIFILM Wako Pure Chemical Corp., reagent grade, granule) and 197 g of CaCl<sub>2</sub> (Kojundo Chemical Laboratory Co., Ltd., >99%) were charged in a graphite crucible (Toyo Tanso Co., Ltd., IG-110 grade, o.d. 80 mm × i.d. 70 mm × height 200 mm) and dried under vacuum at 773 K overnight. The evaporation of metallic Zn was suppressed by submerging the Si–Zn alloy in molten CaCl<sub>2</sub>. After the temperature was increased



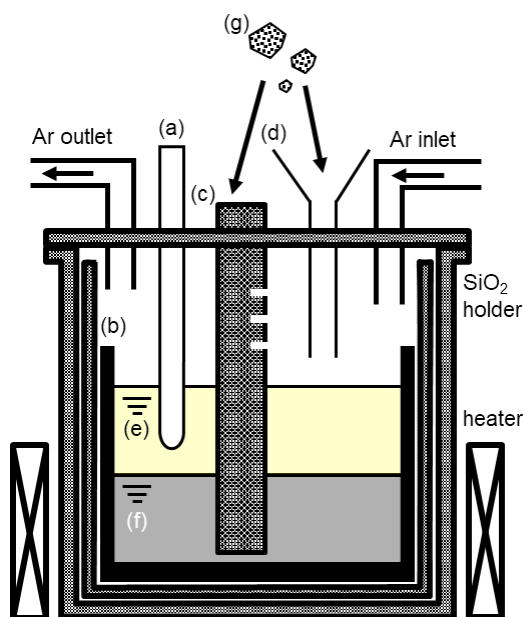


**Figure 6-1** Schematic drawing of the experimental apparatus for the precipitation of solid Si from a liquid Si–Zn alloy. (a) Thermocouple, (b) graphite crucible, (c) carbon tube (Exp. (1)), (d) funnel (Exp. (2)), (e) molten CaCl<sub>2</sub>, (f) liquid Zn, and (g) MG-Si.

to 1123 K in a dry Ar atmosphere, 20.0 g of MG-Si, which is equivalent to 5.0 at.% of the prepared Si–Zn alloy, was charged through a carbon tube (Experiment 1) or a glass funnel (Experiment 2). The carbon tube had several holes cut at the face of the tube side to maintain both bath level and gas pressure equalization between the inside and outside of the tube.

After the temperature was maintained at 1123 K for more than 24 h to sufficiently react Si and Zn, the liquid Si–Zn alloy was cooled. Figure 6-2 shows the temperature changes during the cooling step. In Experiment 1, the temperature was decreased from 1123 K to 723 K over 20 h, then maintained at 723 K for 5 h, and further reduced to 298 K over 20 h. In Experiment 2, the temperature was decreased from 1123 K to 773 K over 35 h, then maintained at 773 K for 10 h, and further decreased to 298 K over 5 h. A lump of Zn metal was recovered from the crucible after dissolution of CaCl<sub>2</sub> with distilled water. The Zn metal lump was dissolved in a 20 wt.% HCl solution prepared from a 36 wt.% solution to recover the precipitated Si granules. The recovered Si granules were then immersed in a 10 wt.% HCl solution (prepared from the 36 wt.% solution) overnight.

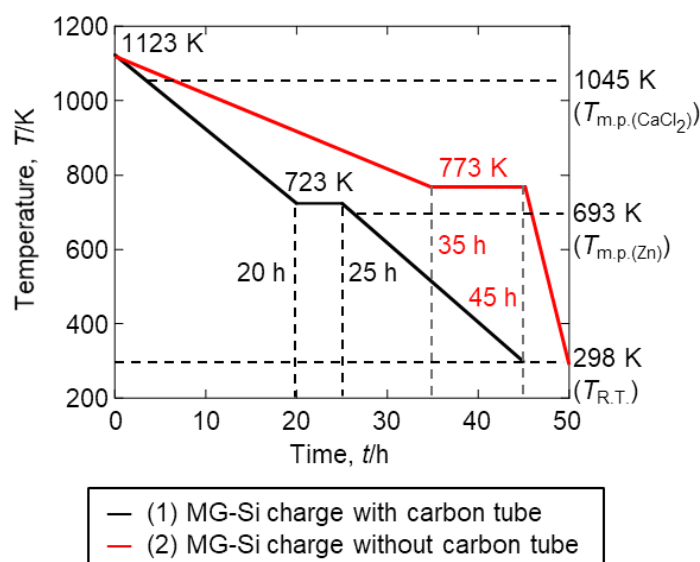


**Figure 6-2** Temperature changes during the cooling step.

### 6.2.2 Si Refinement and Zn Evaporation by the FZ Method

A portion of the Si granules recovered in the precipitation experiment (Experiment 2) was crushed into powder in an agate mortar. Si powder with sizes below 0.1 mm was selected by a sieve and molded into a cylinder with a diameter of approximately 7 mm by isostatic pressing under a pressure of 60 MPa for 1 min. The molded Si cylinder was hung with a platinum wire and inserted into a quartz tube of a floating zone furnace (Canon Machinery Inc., Desktop type A) as a feed Si, as shown in Figure 6-3. A 10N-purity polycrystalline Si rod (Furuuchi Chemical Corp., diameter 5.0 mm) was used as the seed Si. The zone melting was conducted twice to evaporate the residual Zn to obtain a Si ingot in an inverse Ar stream with a uniform speed of 20–30 mm h<sup>-1</sup> and a lamp voltage of 55–65 V. Si wafers were cut out from the prepared Si ingot using a diamond wheel saw (South Bay Technology Inc., SBT650).

### 6.2.3 Impurity Analysis of Si Samples

The analyses of impurity elements in the Si samples were conducted using the high-frequency combustion–infrared absorption method (LECO, CS-LS600) for carbon analysis, inert

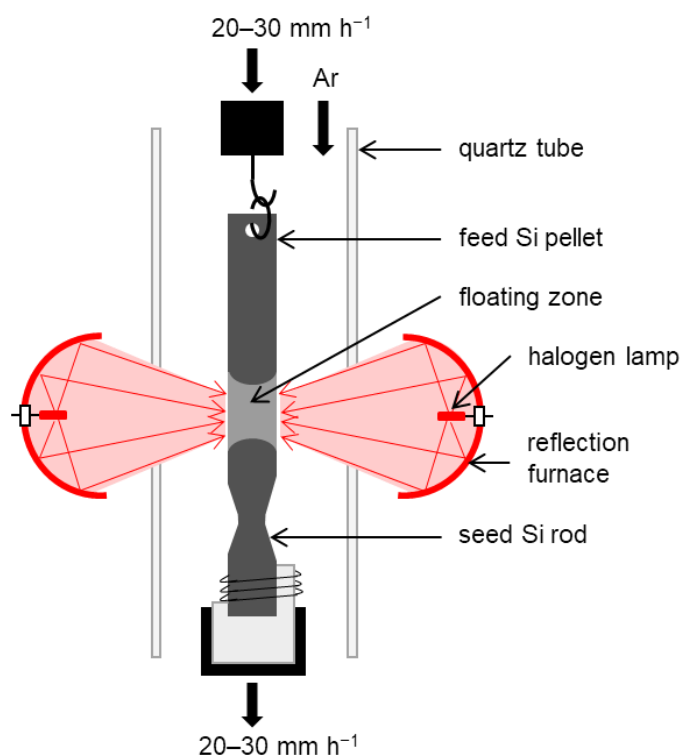


**Figure 6-3 Schematic drawing of the floating zone (FZ) melting method.**

gas fusion–infrared absorption method (LECO, TC600) for oxygen analysis, and glow discharge mass spectrometry (GD-MS; VG Elemental, VG 9000) for the other elements. Si samples were immersed in a HCl solution (20–25 wt.% prepared from the 36 wt.% solution) for 20 min and then washed with distilled water and acetone before GD-MS analysis.

### 6.3 Thermodynamic Calculations

In order to predict the purification ability of the precipitation step, the distribution behavior of the impurity elements was evaluated. When the temperature was lowered to 923 K from the electrolysis temperature of 1123 K, solid Si corresponding to 5 at.% was recovered. Although the liquid Zn equilibrated with solid Si at 923 K contains 1 at.% Si, the distribution behavior of impurities was evaluated assuming that the liquid Zn contained no Si. That is, the distribution coefficients of impurities between solid Si and liquid Zn were calculated at infinite dilution.

When the standard state of impurity element A is defined as its pure stable state at 923 K, the activities of A in an equilibrium state are identical in both phases.

$$a_{A(\text{Zn}(l))} = a_{A(\text{Si}(s))} \quad (6-1)$$

The activity is the product of activity coefficient and mole fraction as follows:

$$\gamma_{A(\text{Zn}(l))} x_{A(\text{Zn}(l))} = \gamma_{A(\text{Si}(s))} x_{A(\text{Si}(s))} \quad (6-2)$$

Here,  $\gamma_{A(\text{Zn}(l))}$  and  $\gamma_{A(\text{Si}(s))}$  are the activity coefficients, and  $x_{A(\text{Zn}(l))}$  and  $x_{A(\text{Si}(s))}$  are the mole fractions of A in liquid Zn and solid Si, respectively. The activity coefficient,  $\gamma_A$ , is identical to the activity coefficient at infinite dilution,  $\gamma_A^\circ$ , when the concentration is low enough and the Henry's law can be applied. Thus, the distribution coefficient of A at infinite dilution,  $k_A^\circ$ , is defined as the ratio of the mole fraction of A in solid Si phase to that in the liquid Zn phase as follows:

$$k_A^\circ = \frac{x_{A(\text{Si}(s))}}{x_{A(\text{Zn}(l))}} \quad (6-3)$$

$$= \frac{\gamma_{A(\text{Zn}(l))}^\circ}{\gamma_{A(\text{Si}(s))}^\circ} \quad (6-4)$$

where,  $\gamma_{A(\text{Zn}(l))}^\circ$  and  $\gamma_{A(\text{Si}(s))}^\circ$  are the activity coefficients of A at infinite dilution in liquid Zn and solid Si, respectively. Although the equilibrium expressed in [equation \(6-1\)](#) is attained for the A–Zn–Si ternary system, the value of  $\gamma_{A(\text{Zn}(l))}^\circ$  and  $\gamma_{A(\text{Si}(s))}^\circ$  can be calculated from A–Zn and A–Si binary systems with the assumption that interactions between impurity and Zn in solid Si and that between impurity and Si in liquid Si can be ignored.

Typical impurity elements of B, C, O, P, Al, Ca, Fe, and Ti were selected for the present evaluation. Since the temperature dependences of  $\gamma_A^\circ$  have been already reported for B–Si [\[1\]](#), Al–Si [\[2\]](#), and Al–Zn [\[3\]](#) binary systems, the values at 923 K were calculated based on these reports. For other systems,  $\gamma_A^\circ$  was evaluated from the phase diagrams and thermodynamic data. [Table 6-1](#) summarizes the equilibrated phases with saturated solid Si or liquid Zn at 923 K, which are given by the binary phase diagrams for the A–Si and A–Zn systems [\[4, 5\]](#). Furthermore, their standard

**Table 6-1** Equilibrated phases with saturated solid Si or liquid Zn at 923 K and their standard Gibbs energy of formation at 923 K.

| Impurity element, A | Equilibrated phase at 923 K / Standard Gibbs energy of formation at 923 K,<br>$\Delta G^\circ_f$ (kJ mol <sup>-1</sup> ) |  |
|---------------------|--|--|
|                     | Solid Si   | Liquid Zn  |
| B                   | SiB <sub>3</sub> (s) / - <sup>a</sup>  | B (s) / 0  |
| C                   | SiC (s) / -65.920 [6]  | C (s) / 0  |
| O                   | SiO <sub>2</sub> (s) / -743.753 [6]  | ZnO (s) / -255.998 [7, 8]                            |
| P                   | SiP (s) / -38.843 [7, 9, 10]   | Zn <sub>3</sub> P <sub>2</sub> (s) / -83.504 [7, 11] |
| Al                  | Al-Si (l) / - <sup>a</sup>   | - <sup>b</sup> / - <sup>a</sup>                      |
| Ca                  | CaSi <sub>2</sub> (s) / -123.916 [9, 10, 12]   | CaZn <sub>13</sub> (s) / -108.861 [13–17]            |
| Fe                  | FeSi <sub>2</sub> (s) / -70.483 [18]   | FeZn <sub>7</sub> (s) / -12.030 [19]                 |
| Ti                  | TiSi <sub>2</sub> (s) / -164.702 [9, 20]   | TiZn <sub>3</sub> (s) / -57.604 [21]                 |

<sup>a</sup> The data were not used to calculate the activity coefficient at infinite dilution because the reported coefficient was used in this study.

<sup>b</sup> Liquid Al-Zn alloy has a wide composition range.

Gibbs energy of formation,  $\Delta G^\circ_f$ , at 923 K is also given in Table 6-1 [6–21].

For some cases, the equilibrium between solid Si and compound  $A_ySi_z$  is considered, where  $y$  and  $z$  are the stoichiometry of the compound. In an equilibrium state, the activities of A in the Si phase,  $a_{A(Si(s, sat))}$ , and in the  $A_ySi_z$  phase,  $a_{A(A_ySi_z)}$ , are identical. It is applicable in the similar manner to the activities of Si  $a_{Si(Si(s, sat))}$  and  $a_{Si(A_ySi_z)}$ .

$$a_{A(Si(s, sat))} = a_{A(A_ySi_z)} \quad (6-5)$$

$$a_{Si(Si(s, sat))} = a_{Si(A_ySi_z)} \quad (6-6)$$

The Gibbs energy of formation of  $A_ySi_z$ ,  $\Delta G^\circ_f(A_ySi_z)$ , is given by the following equation:

$$\Delta G^\circ_f(A_ySi_z) = RT \ln \left( \frac{a_{A(A_ySi_z)}^y a_{Si(A_ySi_z)}^z}{a_{A_ySi_z(A_ySi_z)}} \right) \quad (6-7)$$

Here,  $R$  is the gas constant ( $8.3145 \text{ J mol}^{-1} \text{ K}^{-1}$ ), and  $T$  is the absolute temperature, and  $a_{A_ySi_z(A_ySi_z)}$  is the activity of  $A_ySi_z$  in the  $A_ySi_z$  compound. Here, the standard state of  $A_ySi_z$  is its pure stable state at 923 K. If there is no solubility of  $A_ySi_z$  in other phases,  $a_{A_ySi_z(A_ySi_z)}$  is regarded as unity.

$$a_{A_ySi_z(A_ySi_z)} = 1 \quad (6-8)$$

The activity of Si in the solid Si phase is also regarded as unity because the amount of impurities in the Si phase is very small.

$$a_{Si(Si(s, \text{sat}))} = 1 \quad (6-9)$$

From these equations, the activity of A in the solid Si phase is obtained from the following equation:

$$a_{A(Si(s, \text{sat}))} = \exp\left(\frac{\Delta G_f^\circ(A_ySi_z)}{yRT}\right) \quad (6-10)$$

Then,  $\gamma_{A(Si(s))}^\circ$  is calculated from the solubility of A in the solid Si phase,  $x_{A(Si(s, \text{sat}))}$ , as follows:

$$\gamma_{A(Si(s))}^\circ = \frac{a_{A(Si(s, \text{sat}))}}{x_{A(Si(s, \text{sat}))}} \quad (6-11)$$

$$= \frac{\exp\left(\frac{\Delta G_f^\circ(A_ySi_z)}{yRT}\right)}{x_{A(Si(s, \text{sat}))}} \quad (6-12)$$

In the similar manner,  $\gamma_{A(Zn(l))}^\circ$  is obtained by replacing  $Si(s)$  with  $Zn(l)$  in the above discussion. Here, the activity of Zn in the  $Zn(l)$  phase,  $a_{Zn(Zn(l, \text{sat}))}$ , needs further consideration. As shown in the phase diagrams, the solubility of impurities in the liquid Zn phase can reach several atomic percent at 923 K. Therefore, the value of  $a_{Zn(Zn(l, \text{sat}))}$  cannot be regarded as unity where the standard state is pure liquid Zn, but rather regarded as the mole fraction of Zn,  $x_{Zn(Zn(l, \text{sat}))}$ , assuming Raoult's law.

$$a_{Zn(Zn(l, \text{sat}))} = x_{Zn(Zn(l, \text{sat}))} \quad (6-13)$$

$$a_{Zn(A_yZn_z)} = a_{Zn(Zn(l, \text{sat}))} = 1 - x_{A(Zn(l, \text{sat}))} \quad (6-14)$$

Consequently, the value of  $\gamma_{A(\text{Zn}(l))}^{\circ}$  is obtained as follows:

$$a_{A(\text{Zn}(l, \text{sat}))} = (1 - x_{A(\text{Zn}(l, \text{sat}))})^{-\frac{z}{y}} \exp\left(\frac{\Delta G_{\text{f}}^{\circ}(A_y\text{Zn}_z)}{yRT}\right) \quad (6-15)$$

$$\gamma_{A(\text{Zn}(l))}^{\circ} = \frac{(1 - x_{A(\text{Zn}(l, \text{sat}))})^{-\frac{z}{y}} \exp\left(\frac{\Delta G_{\text{f}}^{\circ}(A_y\text{Zn}_z)}{yRT}\right)}{x_{A(\text{Zn}(l, \text{sat}))}} \quad (6-16)$$

Table 6-2 summarizes the solubilities of the impurity elements in solid Si and liquid Zn phases at 923 K [2, 4, 7, 16, 22–32]. The solubilities of P(Zn(l)), Al(Zn(l)), Ca(Zn(l)), Fe(Zn(l)), and Ti(Zn(l)) were read from the phase diagrams [4, 32]. Most of the other solubility values were calculated from the reported functions of solubility with regards to temperature [2, 4, 7, 16, 22–32]. As for B(Zn(l)), the solubility was calculated from the interaction parameter of liquid B–Zn under the assumption of regular solution model,  $\Omega_{\text{B,Zn}}$ ,  $2.98 \times 10^4 \text{ J mol}^{-1}$  at 923 K, reported by Chen *et al.* [24]. In this calculation, the standard state of B is not a pure solid B, but pure liquid B which is the stable phase at 923 K. When solid B and B-saturated liquid B–Zn are in an equilibrium state,

**Table 6-2 Solubility of each impurity element in solid Si and liquid Zn at 923 K.**

| Impurity element, A | Solubility  |             |  |                 |
|---------------------|---|-------------|--|-----------------|
|                     | In solid Si,<br>$x_{A(\text{Si}(s, \text{sat}))}$ | Ref. number | In liquid Zn,<br>$x_{A(\text{Zn}(l, \text{sat}))}$ | Ref. number     |
| B                   | $2.0 \times 10^{-4}$ <sup>a</sup>                 | [22]        | $4.7 \times 10^{-4}$                               | [7, 16, 23, 24] |
| C                   | $2.2 \times 10^{-11}$ <sup>a</sup>                | [25]        | $2.3 \times 10^{-5}$ <sup>a</sup>                  | [2]             |
| O                   | $1.2 \times 10^{-6}$ <sup>a</sup>                 | [26]        | $3.6 \times 10^{-4}$                               | [27]            |
| P                   | $3.8 \times 10^{-3}$ <sup>a</sup>                 | [28]        | $1.0 \times 10^{-2}$                               | [4]             |
| Al                  | $5.0 \times 10^{-5}$ <sup>a</sup>                 | [2]         | 0.97   | [4]             |
| Ca                  | $6.5 \times 10^{-6}$ <sup>a</sup>                 | [29]        | $3.0 \times 10^{-2}$                               | [4]             |
| Fe                  | $3.2 \times 10^{-13}$ <sup>a</sup>                | [30]        | $2.0 \times 10^{-2}$                               | [4]             |
| Ti                  | $4.7 \times 10^{-17}$ <sup>a</sup>                | [31]        | $5.0 \times 10^{-3}$                               | [32]            |

<sup>a</sup> Extrapolated values

the activity of B in liquid B–Zn with liquid B as the standard state,  $a_{B(l, Zn(l, sat))}$ , is expressed by the Gibbs energy of fusion of B,  $\Delta G_{fus}(B)$ .

$$\ln\left(\frac{a_{B(l, Zn(l, sat))}}{a_{B(l)}}\right) = -\frac{\Delta G_{fus}(B)}{RT} \quad (6-17)$$

Since its standard state is pure liquid ( $a_{B(l)} = 1$ ),

$$\ln a_{B(l, Zn(l, sat))} = -\frac{\Delta G_{fus}(B)}{RT} \quad (6-18)$$

is given. Then,  $a_{B(l, Zn(l, sat))}$  is calculated to be  $2.29 \times 10^{-2}$  at 923 K from the reported  $\Delta G_{fus}(B)$  value of  $2.90 \times 10^4 \text{ J mol}^{-1}$  [7, 16, 17]. In the equilibrium state, the following equation holds.

$$RT \ln a_{B(l, Zn(l, sat))} = \Omega_{B,Zn}(1 - x_{B(Zn(l, sat))})^2 + RT \ln x_{B(Zn(l, sat))} \quad (6-19)$$

By substituting  $a_{B(l, Zn(l, sat))} = 2.29 \times 10^{-2}$  and  $\Omega_{B,Zn} = 2.98 \times 10^4$ , the value of  $x_{B(Zn(l, sat))}$  was calculated to be  $4.7 \times 10^{-4}$ .

The calculated activity coefficients of impurity elements at infinite dilution in the solid Si and the liquid Zn are summarized in Table 6-3. Then, the distribution coefficients can be calculated using Eq. 6-1, which are also listed in Table 6-3. The distribution coefficient of O ( $1.2 \times 10^4$ ) is substantially large, indicating that almost all the O impurity in the liquid Si–Zn alloy transfers to solid Si. On the other hand, the distribution coefficients of C, Al, Ca, Fe, and Ti are  $5.1 \times 10^{-3}$ ,  $7.9 \times 10^{-5}$ ,  $2.3 \times 10^{-3}$ ,  $3.6 \times 10^{-8}$ , and  $2.4 \times 10^{-9}$ , respectively. Thus, these impurities are considered to remain in the liquid Si–Zn alloy during the precipitation step. The removal of B and P is known to be difficult in simple solidification refining from liquid Si because of the large distribution coefficients, that is, 0.8 for B and 0.35 for P [33]. In the present calculation, the distribution coefficients are 0.15 for B and 0.26 for P. The obtained smaller values compared to those for the Si(s)/Si(l) system demonstrate that the effective removal of B and P is possible by utilizing the liquid Si–Zn alloy system. All of these calculations indicate that the electrolytic process using a liquid Si–Zn alloy as a cathode has the advantages of high refining ability and high resistance



**Table 6-3 Activity coefficient of each impurity element at infinite dilution in the solid Si and the liquid Zn with the standard states of their stable phase and distribution coefficient between the solid Si and the liquid Zn at 923 K.**

| Impurity element, A | Activity coefficient at infinite dilution |   | Distribution coefficient, $k_A^{\circ}$ <sup>a</sup> |
|---------------------|---|---|--|
|                     | In solid Si, $\gamma_{A(Si(s))}^{\circ}$  | In liquid Zn, $\gamma_{A(Zn(l))}^{\circ}$ |  |
| B                   | $1.4 \times 10^4$ [1]                     | $2.1 \times 10^3$                         | $1.5 \times 10^{-1}$                                 |
| C                   | $8.6 \times 10^6$                         | $4.4 \times 10^4$                         | $5.1 \times 10^{-3}$                                 |
| O                   | $7.8 \times 10^{-16}$                     | $9.2 \times 10^{-12}$                     | $1.2 \times 10^4$                                    |
| P                   | 1.7                                       | $4.4 \times 10^{-1}$                      | $2.6 \times 10^{-1}$                                 |
| Al                  | $3.3 \times 10^4$ [2]                     | 2.6 [3]                                   | $7.9 \times 10^{-5}$                                 |
| Ca                  | $1.5 \times 10^{-2}$                      | $3.4 \times 10^{-5}$                      | $2.3 \times 10^{-3}$                                 |
| Fe                  | $3.3 \times 10^8$                         | 1.2 × 10                                  | $3.6 \times 10^{-8}$                                 |
| Ti                  | $4.6 \times 10^7$                         | $1.1 \times 10^{-1}$                      | $2.4 \times 10^{-9}$                                 |

<sup>a</sup>  $k_A^{\circ} = \gamma_{A(Zn(l))}^{\circ} / \gamma_{A(Si(s))}^{\circ}$

against impurity inclusion. Even when carbon is deposited onto the cathode by the reduction of  $CO_3^{2-}$  ions produced at a carbon anode, it is not contained in the solid Si phase in the precipitation step. The applicability of graphite anodes in the electrolysis step is a significant advantage for practical applications.

For reference, the distribution coefficients of B for the liquid Si–Al alloy were reported to be 0.49 at 1473 K and 0.22 at 1273 K [1], and those of P were 0.12 at 1373 K and 0.061 at 1173 K [34]. The distribution coefficients of both elements become smaller at lower temperatures. Although 923 K is even lower than the cases of the liquid Si–Al alloy, the distribution coefficients of the liquid Si–Zn alloy, 0.15 for B, and 0.26 for P, are smaller than those for the Si–Al alloy. This is explained by the fact that the affinity of Zn to these impurities is lower than that of Al.

## 6.4 Results and Discussion

### 6.4.1 Si Refining by Solidification from Liquid Si–Zn Alloy and the FZ Method

Figure 6-4(a) shows an optical image of the top view of the Zn lump obtained from the precipitation experiment (1). The top portion consists of a metallic-luster main body and gray–blue parts. Although the bottom part cannot be seen from the figure, the entire bottom showed a metallic luster. Figure 6-4(b) shows a cross-sectional SEM image of the Zn lump. The top portion contained many 100–1000- $\mu\text{m}$  particles. From EDX analysis, only Si was detected for the precipitated particles, while only Zn was detected in the main body. Most precipitated particles were observed at the top of the lump, and a small amount of Si particles were also found at the edge of the middle part of the lump. Considering the densities of liquid Zn,  $\rho_{\text{Zn}(l)} = 6.56 \text{ g cm}^{-3}$  [35], and solid Si,  $\rho_{\text{Si}(s)} = 2.32 \text{ g cm}^{-3}$  [36], at 723 K, Si particles floated at the top of the liquid Zn in the duration of

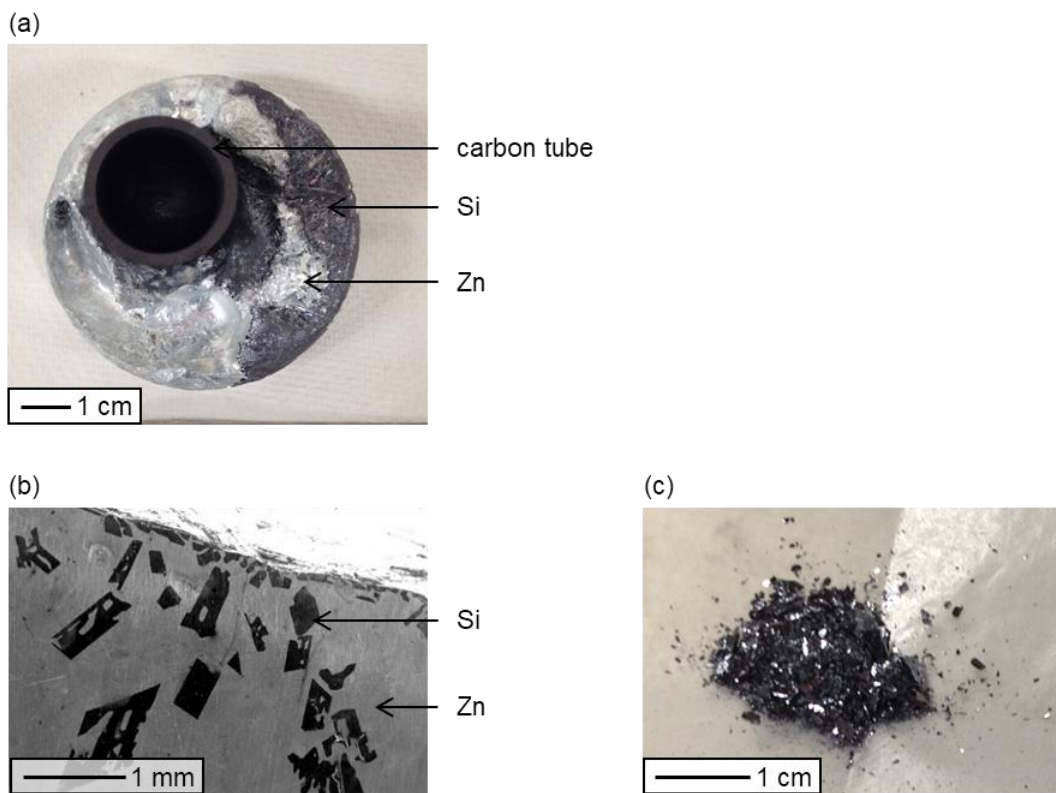


Figure 6-4 (a) Optical image of a top view and (b) SEM image of a cross section of the Zn lump obtained after the precipitation experiment (1) in molten  $\text{CaCl}_2$ , and (c) optical image of the Si granules recovered after acid leaching of the Zn lump.

precipitation. Figure 6-4(c) shows an optical image of the Si granules recovered after acid leaching of the Zn lump. The granules show a size of approximately 1 mm and exhibit a metallic luster.

Figure 6-5 shows a cross-sectional SEM image of the Zn lump obtained from the precipitation experiment (2). Similar to the Zn lump obtained from experiment (1), many Si particles were precipitated in the upper part. On the other hand, the image shows much larger size particles of 300–2000  $\mu\text{m}$  and more inclusion of Zn into the gaps of Si granules, compared with experiment (1). This result was attributed to the progressive crystal growth of Si particles during precipitation at a lower cooling rate (experiment (1):  $20 \text{ K h}^{-1}$ , (2):  $10 \text{ K h}^{-1}$ ).

Figure 6-6(a) shows an optical image of the Si powder obtained by crushing the Si granules prepared in the precipitation experiment (2). From this Si powder, a Si ingot was obtained by FZ melting, as shown in Figure 6-6(b). The ingot showed a gray–blue metallic luster and a diameter of 3–5 mm and length of 25 mm. The non-uniform patterns observed on the surface

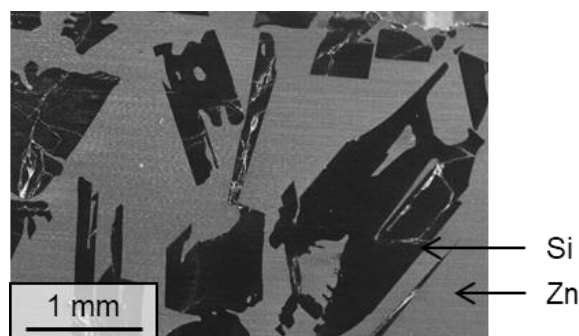


Figure 6-5 SEM image of a cross section of the Zn lump obtained after the precipitation experiment (2) in molten  $\text{CaCl}_2$ .

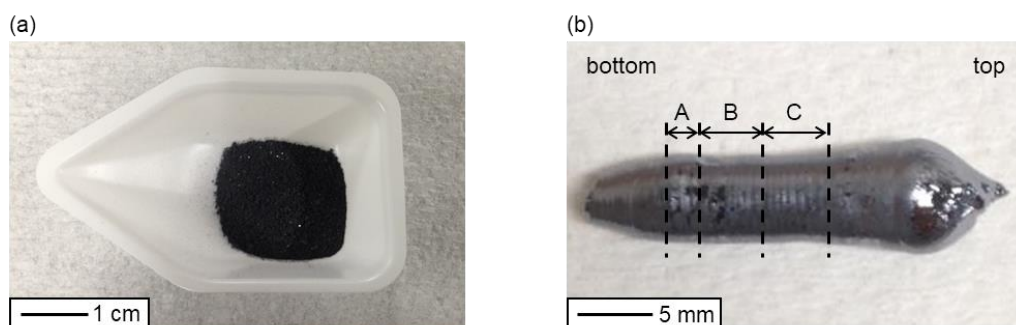


Figure 6-6 Optical images of (a) Si powder for Si ingot and (b) Si ingot obtained by FZ melting.

suggested that the Si ingot is polycrystalline. In general, the crystallinity can be improved by lowering the moving speed during FZ melting. The ingot was cut with a diamond wheel saw at the broken lines indicated in Figure 6-6(b). The sliced wafers were used to analyze the impurity contents. Specifically, parts A, B, and C were used for GD-MS analysis, carbon analysis, and oxygen analysis, respectively.

#### 6.4.2 Impurity Analysis of Si Samples

Table 6-4 lists the impurity contents in the Si granules obtained in the precipitation experiments (1) and (2) and the Si wafers obtained by FZ melting. The values for the original MG-Si are also listed for reference. The removal fractions in the precipitation experiments,  $r_A$ , which were calculated from the contents in the original MG-Si,  $x_{A(\text{MG-Si})}$ , and the precipitated Si,  $x_{A(\text{prec Si})}$ , are shown in parentheses.

$$r_A = \left(1 - \frac{x_{A(\text{prec Si})}}{x_{A(\text{MG-Si})}}\right) \times 100 \quad (6-20)$$

For the precipitated Si granules, the removal fractions of Al, Ca, and Ti exceeded 99%, and the fractions of B, C, and Fe exceeded 90%. The high removal fractions agreed with the low distribution coefficients calculated in section 6.3. It is noteworthy that the removal fraction of B was more than 95%. The removal of B is known to be difficult in the solidification refining from liquid Si because the distribution coefficient between Si(s)/Si(l) is as high as 0.8 [33]. The removal of P has also been achieved at fractions of 54.2% and 66.7%. However, the removal fractions are smaller than expected, which might be due to the formation of a ZnSiP<sub>2</sub> compound with a melting point of 1643 K [37, 38]. Concerning the removal fraction of O, high values of 80.8% and 90.0% were obtained, which is inconsistent with the calculated distribution coefficient of  $1.2 \times 10^4$ . As the concentration of O in MG-Si was obviously higher than the solubility limit in the solid Si phase [39], the presence of some oxides, except for SiO<sub>2</sub>, such as CaO, in MG-Si was indicated. Thus, the dissolution of oxides into molten CaCl<sub>2</sub> contributed to the removal of O.

**Table 6-4 Impurity contents in Si samples with removal fractions and acceptable impurity levels for SOG-Si.**

| Impurity element, A | Impurity content in Si <sup>a</sup> , $x_A$ / ppmw<br>(Removal fraction †, $r_A$ ) |                  |                            |                           | Acceptable level for SOG-Si, $x_{A(SOG)}$ / ppmw |
|---------------------|--|------------------|----------------------------|---------------------------|--|
|                     | MG-Si  | Precipitated Si  |                            | Si wafer after FZ melting |  |
|                     |  | (1)              | (2)                        |                           |  |
| B                   | 11   | 0.6<br>(94.9%)   | 0.55<br>(95.0%)            | 1.9                       | 0.1–0.3  |
| P                   | 96   | 32<br>(66.7%)    | 44<br>(54.2%)              | 13                        | 0.03–0.14  |
| O                   | 400 <sup>b</sup>   | 77<br>(80.8%)    | 40 <sup>b</sup><br>(90.0%) | 10 <sup>b</sup>           | – <sup>d</sup>                                   |
| C                   | 2300 <sup>c</sup>  | 87<br>(96.2%)    | 20 <sup>b</sup><br>(99.1%) | 50 <sup>c</sup>           | <10  |
| Al                  | 770  | <0.5<br>(>99.9%) | <b>0.07</b><br>(>99.9%)    | <b>0.05</b>               | <0.1   |
| Ca                  | 210  | <0.5<br>(>99.8%) | <b>0.11</b><br>(99.9%)     | <b>&lt;0.01</b>           | <0.2   |
| Fe                  | 1900   | 13<br>(99.3%)    | 53<br>(97.2%)              | 0.11                      | <0.1   |
| Ti                  | 150  | <0.1<br>(>99.9%) | 0.74<br>(99.5%)            | <0.01                     | <10 <sup>-3</sup>                                |
| Zn                  | <1   | 310              | 5900                       | <0.01                     | – <sup>d</sup>                                   |

$$† r_A = (1 - x_{A(\text{prec Si})} / x_{A(\text{MG-Si})}) \times 100$$

<sup>a</sup> Analyzed by GD-MS.

<sup>b</sup> Analyzed by IR after inert gas fusion method.

<sup>c</sup> Analyzed by IR after combustion method.

<sup>d</sup> No data

Comparing the impurity contents in the Si granules obtained from the precipitation experiments (1) and (2), larger amount of Zn was detected in experiment (2). This is explained by the larger amount of Zn left in the gaps of the granules, as observed in the cross-sectional SEM image. For other impurity elements, no significant difference was found. Summarizing the above,

high processing rate and small inclusion of Zn can be achieved at a high cooling rate. On the other hand, large Si granules are obtained at a slow cooling rate, which will be advantageous for Si recovery from liquid Si–Zn alloy by filtering.

For the Si wafer obtained by FZ melting, metal elements (Al, Ca, Fe, Ti, and Zn) were further removed from the precipitated Si granules; the total concentration was less than 0.2 ppmw. It should be mentioned that Zn was effectively removed to less than 0.01 ppmw owing to its high vapor pressure [40], even though a relatively large amount of 5900 ppmw remained in the Si granules. In this respect, this contrasts with the previous solidification refining studies from Si–M (M=Al, Cu, Fe, Sn, *etc.*) alloys. The residue of the alloying element in Si is known as one of the major challenges of solidification refining. For the solidification refining from the Si–Al alloy, approximately 400–600 ppmw of Al remained in the precipitated Si [41]. As the distribution coefficient of Al in Si is  $2 \times 10^{-3}$  [33], at least twice the directional solidification refining is required for Al removal. Thus, the extremely easy removal of Zn is considered to be a great advantage as an alloying element. In the Si wafer, P and O were also further removed to 13 ppmw and 10 ppmw, respectively. In contrast, B and C increased compared with the precipitated Si granules, perhaps because carbon is contaminated by a diamond wheel saw. The increase in B needs further study.

Compared with the acceptable level for SOG-Si shown in Table 6-4, the contents of Al and Ca in the Si wafer met the level in spite of their high contents in MG-Si. It is noteworthy that the concentration of O was lower than that in actual Si wafers used for solar cells, that is, approximately 20 ppmw [39], which is produced by the CZ method. Although the contents of Fe, Ti, B, and P were higher than the acceptable level, this is mainly due to the high impurity contents in the starting material of MG-Si. When electrochemically reduced Si, which has lower impurity contents than MG-Si, is used as the starting material, lower concentrations of Fe, Ti, B, and P are expected to be achieved.

## 6.5 Conclusion

The distribution behavior of impurity elements between solid Si and liquid Zn was studied by thermodynamic calculations and experiments. The distribution coefficients of impurity elements were calculated from the reported data at 923 K. The considerably low calculated coefficients suggested that almost all of the C, Al, Ca, and Fe would remain in the liquid Si–Zn alloy during the Si precipitation. As the distribution coefficients of B and P were calculated to be 0.15 and 0.26, respectively, their efficient removals were expected.

Precipitation experiments were successfully performed by submerging the liquid Si–Zn alloy in molten CaCl<sub>2</sub>. From the impurity analysis of the obtained Si granules, high removal fractions were achieved for C, Al, Ca, and Fe, which are consistent with the calculated distribution coefficients. The high removal fraction of B was also confirmed when compared with the solidification from the liquid Si. Contrary to the prediction from the calculation, O was removed from the starting material of MG-Si, which is explained by the dissolution of residual oxides such as CaO into molten CaCl<sub>2</sub>.

The obtained Si granules were transformed into wafers using the FZ melting method. For the Si wafers, the total content of metal impurities (Al, Ca, Fe, Ti, and Zn) was less than 0.2 ppmw, wherein Al and Ca met the acceptable levels for SOG-Si. In the Si wafers, the concentrations of P and O also decreased. In particular, the concentration of Zn decreased from 5900 ppmw in the granules to less than 0.01 ppmw in the wafers, which demonstrates the great advantage of Zn as an alloying element.

## 6.6 Reference List

- [1] T. Yoshikawa and K. Morita, *Metall. Mater. Trans. B*, **36**, 731 (2005).
- [2] T. Yoshikawa and K. Morita, *J. Electrochem. Soc.*, **150**, G465 (2003).
- [3] Y. Chung, J. M. Toguri and R. Sridhar, *Can. Metall. Q.*, **40**, 185 (2001).

- [4] T. B. Massalski, J. L. Murray, L. H. Bennett and H. Baker, *Binary Alloy Phase Diagrams*, 2nd ed., American Society for Metals (1986).
- [5] M. Haemaelaenen and I. Isomaeki, *J. Alloy. Compd.*, **392**, 220 (2005).
- [6] M. W. Chase, Jr., C. A. Davies, J. R. Downey, Jr., D. J. Frurip, R. A. McDonald and A. N. Syverud, *JANAF Thermochemical Tables*, 3rd ed., American Chemical Society (1985).
- [7] I. Barin, *Thermochemical Data of Pure Substances*, 2nd ed., VCH Verlags Gesellschaft (1993).
- [8] B. Landolt, *Thermodynamic Properties of Inorganic Materials, Part IV*, Springer-Verlag (2001).
- [9] O. Knacke, O. Kubaschewski and K. Hesselmann, *Thermochemical Properties of Inorganic Substances*, 2nd ed., Springer-Verlag (1991).
- [10] B. Binnewies and E. Milke, *Thermochemical Data of Elements and Compounds*, 2nd ed., Wiley-VCH (2002).
- [11] M. E. Schlesinger, *Chem. Rev.*, **102**, 4267 (2002).
- [12] I. Barin, *Thermochemical Data of Pure Substances*, 3rd ed., VCH Verlags Gesellschaft (1995).
- [13] I. Barin, O. Knacke and O. Kubaschewski, *Thermochemical Properties of Inorganic Substances*, Springer-Verlag (1977).
- [14] B. J. McBride, S. Gordon and M. A. Reno, *Thermodynamic Data for Fifty Reference Elements*, NASA Technical Paper 3287 (1993).
- [15] C. Malcolm, *NIST-JANAF Thermochemical Tables*, 4th ed., American Chemical Society (1998).
- [16] B. Landolt, *Thermodynamic Properties of Inorganic Materials, Part I*, Springer-Verlag (1999).
- [17] P. J. Spencer, A. D. Pelton, Y. Kang, P. Chartrand and C. D. Fuerst, *CALPHAD*, **32**, 423 (2008).



- [18] I. Barin, *Thermochemical Data of Pure Substances, 1st ed.*, VCH Verlags Gesellschaft (1989).
- [19] G. Reumont, P. Perrot, J. M. Fiorani and J. Hertz, *J. Phase Equilib.*, **21**, 371 (2000).
- [20] V. S. Iorish and G. V. Belov, *On Quality of Adopted Values in Thermodynamic Databases*, Scientific Databases Conference, Japan (1996).
- [21] K. Doi, S. Ono, H. Ohtani and M. Hasebe, *J. Phase Equilibria Diffus.*, **27**, 63 (2006).
- [22] G. L. Vick and K. M. Whittle, *J. Electrochem. Soc.*, **116**, 1142 (1969).
- [23] A. J. Bard, R. Parsons and J. Jordan, *Standard Potentials in Aqueous Solution*, Marcel Dekker Inc. (1985).
- [24] Z. Chen, F. Yin, M. Zhao and Z. Li, *J. Phase Equilibria Diffus.*, **34**, 366 (2013).
- [25] T. Narushima, A. Yamashita, C. Ouchi and Y. Iguchi, *Mater. Trans.*, **43**, 2120 (2002).
- [26] H. A. Wriedt, *Bull. Alloy Phase Diagrams*, **11**, 43 (1990).
- [27] S. Otsuka and Z. Kozuka, *Transactions of the Japan Institute of Metals*, **22**, 558 (1981).
- [28] R. W. Olesinski, N. Kanani and G. J. Abbaschian, *Bull. Alloy Phase Diagrams*, **6**, 130 (1985).
- [29] H. Sigmund, *J. Electrochem. Soc.*, **129**, 2809 (1982).
- [30] E. R. Weber, *Appl. Phys. A*, **A30**, 1 (1983).
- [31] S. Kuge and H. Nakashima, *Jpn. J. Appl. Phys.*, **30**, 2659 (1991).
- [32] H. Okamoto, *J. Phase Equilibria Diffus.*, **29**, 211 (2008).
- [33] F. A. Trumbore, *Bell Syst. Tech. J.*, **39**, 205 (1960).
- [34] T. Yoshikawa and K. Morita, *STAM*, **4**, 531 (2003).
- [35] T. R. Hogness, *J. Am. Chem. Soc.*, **43**, 1621 (1921).
- [36] K. C. Mills and L. Courtney, *ISIJ Int.*, **40**, S130 (2000).
- [37] V. P. Popov and B. R. Pamplin, *J. Cryst. Growth.*, **15**, 129 (1972).
- [38] A. Miller, R. G. Humphreys and B. Chapman, *J. Phys. Colloq.*, **36**, C3-31 (1975).
- [39] Ultra Clean Society (Handotai Kiban Gijutsu Kenkyukai), *Silicon no Kagaku, 1st ed.*, Realize Inc. (1996). [in Japanese]

- [40] M. W. Chase, *NIST–JANAF Thermochemical Tables, 4th ed., Part I Al–Co*, American Chemical Society, and the American Institute of Physics for the National Institute of Standards and Technology (1998).
- [41] T. Yoshikawa and K. Morita, *ISIJ Int.*, **45**, 967 (2005).

## Chapter 7

### General Conclusion

The electrochemical reductions of solid and dissolved  $\text{SiO}_2$  were investigated at a liquid Zn electrode for the establishment of the SOG-Si production process. Firstly, the electrochemical reduction of solid  $\text{SiO}_2$  was investigated in molten  $\text{CaCl}_2$ . With the purpose of productivity improvement, the electrochemical reduction of dissolved  $\text{SiO}_2$  was also investigated in molten  $\text{CaCl}_2$  and eutectic  $\text{NaCl-CaCl}_2$ . The use of  $\text{NaCl-CaCl}_2$  molten salt in the electrolysis step is expected to simplify the process because the same salt can be used in the precipitation step. Also, the distribution behavior of impurity elements was investigated using a liquid Si-Zn alloy prepared from low-purity MG-Si as the pre-study for the precipitation and refining steps. The obtained results are summarized below.

In Chapter 2, the reaction mechanism on the electrochemical reduction of solid  $\text{SiO}_2$  at the liquid Zn electrode was investigated in molten  $\text{CaCl}_2$  at 1123 K. In the cyclic voltammetry, the electrochemical reduction of  $\text{SiO}_2$  was observed from 1.55 V (vs.  $\text{Ca}^{2+}/\text{Ca}$ ) and the formation of liquid Ca-Zn alloy from 0.85 V. From the electrolysis and immersion experiments, the reduction at 0.60 V was confirmed as a mixed mechanism of the direct electrochemical reduction and the indirect reduction by liquid Ca-Zn alloy. Impurity analysis for the obtained Si particles confirmed that the concentrations of the metal elements and P were lower than the target levels for primary Si. It should be mentioned that the indirect reduction of  $\text{SiO}_2$  by Ca-Zn alloy did not increase the Ca content in the Si product because it remained in the liquid Zn phase during precipitation.

In Chapter 3, the molten salts containing different amounts of CaO and  $\text{CaSiO}_3$  were

classified as follows; molten salt (i): 4.0 mol% CaSiO<sub>3</sub> ( $r_{\text{O}^{2-}/\text{SiO}_2} = 1.0$ ), molten salt (ii): 2.0 mol% CaO and 4.0 mol% CaSiO<sub>3</sub> ( $r_{\text{O}^{2-}/\text{SiO}_2} = 1.5$ ), molten salt (iii): 4.0 mol% CaO and 4.0 mol% CaSiO<sub>3</sub> ( $r_{\text{O}^{2-}/\text{SiO}_2} = 2.0$ ). In this chapter, the ionic species and the electrochemical reduction of dissolved SiO<sub>2</sub>, i.e., silicate ions, were investigated in molten CaCl<sub>2</sub> at 1123 K. As the result of Raman spectroscopy, the dominant ion species was determined as SiO<sub>3</sub><sup>2-</sup> in molten salt (i) and SiO<sub>4</sub><sup>4-</sup> in molten salt (iii). In molten salt (ii), the primary dominant species was attributed to SiO<sub>4</sub><sup>4-</sup> and secondary dominant species to Si<sub>2</sub>O<sub>7</sub><sup>6-</sup>. Then the electrochemical reduction of silicate ions was conducted at a graphite electrode. From the results of cyclic voltammetry and potentiostatic electrolysis, molten salt (i) with dominant SiO<sub>3</sub><sup>2-</sup> is considered to be suitable for producing Si–Zn alloy, because its available potential range was widest and apart from the formation of liquid Ca–Zn alloy. Based on the results obtained at the graphite electrode, the electrochemical investigation was conducted at the liquid Zn electrode. From the results of cyclic voltammetry, molten salt (i) with dominant SiO<sub>3</sub><sup>2-</sup> is considered to be suitable for production of Si–Zn alloy in the term of available potential range, which was similar to the results obtained at the graphite electrode. In the potentiostatic electrolysis, the current densities were largest in molten salt (i). The current efficiencies calculated from the weight of recovered Si were as high as approximately 80% in all molten salts. Also, the formation of Ca–Zn alloy did not lead to a low current efficiency because of the indirect reduction of silicate ions by Ca–Zn alloy during the slow cooling period. Therefore, molten salt (i), which gave the largest current densities, is considered to be suitable for the production of Si–Zn alloy.

In Chapters 4 and 5, the molten salts containing different amounts of CaO and CaSiO<sub>3</sub> were classified as follows; molten salt (i): 1.0 mol% CaSiO<sub>3</sub> ( $r_{\text{O}^{2-}/\text{SiO}_2} = 1.0$ ), molten salt (ii): 0.5 mol% CaO and 1.0 mol% CaSiO<sub>3</sub> ( $r_{\text{O}^{2-}/\text{SiO}_2} = 1.5$ ), molten salt (iii): 1.0 mol% CaO and 1.0 mol% CaSiO<sub>3</sub> ( $r_{\text{O}^{2-}/\text{SiO}_2} = 2.0$ ).

In Chapter 4, the ionic species and the electrochemical reduction of silicate ions at a solid graphite electrode were investigated in molten eutectic NaCl–CaCl<sub>2</sub> at 1023 K and 1123 K prior to

the investigation using the liquid Zn electrode. From Raman spectroscopy performed at 1023 K, the dominant ion was attributed to  $\text{SiO}_3^{2-}$  in molten salt (i) and  $\text{SiO}_4^{4-}$  in molten salt (iii). In molten salt (ii), the primary dominant species was determined as  $\text{SiO}_4^{4-}$  and secondary dominant species as  $\text{SiO}_3^{2-}$ . The results of cyclic voltammetry and potentiostatic electrolysis performed at 1023 K showed that the  $\text{SiO}_3^{2-}$  dominated molten salt (i) and the  $\text{SiO}_3^{2-}$  secondarily dominated molten salt (ii) exhibited approximately the same potential range for the electrodeposition of Si. When the similar study was conducted at 1123K, almost the same results were obtained. Since the potential for the electrochemical reduction of  $\text{SiO}_3^{2-}$  was approximately 0.2 V more positive than that of  $\text{SiO}_4^{4-}$ , being more distant from the formation potential of Ca–Zn alloy, molten salt (i) and (ii) are considered to be suitable for the production of Si–Zn alloy at the liquid Zn electrode.

In Chapter 5, the electrochemical reduction of silicate ions was investigated at the liquid Zn electrode in molten NaCl–CaCl<sub>2</sub> at 1023 K and 1123 K. From cyclic voltammetry performed at 1023 K, the electrochemical reduction of dominant  $\text{SiO}_3^{2-}$  was observed from 1.1 V (vs. Na<sup>+</sup>/Na) in molten salt (i), and that of dominant  $\text{SiO}_4^{4-}$  from 0.95 V in molten salt (iii). As the results of potentiostatic electrolysis, high current efficiencies of more than 95% were obtained in the samples obtained at 0.60 V with slow cooling. From the results of ICP-AES analysis, the formed alloy was confirmed to be Ca–Zn only. Although the formation of Ca–Zn alloy proceeded at 0.60 V, the high current efficiencies were achieved because of the indirect reduction of silicate ions by Ca–Zn alloy during the slow cooling period. Cyclic voltammetry performed at 1123 K showed that the electrochemical reduction of dominant  $\text{SiO}_3^{2-}$  started from 1.3 V in molten salt (i), and that of dominant  $\text{SiO}_4^{4-}$  from 1.0 V in molten salt (iii). The simultaneous reactions of the electrochemical reduction of silicate ions and the formation of Ca–Zn were suggested from 0.85 V. For the samples obtained at 0.60 V with slow cooling, the current efficiencies were lower than those obtained at 1023 K, suggesting higher dissolution rate of Ca from Ca–Zn into molten salt at higher temperature.

In Chapter 6, the distribution behavior of impurity elements in the precipitation step was investigated. First, the distribution coefficients of impurity elements at 923 K were calculated using

thermodynamic data, which predicted the efficient removal of C, Al, Ca, Fe, B, and P. Then the precipitation experiments were conducted using MG-Si as the raw material, and the concentration of impurities in the precipitated Si was analyzed. As the result, high removal fractions of C, Al, Ca, Fe, and B were achieved in agreement with the predictions of thermodynamic calculations. Compared with the solidification from the liquid Si, a high removal fraction of B was achieved. On the other hand, contrary to the prediction of thermodynamic calculations, O also showed a high removal fraction. This may be due to the fact that the O in the MG-Si existed as metal oxides and these dissolved in the molten salt. Furthermore, as an initial study on the refining step, Si ingot was fabricated by the floating zone (FZ) melting method using the Si particles obtained in the precipitation experiment. As the result of impurity analysis, the total concentration of metallic impurities was less than 0.2 ppmw, among which Al and Ca achieved the acceptable levels for SOG-Si. In particular, the concentration of Zn was less than 0.01 ppmw, confirming its efficient removal from Si.

Based on the results described above, the electrochemical reduction of  $\text{SiO}_2$  using the liquid Zn electrode is summarized as follows. With the dissolution of  $\text{SiO}_2$ , the current efficiency in molten  $\text{CaCl}_2$  at 1123 K increased to approximately 80%, which was much higher than the electrochemical reduction of solid  $\text{SiO}_2$ . The formation of liquid Ca–Zn alloy proceeded simultaneously at 0.60 V, which also contributed to the reduction of silicate ions, leading to the high current efficiency. In molten  $\text{NaCl–CaCl}_2$ , the highest current efficiency of 97.4% was achieved at 1023 K, which was also the highest value including the results obtained in molten  $\text{CaCl}_2$ . On the other hand, compared with the electrolysis in molten  $\text{CaCl}_2$ , the available potential range in which only the direct electrochemical reduction of dissolved  $\text{SiO}_2$  proceeds was smaller in molten  $\text{NaCl–CaCl}_2$ . Considering that molten  $\text{NaCl–CaCl}_2$  has lower solubility of CaO than molten  $\text{CaCl}_2$ , it would also have lower solubility of  $\text{SiO}_2$ , because  $\text{O}^{2-}$  ion is indeed necessary for the dissolution of  $\text{SiO}_2$ . The higher the solubility of  $\text{SiO}_2$ , the higher the current density and the shorter the electrolysis time will be, which is desirable for the Si production. Therefore, molten

CaCl<sub>2</sub> with higher solubility of SiO<sub>2</sub> is considered to be more suitable than molten NaCl–CaCl<sub>2</sub> for the Si production. From the results of the study on the precipitation and refining steps, Zn, which not only has relatively high removal fractions of impurity elements but also is easy to remove due to its high vapor pressure, is found to have great advantages as the alloying element.

The knowledge obtained in the present study relates to a part of the whole process. In the future, further study and development are needed for the establishment of the practical process. One of the challenges is the establishment of efficient method of Si recovery from the liquid Si–Zn alloy obtained in the electrolysis step. In the present study, the recovery of Si was conducted by cooling the liquid Si–Zn alloys to room temperature and then dissolving the Zn metal lumps in a HCl solution. However, in the precipitation step in the practical process, the precipitated Si is recovered while the Si–Zn alloy is in a liquid state, and then the liquid Si–Zn alloy with reduced Si concentration will be reused as the cathode in the electrolysis step. Therefore, it is necessary to study an efficient method of Si recovery, such as using epitaxial growth on a solid substrate.

The author hopes that the present process will be industrially established in the future, leading to further cost reduction and widespread use of crystalline Si-based solar cells.

# List of Publications

The main parts of this thesis are constructed from the following papers.

## Chapter 2

1. Y. Ma, A. Ido, K. Yasuda, R. Hagiwara, T. Homma and T. Nohira  
“Mechanism of Electrolytic Reduction of SiO<sub>2</sub> at Liquid Zn Cathode in Molten CaCl<sub>2</sub>”  
*Journal of The Electrochemical Society*, **166**(6), D162–D167 (2019).

## Chapter 3

2. Y. Ma, X. Yang, T. Yamamoto, K. Yasuda and T. Nohira  
“Electrodeposition of Si from Silicate Ions at Graphite and Liquid Zn Electrodes in Molten CaCl<sub>2</sub>”  
*Journal of The Electrochemical Society*, submitted.

## Chapter 4

3. Y. Ma, T. Yamamoto, K. Yasuda and T. Nohira  
“Raman Analysis and Electrochemical Reduction of Silicate Ions in Molten NaCl–CaCl<sub>2</sub>”  
*Journal of The Electrochemical Society*, **168**(4), 046515 (2021).

## Chapter 5

4. Y. Ma, K. Yasuda and T. Nohira  
“Electrochemical Reduction of Silicate Ions at Liquid Zn Cathode in Molten NaCl–CaCl<sub>2</sub>”  
*Journal of The Electrochemical Society*, to be submitted.

## Chapter 6

5. Y. Ma, K. Yasuda, A. Ido, T. Shima, M. Zhong, R. Hagiwara and T. Nohira  
“Silicon Refining by Solidification from Liquid Si–Zn Alloy and Floating Zone Method”  
*Materials Transactions*, **62**(3), 403–411 (2021).



# Appendix

## A.1 Previous Studies on the Electrochemical Reduction of SiO<sub>2</sub> for the Production of Other Si Products

### A.1.1 Electrochemical Reduction of SiO<sub>2</sub> for the Production of Si Nanomaterials

The electrochemical reductions of solid and dissolved SiO<sub>2</sub> were also applied to the production of Si nanomaterials [1–15], as listed in [Table A.1-1](#).

**Table A.1-1 Previous studies on the formation of Si nanomaterials using electrochemical reduction of SiO<sub>2</sub> in molten salts.**

| Molten salt                                    | Si precursor   | Temperature / K | Contacting electrode / Substrate | Counter electrode  | (Pseudo) Reference electrode                                       | Morphology of deposited Si | Authors, Year [Ref.]  |
|--|--|-----------------|----------------------------------|--------------------|--|----------------------------|---|
| CaCl <sub>2</sub>                              | SiO <sub>2</sub> pellet                              | 1173            | Mo                               | Pt                 | – <sup>1</sup>   | nanowire                   | Yang <i>et al.</i> , 2009 [1]                                     |
| CaCl <sub>2</sub>                              | SiO <sub>2</sub> pellet                              | 1123            | Mo                               | glass-like carbon  | Ag <sup>+</sup> /Ag in CaCl <sub>2</sub> , Mo–Ca <sup>2+</sup> /Ca | nanowire                   | Nishimura <i>et al.</i> , 2011 [2]                                |
| CaCl <sub>2</sub>                              | quartz plate   | 1123            | Ni                               | graphite           | – <sup>1</sup>   | cluster-like nanostructure | Zhao <i>et al.</i> , 2013 [3]                                     |
| CaCl <sub>2</sub>                              | SiO <sub>2</sub> plate                               | 1123            | Ni                               | carbon             | – <sup>1</sup>   | nanowire array             | Zhao <i>et al.</i> , 2013 [4]                                     |
| CaCl <sub>2</sub>                              | SiO <sub>2</sub> pellet                              | 1173            | Mo                               | graphite           | – <sup>1</sup>   | nanowire                   | Fang <i>et al.</i> , 2015 [5]<br>Fang <i>et al.</i> , 2016 [6, 7] |
| CaCl <sub>2</sub>                              | SiO <sub>2</sub> sheet                               | 1123            | stainless steel                  | graphite           | – <sup>1</sup>   | nanowire                   | Yu <i>et al.</i> , 2020 [8] #                                     |
| NaCl–CaCl <sub>2</sub>                         | SiO <sub>2</sub> pellet                              | 1073            | carbon cloth                     | graphite           | quartz sealed Ag/AgCl [31]   | nanowire                   | Weng and Xiao, 2019 [9] #   |
| NaCl–CaCl <sub>2</sub>                         | SiO <sub>2</sub> pellet                              | 1123            | Mo, Ni                           | graphite           | Ag/AgCl (for CV) <sup>1</sup>                                      | nanotube                   | Weng <i>et al.</i> , 2020 [10] #                                  |
| NaCl–CaCl <sub>2</sub>                         | SiO <sub>2</sub> pellet                              | 973             | unknown                          | graphite           | – <sup>1</sup>   | nanowire                   | Zhang <i>et al.</i> , 2020 [11] #                                 |
| KF–KCl   | K <sub>2</sub> SiF <sub>6</sub> and SiO <sub>2</sub> | 943–1073        | graphite                         | graphite           | – <sup>2</sup>   | nanofiber                  | Zaykov <i>et al.</i> , 2014 [12]                                  |
| KF–KCl   | K <sub>2</sub> SiF <sub>6</sub> and SiO <sub>2</sub> | 1023            | glass-like carbon                | Monocrystalline Si | Monocrystalline Si   | nanofiber                  | Zhuk <i>et al.</i> , 2017 [13]                                    |
| CaCl <sub>2</sub> –CaO                         | SiO <sub>2</sub> nanopowder                          | 1123            | graphite                         | graphite           | – <sup>3</sup>   | micro/nanowire             | Zou <i>et al.</i> , 2020 [14]                                     |
| NaCl–MgCl <sub>2</sub> –CaCl <sub>2</sub> –CaO | CaSiO <sub>3</sub>                                   | 923             | graphite                         | graphite           | – <sup>1</sup>   | nanowire                   | Dong <i>et al.</i> , 2017 [15] #                                  |

<sup>1</sup> Electrodeposition was conducted by 2-electrode constant voltage manner.

<sup>2</sup> Electrodeposition was conducted by 2-electrode pulse manner.

<sup>3</sup> Electrodeposition was conducted by 2-electrode constant current density manner.

# Electrochemical performance was confirmed as the anode material of Li-ion battery.

### A.1.2 Electrochemical Reduction of SiO<sub>2</sub> for the Production of Si Compounds

The production of Si compounds, such as Fe–Si and Mo–Si by the electrochemical reductions of solid and dissolved SiO<sub>2</sub> were also investigated [16–30]. Table A.1-2 summarizes the previous studies.

**Table A.1-2 Previous studies on the formation of Si compounds using electrochemical reduction of SiO<sub>2</sub> in molten salts.**

| Molten salt  | Si precursor   | Temperature / K | Contacting electrode / substrate | Counter electrode  | (Pseudo) Reference electrode                                       | Si compound  | Authors, Year [Ref.]   |
|--|--|-----------------|----------------------------------|--------------------|--|--|--|
| CaCl <sub>2</sub>  | C-coated-SiO <sub>2</sub> pellet                                     | 1123            | Mo                               | graphite           | Ag <sup>+</sup> /Ag in CaCl <sub>2</sub> , Mo–Ca <sup>2+</sup> /Ca | nano SiC   | Nishimura <i>et al.</i> , 2014 [16]  |
| CaCl <sub>2</sub>  | sugar-derived-C-coated-SiO <sub>2</sub> pellet                       | 1123            | Mo                               | graphite           | – <sup>1</sup>   | SiC  | Zhao <i>et al.</i> , 2019 [17]   |
| NaF–NaCl–KCl   | SiO <sub>2</sub>   | 1073–1173       | Cu                               | 80~90% Si–Cu alloy | – <sup>2</sup>   | Cu–Si alloy  | Li <i>et al.</i> , 2008 [18]   |
| NaF–NaCl–KCl   | SiO <sub>2</sub>   | 973–1073        | 3.46 wt.% Si-steel               | graphite           | – <sup>2</sup>   | 6.5 wt.% Si–Fe alloy                                   | Li <i>et al.</i> , 2009 [19]<br>Yang <i>et al.</i> , 2009 [20]<br>Yang <i>et al.</i> , 2010 [21]<br>Yang <i>et al.</i> , 2013 [22]<br>Li <i>et al.</i> , 2017 [23] |
| NaF–NaCl–KCl   | SiO <sub>2</sub><br>(Na <sub>2</sub> B <sub>4</sub> O <sub>7</sub> ) | 1173            | Fe                               | graphite           | – <sup>2</sup>   | Fe <sub>3</sub> Si                                     | Yang <i>et al.</i> , 2009 [24]   |
| NaF–NaCl–KCl   | SiO <sub>2</sub>   | 1073            | Mo                               | graphite           | Pt   | Si + MoSi <sub>2</sub>                                 | Cai <i>et al.</i> , 2010 [25]  |
| NaF–NaCl–KCl   | SiO <sub>2</sub> powder  | 1073–1123       | Mo                               | graphite           | – <sup>2</sup>   | MoSi <sub>2</sub>                                      | He <i>et al.</i> , 2014 [26]   |
| NaF–NaCl–KCl   | SiO <sub>2</sub>   | 1073            | Nb                               | graphite           | – <sup>2,3</sup>   | NbSi <sub>2</sub>                                      | Wang <i>et al.</i> , 2015 [27]   |
| NaF–NaCl–KCl   | SiO <sub>2</sub>   | 973–1073        | 1.2 wt.% Si-steel                | graphite           | – <sup>3</sup>   | 6.5 wt.% Si–Fe alloy                                   | Li <i>et al.</i> , 2019 [28]   |
| NaCl–Na <sub>3</sub> AlF <sub>6</sub>                            | SiO <sub>2</sub><br>(Na <sub>2</sub> MoO <sub>4</sub> )              | 1173–1273       | glass-like carbon                | Pt                 | – <sup>3</sup>   | Mo <sub>3</sub> Si <sub>5</sub> ,<br>MoSi <sub>2</sub> | Malyshev <i>et al.</i> , 1997 [29]   |
| Li <sub>2</sub> CO <sub>3</sub> –Na <sub>2</sub> CO <sub>3</sub> | SiO <sub>2</sub>   | 1023            | stainless steel                  | glass-like carbon  | Pt, glass-like carbon  | granular SiC   | Devyatkin, 2003 [30]   |

<sup>1</sup> Electrodeposition was conducted by 2-electrode constant voltage manner.<sup>2</sup> Electrodeposition was conducted by 2-electrode pulse manner.<sup>3</sup> Electrodeposition was conducted by 2-electrode constant current density manner.

## A.2 Effect of Cooling Rate on Precipitation Behavior of Si from Liquid Si–Zn Alloy

The precipitation behavior of Si from liquid Si–Zn alloy was investigated for the optimization of cooling rate in the precipitation step shown in Figure 1-9. A liquid Si–Zn alloy with 5 at.% Si was prepared from low-purity MG-Si to investigate the purification capability. The precipitation of Si from the liquid Si–Zn alloy was conducted with different cooling rates. The particle size and the impurity contents were analyzed to investigate the effect of cooling rate on the precipitation behavior of Si.

### A.2.1 Experimental

Figure A.2-1 shows the schematic of the experimental apparatus for the precipitation of Si from a liquid Si–Zn alloy. 664 g of metallic Zn (FUJIFILM Wako Pure Chemical Corp., reagent grade, granule) and 291 g of  $\text{CaCl}_2$  powder (FUJIFILM Wako Pure Chemical Corp., reagent grade) were charged in a graphite crucible (Toyo Tanso Co., Ltd., IG-110 grade, o.d. 105 mm  $\times$  i.d. 95

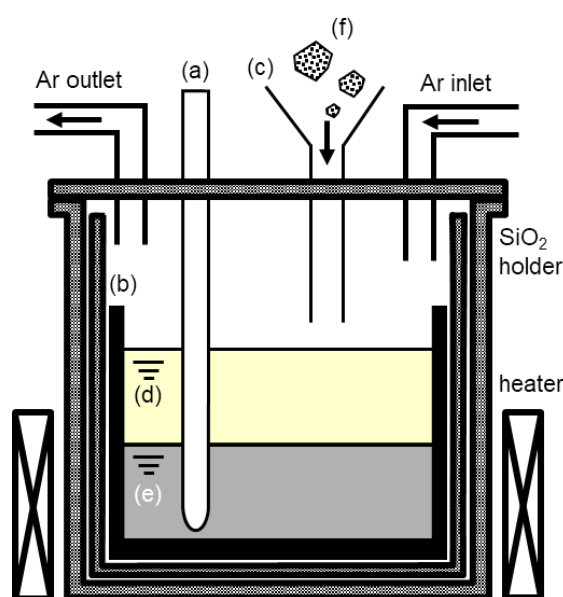
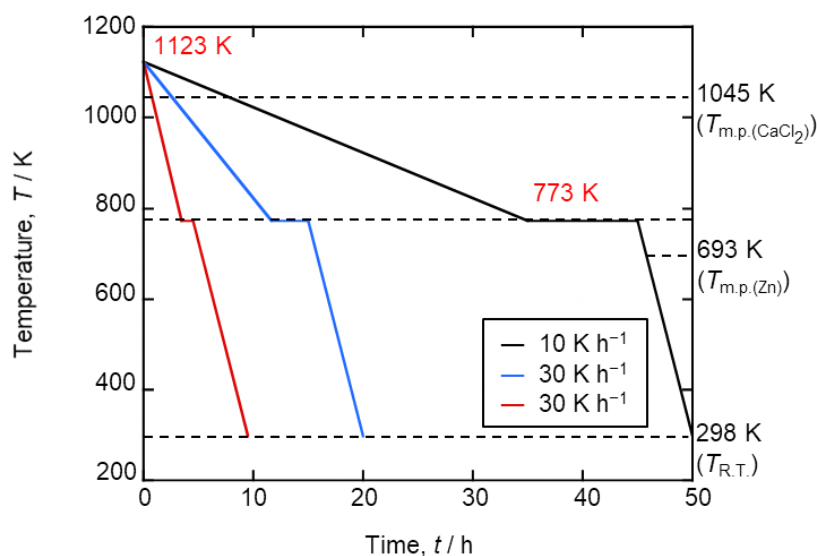


Figure A.2-1 Schematic of the experimental apparatus for the precipitation of solid Si from a liquid Si–Zn alloy. (a) Thermocouple, (b) graphite crucible, (c) funnel, (d) molten  $\text{CaCl}_2$ , (e) liquid Zn, and (f) MG-Si.

mm × height 150 mm) and dried under vacuum at 653 K for 24 h. After the temperature was raised to 1123 K, 15.0 g of MG-Si (FUJIFILM Wako Pure Chemical Corp., granule, >98%), which is equivalent to 5.0 at.% Si–Zn alloy, was charged through a glass funnel. The temperature was maintained at 1123 K for more than 24 h to sufficiently react Si and Zn. Then, the liquid Si–Zn alloy was cooled to 773 K at cooling rates of 10, 30 and 100 K h<sup>-1</sup>. After the temperature was maintained at 773 K for 10 h for the cooling rate of 10 K h<sup>-1</sup>, 3 h 20 min for 30 K h<sup>-1</sup>, and 1 h for 100 K h<sup>-1</sup>, it was further decreased to 298 K for 5 h. The temperature changes during the cooling step were summarized in Figure A.2-2.

A lump of Zn metal was recovered from the crucible after removal of CaCl<sub>2</sub> with distilled water and dissolved in a 20 wt.% HCl solution (prepared from 36 wt.% solution) to recover the precipitated Si granules. The recovered Si granules were then immersed in a 10 wt.% HCl solution prepared from the same HCl solution and a 10 wt.% HNO<sub>3</sub> solution prepared from 60 wt.% HNO<sub>3</sub> solution (FUJIFILM Wako Pure Chemical Corp., reagent grade) overnight, respectively. Distribution of particle size was investigated by sifting the recovered Si granules with sieve meshes of 0.2, 0.5, 1.0, 2.0 mm. The impurity contents in Si granules were analyzed by ICP-AES.

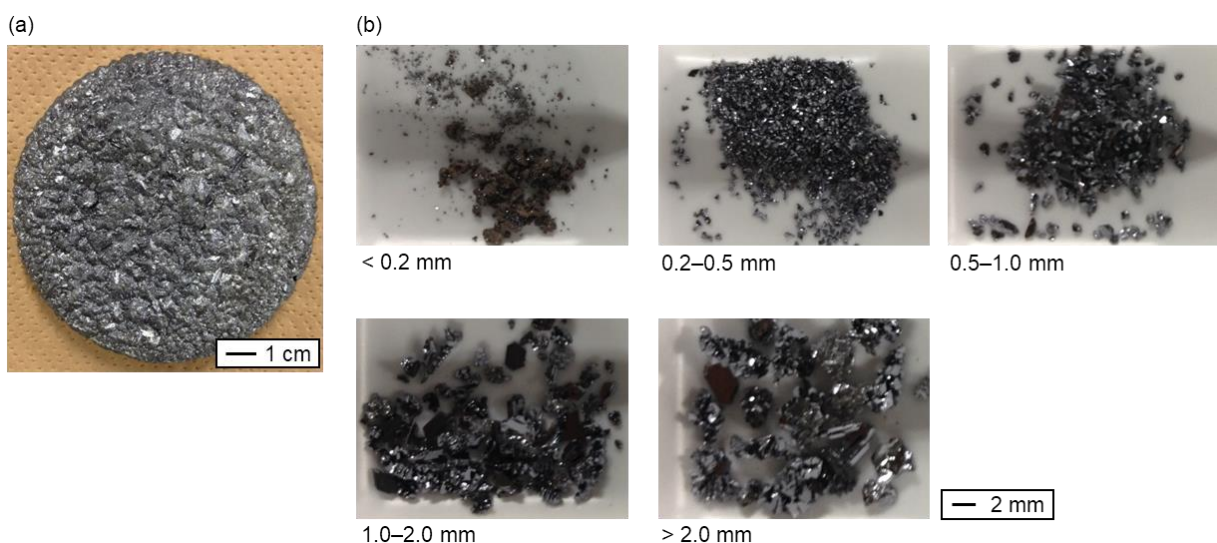


**Figure A.2-2** Temperature changes during the cooling step.

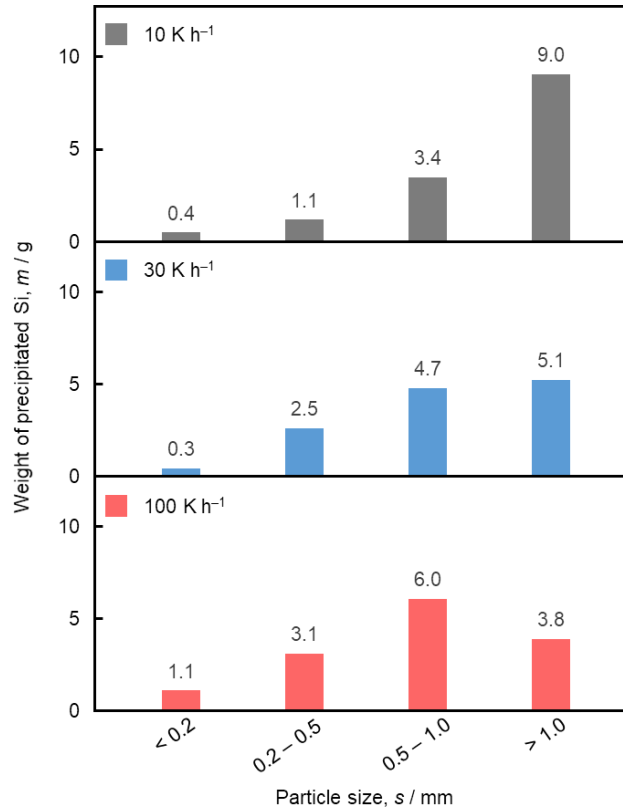
## A.2.2 Results and Discussion

Figure A.2-3(a) shows an optical image of the Zn metal lump obtained at the cooling rate of  $10 \text{ K h}^{-1}$ . Angular precipitates with gray color were observed all over the surface. As described in Chapter 6, Si particles floated at the top of the liquid Zn during the precipitation because the density of solid Si is smaller than that of liquid Zn. Although the bottom part cannot be seen from the figure, the entire bottom showed a metallic luster, which was confirmed as Zn. Si granules with different particle sizes were shown in Figure A.2-3(b). All Si granules showed a metallic luster except the granules with a size smaller than 0.2 mm. The weight distribution of the Si granules by particle size obtained at each cooling rate is shown in Figure A.2-4. The particle sizes with the largest amount were 1–2 mm (48.3%) at  $10 \text{ K h}^{-1}$ , 1–2 mm (37.8%) and 0.5–1 mm (37.0%) at  $30 \text{ K h}^{-1}$ , and 0.5–1 mm (42.9%) at  $100 \text{ K h}^{-1}$ . As the cooling rate increased, larger amount of Si particles with smaller size was precipitated.

Table A.2-1 shows the impurity contents in MG-Si and the precipitated Si with removal fractions for different particle sizes at the cooling rate of  $10 \text{ K h}^{-1}$ . The removal fractions,  $r_A$ , which were calculated from the contents in the original MG-Si,  $x_{A(\text{MG-Si})}$ , and the precipitated Si,  $x_{A(\text{prec Si})}$ ,



**Figure A.2-3** Optical images of (a) Zn metal lump after the removal of salt and (b) precipitated Si granules with different particle sizes obtained at the cooling rate of  $10 \text{ K h}^{-1}$ .



**Figure A.2-4** Weight distribution of precipitated Si granules by particle size obtained at different cooling rate.

are shown in parentheses.

$$r_A = \left(1 - \frac{x_{A(\text{prec Si})}}{x_{A(\text{MG-Si})}}\right) \times 100 \quad (\text{A-1})$$

For the Si granules with particle size larger than 2 mm, the removal fractions of Al and Ca were higher than 99%, Fe and Ti were higher than 95%, and B was 88%. On the other hand, the concentration of P was higher than that in the MG-Si. The formation of P compound with Zn and Si was suggested because the P concentrated in the liquid Zn phase during the Si precipitation. [Figure A.2-5](#) shows the phase diagram of Zn–Si–P system [32]. When assuming the P concentrated in the liquid Zn phase, ZnSiP<sub>2</sub> would possibly form on the precipitated Si in the late stage of the precipitation. The distribution behavior of impurity elements except P and Zn is consistent with the calculated distribution coefficient described in Chapter 6. Comparing the impurity contents for the Si granules with different particle size, the removal fractions of Al showed high values for all



**Table A.2-1 Impurity contents with removal fractions in the precipitated Si with different particle sizes at the cooling rate of 10 K h<sup>-1</sup>.**

| Impurity element, A | Impurity content in Si <sup>a</sup> , $x_A$ / ppmw<br>(Removal fraction †, $r_A$ ) |                       |                     |                     |
|---------------------|--|-----------------------|---------------------|---------------------|
|                     | MG-Si  | >2 mm                 | 1–2 mm              | 0.5–1 mm            |
| B                   | 26   | 3<br>(88%)            | 5<br>(81%)          | 8<br>(69%)          |
| P                   | 40   | 48                    | 48                  | 34<br>(15%)         |
| Al                  | 978  | <0.01<br>(>99.999%)   | <0.01<br>(>99.999%) | <0.01<br>(>99.999%) |
| Ca                  | 77   | <0.0005<br>(>99.999%) | 3<br>(96%)          | 11<br>(86%)         |
| Fe                  | 2485   | 104<br>(96%)          | 558<br>(78%)        | 1599<br>(36%)       |
| Ti                  | 249  | 13<br>(95%)           | 41<br>(84%)         | 90<br>(64%)         |
| Zn                  | 86   | 13286                 | 22098               | 13738               |

<sup>a</sup> Analyzed by ICP-AES.

$$† r_A = (1 - x_{A(\text{prec Si})} / x_{A(\text{MG-Si})}) \times 100$$

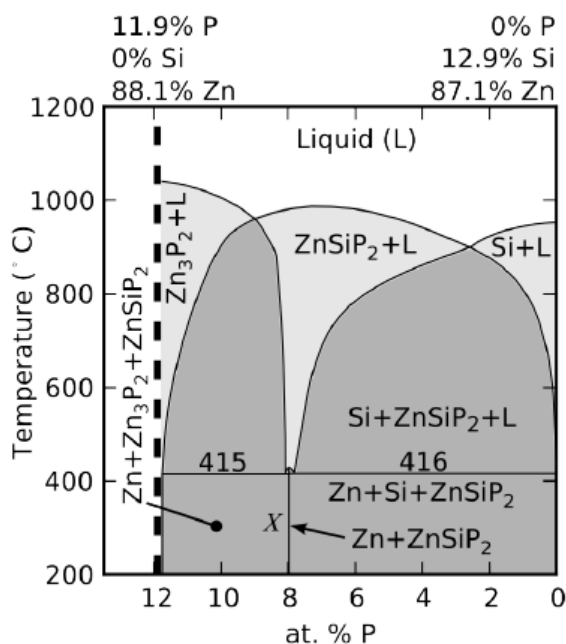


**Figure A.2-5 Phase diagram for the Zn–Si–P system [32].**

particle sizes, while those of B, Ca, Fe and Ti increased with the particle size. For Zn, the correlation between the particle size and the removal fraction was not observed. From all the results, the larger the particle size, the higher the removal fractions for impurities except P and Zn.

Impurity contents in the precipitated Si granules (>2 mm) obtained at different cooling rates are shown in [Table A.2-2](#). It also lists the target levels of primary Si for directional solidification and the acceptable levels for SOG-Si [33]. For Al, despite the cooling rate, high removal fractions of more than 99% were achieved. The removal fractions of B, Ca, Fe and Ti showed a decreasing trend as the cooling rate increased. The concentration of P in the Si granules obtained at all cooling rates increased compared to that in the MG-Si, which also could be explained by the formation of  $ZnSiP_2$ . The concentrations of Al and Ca in the precipitated Si granules were less than the acceptable levels for SOG-Si, even though the low-purity MG-Si was used as the raw material. The contents of Fe and Ti were sufficiently less than the target levels for primary Si, which are considered to be easily removed in the refining step. On the other hand, the concentrations of B and P have not achieved the target level at present, which are mainly due to the high impurity contents in the raw material of MG-Si. When electrochemically reduced Si, which is expected to have lower impurity contents than MG-Si, is used as the starting material, lower concentrations of B and P are expected to be achieved.

**Table A.2-2 Impurity contents with removal fractions in the precipitated Si (>2 mm) obtained at different cooling rates, target impurity levels for primary Si, and acceptable impurity levels for solar-grade Si (SOG-Si).**

| Impurity element,<br>A | Impurity content in Si <sup>a</sup> , $x_A$ / ppmw<br>(Removal fraction <sup>†</sup> , $r_A$ ) |                       |                      |                       | Target level for primary Si <sup>‡</sup> ,<br>$x_{A(\text{primary})}$ / ppmw | Acceptable level for SOG-Si <sup>[33]</sup> ,<br>$x_{A(\text{SOG-Si})}$ / ppmw |
|------------------------|--|-----------------------|----------------------|-----------------------|--|--|
|                        | MG-Si  | 10 K h <sup>-1</sup>  | 30 K h <sup>-1</sup> | 100 K h <sup>-1</sup> |  |  |
| B                      | 26   | 3<br>(88%)            | 9<br>(65%)           | 12<br>(54%)           | 0.13–0.38  | 0.1–0.3  |
| P                      | 40   | 48                    | 77                   | 140                   | 0.086–0.4  | 0.03–0.14  |
| Al                     | 978  | <0.01<br>(>99.999%)   | <0.01<br>(>99.999%)  | <0.01<br>(>99.999%)   | <50  | <0.1   |
| Ca                     | 77   | <0.0005<br>(>99.999%) | 2<br>(97%)           | <0.0005<br>(>99.999%) | <125   | <0.2   |
| Fe                     | 2485   | 104<br>(96%)          | 170<br>(93%)         | 2365<br>(54%)         | <12500   | <0.1   |
| Ti                     | 249  | 5<br>(98%)            | 9<br>(96%)           | 54<br>(78%)           | <100   | <10 <sup>-3</sup>  |
| Zn                     | 86   | 13286                 | 8211                 | 2281                  | – <sup>b</sup>   | – <sup>b</sup>   |

<sup>a</sup> Analyzed by ICP-AES.

<sup>b</sup> No data

<sup>†</sup>  $r_A = (1 - x_{A(\text{prec Si})} / x_{A(\text{MG-Si})}) \times 100$

<sup>‡</sup>  $x_{A(\text{primary})} = x_{A(\text{SOG-Si})} / k^{\circ}_A$

### A.3 Si Recovery from Liquid Si–Zn Alloy by Si Precipitation on Si Rod

Si precipitation on Si rods from liquid Si–Zn alloy was investigated as a method to recover Si while the Si–Zn alloy is in a liquid state. Since the melting point of  $\text{CaCl}_2$  is 1045 K, this is the lower limit of the experimental temperature when using  $\text{CaCl}_2$  as the molten salt for the suppression of Zn evaporation. Therefore, the eutectic  $\text{NaCl–CaCl}_2$  ( $\text{NaCl}:\text{CaCl}_2 = 47.9:52.1$  mol%,  $m.p. = 777$  K [34]) was selected to extend the lower limit of the experimental temperature.

#### A.3.1 Experimental

The schematic of the experimental apparatus for the Si precipitation on a Si rod from liquid Si–Zn alloy is shown in Figure A.3-1. Since the solubility of Si in liquid Zn is 6.0 at.% at 1123 K [35], metallic Zn and MG-Si equivalent to 7.0 at% Si were charged into a graphite crucible to ensure that Si would be saturated in the liquid Si–Zn alloy. The size of the graphite crucible and the weights of used materials are summarized in Table A.3-1.  $\text{NaCl}$  and  $\text{CaCl}_2$  powders in eutectic composition were then charged to the crucible and the mixture was dried under vacuum at 453 K

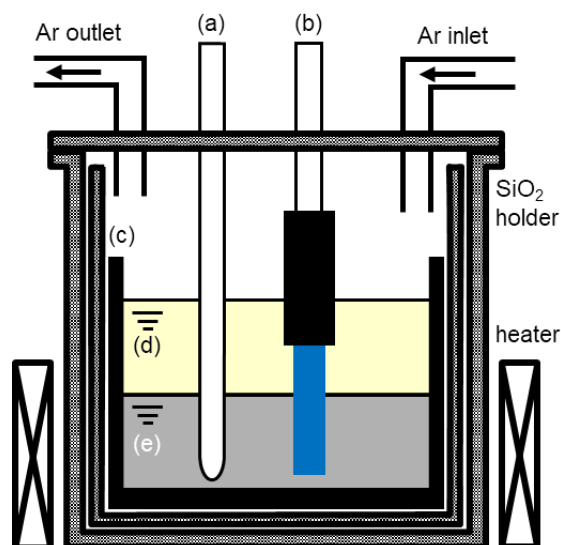


**Figure A.3-1** Schematic of the experimental apparatus for the Si precipitation on a Si rod from liquid Si–Zn alloy. (a) Thermocouple, (b) 10-N Si rod, (c) graphite crucible, (d) molten  $\text{NaCl–CaCl}_2$ , and (e) Si-saturated liquid Si–Zn alloy.

**Table A.3-1 Size of graphite crucible and weight of used materials.**

|        | Size of graphite crucible                | Weight of used materials, <i>m</i> / g |      |      |                   |
|--------|--|--|------|------|-------------------|
|        |  | MG-Si                                  | Zn   | NaCl | CaCl <sub>2</sub> |
| Exp. 1 | o.d. 46 mm × i.d. 40 mm × height 150 mm  | 2.1                                    | 66.3 | 7.5  | 15.7              |
| Exp. 2 | o.d. 105 mm × i.d. 95 mm × height 150 mm | 21.0                                   | 663  | 85   | 175               |

and 653 K for 24 h, respectively. Then the temperature was raised and maintained at 1123 K for more than 24 h to sufficiently react Si and Zn. In Experiment 2, in order to promote the dissolution of MG-Si, the liquid alloy was stirred twice by an Al<sub>2</sub>O<sub>3</sub> tube when the temperature was maintained at 1123 K. Then, a Si rod (Furuuchi Chemical Corp., diameter 6.0 mm, 5N purity) was inserted into the liquid alloy and the temperature was lowered to 923 K over 24 h. After the temperature was maintained at 923 K for 6 h in Experiment 1 and 12 h in Experiment 2, the Si rod was recovered. The liquid Si–Zn alloy was further cooled to 298 K over 5 h. The temperature changes during the cooling step are shown in [Figure A.3-2](#).

Residual salt on the Si rod was removed by distilled water and then Zn was dissolved by a 20 wt.% HCl solution prepared from a 36 wt.% solution. The surface and cross section of the Si rod obtained in Experiment 1 were observed using optical microscopy. For the Si rod obtained in Experiment 2, a part of the Si granules precipitated on the Si rod was recovered and immersed in a 10 wt.% HCl solution prepared from the same HCl solution and a 10 wt.% HNO<sub>3</sub> solution prepared from 60 wt.% HNO<sub>3</sub> solution (FUJIFILM Wako Pure Chemical Corp., reagent grade) overnight, respectively. The impurity contents in the Si granules were analyzed by ICP-AES.

### A.3.2 Results and Discussion

[Figure A.3-3](#) shows the surface and the cross-sectional images of the Si rod obtained in Experiment 1. Epitaxial growth of precipitated Si was observed from the surface image, and a Si layer of approximately 0.3 mm was confirmed from the cross-sectional image. However, the

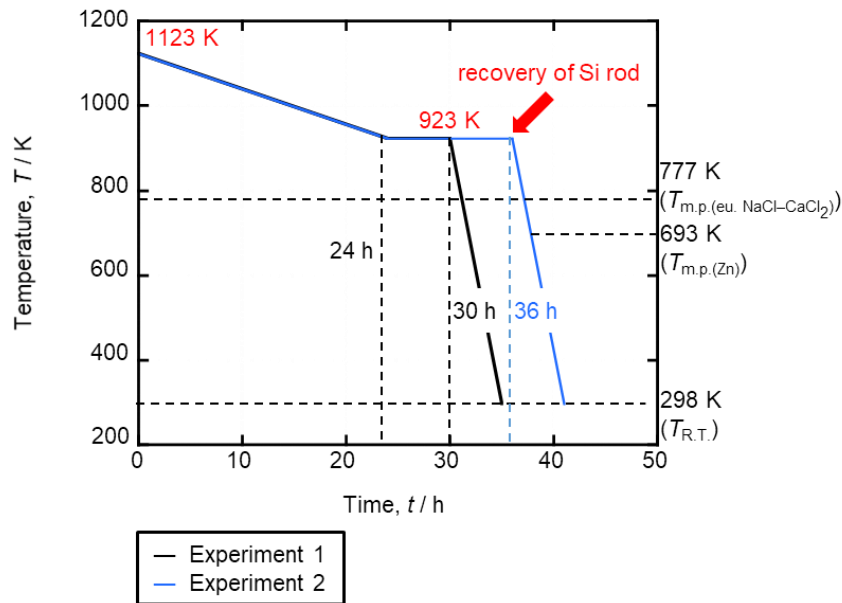


**Figure A.3-2** Temperature changes during the cooling step.

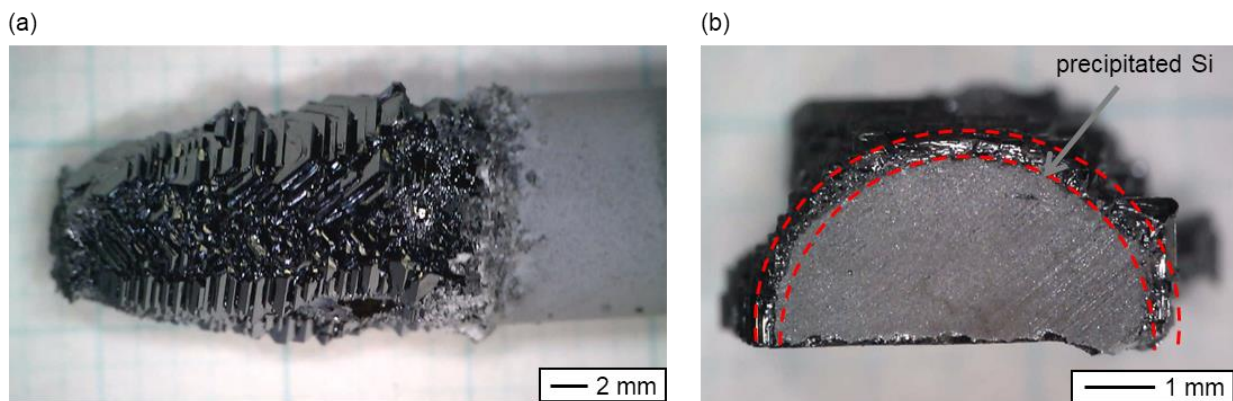


**Figure A.3-3** (a) Surface and (b) cross-sectional images of the Si rod obtained in Experiment 1.

diameter of the Si rod decreased as shown in Figure A.3-3(a), and the weight also decreased by 0.36 g, suggesting the dissolution of the Si rod before the precipitation. In Experiment 1, MG-Si equivalent to 7.0 at.% Si was added to ensure the preparation of Si-saturated (6.0 at.%) Si–Zn alloy at 1123 K. However, undissolved MG-Si was observed at the bottom of the Zn lump, indicating that the Si concentration in the liquid Si–Zn alloy was not saturated. The reason is considered to be the surface oxidation of MG-Si.

In order to promote the dissolution of MG-Si, the liquid alloy was stirred twice during the dissolution of Si at 1123 K. Figure A.3-4 shows the optical images of the Si rod obtained in

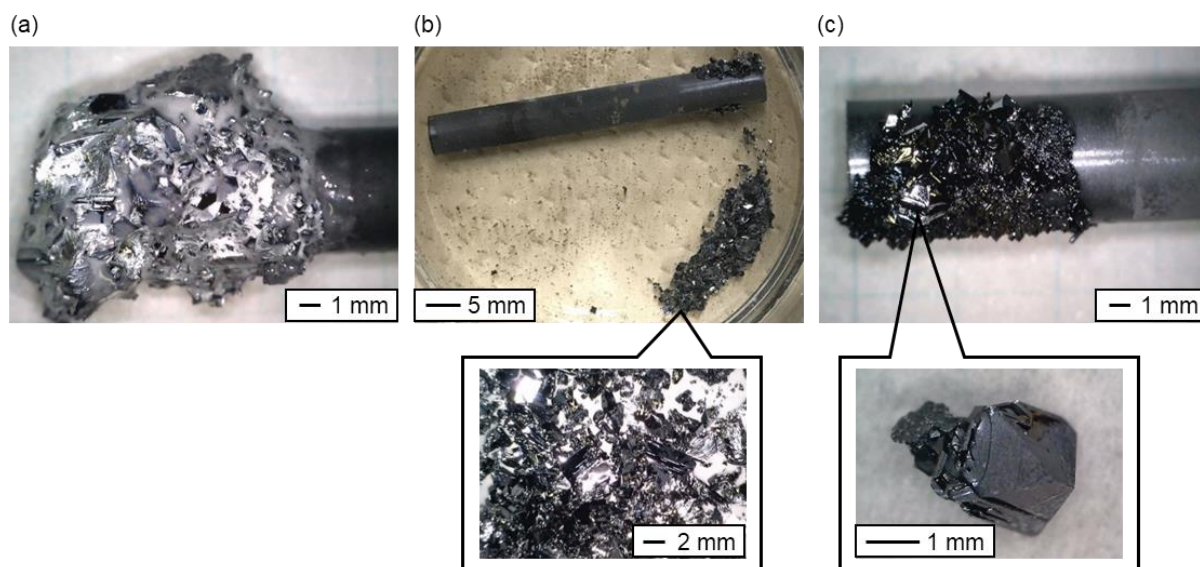


**Figure A.3-4** Optical images of the Si rod (a) recovered from liquid Si-Zn alloy, (b) during the removal of residual Zn, and (c) after the removal of Zn.

Experiment 2. After residual salts and Zn were removed, the precipitation of Si granules with a maximum particle size of approximately 2 mm was confirmed. On the other hand, unlike Experiment 1, Si rod was partially exposed and epitaxial growth of the precipitated Si was not observed. As shown in [Figure A.3-4\(b\)](#), the precipitated Si partially fell off during the removal of residual Zn, suggesting that the adhesion of the precipitated Si was low due to surface oxidation of the Si rod. The total weight of the precipitated Si recovered by the Si rod was calculated from the weight change of the Si rod and the weight of the Si granules fallen off during the removal of residual Zn. As the result, 0.314 g of precipitated Si was recovered by the Si rod, which was only 1.7% of the theoretical Si precipitation (18 g). Considering the result of Experiment 1, efficient Si recovery could be expected by dissolving the surface of the Si rod in the liquid alloy to promote the epitaxial growth of the precipitated Si.

Impurity contents in the Si granules recovered from Experiment 2 are shown in [Table A.3-2](#). The concentrations of impurities were sufficiently smaller than the target levels for primary Si except B and P. The removal fractions were more than 99% for Al and Zn, more than 90% for Ca, Fe, and Ti, 81% for B and 68% for P. The removal fraction of P was much better than the result

**Table A.3-2 Impurity contents with removal fractions in the precipitated Si recovered from the Si rod obtained in Experiment 2, and the target impurity levels for primary Si.**

| Impurity element, A | Impurity content in Si <sup>a</sup> , $x_A$ / ppmw<br>(Removal fraction <sup>†</sup> , $r_A$ ) |                      | Target level for primary Si <sup>‡</sup> ,<br>$x_{A(\text{primary})}$ / ppmw |
|---------------------|--|----------------------|--|
|                     | MG-Si  | Precipitated Si      |  |
| B                   | 26   | 5<br>(81%)           | 0.13–0.38  |
| P                   | 40   | 13<br>(68%)          | 0.086–0.4  |
| Al                  | 978  | 5<br>(99%)           | <50  |
| Ca                  | 77   | 4<br>(95%)           | <125   |
| Fe                  | 2485   | 250<br>(90%)         | <12500   |
| Ti                  | 249  | 6<br>(98%)           | <100   |
| Zn                  | 86   | <0.0075<br>(>99.99%) | – <sup>b</sup>   |

<sup>a</sup> Analyzed by ICP-AES.

<sup>b</sup> No data

$$^{\dagger} r_A = (1 - x_{A(\text{prec Si})} / x_{A(\text{MG-Si})}) \times 100$$

$$^{\ddagger} x_{A(\text{primary})} = x_{A(\text{SOG-Si})} / k_A^{\circ}$$

obtained in section A.2, suggesting that the formation of  $\text{ZnSiP}_2$  was suppressed by keeping the Si–Zn alloy in the liquid state during Si precipitation. It should be mentioned that the concentration of Zn was decreased below the detection limit of ICP-AES, which was much better than the result of the samples recovered from the Zn lump after cooling to room temperature (section A.2). Therefore, Si recovery using a Si rod is expected to reduce the energy consumption in the evaporation removal of residual Zn in the practical process.



## A.4 Reference List

- [1] J. Yang, S. Lu, S. Kan, X. Zhang and J. Du, *Chem. Commun.*, 3273 (2009).
- [2] Y. Nishimura, T. Nohira, K. Kobayashi and R. Hagiwara, *J. Electrochem. Soc.*, **158**, E55 (2011).
- [3] J. Zhao, S. Lu, L. Hu and C. Li, *J. Energy Chem.*, **22**, 819 (2013).
- [4] J. Zhao, J. Li, P. Ying, W. Zhang, L. Meng and C. Li, *Chem. Commun.*, **49**, 4477 (2013).
- [5] S. Fang, H. Wang, J. Yang, S. Lu, B. Yu, J. Wang and C. Zhao, *Mater. Lett.*, **160**, 1 (2015).
- [6] S. Fang, H. Wang, J. Yang, S. Lu, B. Yu, J. Wang and C. Zhao, *J. Phys. Chem. Solids*, **89**, 1 (2016).
- [7] S. Fang, H. Wang, J. Yang, B. Yu and S. Lu, *Faraday Discuss.*, **190**, 433 (2016).
- [8] Z. Yu, N. Wang, S. Fang, X. Qi, Z. Gao, J. Yang and S. Lu, *Ind. Eng. Chem. Res.*, **59**, 1 (2020).
- [9] W. Weng and W. Xiao, *ACS Appl. Energy Mater.*, **2**, 804 (2019).
- [10] W. Weng, J. Yang, J. Zhou, D. Gu and W. Xiao, *Adv. Sci.*, **7**, 2001492 (2020).
- [11] Y. Zhang, Y. Zhang, X. Li, J. Liu, M. Zhang, X. Yang, M. Huang, M. Xu, P. Dong and Z. Zhou, *JOM*, **72**, 2245 (2020).
- [12] Y. P. Zaykov, A. V. Isakov, A. P. Apisarov and O. V. Chemezov, *Russ. J. Non-Ferr. Met.*, **1**, 33 (2014).
- [13] S. Zhuk, V. Isaev, O. Grishenkova, A. Isakov, A. Apisarov and Y. Zaykov, *J. Serb. Chem. Soc.*, **82**, 51 (2017).
- [14] X. Zou, L. Ji, Z. Pang, Q. Xu and X. Lu, *J. Energy Chem.*, **44**, 147 (2020).
- [15] Y. Dong, T. Slade, M. J. Stolt, L. Li, S. N. Girard, L. Mai and S. Jin, *Angew. Chem. Int. Ed.*, **56**, 14453 (2017).
- [16] H. Nishihara, T. Suzuki, H. Itoi, B. An, S. Iwamura, R. Berenguer and T. Kyotani, *Nanoscale*, **6**, 10574 (2014).

- [17] H. Zhao, H. Xie, X. Zhou, J. Qu, Z. Zhao, Q. Song, Z. Ning, P. Xing and H. Yin, *J. Electrochem. Soc.*, **166**, E137 (2019).
- [18] Y. Li, X. Fang, K. Li, J. Liang and Z. Li, Chinese Patent 101306591A (2008). [in Chinese]
- [19] Y. Li, J. Liang, H. Li, G. Tang and W. Tian, *Zhongguo Youse Jinshu Xuebao*, **19**, 714 (2009). [in Chinese]
- [20] H. Yang, Y. Zhang, Y. Li, G. Tang and K. Jia, *Defect Diffus. Forum*, **295-296**, 33 (2009).
- [21] H. Yang, Y. Li, Y. Li, G. Tang, N. He and Y. Zhang, *Adv. Mater. Res.*, **139-141**, 666 (2010).
- [22] H. Yang, L. Shang, G. Tang, Y. Zhang and Y. Li, *Mater. Trans.*, **54**, 1006 (2013).
- [23] H. Li, J. Liang, S. Xie, L. Wang, Y. Li and X. Li, Chinese Patent 107338460A (2017). [in Chinese]
- [24] H. Yang, Y. Zhang, Y. Li, G. Tang and N. He, *Gongneng Cailiao*, **40**, 915 (2009). [in Chinese]
- [25] Z. Cai, Y. Li, X. He and J. Liang, *Metall. Mater. Trans. B*, **41B**, 1033 (2010).
- [26] X. He, Y. Li and Z. Li, *Youse Jinshu, Yelian Bufen*, 21 (2014).
- [27] Y. Wang, H. Yang, Y. Wu, H. Xu, X. Wang and C. Feng, *Diandu Yu Tushi*, **34**, 1160 (2015). [in Chinese]
- [28] H. Li, D. Wang, J. Liang, H. Yan, Z. Cai and R. G. Reddy, *Int. J. Chem. React. Eng.*, **18**, 20190112 (2019).
- [29] V. V. Malyshev, N. N. Uskova and V. I. Shapoval, *Powder Metall. Met. Ceram.*, **36**, 289 (1997).
- [30] S. V. Devyatkin, *J. Min. Metall., Sect. B*, **39**, 303 (2003).
- [31] P. Gao, X. Jin, D. Wang, X. Hu and G. Z. Chen, *J. Electroanal. Chem.*, **579**, 321 (2005).
- [32] A. D. Martinez, E. L. Warren, P. C. Dippo, D. Kuciauskas, B. R. Ortiz, H. Guthrey, A. Duda, A. G. Norman, E. S. Toberer and A. C. Tamboli, *Single Crystal Growth and Phase Stability of Photovoltaic Grade ZnSiP<sub>2</sub> by Flux Technique*, 42nd Photovoltaic Specialist Conference (PVSC), IEEE, New Orleans, LA, USA (2015).

- [33] N. Yuge, M. Abe, K. Hanazawa, H. Baba, N. Nakamura, Y. Kato, Y. Sakaguchi, S. Hiwasa and F. Aratani, *Prog. Photovolt. Res. Appl.*, **9**, 203 (2001).
- [34] G. J. Janz, R. P. T. Tomkins, C. B. Allen, J. R. Downey, G. L. Garner, U. Krebs and S. K. Singer, *J. Phys. Chem. Ref. Data*, **4**, 871 (1975).
- [35] R. W. Olesinski and G. J. Abbaschian, *Bull. Alloy Phase Diagrams*, **6**, 545 (1985).

# Acknowledgement

First of all, the author expresses her sincere gratitude to Professor Toshiyuki Nohira for his guidance, proper suggestions, and fruitful discussions throughout this study, including the concrete advice in the laboratory. The author also would like to express her deepest appreciation for his generous kindness.

The author expresses her appreciation to Professor Rika Hagiwara for his rewarding discussions and valuable suggestions. The author also would like appreciate Professor Takashi Sagawa for careful reading of this thesis and valuable discussions and suggestions.

The deep appreciation goes to Associate Professor Kouji Yasuda, Department of Materials Science and Engineering, Graduate School of Engineering, Kyoto University, for his support on experiments and thermodynamic calculations, deep discussions and concrete advice not only for the research but also for the presentation and writing skills.

Special acknowledgement is given to Associate Professor Tsutomu Kodaki for his useful advice and continuous encouragement throughout this study. Also, the author is deeply grateful to Assistant Professor Takayuki Yamamoto for his support especially on the analysis of Raman spectra, discussions on the research, and valuable suggestions on this thesis. The author also would like to appreciate Assistant Professor Yutaro Norikawa for his helpful discussions and advice on experiments and this thesis. Special thanks are extended to Assistant Professor Xiao Yang, Westlake University, for his valuable advice on the experiments, and continuous encouragement. The author would like to offer her special thanks to Associate Professor Ming Zhong, Northeastern University, for his support especially on the use of floating zone furnace and helpful advice on the experiments. The author is also grateful to Associate Professor Kenji Kawaguchi for his helpful advice on the

experiments. The heartfelt thanks are given to Mr. Junichi Imaru for his technical support especially for constructing experimental systems.

The author would like to show her thanks to all the members of Nohira laboratory for their warm encouragement, and lively discussions. Special appreciation is given to Mr. Akifumi Ido for his support on the experiment and conference presentation. The author expresses her appreciative feelings to Dr. Yumi Katasho, Mr. Hang Hua, Mr. Keigo Aoyama, and Mr. Kouji Hidaka for their warm encouragement and lively discussions. Also, special thanks are given to Ms. Hiromi Takatori and Ms. Naoko Sakamoto for their help in administrative works and daily encouragement.

The author would like to express her acknowledgement to all researchers and students for the technical discussions in the conference, official and unofficial meeting. Deeply appreciation is also given to all people involving the author's research and the chance to learn scientific research.

Finally, I would like to express my deepest gratitude to my parent, boyfriend and his parents for their continual encouragement and unconditional support, which allowed me could finish my study without any worries. Also, special appreciation is given to Yibo Wang and Zhan Xiao, who have taught me the importance of perseverance and the power of love.

March 2022

Yuanjia Ma